Supersymmetric QCD Corrections and Phenomenological Studies in Relation to Coannihilation of Dark Matter

Dissertation
zur Erlangung des Doktorgrades
des Department Physik
der Universität Hamburg

vorgelegt von
Julia Harz

aus
München

Hamburg
2013

Zusammenfassung

In der vorliegenden Doktorarbeit wird eine minimale supersymmetrische Erweiterung des Standard Modells (MSSM) mit erhaltender R-Parität angenommen. Hierbei is das leichteste Neutralino ein guter Kandidat für kalte, dunkle Materie. Durch den Vergleich der theoretisch vorhergesagten Neutralinorestdichte mit dem experimentell sehr genau bestimmten Wert, können strenge Grenzen an den MSSM Parameterraum gesetzt werden. Um die experimentelle Genauigkeit zu erreichen, ist es notwendig Unsicherheiten innerhalb der theoretischen Berechnung zu reduzieren. Eine der Hauptunsicherheiten liegt in der Berechnung des Wirkungsquerschnitts von Annihilations- und Koannihilationsprozessen des Dunkle–Materie–Teilchens.

In einer phenomenologischen Studie untersuchen wir das Zusammenspiel zwischen Neutralino–Neutralino–Annihilation, Neutralino–Stop–Koannihilation und Stop–Stop–Annihilation näher. Wir zeigen, dass Neutralino–Stop–Koannihilation signifikant zur Neutralinorestdichte beitragen kann. Auch hinsichtlich der Entdeckung eines Higgsbosons mit einer Masse von 125 GeV ist dieser Prozess sehr interessant. Auf Grund dieser Motivation haben wir alle supersymmetrischen QCD Korrekturen der Ordnung $\mathcal{O}(\alpha_s)$ zur Neutralino–Squark–Koannihilation berechnet. Wir beschreiben detailliert das von uns gewählte $\overline{\text{DR}}$/on-shell Renormierungsschema zur Behandlung der ultravioletten Divergenzen und präsentieren die sogenannte „phase space slicing"–Methode, mit der wir softe und kollineare Divergenzen isolieren. Zusätzlich gehen wir auf die spezielle Behandlung von auftretenden on-shell Zustände in Propagatoren ein.

Die gesamte Berechnung ist in das Softwarepaket `DM@NLO` implementiert worden und dient somit als Erweiterung zu existierenden Computerprogrammen, die eine numerische Berechnung der Restdichte dunkler Materie durchführen. Diese allerdings verwenden in ihrer Berechnung lediglich Wirkungsquerschnitte, die auf einem effektiven Born–Niveau berechnet worden sind.

Am Beispiel von drei Szenarien untersuchen wir den Einfluss der berechneten Korrekturen auf den Wirkungsquerschnitt der Annihilations- und Koannihilationsprozesse. Hierbei beobachten wir eine Korrektur von bis zu 30 %. Dies wiederum führt zu einer Korrektur von ca. 5-9 % auf die Neutralinorestdichte, was größer als die momentane experimentelle Unsicherheit ist. Es ist daher notwendig, die hier behandelten Korrekturen für eine präzise Vorhersage der Neutralinorestdichte zu berücksichtigen.

Abstract

In this thesis, we assume a minimal supersymmetric extension of the Standard Model (MSSM) with conserved R-parity such that the lightest neutralino is the cold dark matter candidate. A stringent constraint on the MSSM parameter space can be set by the comparison of the predicted neutralino relic density with the experimentally determined value. In order to match the high experimental precision, uncertainties within the theoretical calculation have to be reduced. One of the main uncertainties arises from the cross section of annihilation and coannihilation processes of the dark matter particle.

In a phenomenological study we investigate the interplay of neutralino-neutralino annihilation, neutralino-stop coannihilation and stop-stop annihilation. We demonstrate that neutralino-stop coannihilation contributes significantly to the neutralino relic density and is furthermore very well motivated due to the recent discovery of a 125 GeV Higgs boson.

Due to this ample motivation we have calculated the full $\mathcal{O}(\alpha_s)$ supersymmetric QCD corrections to neutralino-squark coannihilation. We show in detail our $\overline{\text{DR}}$/on-shell renormalization scheme for the treatment of ultraviolet divergences, and describe the phase space slicing method which is used to handle soft and collinear infrared divergences. Further, we comment on the treatment of occurring intermediate on-shell states.

The whole calculation is provided within the numerical tool `DM@NLO` that serves as an extension to existing relic density calculators, which consider only an effective tree-level calculation. Based on three example scenarios we study the impact of the NLO corrections on the total (co)annihilation cross section, and observe corrections of up to 30 %. This leads to a correction of $5 - 9$ % on the relic density, which is larger than the current experimental uncertainty and is, thus, important to be taken into account.

Contents

1 Introduction

Almost hundred years ago, the first hint on the existence of dark matter was found. Since then, the nature of dark matter belongs to one of the biggest unsolved questions in modern physics. Over the past years, many theories have tried to accommodate a dark matter particle within the established theoretical framework. Supersymmetry is probably the most often discussed theory within this context. This is due to the fact that the minimal supersymmetric extension of the Standard Model of particle physics with conserved R-parity provides naturally a good cold dark matter candidate.

The properties of this particle fulfil all the requirements on dark matter which have been set through various experiments. While astrophysical observations are able to give us information about the characteristics dark matter has to possess, we have, however, not yet managed to clearly identify a specific particle forming dark matter. To do so, all over the world, many different astrophysical and collider experiments try to discover such a dark matter particle.

Although we do not exactly know what dark matter is, we know very precisely how much dark matter is around us. Due to measurements of the cosmic microwave background, we have a precise value for the relic density, which describes the amount of dark matter that is present today.

Having a precise measurement of the amount of dark matter on the one hand, and a theory which is able to describe a particle which could account for dark matter on the other hand, we can combine both in order to constrain the theory based on experimental observations. By taking advantage of the interplay between astroparticle and particle physics, further bounds can be considered like the mass of the recently discovered Higgs boson, for instance. Thus, one is able to exclude certain regions in the parameter space of a theory or to identify a particle in case of a discovery.

In order to match theoretical predictions with experimental observations it is crucial that the theoretical uncertainties are at least of the same order of the experimental errors. However, especially with the new data from the Planck satellite, which has measured the cosmic microwave background with an unprecedented precision, the theoretical uncertainties in the prediction of the relic density are larger. Thus, there is a common effort within the community to reduce these uncertainties in order to provide a more precise relic density prediction.

As the relic density depends significantly on the cross section of the (co)annihilation of dark matter particles, one possibility is to improve the calculation of this quantity. As up to now, public computing tools calculate the relic density based on a tree-level

calculation, it is promising to calculate the relevant cross sections at next-to-leading order such that the theoretical uncertainty can be reduced.

Not only pair annihilation of two dark matter particles contributes to the calculation of the relic density, but also coannihilation processes of dark matter with an almost mass degenerate second particle. In case of the minimal supersymmetric extension of the Standard Model (MSSM), for example, coannihilation of neutralinos and stops can occur.

Therefore, we want to study in this work neutralino-stop coannihilation in the context of achieving the experimentally determined relic density as well as with respect to current constraints arising from particle physics. In order to obtain a more precise relic density prediction, we perform a full next-to-leading-order SUSY-QCD calculation to neutralino-squark coannihilation, and study finally its impact on the neutralino relic density.

We demonstrate that the achieved corrections are larger than current experimental uncertainties, and, thus, are important to be taken into account, in particular regarding exclusion bounds within the MSSM parameter space.

The thesis is organized as follows:

In *Chapter 2* we motivate, why Supersymmetry is an appealing extension of the Standard Model of particle physics. We further give the basic theoretical building blocks of Supersymmetry and introduce the MSSM, which we consider in the following. We give an overview of the MSSM particle content including the lightest neutralino, which is assumed to be the dark matter candidate.

In the subsequent *Chapter 3* we focus on dark matter. Evidence for the existence of dark matter is given, and the necessary requirements on a possible dark matter particle are discussed. We further review some frequently studied dark matter candidates, stress their advantages and comment on their shortcomings. Moreover, we give an overview of the current status of different dark matter searches.

Having set the theoretical and experimental foundations, we focus further on the calculation of the relic density in *Chapter 4*, as this will be important to understand the impact of the (co)annihilation cross section. Since we focus on neutralino-stop coannihilation in this work, we show explicitly the calculation of the relic density including these coannihilation processes and conclude with discussing uncertainties which enter the calculation.

In the subsequent *Chapter 5* we discuss the current status of loop corrected (co)annihilation cross sections and introduce the numerical package `DM@NLO`. This code provides the SUSY-QCD corrected cross sections for all relevant processes which enter the relic density computation. It can be used as an extension to existing relic density calculators in order to obtain a more precise theoretical prediction for the relic density.

In *Chapter 6* we concentrate on the phenomenology of neutralino-stop coannihilation. We show the interplay between different (co)annihilation processes to the relic density, and put it in the context of other experimental constraints. A performed

parameter study is discussed, in which we study the interplay of different final states of neutralino-stop coannihilation. Moreover, we introduce three example scenarios, which we will use in order to discuss the impact of the calculated corrections in a later chapter.

The performed one-loop calculation will be topic of *Chapter 7*, where we elaborate on the virtual contributions occurring in the Higgs and vector boson final states. We show all relevant diagrams and introduce our generic implementation within the `DM@NLO` code. The corresponding details regarding the virtual corrections are given in the Appendix.

The renormalization procedure is explained in *Chapter 8*. The chosen renormalization scheme is motivated, and all necessary counterterms which are needed within the calculation are given explicitly.

The treatment of the real contributions is presented in *Chapter 9*. We introduce the phase space slicing method for massive and massless final states in order to treat carefully the occuring soft and collinear divergences. We put this in the context of other approaches and discuss the case of intermediate on-shell states which occur within the calculation of the $W^{\pm}$ final state.

Having discussed in detail the full one-loop calculation, we demonstrate the impact of the loop corrections in *Chapter 10*. We study in detail the effect on the cross section for different final states based on the example scenarios we introduced before. Further, we show the impact on the relic density and show the significant shift on the PLANCK favoured regions of parameter space.

Finally, we conclude in *Chapter 11*.

Parts of the thesis have already been published in Refs. [1, 2]. For those parts, however, we show here more details and updated plots taking into account the latest results of PLANCK.

2 Supersymmetry and the MSSM

With the recent discovery of a Higgs boson [3, 4], particle physics is one step further in solving the question of electroweak symmetry breaking. However, it is still an open question if the discovered particle is *the* Standard Model Higgs boson or merely a Standard Model like Higgs boson of another underlying theory, like Supersymmetry (SUSY), for instance.

As Supersymmetry can explain the existence of a Higgs boson as well as several shortcomings of the Standard Model, it is a well motivated and broadly studied theory. In the following, we will discuss the motivation of Supersymmetry and its underlying theory. Furthermore, we introduce the *Minimal Supersymmetric Standard Model* (MSSM) and the corresponding particle content, which will be necessary for the discussion within this work.

2.1 Motivation of Supersymmetry

The Standard Model of particle physics is an impressive theory which has described fundamental interactions and elementary particles which all have been discovered with dedicated experiments throughout the last decades. Nevertheless, there are still some remaining open questions which cannot be explained by the current Standard Model.

First, we have hints that there is something we call *dark matter*. However, the common Standard Model of particle physics cannot explain dark matter with its known particle content by itself. In order to obey all constraints on dark matter we know so far, a new kind of particle is expected to exist. For a detailed discussion on dark matter we refer to the next chapter 3.

Second, the aesthetic issue of unifying all three gauge couplings at a high scale would require some new physics beyond the Standard Model. New physics could modify the running of the couplings above the electroweak scale such that unification would be possible. Theories which give rise to such a unification are also called *Grand Unified Theories* (GUT).

Another motivation we want to mention for physics beyond the Standard Model concerns the so called *hierarchy problem* [5, 6]. The Standard Model of particle physics is an effective theory and thus, valid up to a mass scale Λ. This scale enters, for instance, the one-loop contributions to the Higgs mass m_h. Thereby, the dominant
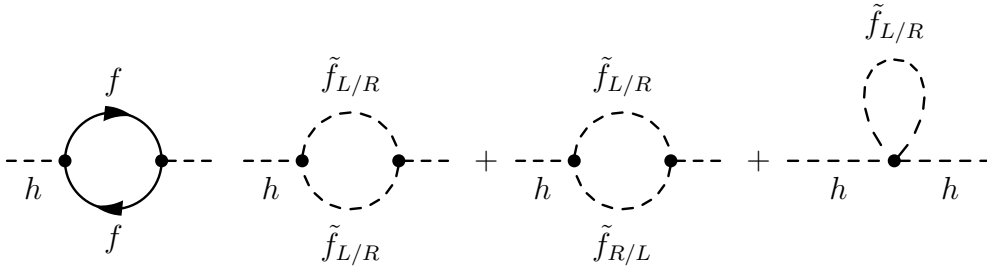
Figure 2.1: Standard Model fermion contribution (left) and scalar contribution (right) to the Higgs self energy.

contribution comes from the fermion loop carrying a quadratic divergence.

$$\Delta m_h^2(f) = \frac{-2\lambda_f^2}{16\pi^2}\Lambda^2 \tag{2.1}$$

With the cutoff-scale being around the Planck-scale, this is in clear discrepancy with expecting the Higgs mass around the electroweak scale bounded by triviality, perturbativity and vacuum stability. A huge fine-tuning would be necessary to cancel this divergence order-by-order. Therefore, a new symmetry which protects the Higgs mass would be much more natural, similar to the gauge or chiral symmetry, which prevents the masses of the gauge bosons or scalars, respectively.

One solution to the hierarchy problem and also to the other aforementioned issues would be Supersymmetry. This theory introduces a bosonic degree of freedom for every Standard Model fermionic degree of freedom and vice versa. The contribution of a supersymmetric scalar particle to the Higgs boson can be written as

$$\Delta m_h^2(\tilde{f}) = 2\frac{\lambda_{\tilde{f}}}{16\pi^2}\Lambda^2. \tag{2.2}$$

Under the assumption of $|\lambda_f|^2 = \lambda_{\tilde{f}}$, the loop of Eq. (2.2) would exactly cancel the quadratically divergent contribution of the fermion loop to the Higgs mass of Eq. (2.1), see Fig. 2.1. The difference in sign arises from the closed fermion loop, the factor two in Eq. (2.2) is due to two chirality states of the scalar particle. Thus, Supersymmetry would prevent the Higgs mass from large quadratic divergences.
As Supersymmetry is able to circumvent all the aforementioned shortcomings of the Standard Model of particle physics, we want to have a closer look on its algebra, the minimal supersymmetric extension of the Standard Model (MSSM), and finally study the SUSY particle spectrum.

2.2 The Theory of SUSY

Supersymmetry is a fascinating theory, not only because of the aforementioned phenomenological consequences, but also from a more mathematical point of view. In the following we want to study the theoretical motivation further, in order to derive the supersymmetric Lagrangian in the end of this section.

2.2.1 SUSY Algebra

Supersymmetry is the only possible way of combining the space-time symmetry of the Poincaré algebra with another continuous symmetry of the S-matrix consistent in a non-trivial way within the relativistic quantum field theory. In the 1960s, the Coleman-Mandula No-Go theorem [7] stated that a Lie algebra containing the Poincarè algebra as a subgroup and another internal symmetry has to be a direct sum and it is not possible to join them in a non-trivial way.

However, in 1975 the Haag-Łopuszańksi-Sohnius theorem [8] claimed on the basis of work which was done by Wess and Zumino, that Supersymmetry can evade the Coleman-Mandula theorem by going beyond usual Lie algebras. Considering graded Lie algebras which also involve anticommutator relations, the Coleman-Mandula Theorem does not apply anymore. Within a Z_2 graded Lie algebra, even (bosonic) and odd (fermionic) generators exist. The bosonic generators of the Lie subalgebra obey the Coleman-Mandula theorem, and is a direct sum of the Poincaré algebra with internal symmetries. The odd generators, however, belong to the $(\frac{1}{2}, 0)$ and $(0, \frac{1}{2})$ representation of the homogeneous Lorentz group. With spinorial generators existing in the fermionic subalgebra, the so-called supercharges Q_α, a transformation between both subalgebras is possible. Thus, a non-trivial fusion of space-time symmetry and a Z_2 graded Lie algebra is achieved.

Thus, the theory of Supersymmetry is the most general continuous symmetry of the S-matrix which is consistent with the Coleman-Mandula theorem. It is an outstanding mathematical and physical motivated theory, which ever since has been a highly attractive and widely discussed topic. For further details concerning the Coleman-Mandula theorem and a detailed derivation of the Haag-Łopuszańksi-Sohnius theorem, we suggest Refs. [9] and [10].

In the following, we focus on N=1 Supersymmetry, such that we consider only one additional fermionic generator $Q_\alpha^{N=1}$. This generator makes the transformation of a fermion to a boson and vice versa possible

$$Q_\alpha|\text{fermion}\rangle = |\text{boson}\rangle \qquad \text{and} \qquad Q_\alpha|\text{boson}\rangle = |\text{fermion}\rangle. \qquad (2.3)$$

The underlying algebra consists of the usual Poincarè algebra, which is given by

$$[P_\mu, P_\nu] = 0, \tag{2.4}$$

$$[M_{\mu\nu}, P_\rho] = i(\eta_{\nu\rho} P_\mu - \eta_{\mu\rho} P_\nu), \tag{2.5}$$

$$[M_{\mu\nu}, M_{\rho\sigma}] = -i(\eta_{\mu\rho} M_{\nu\sigma} - \eta_{\mu\sigma} M_{\nu\rho} - \eta_{\nu\rho} M_{\mu\sigma} - \eta_{\nu\sigma} M_{\mu\rho}), \tag{2.6}$$

where P_μ is the generator of space-time translation and $M_{\mu\nu}$ the generator of the Lorentz-transformations. This is enlarged to the super-Poincarè algebra by

$$\{Q_\alpha, \overline{Q}_{\dot\beta}\} = 2\sigma^\mu_{\alpha\dot\beta} P_\mu \tag{2.7}$$

$$\{\overline{Q}^{\dot\alpha}, Q^\beta\} = 2\sigma^\mu_{\alpha\dot\beta} P_\mu, \tag{2.8}$$

$$\{Q_\alpha, Q_\beta\} = \{\overline{Q}^{\dot\alpha}, \overline{Q}^{\dot\beta}\} = 0 \tag{2.9}$$

$$[Q_\alpha, P^\mu] = [\overline{Q}^{\dot\alpha}, P^\mu] = 0 \tag{2.10}$$

$$[M_{\rho\nu}, Q_\alpha] = -(\sigma_{\mu\nu})^\beta_\alpha Q_\beta \tag{2.11}$$

$$[M_{\rho\nu}, \overline{Q}^{\dot\alpha}] = -(\overline{\sigma}_{\mu\nu})^{\dot\alpha}_{\dot\beta} \overline{Q}^{\dot\beta} \tag{2.12}$$

$$[Q_\alpha, R] = Q_\alpha, [\overline{Q}^{\dot\alpha}, R] = -\overline{Q}_{\dot\alpha} \tag{2.13}$$

where $\sigma^\mu_{\alpha\dot\beta} = (\mathbf{1}, \sigma_i)$ and $\overline{\sigma}^\mu_{\alpha\dot\beta} = (\mathbf{1}, -\sigma_i)$ with σ_i being the Pauli matrices. Q_α is the fermionic spinorial SUSY generator. An additional global U(1)-symmetry of the algebra can be identified, which is called R-invariance. The corresponding generator is indicated by R.

The subscript $\alpha = 1, 2$ indicates the $(\frac{1}{2}, 0)$ representation, whereas $\dot\alpha = 1, 2$ denotes the $(0, \frac{1}{2})$ representation of the homogeneous Lorentz group.

To obtain a complete theory, the usual Minkowski-space with its four "bosonic" commuting space-time coordinates has to be extended by four "fermionic" anticommuting Grassmann variables $\theta_{\alpha=1,2}$ and $\overline{\theta}_{\dot\beta=1,2}$, denoted as two-component Weyl spinors obeying

$$\{\theta_\alpha, \theta_\beta\} = \{\overline{\theta}_{\dot\alpha}, \overline{\theta}_{\dot\beta}\} = \{\theta_\alpha, \overline{\theta}_{\dot\beta}\} = 0. \tag{2.14}$$

These eight coordinates build up the so-called *superspace*.

Defining the following unitary operator in terms of the Hermitian operators P_μ, Q_α and $\overline{Q}_{\dot\alpha}$

$$U(x, \theta, \overline{\theta}) \equiv e^{i(\theta Q + \overline{\theta Q} - x_\mu P^\mu)}, \tag{2.15}$$

we can calculate the product of two of these transformation operators

$$U(a_\mu, \xi, \overline{\xi}) U(x_\mu, \theta, \overline{\theta}) = U(a_\mu + x_\mu - i\theta^\alpha (\sigma_\mu)_{\alpha\dot\beta} \overline{\xi}^{\dot\beta}, \theta + \xi, \overline{\theta} + \overline{\xi}). \tag{2.16}$$

The additional term in the Minkowski-coordinates of the resulting transformation is caused due to the fact that Q and $\overline{Q}$ do not commute. This makes the non-trivial connection of both groups visible.

We can now apply this transformation on a function in superspace $\Phi(x, \theta, \overline{\theta})$, which is called *superfield*. This results in

$$U(a_\mu, \xi, \overline{\xi}) U(x_\mu, \theta, \overline{\theta}) \Phi(0) U^{-1}(x_\mu, \theta, \overline{\theta}) U^{-1}(a_\mu, \xi, \overline{\xi})$$

$$= \Phi(a_\mu + x_\mu - i\theta^\beta (\sigma_\mu)_{\alpha\dot{\beta}} \overline{\xi}^{\dot{\beta}}, \theta + \xi, \overline{\theta} + \overline{\xi}). \tag{2.17}$$

In order to obtain the differential representation of the group operators we analyse the infinitesimal variation of this superfield $\delta_s \Phi$, and obtain

$$Q_\alpha = \frac{\partial}{\partial \theta_\alpha} - i\sigma^\mu_{\alpha\dot{\beta}} \overline{\theta}^{\dot{\beta}} \partial_\mu \qquad \overline{Q}_{\dot{\alpha}} = -\frac{\partial}{\partial \overline{\theta}^{\dot{\alpha}}} + i\theta^\beta \sigma^\mu_{\beta\dot{\alpha}} \partial_\mu. \tag{2.18}$$

The covariant derivatives are defined as

$$D_\alpha = \frac{\partial}{\partial \theta_\alpha} + i\sigma^\mu_{\alpha\dot{\beta}} \overline{\theta}^{\dot{\beta}} \partial_\mu \qquad \overline{D}_{\dot{\alpha}} = -\frac{\partial}{\partial \overline{\theta}^{\dot{\alpha}}} - i\theta^\beta \sigma^\mu_{\beta\dot{\alpha}} \partial_\mu \tag{2.19}$$

and anticommute with supersymmetric transformations

$$\{D_\alpha, Q_\beta\} = \{D_\alpha, \overline{Q}^{\dot{\beta}}\} = \{\overline{D}_{\dot{\alpha}}, Q_\beta\} = \{\overline{D}_{\dot{\alpha}}, \overline{Q}^{\dot{\beta}}\} = 0. \tag{2.20}$$

For further details the reader is referred to Refs. [11–13].

2.2.2 Chiral Superfields

The general scalar superfield can be expanded as a power series in θ and $\overline{\theta}$ in terms of its component fields

$$\begin{aligned} \Phi(x, \theta, \overline{\theta}) &= \phi(x) + \theta\psi(x) + \overline{\theta}\,\overline{\chi}(x) + (\theta\theta)m(x) + (\overline{\theta}\,\overline{\theta})n(x) \\ &+ (\theta\sigma^\mu\overline{\theta})A_\mu(x) + (\theta\theta)\overline{\theta}\,\overline{\lambda}(x) + (\overline{\theta}\,\overline{\theta})\theta\varphi(x) + (\theta\theta)(\overline{\theta}\,\overline{\theta})d(x), \end{aligned} \tag{2.21}$$

where we have suppressed the spinor indices for better readability. With the square of two Grassmann-numbers being zero, the expansion of the superfield is finite. Therefore, a superfield describes a finite multiplet of (component) fields: $\phi(x)$, $m(x)$ and $n(x)$ being complex scalar or pseudo-scalar fields, $\psi(x)$ and $\varphi(x)$ are left-handed Weyl spinor fields and $\overline{\chi}(x)$ and $\overline{\lambda}(x)$ the corresponding right-handed ones. Finally, A_μ denotes a Lorentz four-vector field and $d(x)$ a real scalar field. In the following, we deduce the meaning of these fields in the context of particle physics.

The reducible representation in Eq. (2.21) can be reduced to irreducible superfields

by imposing covariant constraints

$$\overline{D}_{\dot{\alpha}}\Phi(x,\theta,\overline{\theta}) \equiv 0 \tag{2.22}$$

$$D_{\alpha}\Phi^{\dagger}(x,\theta,\overline{\theta}) \equiv 0 \tag{2.23}$$

$$\Phi(x,\theta,\overline{\theta}) \equiv \Phi^{\dagger}(x,\theta,\overline{\theta}). \tag{2.24}$$

The fields which obey the first two conditions, are the so-called *chiral superfields*. The third condition defines a *vector superfield*, which will be addressed in the next section. These chiral superfields are able to describe the chiral Standard Model fermions and their supersymmetric partners. The first condition (2.22) requires a left-handed and the second one (2.23) a right-handed chiral superfield.

By performing a variable transformation $y^{\mu} \equiv x^{\mu} + i\theta\sigma^{\mu}\overline{\theta}$ and requiring the condition (2.22) the left-handed chiral superfield Φ_L becomes

$$\Phi_L(y,\theta) = \phi(y) + \sqrt{2}\theta\psi(y) + (\theta\,\theta)F(y). \tag{2.25}$$

The same is true for the right-handed one

$$\Phi_R(z,\theta) = \phi^*(z) + \sqrt{2}\,\overline{\theta}\,\overline{\psi}(z) + (\overline{\theta}\,\overline{\theta})F^*(z), \tag{2.26}$$

with $z^{\mu} \equiv x^{\mu} - i\theta\sigma^{\mu}\overline{\theta}$.

The component fields transform under infinitesimal transformation as [14]

$$\delta_s\phi(y) = \sqrt{2}\alpha\psi(y) \tag{2.27}$$

$$\delta_s\psi(y) = \sqrt{2}\alpha F(y) + i\sqrt{2}\sigma^{\mu}\overline{\alpha}\partial_{\mu}\phi(y) \tag{2.28}$$

$$\delta_s F(y) = -i\sqrt{2}\,\partial_{\mu}\psi(y)\,\sigma^{\mu}\overline{\alpha}. \tag{2.29}$$

Hereby, Eq. (2.27) demonstrates the transformation of a boson to a fermion, whereas Eq. (2.28) expresses the inverse transformation. The component field $F(y)$ transforms into a total space-time derivative, and thus, the action of this field is invariant under supersymmetric transformation. The component field $F(y)$ is also called an *auxiliary field*.

2.2.3 Vector Superfields

Having now the possibility to describe spin-0 bosons and spin-1/2 fermions based on chiral superfields, we focus in the following on the so-called *vector superfields V*. Thus, the description of spin-1 bosons will also be possible. A vector superfield is defined by the condition of being self-conjugate, see Eq. (2.24). It can be written as

$$\begin{aligned} V(x,\theta,\overline{\theta}) = {} & C(x) + \theta\xi(x) + \overline{\theta}\,\overline{\xi}(x) + (\theta\,\theta)M(x) + (\overline{\theta}\,\overline{\theta})M^*(x) \tag{2.30} \\ & + (\theta\sigma^{\mu}\overline{\theta})A_{\mu}(x) + (\theta\,\theta)\overline{\theta}\,\overline{\lambda}(x) + (\overline{\theta}\,\overline{\theta})\theta\lambda(x) + (\theta\,\theta)(\overline{\theta}\,\overline{\theta})D(x), \end{aligned}$$

where $C(x)$ and $D(x)$ are real scalar fields, $M(x)$ is a complex scalar field, $\xi(x)$ and $\lambda(x)$ are complex spinor fields, and A_μ a real vector field. Having the freedom of choosing an appropriate gauge, we consider the *Wess-Zumino gauge* [13]

$$V_{WZ}(x,\theta,\overline{\theta}) = V(x,\theta,\overline{\theta}) + \Phi(x,\theta,\overline{\theta}) + \Phi^\dagger(x,\theta,\overline{\theta}), \tag{2.31}$$

with Φ being a general chiral superfield. It is the supersymmetric extension of a gauge transformation. With a proper choice, the component fields $\xi(x) = C(x) = M(x) = 0$ vanish.

However, the Wess-Zumino gauge does not fix all gauge freedom, therefore we can assume a conventional Abelian gauge transformation $A_\mu(x) \rightarrow A_\mu(x) + i\partial_\mu\Psi(x)$. Finally, a general vector superfield looks like

$$V(x,\theta,\overline{\theta}) = (\theta\sigma^\mu\overline{\theta})A_\mu(x) + (\theta\,\theta)\overline{\theta}\,\overline{\lambda}(x) + (\overline{\theta}\,\overline{\theta})\theta\lambda(x) + (\theta\,\theta)(\overline{\theta}\,\overline{\theta})D(x), \tag{2.32}$$

where $A_\mu(x)$ is a real vector field, $\lambda(x)$ a complex spinor field and $D(x)$ a real scalar field.

As in the previous case, we call the highest order component field $D(x)$ an auxiliary field. Similar to the auxiliary field F, it transforms as a space-time derivative and thus, its action is invariant under supersymmetric transformation.

2.2.4 Supersymmetric Lagrangian

Finally, we construct the supersymmetric Lagrangian. The action of the Lagrangian has to be invariant under supersymmetric transformations such that the Lagrangian has to vanish up to a total derivative.

To this end, we investigate the product of two and three left-handed chiral superfields

$$\begin{aligned}
\Phi_{L,1}\Phi_{L,2} &= (\phi_1 + \sqrt{2}\theta\psi_1 + (\theta\,\theta)F_1)(\phi_2 + \sqrt{2}\theta\psi_2 + (\theta\,\theta)F_2) \\
&= \phi_1\phi_2 + \sqrt{2}\theta(\phi_1\psi_2 + \psi_2\phi_1) + \theta\theta(\phi_1 F_2 + \phi_2 F_1 - \psi_1\psi_2) \tag{2.33} \\
\Phi_{L,1}\Phi_{L,2}\Phi_{L,3} &= \phi_1\phi_2\phi_3 + \sqrt{2}\theta(\phi_1\phi_2\psi_3 + \phi_1\psi_2\phi_3 + \psi_1\phi_2\phi_3) \\
&+ (\theta\theta)(\phi_1\phi_2 F_3 + \phi_1 F_2\phi_3 + F_1\phi_2\phi_3) \\
&- (\theta\theta)(\psi_1\psi_2\phi_3 + \psi_1\phi_2\psi_3 + \phi_1\psi_2\psi_3). \tag{2.34}
\end{aligned}$$

As already discussed, the component field with the highest order in θ of the expanded chiral superfield transforms under supersymmetric transformation as a total space-time derivative. Thus, the last term of Eq. (2.33) and Eq. (2.34) which is linear in $(\theta\theta)$ is also called *F-term* and contributes to the later Lagrangian.

The $-\psi_1\psi_2$ term of Eq. (2.33) will give rise to a fermion mass term. The $-(\psi_1\psi_2\phi_3 + \psi_1\phi_2\psi_3 + \phi_1\psi_2\psi_3)$ part of Eq. (2.34) describes Yukawa interactions between a scalar particle and two fermionic ones.

The discussion of multiplying more than two chiral fields does not have to be considered, as this would cause terms with mass dimension greater than four. This,

however, would lead to non-renormalizable interactions.

Another possibility of combining chiral superfields is the product of a left-handed chiral superfield with its conjugate, a right-handed chiral superfield. With the product being a vector superfield, the part which is invariant under SUSY transformation is the term linear in $\theta\,\theta\,\overline{\theta}\,\overline{\theta}$

$$\Phi_L\Phi_L^\dagger\big|_D \;\;=\;\; FF^* - \phi\partial_\mu\partial^\mu\phi^* - i\overline{\psi}\sigma_\mu\partial^\mu\psi. \tag{2.35}$$

Therefore, this part is going to be considered for the supersymmetric Lagrangian as well. In the last two expressions of the latter equation we identify two kinetic terms for the scalar component ϕ and the fermionic ψ. The term FF^* of Eq. (2.35) is the scalar superpotential, which is by definition always larger than or equal to zero. A kinetic term for the F component field, does not appear though, which means that this field does not propagate and is only an unphysical, auxiliary field.

The Lagrangian we have constructed so far, can thus be written as

$$\mathcal{L} = \Phi_i\Phi_i^\dagger\big|_D + \left(g_i\Phi_i + \frac{1}{2}m_{ij}\Phi_i\Phi_j + \frac{1}{3}\lambda_{ijk}\Phi_i\Phi_j\Phi_k + h.c.\right)\bigg|_F, \tag{2.36}$$

with the first term being the canonical Kähler potential, and the second term the *superpotential* $\mathcal{W}$

$$\mathcal{W} = \left(g_i\Phi_i + \frac{1}{2}m_{ij}\Phi_i\Phi_j + \frac{1}{3}\lambda_{ijk}\Phi_i\Phi_j\Phi_k + h.c.\right)\bigg|_F. \tag{2.37}$$

Because the Lagrangian does not contain any derivatives of the auxiliary field F one gets simple expressions for the Euler-Lagrange equations

$$\frac{\partial\mathcal{L}}{\partial F_i(x)} \;\;=\;\; F_i^*(x) + g_i + m_{ij}\phi_j(x) + \lambda_{ijk}\phi_j(x)\phi_k(x) = 0 \tag{2.38}$$

$$\frac{\partial\mathcal{L}}{\partial F_i^*(x)} \;\;=\;\; F_i(x) + g_i^* + m_{ij}^*\phi_j^*(x) + \lambda_{ijk}^*\phi_j^*(x)\phi_k^*(x) = 0 \quad\Rightarrow\quad F_i = -\frac{\partial\mathcal{W}^\dagger}{\partial\Phi_i^\dagger},$$

such that the terms containing the component field F can be expressed in terms of the scalar field $\phi(x)$. Therefore, a chiral superfield has only two bosonic degrees of freedom from the complex scalar field ϕ and construct a supermultiplet together with the two fermionic degrees of freedom of the Weyl-spinor field ψ.

However, we have not considered all possible interactions for the final Lagrangian. Next, we focus on the interaction of spin-1 particles and construct the Lagrangian of a supersymmetric Abelian theory. Similar to the electromagnetic field strength $F_{\mu\nu} \equiv \partial^\mu A_\nu - \partial_\nu A_\mu$, a supersymmetric field strength can be defined as [11]

$$W_\alpha \;\;\equiv -\tfrac{1}{4}(\overline{D}\,\overline{D})D_\alpha V(x,\theta,\overline{\theta}) \tag{2.39}$$

$$\overline{W}_{\dot\alpha} \;\;\equiv -\tfrac{1}{4}(D\,D)\overline{D}_{\dot\alpha}V(x,\theta,\overline{\theta}), \tag{2.40}$$

where W_α and $\overline{W}_{\dot\alpha}$ are chiral superfields and invariant under SUSY transformation. Herein $D, \overline{D}$ indicates the auxiliary field, $D_\alpha, \overline{D}_{\dot\alpha}$ the covariant derivatives, and V a general vector superfield. The supersymmetric field strength can be expanded in terms of component fields

$$W_\alpha = \lambda_\alpha(y) + D(y)\theta_\alpha - (\sigma^{\mu\nu}\theta)_\alpha F_{\mu\nu}(y) + i(\theta\theta)\sigma^\mu_{\alpha\dot\beta}\partial_\mu\overline{\lambda}^{\dot\beta}(y) \tag{2.41}$$

$$\overline{W}_{\dot\alpha} = \overline{\lambda}_{\dot\alpha}(z) + D(z)\overline{\theta}_{\dot\alpha} - \epsilon_{\dot\alpha\dot\beta}(\overline{\sigma}^{\mu\nu}\overline{\theta})^{\dot\beta}F_{\mu\nu}(z) - i(\overline{\theta}\,\overline{\theta})(\partial_\mu\lambda(z)\sigma^\mu)_{\dot\alpha}. \tag{2.42}$$

With the supersymmetric field strength being a chiral superfield, also the expression $W_\alpha W^\alpha$ is a chiral superfield, such that the relevant expressions for the Lagrangian are again the terms linear in $\theta\theta$. The corresponding Lagrangian for the Abelian case reads

$$\begin{aligned}
\mathcal{L} &= \frac{1}{4}\left(W^\alpha W_\alpha + \overline{W}_{\dot\alpha}\overline{W}^{\dot\alpha}\right)\Big|_F \\
&= \frac{1}{2}D^2(x) - \frac{1}{4}F_{\mu\nu}(x)F^{\mu\nu}(x) + \frac{i}{2}\lambda(x)\sigma^\mu\partial_\mu\overline{\lambda}(x) - \frac{i}{2}(\partial_\mu\lambda(x))\sigma^\mu\overline{\lambda}(x),
\end{aligned} \tag{2.43}$$

with $z^\mu \equiv x^\mu - i\theta\sigma^\mu\overline{\theta}$, and $y^\mu \equiv x^\mu + i\theta\sigma^\mu\overline{\theta}$, respectively. The auxiliary field $D(x)$ can be again substituted by making use of the equation of motion. The fermion λ which enters the gauge action will be the gaugino.

The last step before obtaining the final Lagrangian is to discuss the non-abelian gauge interactions. A vector field transforms under a general non-abelian supersymmetric gauge transformation as

$$e^{V'} \to e^{-i\Lambda^\dagger}e^V e^{i\Lambda}, \tag{2.44}$$

where Λ denotes a chiral superfield specifying the gauge transformation. A similar generalization is performed for the field strength

$$W_\alpha \to e^{-i\Lambda}W_\alpha e^{i\Lambda} \tag{2.45}$$

$$\overline{W}^{\dot\alpha} \to e^{i\Lambda}\overline{W}^{\dot\alpha}e^{-i\Lambda}. \tag{2.46}$$

Note that in the Abelian case Eq. (2.44) simplifies to Eq. (2.31), with $\Phi + \Phi^\dagger = i\Lambda - i\Lambda^\dagger$.

Taking into account the modified expressions of Eqs. (2.44)–(2.46) and combining Eq. (2.36) with Eq. (2.43), the final supersymmetric Lagrangian is obtained as

$$\mathcal{L} = \Phi_i^\dagger(e^V)_{ij}\Phi_j\Big|_D + \frac{1}{4}\left(W^{\alpha\,a}W_\alpha^a + \overline{W}_{\dot\alpha}^a\overline{W}^{\dot\alpha\,a}\right)\Big|_F + (\mathcal{W}(\Phi_i) + h.c.)\Big|_F, \tag{2.47}$$

where a indicates gauge indices. In terms of component fields we can find [11]

$$
\begin{aligned}
\mathcal{L} &= i\psi_j\sigma_\mu D_{ij}^{\dagger\mu}\overline{\psi}_i + (D_{ij}^\mu\,\phi_j)^\dagger(D_{\mu ik}\,\phi_k)\overline{\lambda}^a - \sqrt{2}g(\overline{\lambda}^a\overline{\psi}_i T_{ij}^a\phi_j + h.c.) \\
&\quad - \frac{1}{4}F_{\mu\nu}^a F^{\mu\nu a} + i\lambda^a\sigma^\mu D_\mu - V(\phi_i, \phi_j^*) - \left[\frac{1}{2}\psi_i\psi_j\mathcal{W}_{ij}(\phi) + h.c.\right], \quad (2.48)
\end{aligned}
$$

where the covariant derivatives are defined as $D_{ij}^\mu = \delta_{ij}\partial^\mu + igA^{\mu a}T_{ij}^a$ with $A^{\mu a}$ being a gauge field, g the corresponding gauge coupling, and T_{ij}^a the generators of the group. The scalar potential consists of

$$
V(\phi_i, \phi_j^*) = F_i F_i^* + \frac{1}{2}D^a D^a, \quad (2.49)
$$

with $F_i = -\frac{\partial\mathcal{W}^\dagger}{\partial\Phi_i^\dagger}$ and $D^a = -g\phi_i^\dagger T_{ij}^a\phi_j$.
On the basis of this most general supersymmetric Lagrangian, supersymmetric extensions to the Standard Model can be constructed. In the following we focus on the smallest possible extension of the Standard Model, the Minimal Supersymmetric Standard Model.

2.3 The Minimal Supersymmetric Standard Model

The Minimal Supersymmetric Standard Model (MSSM) is the smallest possible extension of the Standard Model within $N = 1$ Supersymmetry. An overview of the particle content of the MSSM is given in Tab. 2.1 and Tab. 2.2.

chiral supermultiplets		spin 0	spin 1/2	$SU(3)_C$, $SU(2)_L$, $U(1)_Y$
squarks, quarks	Q	$(\widetilde{u}_L \;\; \widetilde{d}_L)$	$(u_L \;\; d_L)$	$(\,\mathbf{3}\,,\,\mathbf{2}\,,\,\frac{1}{6})$
($\times 3$ generations)	$\overline{u}$	$\widetilde{u}_R^*$	$u_R^\dagger$	$(\,\overline{\mathbf{3}}\,,\,\mathbf{1}\,,\,-\frac{2}{3})$
	$\overline{d}$	$\widetilde{d}_R^*$	$d_R^\dagger$	$(\,\overline{\mathbf{3}}\,,\,\mathbf{1}\,,\,\frac{1}{3})$
sleptons, leptons	L	$(\widetilde{\nu} \;\; \widetilde{e}_L)$	$(\nu \;\; e_L)$	$(\,\mathbf{1}\,,\,\mathbf{2}\,,\,-\frac{1}{2})$
($\times 3$ generations)	$\overline{e}$	$\widetilde{e}_R^*$	$e_R^\dagger$	$(\,\mathbf{1}\,,\,\mathbf{1}\,,\,1)$
Higgs bosons, higgsinos	H_u	$(H_u^+ \;\; H_u^0)$	$(\widetilde{h}_u^+ \;\; \widetilde{h}_u^0)$	$(\,\mathbf{1}\,,\,\mathbf{2}\,,\,+\frac{1}{2})$
	H_d	$(H_d^0 \;\; H_d^-)$	$(\widetilde{h}_d^0 \;\; \widetilde{h}_d^-)$	$(\,\mathbf{1}\,,\,\mathbf{2}\,,\,-\frac{1}{2})$

Table 2.1: Chiral supermultiplets of the MSSM.

vector supermultiplets	spin 1/2	spin 1	$SU(3)_C$, $SU(2)_L$, $U(1)_Y$
gluino, gluon	$\widetilde{g}$	g	(**8**, **1**, 0)
winos, W boson	$\widetilde{\lambda}^{\pm}$ $\widetilde{\lambda}^3$	$W^{\pm}$ W^0	(**1**, **3**, 0)
bino, B boson	$\widetilde{\lambda}'$	B^0	(**1**, **1**, 0)

Table 2.2: Vector supermultiplets of the MSSM.

Each fermionic chirality state which is known from the Standard Model has a cor-
responding spin-0 superpartner, called sfermion. Each pair is embedded in a chiral
supermultiplet, which can be described by a chiral superfield. For each generation
of quarks, a $SU(2)_L$-doublet Q of left-handed chiral supermultiplets exists and two
$SU(2)_L$-singlets of a right-handed chiral supermultiplet $\overline{u}$ and $\overline{d}$. For the leptons
each family has a $SU(2)_L$-doublet L of left-handed chiral supermultiplets and a sin-
glet of a right-handed chiral supermultiplet $\overline{e}$. In comparison to the pure Standard
Model, there exist two Higgs doublets in the MSSM. They are necessary to give
both, up and down quarks masses and to cancel anomalies which are introduced by
the higgsinos. Two chiral supermultiplets containing a Higgs and its superpartner,
the higgsino, build up each Higgs doublet H_u and H_d. The MSSM particle content
concerning gauge bosons is shown in Tab. 2.2. Each gauge boson gets a fermionic
spin-1/2 superpartner, called gaugino.
In order to construct a renormalizable MSSM superpotential the following contribu-
tions of the aforementioned chiral superfields are possible

$$
\begin{align}
\mathcal{W}_{MSSM} &= (y_u)_{ij}\, H_u Q_i \bar{u}_j + (y_d)_{ij}\, H_d Q_i \bar{d}_j + (y_e)_{ij}\, H_d L_i \bar{e}_j - \mu H_d H_u \quad (2.50) \\
\mathcal{W}_{\Delta L=1} &= \frac{1}{2}\lambda^{ijk} L_i L_j \bar{e}_k + \lambda'^{ijk} L_i Q_j \bar{d}_k + \mu'^i L_i H_u \quad (2.51) \\
\mathcal{W}_{\Delta B=1} &= \frac{1}{2}\lambda''^{ijk} \bar{u}_i \bar{d}_j \bar{d}_k, \quad (2.52)
\end{align}
$$

where i, j represent the generation indices, and y_u, y_d and y_e are 3×3 Yukawa cou-
plings equal to the Standard Model. The parameter μ denotes the supersymmetric
mass term of the Higgs doublets and μ' is a three-dimensional parameter. λ, λ' and
λ'' are 3×3 matrices similar to the Yukawa couplings.
In contrast to the Standard Model, terms which violate baryon number B (Eq. (2.52))
or lepton number L (Eq. (2.51)) can occur in the MSSM. Those terms would give
rise to B- and L-violating processes, which have not been experimentally observed
up to now. Due to the non-observation of the proton decay stringent constraints are
set on the couplings $\lambda' \cdot \lambda''$.

To this end, a new multiplicative quantum number, named R-parity, is introduced

$$P_R = (-1)^{3(B-L)+2s}, \tag{2.53}$$

with s being the spin of the particle. Due to this discrete Z_2 symmetry, all Standard Model particles carry even R-parity ($P_R = +1$), while all supersymmetric particles odd ($P_R = -1$). The conservation of R-parity has the effect that all above mentioned B and L violating terms are forbidden. Thus, R-parity conservation is the usual choice in the MSSM. However, for completeness it should be mentioned that there exist other models allowing either B *or* L violating terms, which are not in conflict with the the non-observation of the proton decay (in contrast to B *and* L violating terms). Such models with broken R-parity are currently also of interest and under investigation.

In this work, however, we focus on an R-parity conserved MSSM, such that we end up with the MSSM superpotential of Eq. (2.50).

2.4 SUSY Breaking

Up to now, Standard Model particles and their superpartners would have the same mass. This, however, is obviously not the case as shown by the current experimental observations. To construct a realistic phenomenological model, a kind of Supersymmetry breaking has to be part of the theory.

Another motivation becomes clear by looking again at Eq. 2.50. Here, the dimensionful parameter μ is introduced, which provides masses for the higgsinos, and leads to a non-negative scalar potential

$$|\mu|^2(|H_u^0|^2 + |H_u^+|^2 + |H_d^0|^2 + |H_d^-|^2), \tag{2.54}$$

with a minimum at $H_u^0 = H_d^0 = 0$. This implies that the general MSSM Lagrangian we have introduced so far cannot accommodate electroweak symmetry breaking. Thus, SUSY cannot be an exact symmetry and some mechanism of SUSY breaking has to be considered. One possibility would be spontaneous SUSY breaking, which means, by definition, that the vacuum state is not invariant under SUSY transformations

$$Q_\alpha|0\rangle \neq 0 \quad \text{and} \quad Q_\alpha^\dagger|0\rangle \neq 0, \tag{2.55}$$

where Q_α and $Q_\alpha^\dagger$ are the SUSY generators. In a global Supersymmetry the Hamiltonian operator H is directly related to the SUSY generators

$$H = P^0 = \frac{1}{4}(Q_1 Q_1^\dagger + Q_1^\dagger Q_1 + Q_2 Q_2^\dagger + Q_2^\dagger Q_2), \tag{2.56}$$

which is due to the SUSY algebra, see Eq. (2.8). Thus, for a spontaneously broken Supersymmetry one expects a positive vacuum expectation value (vev)

$$\langle 0|H|0\rangle = \frac{1}{4}(\parallel Q_1|0\rangle \parallel^2 + \parallel Q_1^\dagger|0\rangle \parallel^2 + \parallel Q_2|0\rangle \parallel^2 + \parallel Q_2^\dagger|0\rangle \parallel^2) > 0. \qquad (2.57)$$

With $\langle 0|H|0\rangle = \langle 0|\mathcal{L}|0\rangle = \langle 0|V|0\rangle$, also a positive expectation value is implied for the scalar SUSY potential $\langle 0|V|0\rangle$. By comparing with Eq. (2.49), this can be obtained by

$$\langle 0|F|0\rangle \equiv \Lambda^2 \neq 0 \quad \text{or} \quad \langle 0|D|0\rangle \equiv \Lambda^2 \neq 0, \qquad (2.58)$$

with Λ^2 being the mass scale, and F and D the introduced auxiliary fields. The former possibility is called F-type breaking or O'Raifeartaigh mechanism [15], the latter one D-type breaking or Fayet-Iliopolus mechanism [16]. However, pure D-type or F-type breaking give rise to phenomenological difficulties within the MSSM. Therefore, the idea of a *hidden sector* was born. In this sector the origin of spontaneously broken SUSY could lie which is transferred by messenger interactions to the visible sector of the MSSM via flavour blind interactions. Different approaches exist to realize such a behaviour. One example is *gravity mediated Supersymmetry breaking* [17], where gravity is the messenger of SUSY breaking. In *gauge mediated Supersymmetry breaking* [18], however, gauge forces transfer the breaking to the visible sector. Further details on SUSY breaking can be found in [13, 14, 19].

As we have no clear hint on how SUSY is broken, the usual approach is to break SUSY explicitly by introducing so called *soft SUSY breaking terms*. These have a positive mass dimension in order to maintain the mass hierarchy and not to introduce new divergences. The most general soft SUSY breaking Lagrangian is given by

$$
\begin{aligned}
\mathcal{L}_{soft}^{MSSM} =\ & -\frac{1}{2}\left(M_1\tilde{B}\tilde{B} + M_2\tilde{W}\tilde{W} + M_3\tilde{g}\tilde{g} + h.c.\right) \\
& -\ (M_{\tilde{Q}}^2)_{ij}\,\tilde{Q}_i^\dagger\tilde{Q}_j - (M_{\tilde{u}}^2)_{ij}\,\tilde{\bar{u}}_i^\dagger\tilde{\bar{u}}_j - (M_{\tilde{d}}^2)_{ij}\,\tilde{\bar{d}}_i^\dagger\tilde{\bar{d}}_j \\
& -\ (M_{\tilde{L}}^2)_{ij}\,\tilde{L}_i^\dagger\tilde{L}_j - (M_{\tilde{e}}^2)_{ij}\,\tilde{\bar{e}}_i^\dagger\tilde{\bar{e}}_j \\
& -\ m_{H_u}^2\,H_u^\dagger H_u - m_{H_d}^2\,H_d^\dagger H_d -\ (b_\mu H_d H_u + h.c.) \\
& +\ (A_u)_{ij}\,H_u\tilde{Q}_i\tilde{\bar{u}}_j + (A_d)_{ij}\,H_d\tilde{Q}_i\tilde{\bar{d}}_j + (A_e)_{ij}\,H_d\tilde{L}_i\tilde{\bar{e}}_j + h.c., \quad (2.59)
\end{aligned}
$$

where M_1, M_2 and M_3 are the complex bino, wino and gluino mass parameters and $M_{\tilde{Q}}^2$, $M_{\tilde{L}}^2$, $M_{\tilde{u}}^2$, $M_{\tilde{d}}^2$ and $M_{\tilde{d}}^2$ the 3×3 hermitian matrices of the soft SUSY breaking mass terms of the squarks and sleptons. The third term of Eq. 2.59 introduces the real soft SUSY breaking Higgs mass terms $m_{H_u}^2$ and $m_{H_d}^2$ as well as the complex parameter b, which is defined in dependence of the off-diagonal Higgs squared mass term $m_{12}^2 \equiv b\mu$. The last expression of Eq. 2.59 gives rise to 3×3 complex matrices

of the trilinear coupling A_u, A_d and A_e.

While due to the unbroken MSSM only one additional parameter was introduced, now the soft SUSY broken MSSM counts in total 124 independent parameters, of which 18 are from the Standard Model, one newly introduced by the Higgs sector and 105 by soft SUSY breaking.

2.5 Phenomenological Models

However, not all 105 parameters give rise to physically viable observables. Without any restrictions new sources of CP violation are introduced, Lepton numbers are not separately conserved and flavor-changing neutral currents would be unsuppressed. Considering these constraints, some combinations of the trilinear couplings and the μ-parameter have to be sufficiently small, and stringent constraints on the off-diagonal entries of the sfermionic soft SUSY breaking mass matrices are set [20].

Motivated by grand unified supersymmetric theories the unification of the $SU(3) \times SU(2) \times U(1)$ gauge couplings at some high scale $Q = M_{GUT}$

$$M_1(Q) = M_2(Q) = M_3(Q) = m_{1/2} \tag{2.60}$$

is often assumed, which leads at the electroweak scale to the relation

$$M_3 = \frac{g_s^2}{g^2}M_2 \simeq 3.5M_2 \quad \text{and} \quad M_1 = \frac{5g'^2}{3g^2}M_2 \simeq 0.5M_2, \tag{2.61}$$

with g_s being the strong SU(3) coupling constant. The SU(2) and U(1) gauge couplings are indicated by g' and g, respectively. An often considered, simplified model is the so-called *constrained Minimal Supersymmetric Standard Model* (CMSSM), which reduces the number of free parameters to five. Hereby, the soft SUSY breaking squared scalar masses and the trilinear coupling are assumed to be flavour diagonal and universal

$$\begin{aligned}
M_{\tilde{Q}}^2(Q) &= M_{\tilde{u}}^2(Q) &= M_{\tilde{d}}^2(Q) = m_0^2\mathbf{1} \\
M_{\tilde{L}}^2(Q) &= M_{\tilde{e}}^2(Q) &= m_0^2\mathbf{1} \\
m_{H_u}^2(Q) &= m_{H_d}^2(Q) &= m_0^2 \\
A_u(Q) &= A_d(Q) &= A_e(Q) = A_0\mathbf{1}.
\end{aligned} \tag{2.62}$$

Thus the CMSSM can be described by the following five parameters

$$m_0, \ A_0, \ m_{1/2}, \ \tan\beta, \ \text{and} \ \text{sgn}(\mu), \tag{2.63}$$

with $\tan\beta = v_u/v_d$ being the ratio of the Higgs expectation values. The CMSSM should not be confused with *minimal supergravity* (mSUGRA), which is an example

for a gravity mediated SUSY breaking framework. In mSUGRA two additional constraints $b_0 = A_0 - m_0$ and $m_{3/2} = m_0$ are introduced assuming a simplifying form for the hidden sector [20].

However, the CMSSM is highly challenged by the recent collider searches, thus it is interesting to relax certain constraints and to consider other phenomenological reasonable realizations of Supersymmetry.

One approach is, for example, the assumption of *non-universal Higgs masses* (NUHM). In the NUHM1 model only one parameter is added to the usual CMSSM by assuming $m^2_{H_u}(Q) = m^2_{H_d}(Q) \neq m^2_0$. In NUHM2, however, two parameters are additionally considered, because the squared Higgs mass parameters are not set necessarily equal $m^2_{H_u}(Q) \neq m^2_{H_d}(Q)$ at the high scale.

A more general approach is the *phenomenological Minimal Supersymmetric Standard Model* (pMSSM), which was originally introduced by Refs. [21, 22]. It counts 19 free parameters in total [22] and is a CP-conserving MSSM with minimal flavour violation. The gaugino mass parameters M_1, M_2, and M_3 are assumed not to be necessarily unified at the GUT scale and the three trilinear couplings A_u, A_d and A_e are treated independently (while the first two are negligibly small). Also, the squared sfermion mass matrices are independent parameters. The first and second generation are assumed to be degenerate though. The Higgs sector is described by three parameters: $\tan\beta$, the mass of the pseudoscalar Higgs m_A and the higgsino mass parameter μ.

This kind of model – benefiting, on the one hand, from a reduced number of free parameters, when compared to the MSSM, but still containing enough parameters to study the MSSM without too many constraints – is used in this work.

2.6 The MSSM Particle Content

As a detailed knowledge of the sparticle characteristics is essential for a detailed discussion of the loop calculation, renormalization and the general phenomenology of neutralino-stop coannihilation, we discuss the particle spectrum of the Minimal supersymmetric Standard Model in the following.

2.6.1 Higgs Sector

So far, we have not considered electroweak symmetry breaking $SU(2)_L \times U(1)_Y \rightarrow U(1)_{EM}$. In comparison to the Standard Model this is slightly more involved, as the MSSM contains two Higgs doublets. The scalar potential for the Higgs sector can be written as

$$
\begin{aligned}
V = &(|\mu|^2 + m^2_{H_u})|H^0_u|^2 + (|\mu|^2 + m^2_{H_d})|H^0_d|^2 - (bH^0_u H^0_d + h.c.) \\
&+ \frac{1}{8}(g^2 + g'^2)(|H^0_u|^2 - |H^0_d|^2)^2.
\end{aligned} \tag{2.64}
$$

The corresponding expressions originate from the pure MSSM Lagrangian (see Eq. (2.50)) as well as from the soft SUSY breaking terms (see Eq. (2.50)). Hereby, we have already rotated away the vacuum expectation values for the charged Higgs by taking advantage of $SU(2)_L$ gauge transformations and setting $H_u^+ = H_d^- = 0$ at the minimum. We can then deduce two constraints for maintaining a minimum of the scalar potential

$$2b < 2|\mu|^2 + m_{H_u}^2 + m_{H_d}^2 \quad \text{and} \quad b^2 > (|\mu|^2 + m_{H_u}^2)(|\mu|^2 + m_{H_d}^2), \qquad (2.65)$$

such that H_u^0 and H_d^0 get non-zero vevs $v_u \equiv \langle H_u^0 \rangle$ and $v_d \equiv \langle H_d^0 \rangle$, respectively. The ratio of the two vevs is defined as

$$\tan\beta \equiv \frac{v_u}{v_d} = \frac{\langle H_u^0 \rangle}{\langle H_u^0 \rangle}. \qquad (2.66)$$

Finally, three of the eight degrees of freedom of the two complex Higgs-doublets are Nambu-Goldstone bosons G^0 and $G^\pm$, which become the longitudinal modes of the massive Z^0 and $W^\pm$ bosons. The other five are the Higgs mass eigenstates: two CP-even neutral Higgs bosons h^0 and H^0, one CP-odd neutral Higgs A^0 and two charged ones $H^\pm$. The masses of the aforementioned five Higgs bosons are given by

$$m_{A^0}^2 = 2b/\sin(2\beta) = 2|\mu|^2 + m_{H_u}^2 + m_{H_d}^2 \qquad (2.67)$$

$$m_{h^0,H^0}^2 = \frac{1}{2}\left(m_{A^0}^2 + m_Z^2 \mp \sqrt{(m_{A^0}^2 - m_Z^2)^2 + 4m_Z^2 m_{A^0}^2 \sin^2(2\beta)}\right) \qquad (2.68)$$

$$m_{H^\pm}^2 = m_{A^0}^2 + m_W^2. \qquad (2.69)$$

2.6.2 Neutralino and Chargino Sector

Due to electroweak symmetry breaking, higgsinos and gauginos mix with each other. The neutral higgsinos $\tilde{H}_u^0$ and $\tilde{H}_d^0$ as well as the neutral gauginos $\tilde{B}$ and $\tilde{W}^0$ form the four mass eigenstates called *neutralinos* $\tilde{\chi}_{i=1,2,3,4}$.
The charged higgsinos $\tilde{H}_u^+$ and $\tilde{H}_d^-$ and the charged gauginos $\tilde{W}^+$ and $\tilde{W}^-$ combine to the four mass eigenstates called *charginos* $\tilde{\chi}_{i=1,2}^\pm$.
The part of the Lagrangian which defines the neutralino masses is given by

$$\mathcal{L} = -\frac{1}{2}(\psi^0)^T \mathcal{M}_{\tilde{\chi}^0} \psi^0 + \text{h.c.}, \qquad (2.70)$$

with $\psi^0 = (\tilde{B}, \tilde{W}^0, \tilde{H}_d^0, \tilde{H}_u^0)$ being the gauge eigenstate basis of the neutralinos. The mass matrix $\mathcal{M}_{\tilde{\chi}^0}$ is obtained as

$$\mathcal{M}_{\tilde{\chi}^0} = \begin{pmatrix} M_1 & 0 & -m_Z \sin\theta_W \, \cos\beta & m_Z \sin\theta_W \sin\beta \\ 0 & M_2 & m_Z \cos\theta_W \, \cos\beta & -m_Z \cos\theta_W \sin\beta \\ -m_Z \sin\theta_W \, \cos\beta & m_Z \cos\theta_W \, \cos\beta & 0 & -\mu \\ m_Z \sin\theta_W \sin\beta & -m_Z \cos\theta_W \sin\beta & -\mu & 0 \end{pmatrix}.$$

(2.71)

Diagonalizing the mass matrix with the unitary matrix N, we get the following neutralino masses

$$N^* \mathcal{M}_{\tilde{\chi}^0} \, N^{-1} = diag(m_{\tilde{\chi}_1^0}, m_{\tilde{\chi}_2^0}, m_{\tilde{\chi}_3^0}, m_{\tilde{\chi}_4^0}),$$

(2.72)

with $m_{\tilde{\chi}_1^0}$ being defined as the mass of the lightest neutralino and $m_{\tilde{\chi}_4^0}$ of the heaviest. The mass eigenstates of the neutralinos are given by

$$\tilde{\chi}_i^0 = N_{ij} \, \psi_j^0 \qquad i,j = 1,\ldots,4\,.$$

(2.73)

In the MSSM, the lightest neutralino is very often also the lightest supersymmetric particle (LSP). Due to R-parity conservation, the LSP is stable, and all supersymmetric particles decay into the LSP at some point. The lightest neutralino is at the same time also a very good dark matter candidate.

The charginos can be obtained in a similar manner. The relevant term of the Lagrangian is given by

$$\mathcal{L} = -\frac{1}{2}(\psi^\pm)^T \mathcal{M}_{\tilde{\chi}^\pm} \psi^\pm + \text{h.c.},$$

(2.74)

with $\psi^0 = (\tilde{W}^+, \tilde{H}_u^+, \tilde{W}^-, \tilde{H}_d^-)$ denoting their gauge eigenstate basis. The mass matrix $\mathcal{M}_{\tilde{\chi}^\pm}$ can be expressed in 2×2 block form

$$\mathcal{M}_{\tilde{\chi}^\pm} = \begin{pmatrix} 0 & X^T \\ X & 0 \end{pmatrix},$$

(2.75)

with

$$X = \begin{pmatrix} M_2 & \sqrt{2}\, m_W \sin\beta \\ \sqrt{2}\, m_W \cos\beta & \mu \end{pmatrix}.$$

(2.76)

This asymmetric mass matrix can be diagonalized by the two unitary matrices W and V

$$W^* \mathcal{M}_{\tilde{\chi}^\pm} V^{-1} = diag(m_{\tilde{\chi}_1^\pm}, m_{\tilde{\chi}_2^\pm}).$$

(2.77)

Finally, the mass eigenstates of the charginos are given by

$$\begin{pmatrix} \tilde{\chi}_1^+ \\ \tilde{\chi}_2^+ \end{pmatrix} = V \begin{pmatrix} \tilde{W}^+ \\ \tilde{H}_u^+ \end{pmatrix} \quad \text{and} \quad \begin{pmatrix} \tilde{\chi}_1^- \\ \tilde{\chi}_2^- \end{pmatrix} = W \begin{pmatrix} \tilde{W}^- \\ \tilde{H}_d^- \end{pmatrix}. \tag{2.78}$$

2.6.3 Sfermion Sector

In the following, we focus on the part of the Lagrangian which describes the masses of the sfermions. For this, we define a six component vector $\phi_{\tilde{f}} = \begin{pmatrix} \tilde{f}_L \\ \tilde{f}_R \end{pmatrix}$ which consists of the left-handed and right-handed gauge eigenstates of all generations with $\tilde{f} = \tilde{u}, \tilde{d}, \tilde{e}, \tilde{\nu}$ (however, for $\tilde{\nu}$ we set $\tilde{\nu}_R = 0$). Thus, the sfermion masses are given by the following part of the Lagrangian

$$\mathcal{L}_{\tilde{f}} = -\phi_{\tilde{f}}^\dagger \mathcal{M}_{\tilde{f}}^2 \phi_{\tilde{f}}, \tag{2.79}$$

with the mass matrix being a 2×2 Hermitian matrix consisting of 3×3 blocks

$$\mathcal{M}_{\tilde{f}}^2 = \begin{pmatrix} M_{\tilde{f}_L}^2 & M_{\tilde{f}_{LR}}^2 \\ M_{\tilde{f}_{LR}}^{2\dagger} & M_{\tilde{f}_R}^2 \end{pmatrix}. \tag{2.80}$$

For squarks the diagonal entries can be written as

$$M_{\tilde{f}_L}^2 = M_{\tilde{Q}_{\tilde{f}}}^2 + m_f^2 + m_Z^2[T_{\tilde{f}}^3 - Q_{\tilde{f}} \sin^2 \theta_W] \cos(2\beta)\mathbf{1} \tag{2.81}$$

$$M_{\tilde{f}_R}^2 = M_{\tilde{u}_{\tilde{f}}}^2 + m_f^2 + m_Z^2 Q_{\tilde{f}} \sin^2 \theta_W \cos(2\beta)\mathbf{1} \tag{2.82}$$

$$M_{\tilde{f}_R}^2 = M_{\tilde{d}_{\tilde{f}}}^2 + m_f^2 + m_Z^2 Q_{\tilde{f}} \sin^2 \theta_W \cos(2\beta)\mathbf{1}. \tag{2.83}$$

Similarly, the corresponding 3×3 matrices for the sleptons are given by

$$M_{\tilde{f}_L}^2 = M_{\tilde{L}_{\tilde{f}}}^2 + m_f^2 + m_Z^2[T_{\tilde{f}}^3 - Q_{\tilde{f}} \sin^2 \theta_W] \cos(2\beta)\mathbf{1} \tag{2.84}$$

$$M_{\tilde{f}_R}^2 = M_{\tilde{e}_{\tilde{f}}}^2 + m_f^2 + m_Z^2 Q_{\tilde{f}} \sin^2 \theta_W \cos(2\beta)\mathbf{1}. \tag{2.85}$$

Hereby, $M_{\tilde{Q}_{\tilde{f}}}^2$, $M_{\tilde{u}_{\tilde{f}}}^2$, $M_{\tilde{d}_{\tilde{f}}}^2$, $M_{\tilde{L}_{\tilde{f}}}^2$, and $M_{\tilde{e}_{\tilde{f}}}^2$ are the soft SUSY breaking mass terms, m_f the fermion mass of the corresponding family, $Q_{\tilde{f}}$ the electric charge, and $T_{\tilde{f}}^3$ the third component of the weak isospin of $\tilde{f}_L$.

The off-diagonal entries of the mass matrix $\mathcal{M}_{\tilde{f}}^2$ can be expressed for both, squarks and sleptons, as

$$M_{\tilde{f}_{LR}}^2 = m_f(A_f^* - \mu \cot \beta) \quad \text{for up} - \text{type sfermions} \tag{2.86}$$

$$M_{\tilde{f}_{LR}}^2 = m_f(A_f^* - \mu \tan \beta) \quad \text{for down} - \text{type sfermions}, \tag{2.87}$$

where A_f denotes the trilinear coupling and μ the higgsino parameter.

As the off-diagonal entries are proportional to the fermion masses, the mixing of the first and second generation squarks is quite small. By rotating with the 6×6 unitary matrix U the mass matrix can be diagonalized

$$\mathcal{M}_{\tilde{f}}^{2(D)} = U^\dagger \mathcal{M}_{\tilde{f}}^2 U, \tag{2.88}$$

and we find the six sfermion mass eigenstates $\tilde{f}_i$

$$\tilde{f}_i = U_{ji}^* \, \tilde{f}_{jL} + U_{i,j+3}^* \, \tilde{f}_{jR} \quad j = 1 \ldots 3, \tag{2.89}$$

where $i = 1$ denotes the lightest and $i = 6$ the heaviest sfermion mass eigenstate. Thus, we have a complete picture of the supersymmetric mass spectrum which is of interest for the further work. In particular in Chap. 8, in which the renormalization of the loop calculation will be discussed, the introduced definitions will be used.

3 Dark Matter

One of the compelling open problems of modern physics is to identify the nature of dark matter. In the following, we want to mention several examples which give us proof of its existence, summarise the key characteristics which dark matter has to fulfil in order to be in agreement with all experimental observations and give an overview of the current status of different dark matter searches.

3.1 Evidence for the Existence of Dark Matter

The observations made by Fritz Zwicky in 1933 [23] are often referred to be the first observational hint for dark matter. But already earlier, in 1922, James Jeans suggested that "there must be about three dark stars in the universe to every bright star" and a general concept of dark matter was proposed by Edward Fournier d'Albe in 1907 [24, 25].
Since these early observations were made, hints for the existence of this kind of matter have been growing. In the following, we want to give an overview of the most convincing evidence for the existence of dark matter we know nowadays. The subsequent discussed experimental observations of dark matter are not meant to be a complete list, however, they should give a general flavour of various kinds of observations which point us to some kind of matter, whose nature we do not know up to now exactly. For a review about dark matter the reader is referred to [24, 26].

3.1.1 Velocity Distribution of Galaxies within the Coma Cluster

The first renowned observation of dark matter was achieved by Fritz Zwicky in 1933, who studied the Coma cluster [23]. By observing doppler shifts in galactic spectra, he was able to calculate the velocity dispersion of the individual galaxies within the Coma cluster $v_{obs} = v_0 \pm \sigma$, with v_0 being the velocity of the total Coma cluster with respect to us. Thus, the average kinetic energy of the galaxies can be calculated as

$$\langle T \rangle \approx \frac{3}{2} m \sigma^2. \qquad (3.1)$$

Under the assumption of only gravitational interactions and Newtonian gravity, the average gravitational potential energy is given by the third Keplerian law

$$\langle V \rangle \approx - G \, \frac{2mM}{R},$$ (3.2)

where m indicates the average mass of an individual galaxy of the cluster, M the mass of the total cluster, and R describes its radius. According to the virial theorem $\langle T \rangle = -\frac{1}{2}\langle V \rangle$, the total mass of the Coma cluster is calculable. Performing this analysis, a mass for the Coma cluster of $M_{cluster} \approx 4.5 \times 10^{13} M_\odot$ was found. This value exceeds the mass which was measured by mass-to-light ratios by far. Due to these measurements, a mass of only 2 % of $M_{cluster}$ was expected [27]. Because of this discrepancy, it was clear that there has to be some other kind of non-visible matter which could explain the much higher mass predicted by the virial theorem.

3.1.2 Rotation Curves of Spiral Galaxies

Also, on the scale of individual galaxies, the claim of the existence of dark matter has been confirmed. Studying the circular velocity distribution of stars and gas of a single spiral galaxy as a function of the distance to the galactic centre shows an interesting behaviour.

According to Newtonian dynamic the circular velocity can be written as

$$v_c(r) = \sqrt{\frac{G \, M(r)}{r}},$$ (3.3)

where $M(r) = 4\pi \int_0^r dr' r'^2 \rho(r')$ describes the total mass up to a radius r of the galaxy, with $\rho(r)$ describing the mass density profile and G the Newtonian constant. For the area beyond the visible disk, one would expect a decreasing behaviour $\propto 1/\sqrt{r}$. But in contrast to these expectations, measurements tell us that, however, the velocity distribution v_c stays constant. Fig. 3.1 shows as example the `NGC 6503` spiral galaxy, where this behaviour is clearly visible. This observation could imply the existence of a dark matter halo with a density distribution of $\rho \propto 1/r^2$ larger than the visible disk and would lead to the observed constant velocity distribution outside the visible galaxy [26]. The different contributions to the measured velocity distribution are also depicted in Fig. 3.1. It is nicely visible that adding up all single contributions which arise from the matter disk, the gas and a possible dark matter halo, would lead exactly to the observed behaviour.

3.1.3 Weak Gravitational Lensing Effects of the Bullet Cluster

A more recent experimental observation and hint for the existence of dark matter is the so-called *bullet cluster*. In Fig. 3.2 an X-ray image of the two merging galaxy
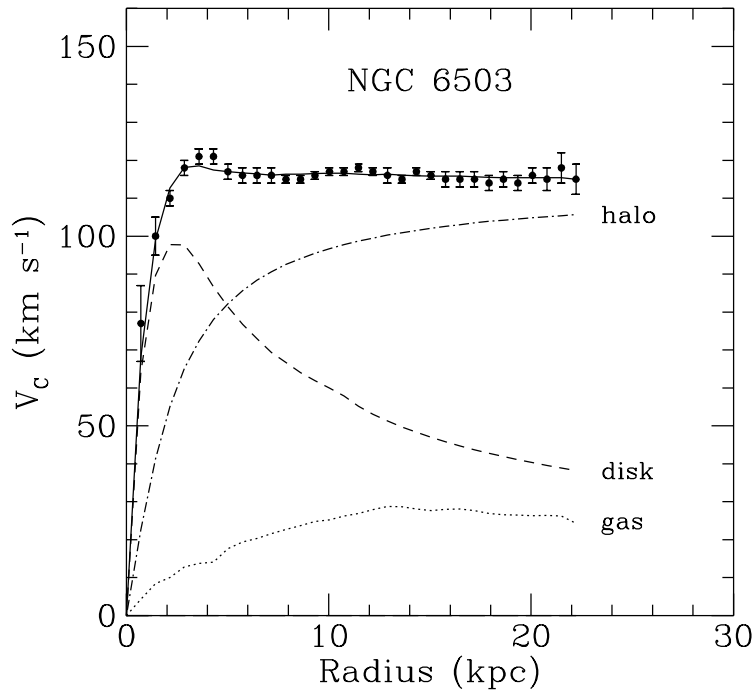
Figure 3.1: Velocity distribution of the spiral galaxy `NGC 6503`. The data points depict the observed velocity distribution. The contributions of the gas and the matter disk alone would give rise to the dotted and dashed line, respectively. A dark matter halo with a density distribution of $\rho \propto 1/r^2$ would lead to the distribution which is shown as dashed-dotted line. By considering all three possible contributions, the solid line is obtained, which is in very good agreement with the observed data. Figure taken from [28].

27

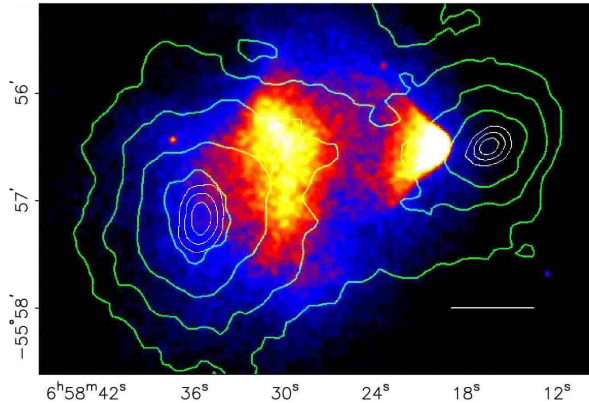Figure 3.2: Image of the bullet cluster (merging cluster `1E0657-558`) taken by the Chandra telescope. The green contours show the gravitational potential reconstructed by weak gravitational lensing. In blue the X-ray emission of the intergalactic hot plasma is visible. Red to yellow colours show the shock cones of the colliding gas of the two subclusters. Image taken from [29].

clusters `1E0657-558` obtained by the Chandra telescope in 2006 [29] is shown. In red to yellow colours, the X-ray emission of the colliding shock cones of the hot gas is visible, while in blue the distribution of the intergalactic hot plasma is depicted. The latter makes up the main visible component of the total cluster mass. Additionally, the gravitational potential of the two merging clusters depicted in green contours in Fig 3.2 was obtained via weak gravitational lensing methods.

Comparing both distributions, an 8 σ significance spatial offset of the centre of the total mass with respect to the centre of the baryonic mass was determined. This leads to the assumption that the two galaxy clusters consist mostly of dark matter which is weakly interacting, and can thus pass each other unhinderedly. The visible gas, however, interacts heavily, which is observable due to the shock cones. As this observation cannot be explained only by theories modifying the gravitational force law (MOND, see Sec. 3.3), this is a clear evidence for the existence of dark matter. Within the bullet cluster, this invisible kind of matter makes up the majority of the total mass.

3.1.4 Cosmic Microwave Background

Whereas the aforementioned observations show clear evidence for the existence of dark matter, they do not allow us to determine the total amount of dark matter in our universe. However, with exact measurement of the cosmic microwave background (CMB), one can very precisely determine the dark matter relic density.

During the evolution of the universe, shortly after the recombination of electrons and atoms, the photons decouple and can propagate without scattering. This cosmic microwave background is an almost perfect black body spectrum with T=2.726 K

and is globally isotropic up to a level of 10^{-5}. In the 1990s, the COBE satellite was able to confirm the isotropic black body spectrum of the CMB, and discovered the first hint of a dipole anisotropy [30]. This was a big success in order to support the Big Bang Theory with its theoretical framework. The measurements have been even more refined by WMAP by improving the measurements of tiny density fluctuations in the early universe [31–34]. There are several effects which can affect the temperature of the photons: Fluctuations in the energy density of the photons at the time of last scattering, a Doppler shift or the Sachs-Wolfe effect as well as the integrated Sachs-Wolfe effect. For more details on these effects the interested reader is referred to Ref. [35]. The observed temperature fluctuations can be theoretically described by a 2-dimensional power spectrum [26]

$$\frac{\delta T}{T}(\theta, \phi) = \sum_{l=2}^{+\infty} \sum_{m=-l}^{+l} a_{lm} Y_{lm}(\theta, \phi), \tag{3.4}$$

where $Y_{lm}(\theta, \phi)$ indicates the spherical harmonics which depend on the polar angles θ and ϕ which parametrise the sky. The variance of thermal fluctuations can then be expressed as follows

$$\left\langle \left(\frac{\delta T}{T} \right)^2 \right\rangle = \frac{\int_0^{2\pi} \int_0^{\pi} \left(\frac{\delta T}{T} \right)^2 d\theta \sin\phi \, d\phi}{\int_0^{2\pi} \int_0^{\pi} d\theta \sin\phi \, d\phi}. \tag{3.5}$$

Integrating over the polar coordinates and using the orthogonality relation of the spherical harmonics we arrive at

$$\left\langle \left(\frac{\delta T}{T} \right)^2 \right\rangle = \frac{1}{4\pi} \sum_{lm} \sum_{l'm'} \int_0^{2\pi} \int_0^{\pi} a_{lm} a_{l'm'} Y_{lm}(\theta, \phi) Y_{l'm'}(\theta, \phi) d\theta \sin\phi \, d\phi. \tag{3.6}$$

As observations confirm the assumption that these small temperature fluctuations are Gaussian-like distributed, we can reformulate the previous expression further to

$$\left\langle \left(\frac{\delta T}{T} \right)^2 \right\rangle = \frac{1}{4\pi} \sum_{lm} a_{lm} a_{l'm'} \delta_{ll'} \delta_{mm'} \tag{3.7}$$

$$= \frac{1}{4\pi} \sum_{l=2}^{+\infty} \sum_{m=-l}^{+l} a_{lm}^2 \tag{3.8}$$

$$= \frac{1}{4\pi} \sum_{l=2}^{+\infty} (2l+1) C_l, \tag{3.9}$$

where we made use of the following definition of the variance C_l of a_{lm} in the last step

$$C_l \equiv \langle a_{lm}^2 \rangle_m = \frac{1}{(2l+1)} \sum_{m=-l}^{+l} a_{lm}^2.$$

(3.10)

After making the following final assumption, see also Ref. [36],

$$\frac{1}{4\pi} \sum_{l=2}^{+\infty} (2l+1)C_l \approx \int \frac{l(l+1)}{2\pi} C_l \, d(\ln l)$$

(3.11)

we end up with the established description of the 2-dimensional power spectrum in order to describe the CMB properly. Usually, the power spectrum of the CMB is plotted in terms of $l(l+1)C_l/(2\pi)$ as a function of the multipole moments l. Fig. 3.3 shows the latest data of PLANCK, where the perfect description by using this approach is visible. Under the assumption of a specific cosmological model, a Likelihood-fit of the power spectrum in dependence of astrophysical key parameters is possible. Most commonly the ΛCDM model is assumed to describe cosmology with the help of essentially six different parameters: The energy content of baryons $\Omega_{\mathrm{b}}h^2$, the physical dark matter density $\Omega_{\mathrm{CDM}}h^2$ and the Hubble expansion rate H_0. The amplitude A_s of the power law spectrum $P_0(k) \propto A_s k^{n_s-1}$ contains the optical depth parameter τ, and the spectral index n_s describes the initial perturbations. This minimal set of six parameters can be used to fit the observed data with a likelihood analysis and, thus, to extract a precise value of the relic density. For more details we refer to Ref. [38]. Taking into account the PLANCK data, the latest results [37] are obtained as

$$\Omega_{\mathrm{b}}h^2 = 0.02205 \pm 0.00028 \qquad \Omega_{\mathrm{CDM}}h^2 = 0.1199 \pm 0.0027,$$

(3.12)

with h being the Hubble constant in units of 100 km/(s·Mpc). Besides studying the cosmic microwave background, there are also other methods to study the exact value of the total amount of dark matter in the universe: The redshift survey by the Sloan Digital Sky Survey (SDSS), the study of baryon acoustic oscillations (BAO), which are caused by acoustic waves which existed in the early universe, or the analysis of the Lyman-alpha forest, which is the sum of absorption lines arising from the Lyman-alpha transition of the neutral hydrogen in the spectra of distant galaxies and quasars.

3.2 Requirements on a Dark Matter Candidate

Considering these various observations of non-luminous matter, there is clear evidence for the existence of dark matter at a huge range of scales: Experimental observations attest the presence of dark matter from the size of galaxies due to ro-
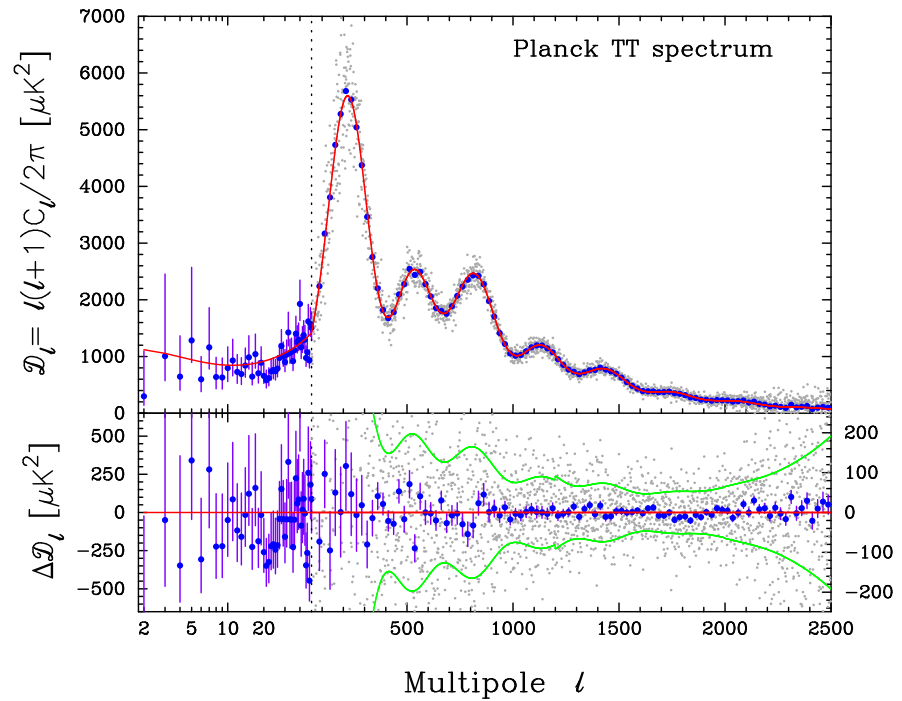
Figure 3.3: PLANCK foreground-subtracted temperature power spectrum under the assumption of a ΛCDM model. The grey dots show the power spectrum multipole-by-multipole, the blue points depict averages in bands of $\Delta l \approx 31$. The best fit assuming a ΛCDM model is shown in red and in perfect agreement with the data. In green the $\pm 1\sigma$ error on the individual mulitpoles is depicted. Image taken from [37].

tation curves, to clusters of galaxies by the virial theorem up to cosmological scales by the CMB.

Although the relic density of dark matter can be determined very precisely, the question still remains, what the nature of dark matter is and which theory is able to explain this kind of matter considering all recent observations.

An extensive overview about requirements on a dark matter candidate is given in Ref. [39], where a ten-point test is introduced. We will follow this approach and distinguish these points into two categories: pure requirements on a dark matter particle, which we want to focus on in the following, and compatibleness of different candidates to current dark matter searches. The latter will be addressed in the dedicated Section 3.4.

Considering the previously discussed observations for dark matter, a possible dark matter candidate has to fulfil the following characteristics:

Non-baryonic. In order to be consistent with the observations concerning the bullet cluster, the CMB and to match the requirements regarding the big bang nucleosynthesis (BBN), dark matter has to be *non-baryonic*. Furthermore, it has to match the experimentally determined relic density as given in Eq. (3.12).

Stable. Moreover, a potential dark matter particle has to be *stable*. This means that its lifetime has to exceed at least the present age of our universe. According to the estimates of the Hubble Space Telescope Key Project, a lifetime of $\tau \geqq 4.3 \times 10^{17} s$ is required (see e.g. Ref. [40]).

Neutral. As the feature of non-luminosity serves even as eponym for dark matter, the new kind of matter has to be electrically neutral. Also a colour charged particle is very unlikely regarding different constraints: Those could have an impact on the stability of disks of spiral galaxies [41], or even disrupt elements generated by the big bang nucleosynthesis [42]. Charged particles could also lead to interferences with CMB anisotropies and with the large scale structure power spectrum [43]. To be consistent with direct detection (further details can be found in Sec. 3.4) they should have only small couplings to bosons charged under $SU(2)$. All together, dark matter is expected to be an *electrically neutral* and *colour singlet* particle. Considering the observations regarding the bullet cluster, dark matter is also supposed to be *collisionless* [29].

Cold. Dark matter can be distinguished by being cold, warm or hot. The large scale structures, which we can observe today in our universe are dependent on microscopic properties of the dark matter candidate during the evolution of the early universe. When the universe became matter dominated, the dark matter density perturbations started to grow and cause fluctuations in the fluid of baryons and photons around the dark matter gravitational potential wells. Whereas photons decoupled

right after recombination, the baryons kept trapped in the potential wells and their density perturbations grew further. This means that the large scale structures we can observe today, have grown from tiny perturbations initiated by dark matter [39, 44].

Depending on whether dark matter was non-relativistic or relativistic at decoupling, it is called *cold* or *hot*, respectively. Dark matter with velocity dispersion between these two extrema is called *warm*. The distance which a dark matter particle can cover until it is gravitationally trapped is called *free-streaming length*. This means that only density perturbations from scales of the free-streaming length are possible. As hot dark matter has a large free-streaming length, structure formation at small scales is washed out. This implies that hot dark matter favours a top-down ansatz for structure formation: Smaller structures could only be produced by fragmentation of larger ones. This is in contradiction to current N-body simulations and current observations of the age of galaxies and galaxy clusters. Due to this, hot dark matter is clearly disfavoured as the main dark matter component [45].

Cold dark matter, however, has become non-relativistic long before the matter dominated era. With a small free-streaming length, perturbations on small scales are possible and structure formation can evolve from a bottom-up approach. Taking cold dark matter as initial condition for N-body simulations is in good agreement with today's observed large scale structures. However, some discrepancies appear when comparing simulations with the realization in nature. For instance, the number of predicted satellite halos in the Milky Way exceeds the number of observed dwarf galaxies [46, 47]. This is often referred to as *missing satellites problem*.

Therefore, warm dark matter, for instance, was taken into consideration with a free-streaming length of the order of galaxies such that the formation of smaller structures is suppressed. By studying the growth of structures in galaxy clusters and the Lyman-α-forest, a lower limit on the warm dark matter mass can be set, which is quite stringent [48]. Another prominent alternative is interacting dark matter (IDM), which is able to solve the aforementioned discrepancies arising in simulations [49].

However, Halo profiles, which cause problems within N-body simulations with respect to cold dark matter are highly sensible to small deviations from the primordial spectrum. Therefore, cold dark matter counts still as the preferred realisation of dark matter. In particular, several astrophysical processes exist which could solve these discrepancies [50, 51].

Consistent with Big Bang Nucleosynthesis. Furthermore, the dark matter candidate should also be *in agreement with big bang nucleosynthesis* (BBN). The theory of big bang nucleosynthesis can predict the abundance of light elements which were produced within the first three minutes after the big bang and is in very good agreement with today's observations [39]. For a more detailed review on this topic we refer to Ref. [52].

Changes in the prediction of BBN could arise from the existence of additional rel-

ativistic particles, for example. They could lead to a faster expansion rate, which would result in an earlier freeze-out of the neutron-to-proton ratio and thus to a higher He^4 abundance [53]. But also decaying particles during the BBN can modify the predictions of big bang nucleosynthesis [54]. However, BBN predicts today's observations very precisely.

Consistent with Stellar Evolution. Finally, also the *stellar evolution* has to remain unchanged. For example, light, weakly interacting particles produced in the hot plasma of stars could escape without further interactions and could, thus, lead to an energy loss of the stars, which would modify the stellar evolution [55].

All in all, there are stringent requirements on the properties which a viable dark matter candidate should feature. In the following we give an overview of different proposed dark matter candidates and their current viability.

3.3 Dark Matter Candidates

In principle, two major approaches exist to explain the experimental discrepancies discussed in Sec. 3.1. First, these observations could be evidence for dark matter and could be described with the help of a (new) particle. Second, changes in theory on the astrophysical scale could be necessary and sufficient such that the introduction of new particles is not needed. After discussing the latter case, different dark matter candidates will be addressed in the context of their viability regarding experimental observations and the aforementioned criteria.

3.3.1 Alternative Theories without a Particle Candidate

Although it is well-established that something like dark matter has to exist (therefore we already introduced "dark matter" as the possible solution in order to explain the observations from the beginning of this thesis), we want to mention two of the most discussed alternative approaches for completeness. However, both possible explanations have serious drawbacks such that they cannot exist without any additional non-baryonic matter.

Modified Newtonian Dynamics (MOND). A widely discussed alternative theory in order to explain the observation of dark matter is *Modified Newtonian Dynamics* (MOND) [56]. The motivation of this theory lies in the explanation of the discrepancy in the observation of rotation curves not by the introduction of dark matter (cf. Sec. 3.1.2), but by a breakdown of Newtonian dynamics in the limit of small accel-

erations. In MOND, a constant of the dimension of an acceleration a_0 is introduced

$$a^2/a_0 = MGr^{-2} \tag{3.13}$$

such that the standard Newtonian dynamics is a good approximation for accelerations much larger than the introduced constant $a \gg a_0$. The behaviour in the other limit $a_0 \ll a$ gives rise to an acceleration and is described by an underlying theory, see Ref. [57].

Already in 1999 it was claimed that resolving the virial discrepancy in galaxy clusters is not possible only by MOND, but needs additional, undetected matter [58]. This was confirmed furthermore by the observations concerning the bullet cluster. Although people still claim that MOND is a viable theory in combination with a kind of not yet detected matter (which could be also baryonic) [59], the original motivation of MOND - explaining the observation of rotation curves without any additional matter - is not valid any more.

Massive Astrophysical Compact Halo Objects (MACHOs). Another alternative explanation in contrast to dark matter is the existence of *Massive astrophysical compact halo objects* (MACHO). These are astronomical objects which are built out of baryonic matter without emitting radiation. This definition would be satisfied by black holes, neutron stars or different kinds of dwarfs, for instance. However, as discussed before, observations of the cosmic microwave background, baryon acoustic oscillations or the knowledge of the large scale structures set stringent limits on the baryonic amount of matter. Regardless of the presence or absence of MACHOS, a large fraction of non-baryonic matter is necessary to be consistent with experimental observations. For a more detailed review about the status of MACHOS, we refer the reader to Ref. [60].

3.3.2 Particle Dark Matter Candidates

The aforementioned theories tried to explain the observational discrepancies by modifying gravitation or by an astrophysical explanation. In the end, however, both approaches require an additional kind of matter to account for all observations. Therefore, different particle candidates are discussed in the literature trying to solve the question of the nature of dark matter. Due to very detailed observations, stringent requirements on potential particle candidates are imposed. In order to put the candidate studied in this work in the global context, a brief overview of some of the most popular particle dark matter candidates is given in the following.

Standard Model like Neutrinos. The most straightforward approach is the attempt to explain dark matter by already well-known particles within the Standard Model of particle physics. One once widely discussed candidate has been the *Standard Model like neutrino*. With an upper mass limit of $m_\nu < 2.05$ eV (95 % C.L.) set by tritium β-decay experiments [20], an upper bound on the relic density of roughly $\Omega_\nu h^2 \lesssim 0.07$ [26] can be assumed. This is in contradiction to current measurements of the relic density such that the neutrino as dark matter candidate cannot account for the dominant component of dark matter. Even more stringent constraints arise from combining PLANCK data and observations of the large-scale matter power structure, as recently shown in Ref. [61]. Together with baryon acoustic oscillations and the lower limit from neutrino oscillation experiments, the sum of the neutrino masses is restricted to $0.05\ eV < \sum m_\nu < 0.15\ eV$. As the neutrino was thermally produced in the early universe and decoupled quite early relativistically at around $T \approx 1$ MeV [39], this makes the neutrino a prototype for hot dark matter. As discussed earlier, this characteristic disfavours the neutrino as a major ingredient of dark matter [45]. However, small amounts of hot dark matter could be realized as long as agreement with the large scale structure and the CMB data is ensured.

Sterile Neutrinos. One possible extension of the Standard Model is the introduction of right-handed neutrinos. They could simultaneously explain neutrino oscillations and as they are sterile with respect to weak interactions (apart from mixing), they are considered as dark matter candidates [62]. In the simplest approach the active neutrinos would have light masses whereas the *sterile* ones are quite heavy. Through a see-saw like mechanism or some flavour symmetries it is possible to create one light sterile neutrino in the keV-range, which could account for dark matter. As recently shown, this kind of dark matter is under several assumptions still valid and could explain dark matter, neutrino oscillations and baryon asymmetry [63, 64]. But still, there are stringent bounds on such a warm dark matter particle [48, 65, 66].

Axions. The initial idea of introducing *axions* was to give a solution to the strong CP-problem. This problem describes the contradiction between QCD allowing a CP-violating flavour singlet interaction and the non-observation of the electric dipole moment of the neutron. One possible solution to this problem is the introduction of a Peccei-Quinn symmetry [67]. By breaking this global symmetry spontaneously, a goldstone boson arises, the so-called axion. A review about axions and the strong CP-problem is given in Ref. [68].
According to laboratory searches, stellar cooling and dynamics of supernova `1987A`, the axion has to be very light ($m_a \lesssim 0.01$ eV) (see e.g. [26]). But as the calculation of the relic density highly depends on the corresponding production mechanism, the theoretically predicted value is quite uncertain. Nevertheless, it is still possible to find a range in the parameter space where the axion fulfils all constraints and is therefore still a viable dark matter candidate [69].

Neutralinos.   After discussing dark matter candidates arising from minimalistic extensions of the Standard Model, we focus now on the candidates which are given due to Supersymmetry. An overview of the cornerstones of Supersymmetry is given in the previous chapter 2. The most prominent and well-known particle is hereby certainly the *neutralino*. In an *R*-parity conserving MSSM the neutralino can be the lightest supersymmetric particle in a wide range of the parameter space and thus, represents a good cold dark matter candidate. It belongs to the group of weakly interacting massive particles (WIMPs). Its predicted relic abundance fits coincidentally very well to the measured one. This is also often referred to as the *WIMP-miracle* and makes it to one of the most intensively studied dark matter candidates. As shown in Tab. 3.1, it is still in very good agreement with all experimental observations. As the neutralino is the subject of the present work, we will devote further discussion on its phenomenology to the later chapters.

Sneutrinos.   The superpartners of the already discussed neutrinos are also considered as dark matter candidates. Left-handed *sneutrinos* are already ruled out because of direct dark matter detection experiments or a too small relic abundance, respectively [70, 71]. However, right-handed sneutrinos are still a viable option, but already quite constrained. Whereas light sneutrinos are excluded by the discovery of a Higgs boson with a mass of around 125-126 GeV, heavy sneutrinos can still be a viable, but quite constrained dark matter candidate. For further details see for instance Ref. [72].

Gravitinos.   In case that SUSY is not only a global, but a local symmetry, supergravity could exist. This would result in a new particle: The *gravitino* which is the superpartner of the graviton. For example, in gauge-mediated or gravity-mediated scenarios, the gravitino can be the lightest supersymmetric particle and is stable. Thus, it can also be a possible dark matter candidate. However, they have to face stringent constraints concerning their mass, their life time and the reheating temperature. Long lived gravitinos, for instance, can give rise to problems for cosmology. Also, if the reheating temperature is not low enough, an overproduction in the early universe is caused [26]. But there are many interesting scenarios depending on the next-to-lightest supersymmetric particle in which these constraints can be circumvented [73, 74].

Axinos.   When extending the MSSM with the Peccei-Quinn mechanism, a superpartner to the axion is introduced: the so-called *axino*, which can be also a viable dark matter candidate. Axinos are extremely weakly interacting particles since their couplings are suppressed. Depending on the way Supersymmetry is broken the axino has a mass between the eV and GeV scale [73, 75].

WIMPless Dark Matter. More recently there is also discussion about the so-called *WIMPless dark matter*. Hereby, it is claimed that the existence of a WIMP-miracle does not necessarily imply the existence of WIMPs as dark matter. In WIMPless models, dark matter is part of a hidden sector and can feature scalar or fermionic properties. On the basis of the WIMPless ansatz, models can be introduced where particles have naturally the right thermal relic density, but neither weak-scale masses nor weak force interactions [76]. This opens up new room for experimental tests. One possibility and recently discussed realization, for example, is isospin-violating dark matter, which is still in agreement with all current collider and low-energy bounds [77].

Dynamical Dark Matter. A quite new development is the approach of *dynamical dark matter*. The idea of dynamical dark matter is quite different in comparison to the usual approach. Whereas normally one dominant dark matter candidate is assumed, the theory of dynamical dark matter is not based on one stable dark matter particle which accounts for most of the observed dark matter. In this ansatz, a whole ensemble of different, not necessarily stable dark matter candidates is assumed, which is balanced with the relic density [78]. A quite natural realization is found in the framework of large extra dimensions with an infinite tower of Kaluza-Klein states. A proof of principle is given in [78], where the KK excitations of a bulk axion makes the dark matter ensemble. It is shown that this is in agreement with all up now known collider, astrophysical and cosmological constraints and should be taken into consideration in order to identify the nature of dark matter.

Further Candidates. There are a lot of other extensions to the standard model with corresponding dark matter candidates, which cannot be mentioned all in detail at this point. For instance, in the framework of universal extra dimensions with conserved KK-parity the lightest Kaluza-Klein particle is stable and provides a suitable dark matter candidate, which is similar to the neutralino [79].
Another simple extension to the standard model is the inert doublet model. In this model, a second Higgs doublet with complex scalar fields is introduced, which couples to Standard Model scalars and gauge bosons, but not to fermions. This model incorporates a viable dark matter candidate and provides an interesting phenomenology as the SM-like Higgs boson is the main exchange particle between the dark and visible sector [80].
A huge variety of other candidates is discussed in literature, like Champs [81] or Wimpzillas [82]. For more details we refer to reviews in Refs. [26, 39, 83, 84].

Conclusions. We have discussed various dark matter candidates and approaches to explain the observation of dark matter in general. From now on, we focus only on the neutralino as a dark matter candidate. As this particle naturally evolves out of Supersymmetry and is in agreement with all current observations, this is highly

DM candidate	I. Ωh^2	II. Cold	III. Neutral	IV. BBN	V. Stars	VI. Self	VII. Direct	VIII. γ-rays	IX. Astro	X. Probed	Result
SM Neutrinos	×	×	✓	✓	✓	✓	✓	–	–	✓	×
Sterile Neutrinos	∼	∼	✓	✓	✓	✓	✓	✓	✓!	✓	∼
Neutralino	✓	✓	✓	✓	✓	✓	✓!	✓!	✓!	✓	✓
Gravitino	✓	✓	✓	∼	✓	✓	✓	✓	✓	✓	∼
Gravitino (broken R-parity)	✓	✓	✓	✓	✓	✓	✓	✓	✓	✓	✓
Sneutrino $\tilde{\nu}_L$	∼	✓	✓	✓	✓	✓	×	✓!	✓!	✓	×
Sneutrino $\tilde{\nu}_R$	✓	✓	✓	✓	✓	✓	✓!	✓!	✓!	✓	✓
Axino	✓	✓	✓	✓	✓	✓	✓	✓	✓	✓	✓
SUSY Q-balls	✓	✓	✓	✓	∼	–	✓!	✓	✓	✓	∼
B^1 **UED**	✓	✓	✓	✓	✓	✓	✓!	✓!	✓!	✓	✓
First level graviton UED	✓	✓	✓	✓	✓	✓	✓	×	×	✓	×
Axion	✓	✓	✓	✓	✓	✓	✓!	✓	✓	✓	✓
Heavy photon (Little Higgs)	✓	✓	✓	✓	✓	✓	✓	✓!	✓!	✓	✓
Inert Higgs model	✓	✓	✓	✓	✓	✓	✓	✓!	–	✓	✓
Champs	✓	✓	×	✓	×	–	–	–	–	✓	×
Wimpzillas	✓	✓	✓	✓	✓	✓	✓	✓	✓	∼	∼

Table 3.1: Test performance of selected DM candidates. The ✓ symbol is used when the candidates satisfy the corresponding requirement, and it is accompanied by a ! symbol, in the case that present and upcoming experiment will soon probe a significant portion of the candidate's parameter space. If the requirement can be satisfied only in less natural, or non-standard scenarios, or in the case of tension with observational data, the symbol ∼ is used instead. Candidates with a ∼ symbol in the last column, where the final result is shown, should still be considered viable. If one of the requirements is not satisfied, then the symbol × is used, and since these requirements are *necessary* conditions, the presence of a single × is sufficent to rule out the particle as a viable DM candidate. Overview table taken from [39] and slightly modified.

motivated. In the light of the recent discovery of a Higgs boson, the realization of Supersymmetry and thus a neutralino as dark matter particle is very interesting.

However, we want to stress clearly at this point that there is also the possibility of the coexistence of different dark matter particles. Assuming that the studied particle is only subdominantly contributing, the lower bound of the relic density is weakened. The upper bound though, remains a strict limit.

In addition to that, the standard cosmological model, the ΛCDM model, is usually assumed. One should be aware that constraints on dark matter could change under the assumption of another model.

After this short overview of different possible dark matter candidates, we focus in the following on the status of current dark matter searches, in particular regarding WIMPs.

3.4 Current Status of Dark Matter Searches

Since the existence of dark matter has been acknowledged, explicit searches are the next step in order to determine its nature. As a weakly interacting massive particle (WIMP) is the mostly favoured and discussed candidate, different search strategies are pursued in order to find such a particle.

Fig. 3.4 shows the possible three categories of processes which a WIMP and a standard model particle can feature via an effective coupling. As depicted in Fig. 3.4, depending on the specific process different search strategies can be used: direct, indirect and collider searches.

In the following, we want to give a brief overview of the current status of these searches, in order to set them into the context of our study.
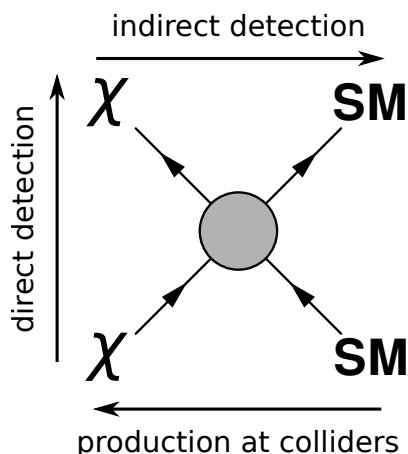

Figure 3.4: Schematic overview of processes involving dark matter and Standard Model particles, and their corresponding search strategy.

3.4.1 Indirect Detection

One possibility in trying to identify dark matter is via indirect detection experiments. The basic principle is to detect signatures of annihilating or decaying dark matter particles into SM particles, which after showering and hadronization give rise to energetic cosmic rays of charged particles (like electrons and positrons, protons and antiprotons, deuterium and antideuterium), photons or neutrinos. According to the obtained spectrum, one can draw a conclusion on the underlying standard model particles and thus on the interaction of the DM particle with SM particles.

The biggest challenge concerning these searches is to look for channels and energy ranges in which the astrophysical background is small compared to the expected signal. From the obtained spectrum one can then draw conclusions on the initial SM particles and thus on the interaction between DM particles and SM particles. This allows us to get more hints concerning the properties of dark matter.

In the following, we discuss in particular three different types of particle fluxes which are studied in the context of indirect detection experiments. Especially, Refs. [85–87] are interesting concerning this topic and have been considered for detailed information.

Charged Cosmic Rays. Key-experiments in the detection of charged cosmic rays are the PAMELA and FERMI satellites, the HESS telescope and the AMS spectrometer. The latest results were published by FERMI (2011) and AMS (2013).

The left subfigure of Fig. 3.5 shows the positron fraction $e^+/(e^+ + e^-)$ as a function of the energy. Most recently, the results of AMS-02 have been published, which are depicted in red. They are in agreement with the results from Fermi (green) and PAMELA (blue). The new results show much smaller errors and are obtained on the basis of only 10% of the total data that is expected from AMS-02 in the future. Consistently, for all experiments a steep increase in the energy spectrum of the positron fraction is visible. This is, however, in disagreement with the expectation that the fraction of positrons decreases with increasing energy, assuming the standard scenario in which cosmic ray positrons are mainly produced by secondary processes. The observed clear enhancement for high energies is thus a sign for a new physical phenomena, whether arising from particle physics or astrophysics, and is in agreement among all experiments. By contrast, the spectrum of the antiproton flux does not show any excess over background, which is depicted in grey in Fig. 3.5. This is also still valid for the recent AMS data.

Interpreting the excess in the positron flux in terms of dark matter, its properties are quite constrained: In order to explain the observation of a positron excess, while seeing no deviation in the antiproton distribution, the dark matter particle has to annihilate exclusively into leptonic channels. To reproduce the deviation from background for the $e^+ + e^-$ spectrum, a particle of a few TeV and a large annihilation cross section is required.

The search for antideuterons, which are boundstates of an antiproton and an an-
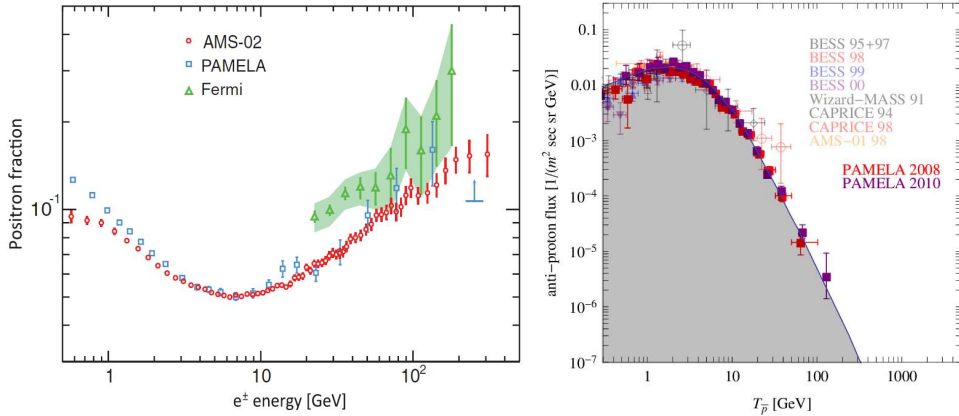
Figure 3.5: Comparison of different indirect detection experiments regarding positron fraction and antiproton flux. Left: positron fraction, compilation of Fermi, PAMELA and recent AMS-02 data [88]. Right: antiproton flux, compilation of older and recent data. Astrophysical background is depicted in grey [86].

tineutron, is also interesting in this context. They are supposed to be a smoking gun evidence for dark matter, however, until now they have not been observed in nature [87]. One expects antideuterons to be produced via coalescence of an antiproton and an antineutron in connection with a dark matter annihilation event. Experiments like GAPS and AMS-02 are searching for such states.

Photons. Having hints for dark matter from the positron flux, an enhanced γ-ray emission would be consistently expected. In addition to that, a γ-ray signal is usually expected to be a much more natural channel for dark matter searches, since it should appear already for lower annihilation rates. The annihilation of dark matter gives rise to prompt photons, either by direct photon production or by bremsstrahlung. Also through the inverse Compton effect or synchrotron radiation, photons are assumed to be produced. The main experiments in investigating these γ-rays above 1 GeV are the FERMI satellite, but also Imaging Atmospheric Cherenkov Telescope (IACT) are involved, like HESS and VERITAS. They use as target the Milky Way galactic center, regions of the galactic halo, or large scale structures, for example.

For a long time, no anomalous signature above the background has been observed, in contrast to the expected signal regarding the positron results. Thus, mainly upper limits on the dark matter annihilation cross section have been set. In conclusion, both observations are highly contradictory. Therefore, it has been already considered that the enhanced positron signal results from an unknown astrophysical source, like pulsars or supernovae remnants (see e.g. [89]). Quite recently, a claim of having found some dark matter signal has been published. A γ-ray line around 130 GeV in the publicly available FERMI data has been observed [90]. Up to now, this observation has attracted quite some attention. However, it still has to be clarified whether the

observation is a dark matter signal, statistical fluctuation, or a detector effect. A study in Ref. [91] addressing the systematic uncertainties, however, sees still this line. Clear exploration will be expected at least in 2015, when more data from the inner galaxy will be available, which will allow a better analysis [92].

In summary, this is one of the most interesting recent developments, although it still needs time to clarify this kind of signal.

Neutrinos. As neutrinos can cover large distances of dense matter quite unhinderedly in the galaxy, they are also among the interesting final state particles of dark matter annihilation. Their detection, however, is more involved. They can only be investigated by secondary particles caused by interactions with target material, which is also susceptible for cosmic muons. Recent experiments are SuperKamiokande or Icecube, for instance.

However, these experiments have not detected any hint of dark matter so far such that only bounds on the dark matter annihilation cross section and the scattering cross section with nuclei have been set [93, 94].

Conclusions. Considering all results obtained by indirect detection experiments, no clear hint for dark matter is given so far. Especially comparing the excess in the positron flux with other surveys, the results are highly contradictory. As also pulsars, for instance, could explain high energy cosmic ray positrons, it is still too early to draw any conclusions. However, with the claim of a γ-ray line, this field has achieved an enormous rise in attention. But also concerning this observation, one has to wait for more data in order to judge whether it is a hint for dark matter, a signal of astrophysical sources, or other statistical or systematic uncertainties.

3.4.2 Direct Detection

Another possibility of searching for dark matter signals is to look for scattering of a dark matter particle with particles of the standard model, which is referred to as *direct detection*. For further reviews Refs. [95, 96] are recommended.

In order to investigate this kind of interaction, detectors are designed to detect potential WIMPs which are recoiling off a specific target material in dedicated experiments. For weakly interacting particles the interaction rate is expected to be of the order of roughly one event per 10 kg-days. In addition, radiative background is also a serious problem, as it can fake a possible WIMP signal. Therefore, generally a lot of effort is invested into the shielding of these experiments.

The detection principles can be divided into three categories: Probing dark matter through phonons, ioniziation, and scintillation. As these different signal types are sensitive in different energy regions, a combination of at least two different principles is used in order to get the best possible distinction between background and signal, in connection with a widely probed energy range. Fig. 3.6 gives an overview of the
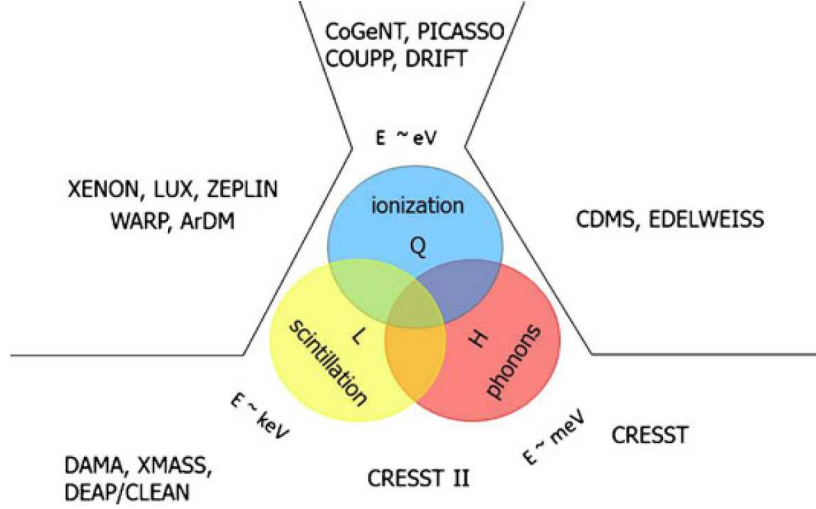
Figure 3.6: Measurement principles of different direct detection experiments. By probing dark matter through interactions with standard model particles, signals can be detected through ioniziation, scintillation and phonons according to the used detector material. Usually, experiments make use of two of these detections principles in order to obtain an involved signal to background ratio and to access a wide energy range. Figure taken from [97].

used methods for the different existing direct detection experiments.

Direct detection experiments are able to probe spin-dependent (axial-vector) as well as spin-independent (scalar) couplings. When a WIMP couples to the spin content of a nucleon, the cross section for this scattering is proportional to $J(J+1)$ and thus mainly sensitive to the angular momentum, but not to the number of nucleons. By contrast, for the spin-independent case the mass of the target is the decisive factor. Therefore, spin-independent scattering dominates for experiments with heavy targets [26].

Fig. 3.7 and Fig. 3.8 show the recent status of upper limits on the scattering cross section set by direct detection experiments.

First, we focus on the spin-dependent results: As it can be seen in Fig. 3.7 the most stringent constraint for pure neutron couplings above 6 GeV/c^2 is provided by XENON100 with a minimum WIMP-neutron cross section of 3.5×10^{-40}cm^2 [98]. XENON100 is an experiment which uses Xenon as target material and is operated in the Gran Sasso National Laboratory in Italy. It makes use of scintillation and ioniziation as detection principles. As the used isotopes ^{129}Xe and ^{131}Xe contain an odd number of protons (by contrast to the even number of neutrons) XENON100 is not that sensitive to proton couplings. This can be seen in the second plot of Fig. 3.7. Here, dedicated experiments like PICASSO [99], COUPP [100] or SIMPLE [101] set the most stringent constraints. This results from their used target material containing fluorine, which features an odd number of nucleons. Also IceCube pro-
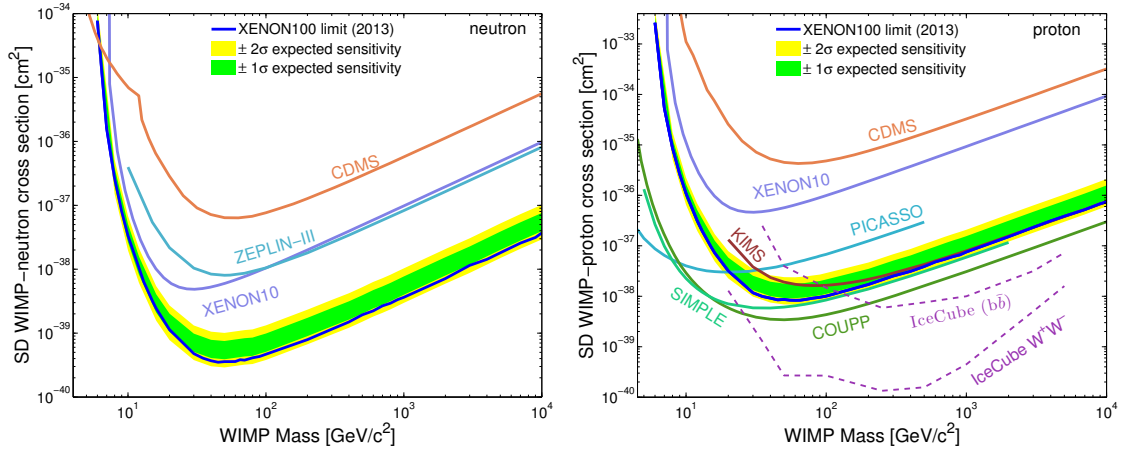
Figure 3.7: Upper limits on the spin-dependent WIMP-nucleon cross section at 90 % C.L. On the left hand side, bounds on the cross section of a WIMP scattering off a neutron is shown, on the right hand side the same for the proton. Figures taken from [98].

vides stringent constraints on the scattering cross section above a WIMP mass of around 30 GeV through certain channels [94].

The spin-independent results are depicted in Fig. 3.8. Here, also XENON100 sets the most rigorous limit for a WIMP mass of above 8 GeV/c^2. A minimum is reached at 55 GeV/c^2 with a corresponding cross section of 2.0×10^{-45}cm^2 [102]. These limits are, however, in high tension with the results from DAMA/LIBRA, CoGeNT, CRESST-II and quite recently also CDMS. All these experiments claim an excess of events in their signal regions, but almost every one of them in a different region of parameter space.

The first positive signal seen in a dark matter search was found in an annual modulation of the DAMA/NaI experiment, which was confirmed later also by the DAMA/LIBRA experiment [103]. Both scintillation experiments are located at the Gran Sasso National Laboratory in Italy. The detected modulation is compatible with the signal expected by dark matter particles of the Galactic Halo. The model independent evidence of dark matter was further confirmed on an 8.9 σ confidence level by taking into account the new data sets of DAMA/LIBRA [104]. But as shown in Fig. 3.8 the favoured regions of DAMA are in tension with signals and exclusion limits of the other experiments. To clarify if the observed annual modulation comes from some unknown astrophysical source or if it is in fact an evidence for dark matter, a similar experiment DM-Ice is planned at the south pole [105].

Also CRESST-II claims to have found a sign of dark matter. 77 events were found in the acceptance region, which cannot be explained by the known background sources. A maximum likelihood analysis favours a WIMP mass of 12 GeV and 25 GeV for a cross section of 3.7×10^{-41}cm^2 and 1.6×10^{-42}cm^2, respectively [106, 107]. But as mentioned before, this result is in disagreement with the DAMA experiment (see
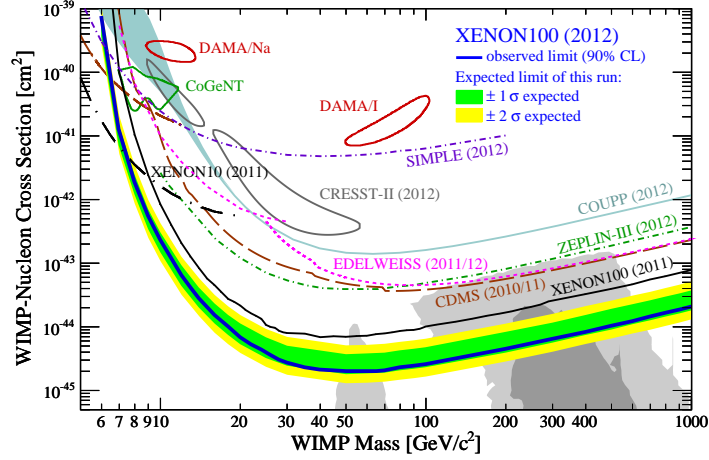
Figure 3.8: Status of current direct dark matter searches regarding spin-independent WIMP-nucleon scattering. The green/yellow band shows the $1\sigma/2\sigma$ expected sensitivity of XENON100, the blue line the resulting exclusion limit at 90 % C.L.. The recent status of other direct dark matter searches are shown by lines of different colours. Exclusion limits are depicted for 90 % C.L., detection claims at 2σ. The grey area shows the favoured region of the CMSSM parameter space. Figure taken from [102].

Fig. 3.8). In the 2006-2007 data set, CDMS had no sign for a dark matter excess [110]. However, quite recently the CDMS experiment has updated its analysis and claims now an excess, which might be compatible with the CoGeNT results. This is depicted in more detail in Fig. 3.9, which shows a zoom of the parameter plane of Fig. 3.8, but with the newly published CDMS excess. They claim now an excess at $10 \text{ GeV}/c^2$ with $2.4 \times 10^{-41} \text{cm}^2$ [108]. This is compatible with the results by CoGent claiming an excess at around 7 GeV with a cross section of around 10^{-40} cm^2 [111, 112]. Whereas these two experiments are in agreement, they are still in tension with the other experiments, especially with XENON10 and XENON100, which already excluded this region.

All in all, it is quite difficult to draw a conclusion at this point, as there are lot of contradictory observations and exclusion limits. Therefore upgrades and new detectors are developed to get a step further in identifying the nature of dark matter.

3.4.3 Collider Searches

The pair production of dark matter particles is the third interaction possibility and opens the opportunity to look for dark matter at colliders. In many models this interaction occurs via an exchange of a heavy mediator which can then be integrated out at low energies. Under this assumption, an effective field theory approach is possible, where the interaction is described via a higher dimensional operator. This allows one to study dark matter production in a model independent way and to set
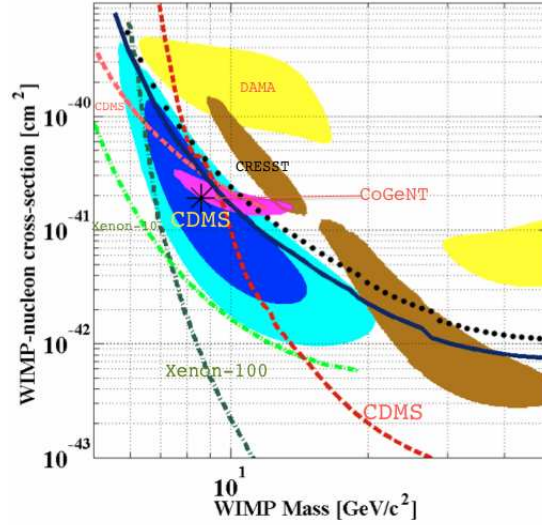
Figure 3.9: Zoom in the parameter plane shown in Fig. 3.8 with newly updated CDMS results. Figure originally published in [108], version with labels taken from [109].

limits to different interaction possibilities at the same time.

As the final state dark matter particles are not visible in detectors, analyses are focused on detecting initial state radiation. By setting limits on mono-photon or mono-jet cross sections in collider searches, constraints can be derived on the coefficients multiplying these effective operators, which are connected to the suppression scale where new physics appears. These constraints can then be translated into bounds on the dark matter-nucleon scattering cross sections probed in direct detection experiments.

Especially for low WIMP masses, collider searches can be more sensitive than direct detection searches, as already shown in analyses for LEP [113], Tevatron [114], LHC [115–117] or the future ILC [118, 119]. On top of that, this approach does not suffer from astrophysical or nuclear uncertainties. Therefore, a combination of collider searches together with searches of direct detection experiments can strengthen the already strong limits.

The current status of these searches at the LHC is depicted in Fig. 3.10 for the ATLAS and in Fig. 3.11 for the CMS experiment. Both figures show the upper limit on the WIMP-nucleon cross section at 90% C.L. in dependence of the WIMP mass for spin-independent and spin-dependent interactions. For each effective operator the corresponding bound on the cross section is shown. The ATLAS study distinguishes five different effective operators: Assuming quarks in the initial state, a scalar (D1) and vector operator (D5) are studied. The scalar contact operator D11 takes into account gluons in the initial state. For the spin-dependent case, an axial-vector like
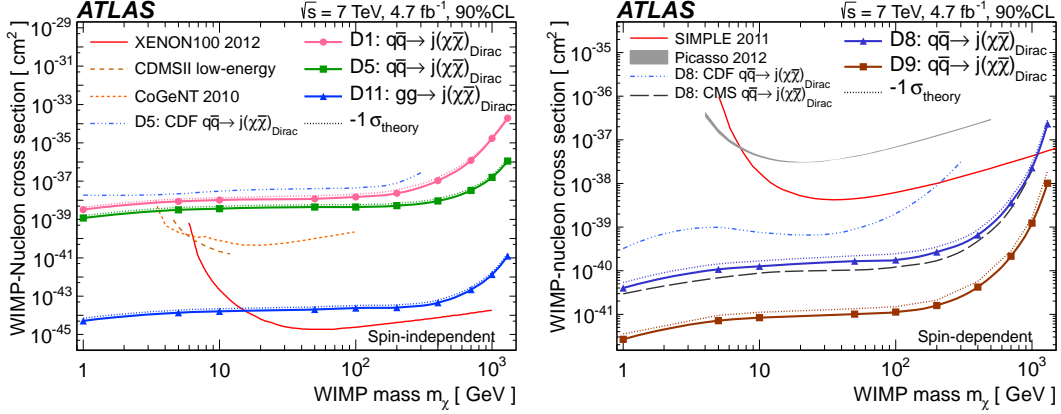
Figure 3.10: 90% C.L. limits on the WIMP-nucleon scattering cross section in dependence of the WIMP mass at the ATLAS experiment. The thick lines are the observed bounds excluding theoretical uncertainties. The limits involving quarks assume four light flavours with equal coupling strength to the WIMPs. For comparison, the limits of different direct detection experiments are shown. On the left hand side the spin-independent case is depicted. The scalar effective operator D1 and vector like operator D5 describe a coupling to quarks in the initial state. By contrast, the scalar operator D11 assumes gluons in the initial state. On the right hand side the spin-dependent case is shown. Both operators assume quarks in the initial state, with D8 being an axial-vector and D9 a tensor operator. For more details we refer to Ref. [120], from where the figures are taken.

contact operator D8 and a tensor like operator D9 are considered. In all cases which involve quarks, four light flavours with equal coupling strength to WIMPs are assumed.

In the CMS study only two cases are distinguished. For the spin-independent interaction a vectorial effective operator is considered, for the spin-dependent case an axial-vector one.

Both analyses show clearly that collider searches feature a very good sensitivity in the low WIMP mass region. Especially, for masses lower than 10 GeV the LHC is a powerful tool and more sensitive than direct searches. As depicted in both figures, the LHC exceeds the stringent limits of the CDF experiment at Tevatron.

Quite recently it was shown in Ref. [117] that for many models with an s-channel dark matter coupling to $q\bar{q}$ pairs, not only the production of a dark matter pair via a heavy mediator, but also the production of a $q\bar{q}$ pair in the final state is interesting for setting bounds on the dark matter coupling. Having the same underlying theory, upper limits on the respective effective coupling can be translated into each other. In the analysis of [117] it has been shown, that the experimentally obtained limits on the quark contact interaction at the LHC give stronger translated limits on the dark matter coupling than dedicated searches for dark matter pair production.
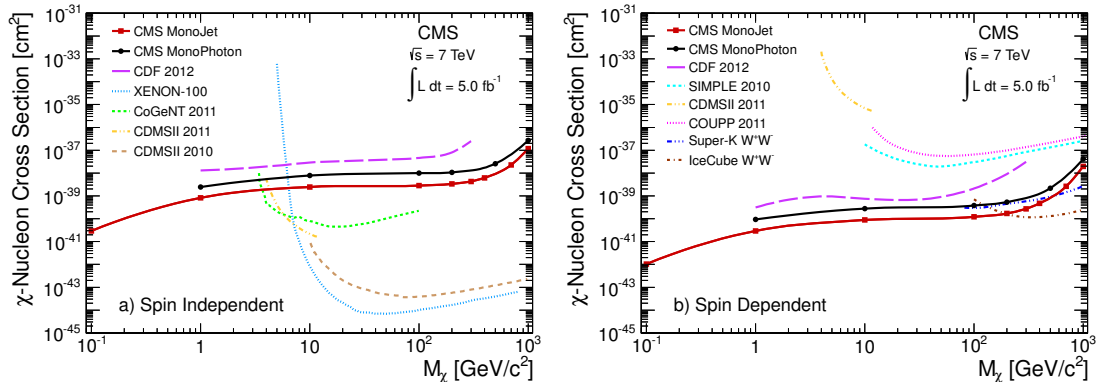
Figure 3.11: 90% C.L. upper limits on the WIMP-nucleon scattering cross section in dependence of the WIMP mass at the CMS experiment. In this study interaction between two quarks and a dark matter pair is assumed, with the WIMP being a Dirac fermion. On the left hand side the spin-independent case under the assumption of a vector effective operator is depicted. The spin-dependent case with an axial-vector operator is shown on the right hand side. For further comparison limits, of other direct detection experiments are shown. For more details we refer to Ref. [121], from where the figures are taken.

When assuming a certain model, like Supersymmetry, more specific searches can be performed. Typically, experiments look for events with a high final state multiplicity and large missing energy. Such a signature is expected if heavy supersymmetric particles get produced at the collider and decay via cascades to the lightest supersymmetric particle. This can be the lightest neutralino, which is a stable particle and a good cold dark matter candidate. Escaping the detector unhinderedly, this leads to the expectation of large missing energy.

Conclusions. We know many observational hints for the existence of dark matter. With the help of different theories and particle species we are able to give possible explanations for the invisible matter of our universe. On the experimental side, collider searches are still only able to set exclusion limits on possible dark matter couplings (see Sec. 3.4.3), direct searches, however, claim the first experimental excesses in detecting dark matter. But as discussed in Sec. 3.4.2, although some collaborations agree, most observations are still contradictory. The very same is true for indirect searches.

As for the analysis studied in this thesis the relic density sets the most stringent constraint, only this bound will be considered. However, it will be interesting what the future will tell us regarding direct and indirect detection, as well as collider searches.

4 Dark Matter Relic Density

As in this thesis the impact of one-loop corrections on the relic density is studied, we focus in this chapter on the calculation of the relic density in order to discuss different sources of uncertainties in the second section.

4.1 Calculation of the Relic Density

First, we discuss the calculation of the relic density starting with the Boltzmann equation. Detailed literature on different aspects of the here shown derivation can be found in Refs. [44, 122–124].

4.1.1 The Boltzmann Equation

A distribution of an ensemble of particles within a certain phase space can be described by the Liouville equation. If the particles of this ensemble interact only on short distances, and one can assume that at most two particles are interacting with each other (which means that their density is not too high) the system can be described by the Boltzmann equation

$$\hat{\boldsymbol{L}}[f] = \boldsymbol{C}[f], \tag{4.1}$$

where $\hat{\boldsymbol{L}}$ stands for the Liouville operator, which describes the change of the particle phase space density per time. The collision operator $\boldsymbol{C}$ models the rate of change in the number of particles per phase space volume due to the interaction with other particles (for more details on hydrodynamics in astrophysics see e.g. Ref. [125] and references therein). As the particles which existed during the evolution of the universe, were relativistic, a covariant and relativistic generalization of the Liouville operator has to be considered

$$\hat{\boldsymbol{L}} = p^\alpha \frac{\partial}{\partial x^\alpha} - \Gamma^\alpha_{\beta\gamma} p^\beta p^\gamma \frac{\partial}{\partial p^\alpha}. \tag{4.2}$$

By further assuming the universe to be homogeneous and isotropic, the phase space distribution function of particles simplifies to $f = f(|\vec{\boldsymbol{p}}|, t)$. In the Robertson-Walker

metric, the Liouville operator can be written as

$$\hat{\boldsymbol{L}}[f(E,t)] = E\frac{\partial f}{\partial t} - \frac{\dot{a}}{a}|\vec{\boldsymbol{p}}|^2\frac{\partial f}{\partial E}, \tag{4.3}$$

with a being the scale factor of the expansion of the universe.

We use the following definition of the number density

$$n(t) = \frac{g}{(2\pi)^3}\int d^3p\, f(E,t), \tag{4.4}$$

where g accounts for the number of degrees of freedom of the corresponding particle. Taking into account Eq. (4.3) the ansatz of Eq. (4.1) can be integrated by parts such that we arrive at

$$\dot{n} + 3Hn = \frac{g}{(2\pi)^3}\int \boldsymbol{C}[f]\frac{d^3p}{(2\pi)^3E}, \tag{4.5}$$

with $H \equiv \dot{a}/a$ being the Hubble expansion rate. Further details regarding the derivation of the Liouville operator in the Robertson-Walker metric can be found in Refs. [44, 124].

In a second step we focus on the derivation of the collision operator $\boldsymbol{C}$. For the time being, we consider only annihilation processes of dark matter particles into Standard Model particles $\chi(p_1)\bar{\chi}(p_2) \leftrightarrow \mathrm{X}(k_1)\bar{\mathrm{X}}(k_2)$, and vice versa. The collision term can be written in the form

$$\begin{aligned}
\boldsymbol{C} &= \frac{1}{2\,g_\chi}\sum_X \int \frac{d^3k_1}{(2\pi)^3 2\omega_1}\int \frac{d^3k_2}{(2\pi)^3 2\omega_2}\int \frac{d^3p_2}{(2\pi)^3 2E_2}(2\pi)^4\delta^{(4)}(p_1 + p_2 - k_1 - k_2) \\
&\quad \times \left[|\mathcal{M}|^2_{\chi\bar{\chi}\to\mathrm{X}\bar{\mathrm{X}}}\, f(E_1)f(E_2)[1 \pm g(\omega_1)][1 \pm g(\omega_2)] \right. \\
&\quad - \left. |\mathcal{M}|^2_{\mathrm{X}\bar{\mathrm{X}}\to\chi\bar{\chi}}\, g(\omega_1)g(\omega_2)[1 \pm f(E_1)][1 \pm f(E_2)]\right],
\end{aligned} \tag{4.6}$$

with $p^\mu = (E, \vec{\boldsymbol{p}})$ and $k^\mu = (\omega, \vec{\boldsymbol{k}})$. The squared matrix elements contain already the summation over all possible Standard Model particles X, as well as the summation and averaging over internal degrees of freedom. The factors $g(\omega_{1,2})$ stand for the Fermi-Dirac or Bose-Einstein distribution functions of the Standard Model particles, whereas the factors $f(E_{1,2})$ describe the distribution of the dark matter particles. As we are interested in regimes where for non-relativistic dark matter $T \ll E$ holds, the quantum statistics can be neglected and a Maxwell-Boltzmann distribution $f(E_{1,2})$ can be assumed. Thus, we can also neglect the distribution of the final state particles in the following. Due to the assumption $T \ll E$ for the non-relativistic dark matter particles, the approximation of $[1 \pm f(E_1)] \to 1$ is possible, and as a result of momentum conservation $[1 \pm g(\omega_1)] \to 1$ also holds.

Considering these assumptions, we can further simplify the expression of Eq. (4.6).

Taking into account also CP-invariance we finally arrive at

$$
\begin{aligned}
\boldsymbol{C} =\ & \frac{1}{2\,g_\chi} \sum_X \int \frac{d^3k_1}{(2\pi)^3 2\omega_1} \int \frac{d^3k_2}{(2\pi)^3 2\omega_2} \int \frac{d^3p_2}{(2\pi)^3 2E_2} (2\pi)^4 \delta^{(4)}(p_1 + p_2 - k_1 - k_2) \\
& \times\ |\mathcal{M}|^2_{\chi\bar\chi \to X\bar X} \left[f_{eq}(\omega_1) f_{eq}(\omega_2) - f(E_1) f(E_2) \right].
\end{aligned}
\tag{4.7}
$$

As in thermal equilibrium annihilation and creation processes should happen equally, we have substituted $g(\omega_1)g(\omega_2) \to f_{eq}(E_1)f_{eq}(E_2)$ when going from Eq. (4.6) to Eq. (4.7), assuming zero chemical potential for the Standard Model particles X. Integrating now over the two momenta of the final state particles X$\bar{\text{X}}$ and defining the relative velocity of the two annihilating particles $\chi\bar\chi$ according to $v_{rel} \equiv (E_1 E_2)^{-1}\sqrt{(p_1 \cdot p_2)^2 - m_\chi^4}$ the expression of Eq. (4.7) can be written as

$$
\boldsymbol{C} = \frac{1}{2\,g_\chi} \sum_X \int \frac{d^3p_2}{(2\pi)^3}\, 2E_2\, v_{rel}\, \sigma_{\chi\bar\chi \to X\bar X} \left[f_{eq}(E_1) f_{eq}(E_2) - f(E_1) f(E_2) \right].
\tag{4.8}
$$

The Maxwell-Boltzmann distribution $f(E_{1,2})$ of the dark matter particles can be expressed in terms of the distribution in thermal equilibrium and the part containing the chemical potential μ as follows $f(E_{1,2}) = f_{eq}(E_{1,2})\, e^{\frac{-\mu}{T}}$. This allows us to factor out the Maxwell-Boltzmann distribution of thermal equilibrium $f_{eq}(E_{1,2})$. Performing the last integration of Eq. (4.5) the collision term is then given by

$$
\frac{g_\chi}{(2\pi)^3} \int \boldsymbol{C}[f] \frac{d^3p_1}{(2\pi)^3 E_1} = -\langle \sigma v_{rel} \rangle (n_\chi^2 - n_\chi^{eq2})
\tag{4.9}
$$

with the thermal averaged cross section defined as

$$
\langle \sigma\, v_{rel} \rangle = \frac{g_\chi^2}{n_\chi^{eq2}} \int \frac{d^3p_1}{(2\pi)^3} \int \frac{d^3p_2}{(2\pi)^3} v_{rel}\, \sigma_{\chi\bar\chi \to X\bar X}\, f_{eq}(E_1) f_{eq}(E_2).
\tag{4.10}
$$

To this end, the Boltzmann equation can be written in the well-known form

$$
\dot{n}_\chi + 3\,H\,n_\chi = -\langle \sigma v_{rel} \rangle (n_\chi^2 - n_\chi^{eq2}).
\tag{4.11}
$$

In the very young universe, at high temperatures, the Hubble expansion term can be neglected and the interaction term is dominant. With cooling down, the number density of thermal equilibrium decreases with a Boltzmann factor, which is depicted as a solid line in Fig. 4.1. However, at some point, the particles become non-relativistic and their interaction rate is smaller than the Hubble expansion rate of the universe, until the former can be completely neglected. This point of chemical decoupling at which no annihilation processes take place anymore, is called *freeze-out*. Since then, the comoving number density stays constant (dashed line in Fig. 4.1) and results in the today's measurable relic density.
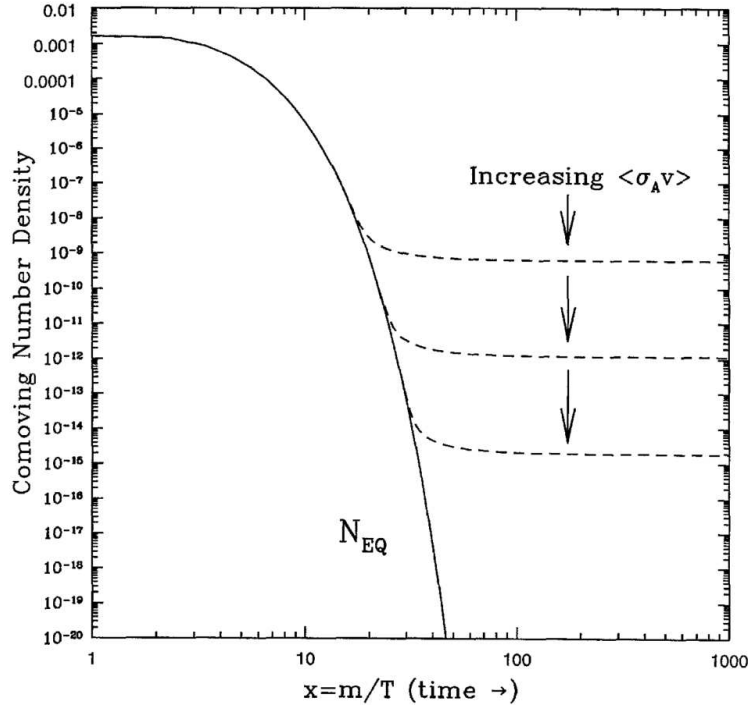
Figure 4.1: Overview of the evolution of the comoving number density in dependence of time in parameters of x (for further details see 4.1.4) in the early universe. The dark matter comoving number density in equilibrium is depicted as solid line. At freeze-out, the chemical decoupling takes place such that the actual number density follows the dashed line. Graphic taken from [126], originally published in [44].

4.1.2 Boltzmann Equation including Coannihilation Processes

Up to now, we have neglected other supersymmetric particles which could interact with the lightest supersymmetric particle, the dark matter particle. However, in Ref. [127] it was shown the first time that coannihilation processes, the interaction of a particle that is almost mass degenerate with the dark matter particle, can contribute significantly to the dark matter relic abundance. A detailed derivation of the Boltzmann equation including coannihilation processes can be found in Refs. [128, 129].

To include all possible interactions, we consider N supersymmetric particles χ_i where $i = 1, \ldots, N$ with the corresponding masses m_i and their internal degrees of freedom g_i. Considering R-parity conservation, we assume the following mass ordering $m_\chi \equiv m_1 \leq m_2 \leq \cdots \leq m_N$. Similar to the derivation of the Boltzmann equation

for a single annihilation channel, now a set of Boltzmann equations can be derived

$$
\begin{aligned}
\dot{n}_i + 3\,H\,n_i = \quad & - \sum_{j=1}^{N} \langle \sigma_{ij} v_{ij} \rangle (n_i n_j - n_i^{eq} n_j^{eq}) \\
& - \sum_{X} \sum_{i \neq j} [\langle \sigma'_{Xij} v_{ij} \rangle (n_i n_X - n_i^{eq} n_X^{eq}) - \langle \sigma'_{Xji} v_{ij} \rangle (n_j n_X - n_j^{eq} n_X^{eq})] \\
& - \sum_{i \neq j} [\Gamma_{ij} (n_i - n_i^{eq}) - \Gamma_{ji} (n_j - n_j^{eq})],
\end{aligned}
\tag{4.12}
$$

where X and Y describe a set of all Standard Model particles. The first term of the right hand side of Eq. (4.12) denotes the annihilation processes of different supersymmetric particles $\chi_i \chi_j$ with the total cross section

$$
\sigma_{ij} = \sum_{X} \sigma(\chi_i \chi_j \to X).
\tag{4.13}
$$

The second term describes $\chi_i \to \chi_j$ conversions by scattering off the cosmic thermal background of Standard Model particles with the corresponding inclusive scattering cross section

$$
\sigma'_{Xij} = \sum_{Y} \sigma(\chi_i X \to \chi_j Y).
\tag{4.14}
$$

The last term considers χ_j decays, with

$$
\Gamma_{ij} = \sum_{X} \Gamma(\chi_i \to \chi_j X)
\tag{4.15}
$$

being the decay rate. The relative velocity between two annihilating particles $\chi_i \chi_j$ is defined similarly to the previous case

$$
v_{ij} = \frac{\sqrt{(p_i \cdot p_j)^2 - m_i^2 m_j^2}}{E_i E_j}.
\tag{4.16}
$$

As all supersymmetric particles will finally decay into the lightest supersymmetric particle, we can simplify the coupled Boltzmann equations to a single one depending on the number density of the lightest supersymmetric particle with $n = \sum_{i=1}^{N} n_i$. Performing this sum, the second and third term of Eq. (4.12) cancel, and we end up with

$$
\dot{n} + 3\,H\,n = \quad - \sum_{j=1}^{N} \langle \sigma_{ij} v_{ij} \rangle (n_i n_j - n_i^{eq} n_j^{eq}).
\tag{4.17}
$$

Nevertheless, the scattering of supersymmetric particles off the thermal background plays a crucial role. As the number density n_i of the supersymmetric particles is Boltzmann suppressed due to their non-relativistic behaviour, the number density n_X of the relativistic Standard Model particles is much higher. With the scattering cross section σ'_{Xij} being of the same order of magnitude as the annihilation cross section σ_{ij}, the scattering rate is much higher than the annihilation one. Therefore, the supersymmetric particles remain in thermal equilibrium with the thermal background and their ratios can be assumed to be equal to their equilibrium ones

$$\frac{n_i}{n} \simeq \frac{n_i^{eq}}{n^{eq}}.$$

(4.18)

Thus, the Boltzmann equation can be written as

$$\dot{n} + 3\,H\,n = -\langle \sigma_{eff} v \rangle (n^2 - n_{eq}^2).$$

(4.19)

This equation looks quite similar to Eq. (4.11), but the annihilation rate is substituted by

$$\langle \sigma_{eff} v \rangle = \sum_{ij} \langle \sigma_{ij} v_{ij} \rangle \frac{n_i^{eq}}{n^{eq}} \frac{n_j^{eq}}{n^{eq}}$$

(4.20)

and takes now into account also coannihilation processes. Such processes are usually Boltzmann suppressed

$$\frac{n_i^{eq}}{n^{eq}} \propto \exp[-(m_i - m_\chi)/T],$$

(4.21)

unless a second particle is almost mass degenerate with the dark matter particle.
Assuming the lightest neutralino to be the dark matter particle, a light stop with a rather long lifetime can be such a degenerate NLSP, for instance. In this case, neutralino-stop coannihilation becomes possible. For an even smaller mass gap stop-stop annihilation can also play a crucial role. It was claimed in Ref. [127, 130, 131] for the first time that by neglecting coannihilation processes, errors of more than two orders of magnitude can occur regarding the relic density calculation.
Therefore, the consideration of coannihilation processes is well motivated and thus those processes are topic of this thesis. For further studies on the importance of neutralino-stop coannihilation compared to pure neutralino-neutralino annihilation, we refer to Chapter 6.

4.1.3 Thermal Averaging

Some more effort is needed to calculate the thermal averaged effective cross section of Eq. (4.20). Whereas Ref. [123] has derived this quantity only for annihilation pro-

cesses, in Ref. [128] it has been extensively studied for the more general case including also coannihilation processes. To this end, we want to follow Refs. [128, 129] for the expressions which are relevant for the computation of the total (co)annihilation cross section and the later relic density computation.

The total number density in equilibrium can be written as

$$n^{eq} = \sum_i n_i^{eq} = \sum_i \frac{g_i}{(2\pi)^3} \int d^3p_i e^{-E_i/T} = \frac{T}{2\pi^2} \sum_i g_i m_i^2 K_2 \left(\frac{m_i}{T} \right), \qquad (4.22)$$

with K_2 being the modified Bessel function of the second kind of order two. From now on, we assume Boltzmann statistics, which holds for the non-relativistic dark matter particle.

The nominator of Eq. (4.20) can be reformulated

$$\sum_{ij} \langle \sigma_{ij} v_{ij} \rangle n_i^{eq} n_j^{eq} = \sum_{ij} \int W_{ij} g_i g_j e^{-E_i/T} e^{-E_j/T} \frac{d^3p_i}{(2\pi)^3 2E_i} \frac{d^3p_j}{(2\pi)^3 2E_j}, \qquad (4.23)$$

with $W_{ij} = 4E_i E_j \sigma_{ij} v_{ij}$ being the annihilation rate per unit volume. After some reformulation of the integration variables and performing the first integration we end up with

$$\sum_{ij} \langle \sigma_{ij} v_{ij} \rangle n_i^{eq} n_j^{eq} = \frac{T}{32\pi^4} \sum_{ij} \int_{(m_i+m_j)^2}^{\infty} ds\, g_i g_j\, p_{ij} W_{ij} K_1 \left(\frac{\sqrt{s}}{T} \right), \qquad (4.24)$$

where p_{ij} denotes the momentum of particle χ_i (or χ_j) in the center-of-mass frame of the pair $\chi_i \chi_j$. Defining now an effective annhilation rate W_{eff}

$$\sum_{ij} g_i g_j p_{ij} W_{ij} = g_\chi^2 p_{eff} W_{eff} \qquad (4.25)$$

with

$$p_{eff} = p_{11} = \frac{1}{2} \sqrt{s - 4m_1^2} \qquad (4.26)$$

we finally get

$$\sum_{ij} \langle \sigma_{ij} v_{ij} \rangle n_i^{eq} n_j^{eq} = \frac{g_\chi^2 T}{4\pi^4} \int_0^\infty dp_{eff}\, p_{eff}^2 W_{eff} K_1 \left(\frac{\sqrt{s}}{T} \right). \qquad (4.27)$$

Inserting Eq. (4.27) together with Eq. (4.22) in the initial expression of Eq. (4.20) we arrive at

$$\langle \sigma_{eff} v \rangle = \frac{\int_0^\infty dp_{eff} p_{eff}^2 W_{eff} K_1\left(\frac{\sqrt{s}}{T}\right)}{m_\chi^4 T \left[\sum_i \frac{g_i}{g_\chi} \frac{m_i^2}{m_\chi^2} K_2\left(\frac{m_i}{T}\right)\right]^2}, \tag{4.28}$$

where we consider annihilation as well as coannihilation processes. If we neglect coannihilation processes this equation reduces correctly to the effective annihilation rate given in Ref. [123].

With this convenient expression for the thermal averaged cross section (Eq. (4.28)), and the general Boltzmann equation which now takes into account both, annihilation and coannihilation processes (Eq. (4.19)), the usual derivation of the relic density can be performed.

4.1.4 Computation of the Relic Density

In order to finally compute the relic density, we introduce the yield Y, the ratio of the number density d and the entropy density s

$$Y = \frac{n}{s}. \tag{4.29}$$

Assuming entropy conservation $\partial_t(a^3 s) = 0$ the effective Boltzmann equation Eq. (4.19) can be expressed as

$$\dot{Y} = -s \langle \sigma_{eff} v \rangle (Y^2 - Y_{eq}^2). \tag{4.30}$$

Introducing the variable

$$x = \frac{m_\chi}{T} \tag{4.31}$$

and performing some variable shuffling $\dot{Y} = \frac{dY}{dx}\frac{dx}{dT}\frac{dT}{ds}\frac{ds}{dt} = \frac{dY}{dx}\frac{x^2}{m_\chi} 3Hs\frac{dT}{ds}$ the Boltzmann equation can be reformulated to

$$\frac{dY}{dx} = -\frac{m_\chi}{x^2}\frac{1}{3H}\frac{ds}{dT}\langle \sigma_{eff} v \rangle (Y^2 - Y_{eq}^2). \tag{4.32}$$

As a next step, we make use of the Friedmann equation

$$H^2 = \frac{8\pi G\rho}{3}, \tag{4.33}$$

with G being the gravitational constant and ρ denoting the total energy density of the universe. Taking also into account the definition of the effective degrees of freedom for the energy density $\rho = g_{eff}(T)\frac{\pi^2}{30}T^4$ and entropy density $s = h_{eff}(T)\frac{2\pi^2}{45}T^3$, we arrive at [123]

$$\frac{dY}{dx} = -\sqrt{\frac{\pi}{45G}}\frac{g_\star^{1/2}m_\chi}{x^2}\langle\sigma_{eff}v\rangle(Y^2 - Y_{eq}^2), \tag{4.34}$$

while the quantity $g_\star^{1/2}$ describes the effective degrees of freedom of the universe and is defined as

$$g_\star^{1/2} = \frac{h_{eff}}{\sqrt{g_{eff}}}\left(1 + \frac{T}{2h_{eff}}\frac{dh_{eff}}{dT}\right). \tag{4.35}$$

The variable Y_{eq} denoting the yield at equilibrium is given by [128]

$$Y_{eq} = \frac{n_{eq}}{s} = \frac{45x^2}{4\pi^4 h_{eff}(T)}\sum_i g_i\left(\frac{m_i}{m_\chi}\right)^2 K_2\left(x\frac{m_i}{m_\chi}\right). \tag{4.36}$$

By integrating Eq. (4.34) from $x = 0$ to $x_0 = m_\chi/T_0$ with T_0 being the photon temperature of the universe today, we get our aimed result, the current yield Y_0.

Finally, today's relic density can be calculated. It is defined as the ratio of the actual density of the universe ρ_χ^0 to the critical density ρ_{crit}, and can be expressed in dependence of the just derived parameter Y_0

$$\Omega_\chi = \frac{\rho_\chi^0}{\rho_{crit}} = \frac{m_\chi s_0}{\rho_{crit}}Y_0. \tag{4.37}$$

Hereby, the critical density is defined as $\rho_{crit} = 3H^2/8\pi G$ and s_0 denotes today's entropy density, which is $s_0 = \frac{2\pi^2}{45}h_{eff}(T_\gamma)T_\gamma^3$ with $T_\gamma = 2.72548 \pm 0.00057$ K [132]. Roughly speaking today's relic density is approximately inversely proportional to the thermal averaged total (co)annihilation cross section

$$\Omega_\chi h^2 \propto \frac{1}{\langle\sigma_{eff}v\rangle}. \tag{4.38}$$

This is also visible in Fig. 4.1, where an increasing (co)annihilation cross section leads to a smaller comoving number density and thus, to a smaller relic density.

Due to this connection, particle physics plays an important role in the calculation of the relic density: The theoretical prediction of the relic abundance is highly dependent on the mass configuration of the contributing particles and thus on the specific parameter point within the MSSM. In order to pursue dedicated studies of the parameter space including the constraints from relic density measurements, sophisticated pieces of software have been developed. Public software tools like `Mi-`

`crOMEGAs` [133–135], `DarkSUSY` [136] and `SuperIsoRelic` [137] allow one to compute the theoretical prediction of the relic density for a specific point in the parameter space. However, such a computation has to face also possible sources of uncertainties, which are the topic of the subsequent section.

4.2 Uncertainties within the Computation of the Relic Density

The Cosmological Model. The relic density is an interesting parameter for constraining the parameter space. Therefore, it is crucial to be aware of uncertainties which affect the experimental determination and the theoretical calculation of the relic abundance. As particle physics as well as astrophysics and cosmology enter the computation, all disciplines have to be considered for an overall error estimation.

A first possible source of uncertainty lies in the extraction of the relic density out of experimental data. Although this is possible to a very precise value with data from WMAP and PLANCK (see Eq. (3.12)), the analysis of the CMB, as discussed in Sec. 3.1.4 is based on an essential assumption of the realisation of a standard cosmological model (ΛCDM). The ΛCDM model describes cosmology with the help of essentially six different parameters: The energy content of baryons Ω_b, the physical dark matter density Ω_c and the Hubble expansion rate H_0. Moreover, the amplitude A_s of the power law spectrum $P_0(k) \propto A_s k^{n_s-1}$ with the spectral index n_s which describes the initial perturbations and finally the optical depth parameter τ. This minimal set of six parameters is used to fit the observed data with a likelihood analysis and to extract a precise value of the relic density. It was shown that by introducing more parameters the constraints on the relic density can be relaxed. In Ref. [138] a study that considered five additional physical parameters (e.g. nonzero neutrino masses, etc.) was performed and a relaxation of the relic density by a factor two was found.

As the ΛCDM model is capable of describing our universe very well, there is no need to enlarge the number of parameters at this point. However, one should be aware of this assumption which enters the determination of the relic density from the very beginning.

Hubble Expansion Rate. Another uncertainty arising from cosmology concerns the assumptions that are made within the ΛCDM model. For instance, a variation in the Hubble expansion rate H_0 before nucleosynthesis could be possible. In Ref. [139], the consequence of a modified expansion rate was studied by introducing a new dark density which varies with temperature in addition to the radiation density. The Friedmann equation is then modified by a dark density ρ_D in addition to the usual radiation density ρ_{rad} to the expression $H^2 = \frac{8\pi G}{3}(\rho_{rad} + \rho_D)$, and enters the Boltzmann equation (see Eq. (4.32)). Thus, the freeze-out temperature is changed

and the theoretical prediction of the relic abundance gets affected. Even small modifications, which would have no impact on the cosmological observations and would still be in agreement with BBN, could change the relic density. In Ref. [139] it was shown that such modifications could significantly change the relic density prediction, but are still undetectable in cosmological observations, and would be still in agreement with BBN. If one wants to take into account a possible variation in the Hubble expansion, it is suggested to consider only an upper bound for the relic density. This is also compatible with the possibility of dark matter being composed of several components [139].

Effective Degrees of Freedom of the Universe. As pointed out in Ref. [140], the calculation of the relic abundance depends on the effective number of relativistic degrees of freedom of the universe at the freeze-out temperature (see Eq. (4.34) and Eq. (4.35)). Usually, it is assumed that above the QCD confinement critical temperature of $T_c \sim 200$ MeV, the quark gluon plasma is weakly interacting due to asymptotic freedom. This would mean that such particles could be treated as an ideal gas. However, it was shown that at high temperatures this is not completely true, and an improved equation of state has to be considered.

In Ref. [140] a correction factor for the coloured degrees of freedom was taken into account in the derivation of g_{eff} and h_{eff}, which enter directly the relic density calculation (cf. Eqs. 4.34 and 4.35). This correction was derived from lattice and perturbative calculations. Taking these changes into account, the value of the relic density was compared to the default value of `DarkSUSY`. This public tool, as well as `micrOMEGAs`, uses a linear potential to describe the interaction between quarks and gluons in that temperature regime, which almost corresponds to an ideal gas behaviour. It was shown that by taking into account these QCD corrections, the relic density is increased by 1.5-3.5 % in some example mSUGRA benchmark scenarios. Therefore, it might be interesting to include these corrections in public tools like `micrOMEGAs` or `DarkSUSY`.

Finite Temperature Effects. Furthermore, we have to consider that the calculation of the Boltzmann equation and thus of the required (co)annihilation cross section has to be performed at finite temperatures. However, at finite temperatures quantum mechanics cannot be described by the S-matrix alone. Instead, the expectation value at zero temperature has to be replaced by the sum over a complete set of states, such that perturbation theory leads to a corrected set of Feynman rules for the S-matrix elements. This was analysed in several studies, see Ref. [141, 142]. Considering typical benchmark scenarios, it was shown that these effects are only of the order of 10^{-4} and therefore below the detection limit of current and future relic density observation experiments [142].

Three-body Processes. In the calculation of the relic density, so far only the (co)annihilation into two-body final states or three-body final states with a massless gauge boson has been considered (see ansatz in Eq. (4.12)). However, it was shown by Ref. [143] that taking into account the three-body final states consisting of a real and a virtual massive particle such as $WW^*(\to Wf\bar{f}')$ and $t\bar{t}^*(\to tW\bar{b})$ could result in an effect on the dark matter relic density. As shown in Ref. [143] though, this is not a generic feature within the MSSM, but a threshold effect and thus parameter point dependent. Also processes which are usually helicity suppressed can significantly contribute, when considering an additional vector boson in the $f\bar{f}$ final state [144]. However, public tools like `micrOMEGAs` or `DarkSUSY` do not take them fully into account.

Determination of Mass Parameters. Another uncertainty that affects the prediction of the relic abundance is based on the precision of the MSSM parameters which enter via the computation of the different (co)annihilation processes. In order to calculate the cross section of these processes in an underlying model, dedicated software tools are necessary to relate the theoretical models, often defined at the GUT-scale, to observable parameters at the SUSY-scale. Those programs solve the renormalization group equations at two-loop order and calculate essential parameters like masses and couplings of supersymmetric particles including higher-order corrections. Among the most used tools are `SPheno` [145], `SOFTSUSY` [146], `Isajet` [147] and `Suspect` [21]. When using them, one has to be aware of the several sources of uncertainties that depend on the precision of implemented routines and approximations, which in the end also affect the relic density computation.

In Ref. [148], the first broad comparison between the aforementioned programs was performed in order to estimate the current theoretical uncertainty in using them. It was found that the theoretical error is quite parameter point dependent, with especially the focus point region and high $\tan\beta$ regime showing the largest error. This study was also extended to investigate the error of these public tools on the relic density prediction [149–152]. Generally, all investigated spectrum calculators were quite well in agreement. However, even small differences in the computation of the supersymmetric masses can have a serious impact on the relic density. In Ref. [152] it was claimed that the spectrum uncertainties are larger than the experimental uncertainty from PLANCK, or even WMAP. However, the spectrum calculators have undergone an improvement since the appearance of the referenced paper, such that a study with recent versions of the programs would be interesting.

Higher Order Corrections. Another source of uncertainty is related the precision of the calculated (co)annihilation cross sections for computing the relic density. Currently available public tools like `micrOMEGAs` or `DarkSUSY` use only tree-level cross sections with some effective couplings. A much more precise prediction of the relic density could be achieved by taking into account full next-to-leading order calcula-

tions in order to determine the (co)annihilation cross section. This would change the computed relic density of around $\mathcal{O}(10\%)$. The impact on the relic density of such corrections will be discussed in more detail in Chap. 10.

Conclusions. Altogether, there are a few sources of uncertainties arising in the theoretical prediction of the relic abundance. Especially in the light of the precise data from PLANCK, which were recently published, a common effort is needed to reduce the theoretical uncertainties. This work focuses in particular on the improvement of the precision of the (co)annihilation cross section by calculating next-to-leading order corrections of $\mathcal{O}(\alpha_s)$, which promise to have a significant impact on the relic density prediction.

In the subsequent chapter the tool `DM@NLO` is introduced. `DM@NLO` is developed in order to serve as an extension to the publicly available tools and provides SUSY-QCD corrections to the necessary coannihilation and annihilation processes.

5 DM@NLO – a Tool for an Improved Relic Density Prediction

5.1 Status of Loop Calculations to (Co)annihilation

Being aware of the different uncertainties which can arise in the computation of the relic density, a common theoretical effort is needed to reduce possible error sources. As public tools like `MicrOMEGAs` and `DarkSUSY` compute the relic density only based on a tree-level calculation with few effective couplings (for some more details see Sec. 8.3.3), one possibility is to increase the precision of the computation by considering loop corrections.

A first step to increase the precision of the (co)annihilation cross section, is to consider more involved effective coupling approaches than those used in public dark matter tools. This has been studied for instance by Ref. [153]. They have investigated the effect of two-point function corrections to chargino and neutralino lines on the annihilation cross section, as well as the influence of one-loop corrected neutralino masses. It was shown that the size of the resulting corrections to the relic density prediction highly depends on the point of parameter space, but can reach around 3%.

The impact of electroweak corrections at full next-to-leading order to neutralino annihilation was studied for selected scenarios by Refs. [154, 155]. It was demonstrated that these corrections can be large and should be taken into account for a precise relic density prediction. Thus, for global parameter studies it is advised to consider a full next-to-leading order calculation, especially, if one desires to match the precision of the PLANCK satellite. In particular for electroweak one-loop corrections they have developed the automatized one-loop package `Sloops`, which can be linked to `MicrOMEGAs`, for instance. However, it is so far not optimized for performing a full QCD next-to-leading order calculation.

Therefore, our collaboration develops the package `DM@NLO`, which provides the full NLO-QCD corrections in order to obtain a more precise prediction of the relic density. The starting point has been the study of one-loop corrections to the pure annihilation processes of two neutralinos into quarks [156–158], where a significant impact on the relic density was demonstrated. Although, not so many diagrams contribute in the case of SUSY-QCD corrections than for electroweak corrections, they give nevertheless rise to roughly the same impact on the relic density due to being proportional to α_s. An example will be shown in the next section.

A first generic estimate of SUSY-QCD corrections on bino-stop coannihilation was already performed in Ref. [159]. However, within the latter study only two out of eight possible final states were considered ($\tilde{\chi}_1^0 \tilde{t}_1 \to b\,W^+$ and $\tilde{\chi}_1^0 \tilde{t}_1 \to t\,g$) and the leading QCD corrections were calculated. A significant impact on the neutralino relic density was demonstrated, reaching more than 50% in some regions of the parameter space.

However, the first full next-to-leading order calculation of $\mathcal{O}(\alpha_s)$ considering all possible coannihilation and annihilation channels is the aim of our common project. The full calculation will be provided for public use in the software package DM@NLO.

5.2 The Software Package DM@NLO

The tool DM@NLO will provide all annihilation and coannihilation cross sections needed for the calculation of the neutralino relic density at full next-to-leading order considering SUSY-QCD corrections. Fig. 5.1 shows an overview of all the processes that are included or will be included in the near future.
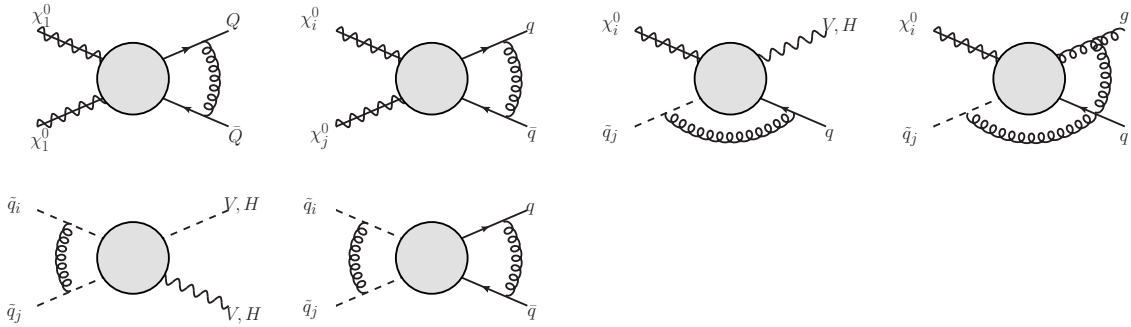

Figure 5.1: Schematic overview of the different processes for which DM@NLO will provide SUSY-QCD corrections. The grey circle indicates all "internal" corrections including vertex and propagator contributions. The gluon line gives rise to additional "external" corrections (box diagrams). The focus of this work is on the neutralino-stop coannihilation into all final states.

All channels concerning neutralino-neutralino annihilation into heavy quarks are already implemented within the package DM@NLO and have been extensively phenomenologically studied (see Ref. [156–158]). The calculation and implementation of neutralino-stop coannihilation is the aim of this thesis. The results regarding coannihilation involving an electroweak vector or Higgs boson in the final state have been already published [1]. The calculation of neutralino-stop coannihilation with a gluon in the final state has been finalized. However, final plots are not yet shown, as a last missing final cross-check has to be performed.

Within our collaboration we are also currently working on corrections to the processes of stop-stop coannihilation. The implementation of the gaugino annihilation processes into light quarks is also under development. In the future, we also plan to
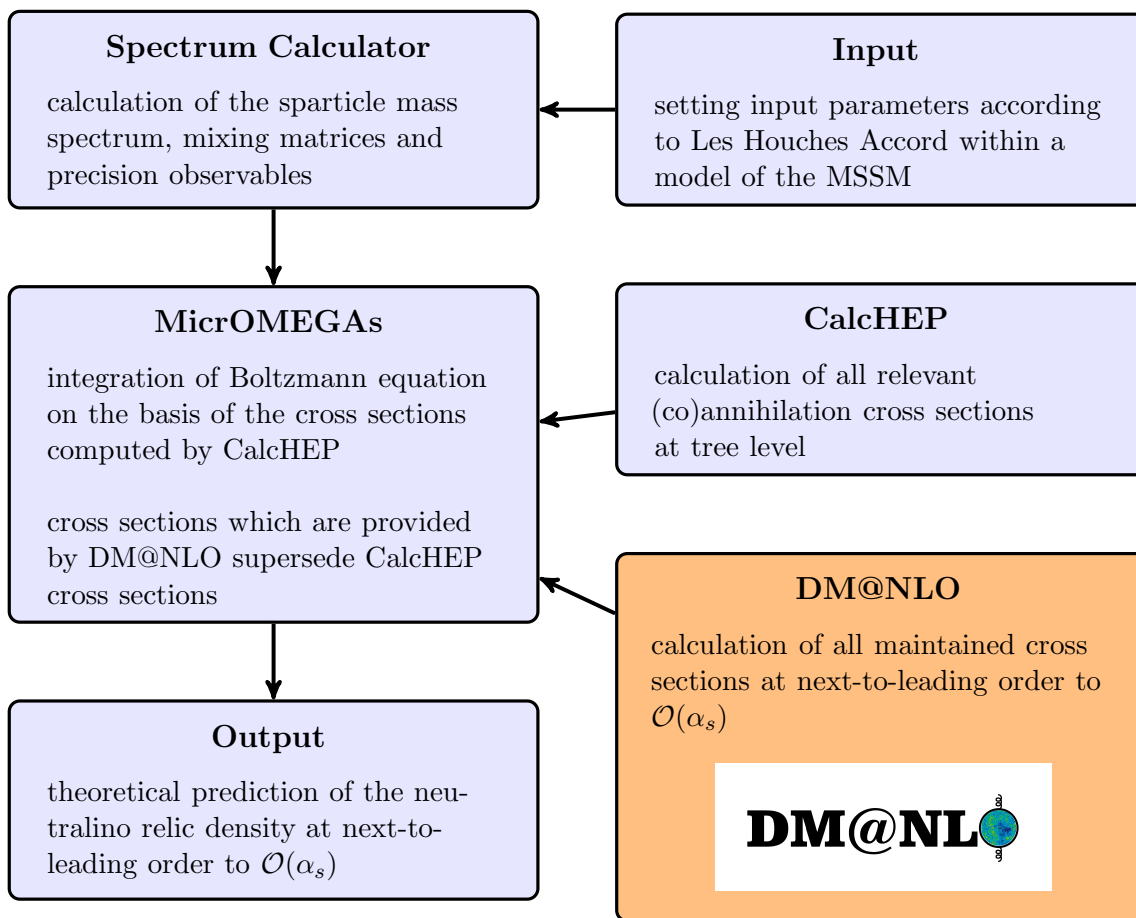
Spectrum Calculator	Input
calculation of the sparticle mass spectrum, mixing matrices and precision observables	setting input parameters according to Les Houches Accord within a model of the MSSM

MicrOMEGAs	CalcHEP
integration of Boltzmann equation on the basis of the cross sections computed by CalcHEP	calculation of all relevant (co)annihilation cross sections at tree level
cross sections which are provided by DM@NLO supersede CalcHEP cross sections	

Output	DM@NLO
theoretical prediction of the neutralino relic density at next-to-leading order to $\mathcal{O}(\alpha_s)$	calculation of all maintained cross sections at next-to-leading order to $\mathcal{O}(\alpha_s)$

Figure 5.2: Flow chart of a typical numerical relic density computation involving `DM@NLO` in the software chain.

extend the project to further models, like the NMSSM.

Providing the one-loop corrected cross sections as a tool for the community, it can be used for a precise neutralino relic density prediction within parameter studies or global fits, for instance. In Fig. 5.1 a flow chart of a typical numerical relic density computation involving `DM@NLO` is depicted. The `DM@NLO` package can be used for all specific models within an R-parity conserved MSSM in order to calculate the neutralino relic density on the basis of cross sections at next-to-leading order. The user can provide a usual input file according to the SUSY Les Houches Accord conventions [160, 161], which will then be used to calculate the sparticle masses, mixing angles and precision observables by a spectrum calculator of choice. The set-up has been already tested for `SoftSUSY`, `Suspect` and `SPheno`. The latter is used for the parameter study of this thesis. The calculated parameters are used by `MicrOMEGAs` to compute the necessary (co)annihilation cross sections by using internally the built-in version of `CalcHEP`. `MicrOMEGAs` is then able to calculate the neutralino relic density by integrating the Boltzmann equation.

In order to calculate the relic density on the basis of next-to-leading order processes, the package `DM@NLO`, which is has been written in `Fortran`, can be easily linked as a library to `MicrOMEGAs`. As soon as one process which is needed for the relic density calculation is provided by `DM@NLO` at next-to-leading order, the corresponding tree-level cross section originally calculated by `CalcHEP` is substituted. This is made possible due to a dedicated interface to `MicrOMEGAs`. The same kind of interface is also planned for `DarkSUSY` in the near future.

5.3 `DM@NLO` and Neutralino Annihilation

The first published example that is part of the common project `DM@NLO` concerns neutralino annihilation into heavy quarks [157, 158]. Although this is not part of this thesis, we want to give a brief idea of the order of magnitude of the achieved corrections to the relic density, in order to put it later in the global context. The relevant tree-level diagrams are depicted in Fig. 5.3.

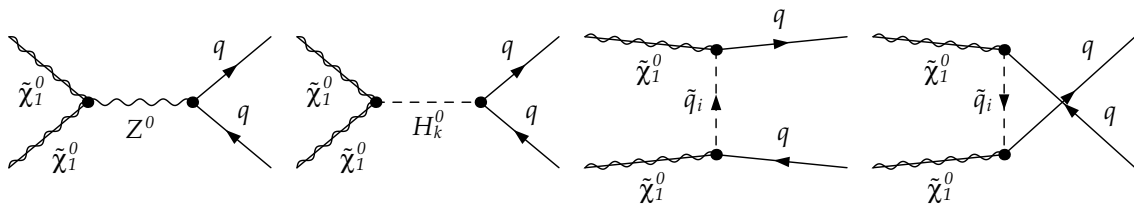The full SUSY-QCD corrections of $\mathcal{O}(\alpha_s)$ have been calculated and it has been

Figure 5.3: Tree-level diagrams which contribute to neutralino annihilation into heavy quarks: s-channel exchange of a Z-boson and neutral Higgs boson ($H_k^0 = h^0, H^0, A^0$) as well as t-and u-channel exchange of squarks. Figure taken from Ref. [157].

shown that a huge impact is caused by these corrections (see Ref. [158]). An idea of the size of the corrections gives Fig. 5.4, in which for an mSUGRA example point ($m_0 = 1800$ GeV, $m_{1/2} = 131$ GeV, $A_0 = -1500$ GeV, sgn(μ)$=+$ and $\tan\beta = 10$) the effect of the radiative corrections on the cross section (left panel) and the relic density (right panel) is shown. In this example point, neutralino annihilation into heavy bottom quarks contributes by 86 % to the total (co)annihilation cross section. In the left panel, the cross section in dependence of the center-of-mass momentum is depicted and clearly demonstrates a huge shift with respect to the result obtained by a pure `MicrOMEGAs` calculation. The observed peak at around $p_{cm} = 20$ GeV arises from the resonance of the lightest Higgs boson. The light brown area in the plot shows, in arbitrary units, the Boltzmann distribution function resulting from thermal averaging (c.f. 4.28). It gives a ballpark, for the range of the center-of-mass momentum p_{cm} in which the relic density calculation is relevant. Due to sizeable corrections to the cross section of processes which contribute significantly to the
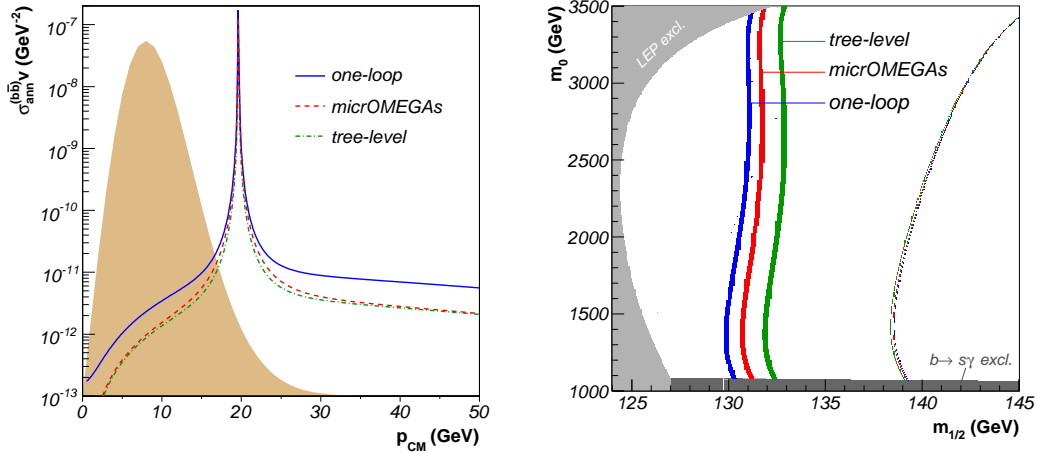
Figure 5.4: Impact of the SUSY-QCD corrections to neutralino-neutralino annihilation into heavy quarks. The left panel shows the effect of the radiative corrections on the cross section as a function of the center-of-mass momentum. The right panel depicts the neutralino relic density in dependence of the gaugino mass parameter $m_{1/2}$. Different colours show the result by using the pure `MicrOMEGAs` tree-level, the `DM@NLO` tree-level and the SUSY-QCD corrected results by `DM@NLO`. Figures taken from Ref. [158].

total cross section, a clear shift of the WMAP preferred region of parameter space is observed (see right panel of Fig. 5.4). In total, a correction of around 10 % with respect to the effective tree-level calculation of `MicrOMEGAs` is obtained. This results due to the fact that, in particular for low $\tan\beta$, the resummed corrections which are included in `MicrOMEGAs` are suppressed such that the SUSY-QCD corrections get even more important. However, it should of course be noted that at the time this study was performed, no Higgs particle had been discovered. Also more severe constraints coming from the Planck satellite could not have been taken into account at that time.

Conclusions. We have demonstrated that the full next-to-leading order corrections to the annihilation processes show significant impact on the neutralino relic density. Especially with the experimental constraints getting more and more precise, reducing the theoretical uncertainties becomes even more relevant. Motivated by the compelling results for neutralino annihilation and the aforementioned first estimation of a similar impact for neutralino-stop coannihilation [159], it was decided that `DM@NLO` should be extended by the latter processes. Thus, we discuss in the following the interesting phenomenology of neutralino-stop coannihilation, before proceeding to the radiative corrections to these processes.

6 Phenomenology of Neutralino-Stop Coannihilation

The implementation of our calculation within the `DM@NLO` code is generic such that it can be used for any neutralino-squark coannihilation process. As neutralino-stop coannihilation is the most realistic scenario with respect to the recent experimental constraints, however, we want to focus on this process in the following.

In order to discuss the phenomenology of neutralino-stop coannihilation broadly, it is interesting to study its role within the global context. To do so, it is worth to investigate its contribution to the total amount of the relic density and its connection to current experimental bounds.

Thus, we address in the following the phenomenological motivation of neutralino-stop coannihilation in general, study its characteristics within the pMSSM and have a closer look at three different scenarios.

6.1 Phenomenological Motivation

There is ample motivation for scenarios featuring neutralino-stop coannihilation. In the following, we want to discuss three different aspects, starting with the focus on the neutralino relic density.

Neutralino Relic Density. In section 4.1.2 we have already discussed theoretically the need of including coannihilation processes in order to obtain a precise and correct prediction of the relic density. Now we want to further study the explicit contribution of neutralino-stop coannihilation in comparison to other channels.

The different $2 \rightarrow 2$ processes contributing to neutralino-stop coannihilation are depicted in Fig. 6.1. In total, eight different final states are possible. First, there are processes with a quark and a neutral, pseudo-scalar or charged Higgs boson in the final state ($h^0, H^0, A^0, H^\pm$). Second, a neutralino and stop can annihilate into a quark and an electroweak vector boson ($Z, W^\pm, \gamma$), and finally, coannihilation into a quark and a gluon (g) is possible. All processes have in common that they feature an s-channel exchange via a quark and a t-channel exchange via a squark. However, the u-channel exchange of a neutralino or chargino, respectively, does not exist for a gluon or photon in the final state.

Those neutralino-stop coannihilation channels compete with other possible processes
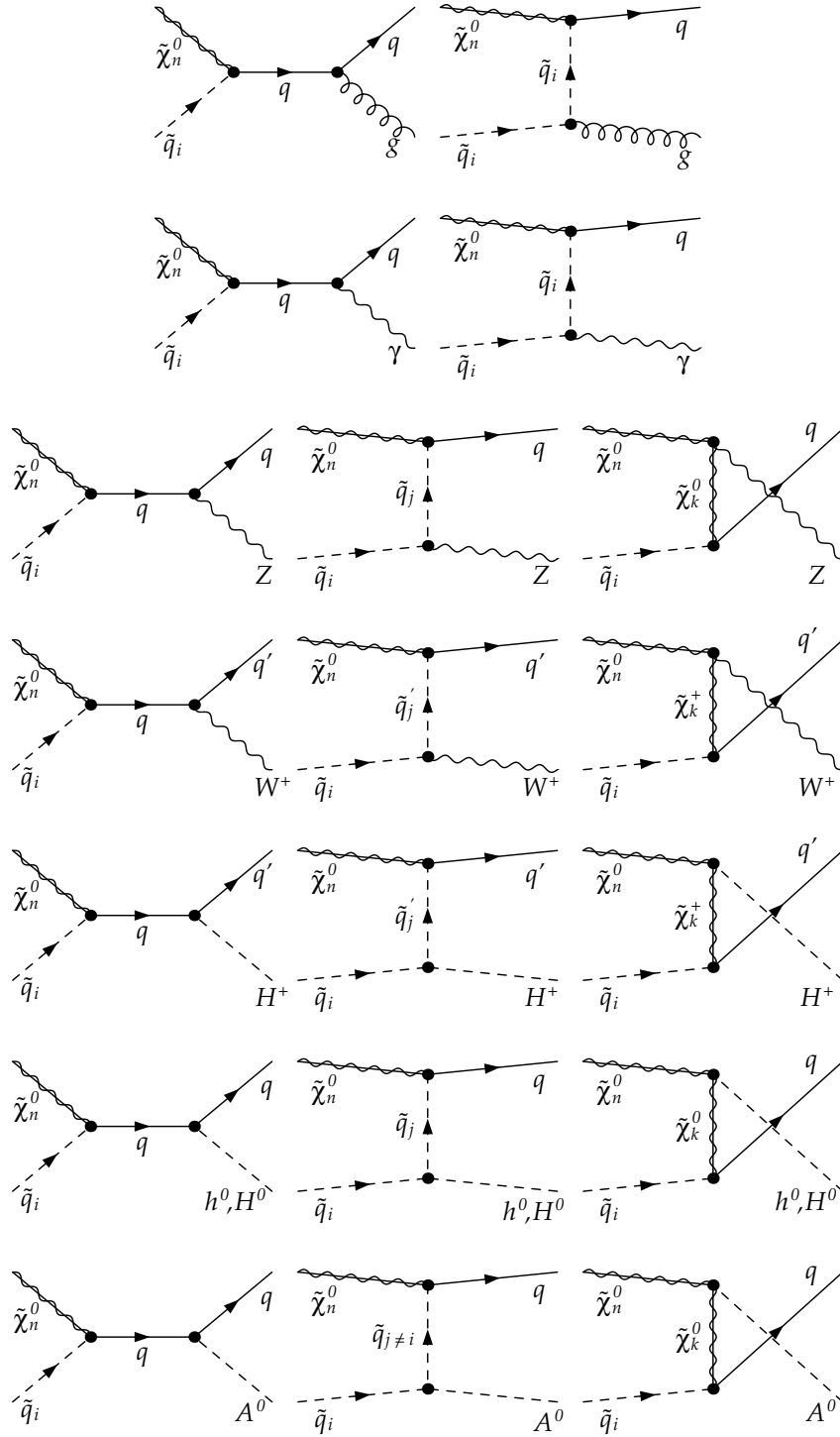
Figure 6.1: Tree-level diagrams contributing to neutralino-squark coannihilation. Eight different processes can be distinguished with either a Higgs boson (h^0, H^0, A^0, H^+), an electroweak vector boson (Z, W^+, γ) or a gluon (g) in the final state. A change of fermion types is marked by a prime within the diagrams. Different mass eigenstates are denoted by a different index i, j, k, n.

inital states	final states
$\tilde{\chi}_i^0 \tilde{\chi}_j^0$	$t\bar{t}, b\bar{b}, q\bar{q}, ll, WW$
$\tilde{\chi}_i^\pm \tilde{\chi}_j^\pm$	$t\bar{t}, b\bar{b}, q\bar{q}, l\bar{l}$
$\tilde{\chi}_1^0 \tilde{t}_1$	$th^0, tH^0, tA^0, tH^+, tZ^0, tW^+, t\gamma, tg$
$\tilde{t}_1 \tilde{t}_1^*$	$h^0 h^0, H^0 H^0, A^0 A^0, H^+ H^-, h^0 H^0, h^0 A^0, H^0 A^0$
	$Z^0 h^0, Z^0 H^0, Z^0 A^0, W^\pm H^\mp$
	$gg, gH^0, gh^0, gZ^0, g\gamma$
	$t\bar{t}, b\bar{b}, q\bar{q}$
$\tilde{t}_1 \tilde{l}$	$tl, b\nu$
$\tilde{t}_1 \tilde{l}^*$	$t\bar{l}$

Table 6.1: Selection of the most relevant annihilation and coannihilation processes contributing to the neutralino relic density.

contributing to the neutralino relic density. An overview of the most relevant contributions is given in Tab. 6.1.

In order to thoroughly understand the interplay of annihilation and coannihilation channels, we study their interplay in dependence of the relative mass difference between the neutralino and stop

$$\Delta M = (m_{\tilde{t}_1} - m_{\tilde{\chi}_1})/m_{\tilde{\chi}_1}. \tag{6.1}$$

This parameter is motivated by the Boltzmann factor

$$\frac{n_i^{eq}}{n^{eq}} \propto \exp\left[-(m_i - m_\chi)/T\right] = \exp[-(m_i - m_\chi)/(m_\chi x)], \tag{6.2}$$

which enters the effective coannihilation cross section (see Eq. (4.20)), and can be reformulated in dependence of the relative mass difference using the definition of Eq. (4.31). Thus, the relevant parameter is not the pure mass difference, but the relative mass difference with respect to the dark matter mass.

We have chosen an example scenario (Scenario II of Tab. 6.2, which will be introduced in more detail in Section 6.3) and have varied the bino mass parameter M_1 in order to obtain a change in the relative mass difference ΔM. For this study we have used the default `MicrOMEGAs` package in combination with `SPheno`. Fig. 6.2 shows the obtained results.
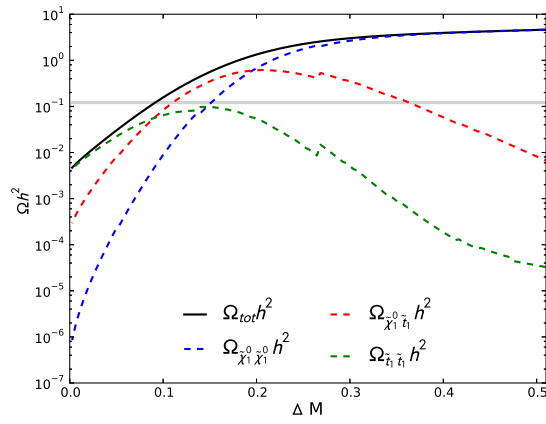
We show the relative weights of $\tilde{\chi}_1^0 \tilde{\chi}_1^0$-annihilation (dashed blue), $\tilde{\chi}_1^0 \tilde{t}_1$-coannihilation (dashed red) and $\tilde{t}_1 \tilde{t}_1^{(*)}$-annihilation (dashed green) to the total thermal averaged cross section in Fig. 6.2(a). Furthermore, the contributing subprocesses of neutralino-stop coannihilation are depicted (dotted lines). When the neutralino and stop mass are almost degenerate, stops are quite long-lived, and stop-stop annihilation plays a crucial role. However, with the mass difference getting bigger, stop-stop annihilation gets rapidly suppressed. This is caused by the dependence of the effective coannihilation cross section (cf. Eq. 4.20) on two powers of the Boltzmann factor
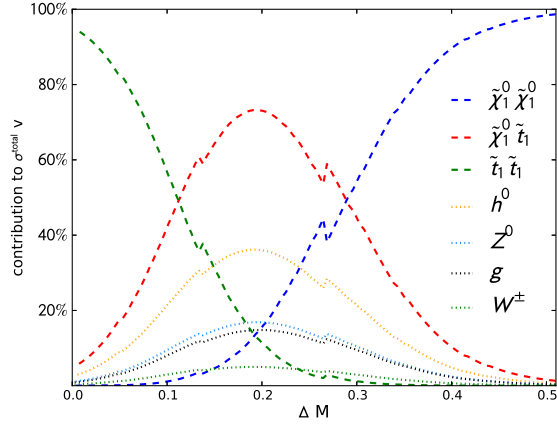
(a)
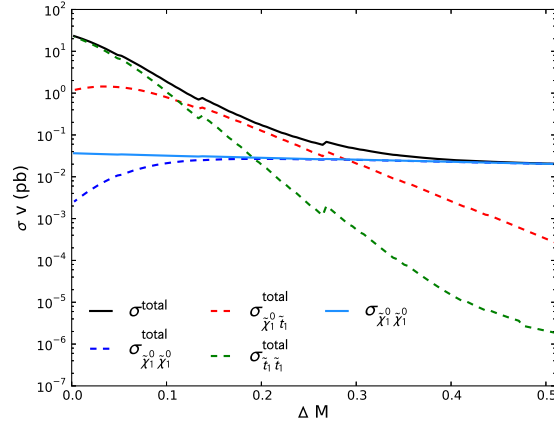
(b)

(c)

Figure 6.2: Contribution of $\tilde{\chi}_1^0\tilde{\chi}_1^0$-annihilation (blue), $\tilde{\chi}_1^0\tilde{t}_1$-coannihilation (red) and $\tilde{t}_1\tilde{t}_1^{(*)}$-annihilation (green) to the total thermal averaged cross section as relative weights (a) and in absolute values (b) as well as their contributions to the neutralino relic density (c).

$n^{eq}_{\tilde{t}_1}/n^{eq} \propto \exp[-(m_{\tilde{t}_1} - m_\chi)/T]$. At around $\Delta M \approx 0.1$ the annihilation of two stops gets less dominant, and neutralino-stop coannihilation starts to dominate as it depends only on the single power of $n^{eq}_{\tilde{t}_1}/n^{eq} \propto \exp[-(m_{\tilde{t}_1} - m_\chi)/T]$. With larger mass splitting between the neutralino and stop, all channels involving a stop in the initial state are suppressed. This leads to an increase of the relative contribution of the pure neutralino-neutralino annihilation, until it finally dominates the total cross section. Furthermore, Fig. 6.2(a) shows the most important subprocesses contributing to neutralino-stop coannihilation for Scenario II. The final state with a light Higgs boson, especially, dominates the cross section by far. The processes with a Z boson or a gluon in the final state are the next to dominant ones, whereas the W boson contributes only to a much smaller extent. By contrast, the contributions of the remaining final states are almost negligible, and thus not shown. The visible spikes in Fig. 6.2 are caused due to numerical instabilities of `MicrOMEGAs`. Further discussion regarding the interplay of the different subprocesses to neutralino-stop coannihilation is postponed to the subsequent sections.

In Fig. 6.2(b), the absolute contribution of the different processes to the thermal averaged total (co)annihilation cross section times velocity is depicted. The different contributions are shown in the same colour code as in Fig. 6.2(a). The solid black and blue line are especially interesting. The black line shows the total (co)annihilation cross section. The solid blue line shows the total cross section without taking into account coannihilation processes, but only with pure annihilation. Here, it becomes obvious, why it is necessary to consider coannihilation in order to obtain a precise relic density prediction. In case of mass degeneracy the contributions originating from $\tilde{\chi}^0_1\tilde{\chi}^0_1$ or $\tilde{\chi}^0_1\tilde{t}_1$ processes dominate by far the total cross section. One might recognize further that the contribution of neutralino-neutralino annihilation to the total (co)annihilation cross section (dashed dark blue) is not exactly the same as the line considering pure annihilation (solid light blue). This arises from the number density weighting factors which multiply each single (co)annihilation cross section in case of the total effective (co)annihilation cross section (see Eq. 4.20 with Eq. 4.21). This leads to the different behaviour in contrast to the pure annihilation cross section (cf. Eq. 4.11). Moreover, it is clearly visible that for small mass differences between the NLSP and LSP, stop-stop coannihilation is the driving process. Its large cross section significantly enhances the total effective cross section, until it finally abruptly ends due to Boltzmann suppression. In the intermediate mass difference range neutralino-stop coannihilation is important with its moderate cross sections, until the dominance of neutralino-neutralino annihilation leads with small cross sections to a smaller total cross section.

In order to obtain a value for the neutralino relic density which is compatible with the measurements of WMAP and PLANCK, one needs a quite specific value for the effective cross section. The connection between the relic density and the total effective thermal averaged cross section has been deduced in Eq. (4.38) and Eq. (4.34). Roughly speaking, the relic density is approximately inversely proportional to the to-

tal effective cross section. However, this is only an approximation, as the neutralino mass, which has been varied for studying the dependence on the mass difference, enters also directly equation Eq. (4.34).

In Fig. 6.2(c) the contribution of the different processes to the relic density is shown. A grey band indicates the region which is favoured by the PLANCK measurements. While for the dominating neutralino-neutralino annihilation the relic abundance is too high, for dominating stop-stop annihilation the relic density is too small. However, in the region with significant contribution of neutralino-stop coannihilation the relic density lies in the right ballpark. This emphasises the need of going beyond pure neutralino-pair annihilation for the relic density prediction in order not to overclose the universe, for example, by studying coannihilation.

This topic has been addressed by many publications considering different types of coannihilation [162–166]. For a complete picture also stau coannihilation must not be neglected [167]. As it receives only electroweak corrections, it is, however, not relevant for this study.

At this point one should state that the importance of neutralino-stop coannihilation depends strongly on the SUSY mass spectrum, and thus, on the studied parameter point. However, it is a generally true statement that in particular the right admixture of all kinds of (co)annihilation processes is important to finally obtain a precise prediction for the relic density.

Electroweak Baryogenesis and the Naturalness of SUSY. A light stop is not only interesting in order to obtain the right value of the relic abundance, it is also motivated by several other phenomenological aspects: Electroweak baryogenesis, for instance, might only be realized within the MSSM in the presence of light stops. Therefore, light stop scenarios are extensively studied in the context of achieving electroweak baryogenesis [168–170].

Another motivation for light stops arises when discussing the naturalness of SUSY models. In terms of natural electroweak symmetry breaking a general bottom-up approach expects higgsinos, stops and gluinos being not too far away above the electroweak scale, whereas the rest of the spectrum could also be beyond the current kinematic reach of the LHC. The LHC is able to probe a "natural" realization of SUSY (for more details see Ref. [171]). However, a mass degeneracy between the lightest neutralino and the NLSP weakens the exclusion potential on the third generation squark masses, since a degeneracy results in events with soft decay products [172, 173] the detection is very sophisticated at a hadron collider.

Discovery of a 125 GeV Higgs Boson. Another reason for the phenomenological interest in light stop scenarios, lies in the recent discovery of a Higgs boson of around 125 GeV [3, 4]. Interpreting the new particle as a light CP-even Higgs boson (h^0) within the MSSM, specific parameter configurations are favoured. This has been studied in great detail during the last year, see for example Refs. [174–177]. All

studies have in common that a light stop scenario is discussed as an interesting possible realization. This is due to the mechanism through which the lightest Higgs boson obtains its mass. Within the MSSM, the Higgs mass gets leading contributions from loop corrections including stops. In the decoupling limit, when $m_A \gg M_Z$, the Higgs mass corrected by dominant one-loop corrections can be expressed as [175, 178]

$$m_{h^0}^2 \approx m_Z^2 \cos^2 2\beta + \frac{3g^2 m_t^4}{8\pi^2 m_W^2} \left[\ln \frac{M_{\mathrm{SUSY}}^2}{m_t^2} + \frac{X_t^2}{M_{\mathrm{SUSY}}^2} \left(1 - \frac{X_t^2}{12\, M_{\mathrm{SUSY}}^2} \right) \right] , \quad (6.3)$$

with $X_t \equiv A_t - \mu / \tan\beta$ and the SUSY mass scale $M_{\mathrm{SUSY}} = \sqrt{m_{\tilde{t}_1} m_{\tilde{t}_2}}$. It is obvious that the mass of the lightest Higgs boson is highly dependent on the ratio X_t / M_{SUSY} when the stops are significantly heavier than the top quark. This means that in order to get a Higgs mass in the right ballpark, a large X_t parameter is of interest, which also leads also to a large stop mass splitting (cf. Eq. (2.87)) and thus to a light stop scenario. The maximal contribution from stop mixing is obtained for $|X_t| \sim \sqrt{6} M_{\mathrm{SUSY}}$. This means that especially a sizable trilinear coupling A_t is favoured.

For completeness one should also mention that studies are undertaken considering not only the low scale M_{SUSY} parameter space. In such a model the right relic density could also be achieved by higgsino like neutralinos, however, these are in tension with constraints of $(g-2)_\mu$, for instance. For further details see e.g. [179].

Conclusions. There are ample reasons to study a light stop scenario and in particular neutralino-stop coannihilation in more detail. In order to find scenarios with a dominating contribution of neutralino-stop coannihilation, we have performed a parameter scan within the pMSSM, which shall be the topic of the following section.

6.2 Parameter Study within the pMSSM

In order to quantify the relative importance of the processes which contribute to neutralino-stop coannihilation (see Fig. 6.1) a random scan in the phenomenological MSSM (pMSSM) has been performed. The pMSSM, which was originally introduced by Refs. [21, 22], counts 19 free parameters in total. For our study we have made some simplifying assumptions such that we have taken into account eight independent parameters (pMSSM8).

In the pMSSM8, the slepton sector is characterized by one single mass parameter $M_{\tilde{\ell}}$. The squark sector is described by $M_{\tilde{q}_{1,2}}$ for both, first and second generation squarks, and the mass parameter $M_{\tilde{q}_3}$ fixes the third generation left- and right-handed squarks. Except for A_t, all the other trilinear couplings are set to zero, as they do not have a significant impact on our study. For instance, the bottom quark mixing is mostly driven by $\mu \tan\beta$, but not by A_b. However, to be consistent with the usual SLHA2-input parameter settings [161], we parameterize the top trilinear

coupling as $T_t = Y_t A_t$, with Y_t being the top Yukawa coupling. Respecting the GUT relation $2M_1 = M_2 = M_3/3$, the bino, wino and gluino masses can be defined through the bino mass parameter M_1. The Higgs sector is characterized by three parameters: The higgsino mass parameter μ, the pole mass of the pseudoscalar Higgs boson m_A, and $\tan\beta$, the ratio of the vacuum expectation values of the two Higgs doublets. According to the SPA-convention [180] the soft-breaking mass parameters are defined at the scale Q = 1 TeV.

For the calculation of the supersymmetric mass spectrum we have used `SPheno` (version `3.2.1`[1]). The neutralino relic density as well as the individual (co)annihilation channels have been evaluated using `micrOMEGAs` (version `2.4.1`). The standard model parameters have been defined according to Ref. [20].

In order to qualitatively study the behaviour of the different channels contributing to neutralino-stop coannihilation, we have performed a random scan with 1.2 million parameter sets, allowing the eight input-parameters lying in the following ranges

$$
\begin{aligned}
500 \text{ GeV} &\leq M_{\tilde{q}_{1,2}} \leq 4000 \text{ GeV}, \\
100 \text{ GeV} &\leq M_{\tilde{q}_3} \leq 2500 \text{ GeV}, \\
500 \text{ GeV} &\leq M_{\tilde{\ell}} \leq 4000 \text{ GeV}, \\
& |T_t| \leq 5000 \text{ GeV}, \\
200 \text{ GeV} &\leq M_1 \leq 1000 \text{ GeV}, \\
100 \text{ GeV} &\leq m_A \leq 2000 \text{ GeV}, \\
& |\mu| \leq 3000 \text{ GeV}, \\
2 &\leq \tan\beta \leq 50.
\end{aligned}
\tag{6.4}
$$

Fig. 6.3 shows the results which have been obtained by the scan in dependence of the four most interesting input parameters M_1, $M_{\tilde{q}_3}$, T_t, and $\tan\beta$. The influence of the remaining input parameters, such as those related to first and second generation squarks, sbottoms, and sleptons, as well as the higgsinos, is less important in this context. Therefore, the corresponding dependencies are not shown. The relative contributions of all eight coannihilation final states are depicted. The corresponding colour code can be found in the caption of Fig. 6.3. With each dot representing the

---

[1]During the writing of the thesis a new `SPheno` version was released, where a bug was reported that has an impact on the Higgs mass for specific scenarios. Having Higgs bosons only in the final state, this does not change the conclusion or the impact of the loop corrections to neutralino-stop coannihilation. It might slightly change the result of the cut on the Higgs mass. However, the uncertainties of different spectrum generators are non-negligible, which results in a different admixture of (co)annihilation processes.

Therefore, a completely revised study is only reasonable, when considering all corrected (co)annihilation channels within the `DM@NLO` project. As a new study would have to include also corrections to neutralino-neutralino and stop-stop annihilation this is beyond the scope of this thesis and therefore not yet addressed. However, it will be taken into account in the next publication.

contribution of one neutralino-stop channel, up to eight dots per parameter set can appear.

The result, without considering any experimental constraints, is depicted in the first row of Fig. 6.3. It can be seen that statistically the final state containing a top and the lightest Higgs boson is the most dominant one with contributions up to 60 % in particular for large trilinear couplings. As this coupling is involved in the Higgs-squark-squark-coupling appearing in the t-channel, the contribution of this process is significantly enhanced. The next-to-largest contribution arises from the gluon final state, which is dominant for a lower value of the trilinear coupling. The heavy CP-even Higgs boson H^0- and the Z^0-boson contribute similarly, followed by the contributions of the $W^\pm$-boson and charged Higgs boson. The photon channel, however, is less important.

Since we want to study the performed one-loop calculation on the basis of realistic and thus experimentally viable scenarios, we apply the following three cuts on the raw data

$$120\,\text{GeV} \leq \qquad m_{h^0} \qquad \leq 130\,\text{GeV}, \tag{6.5}$$

$$0.1064 \leq \qquad \Omega_\chi h^2 \qquad \leq 0.1334, \tag{6.6}$$

$$2.77 \cdot 10^{-4} \leq \quad \text{BR}(b \to s\gamma) \quad \leq 4.33 \cdot 10^{-4}. \tag{6.7}$$

The first selection cut imposes a cut on the Higgs mass, which was measured to be $125.5 \pm 0.2^{+0.5}_{-0.6}$ GeV [181]. For the following analyses we allow the Higgs mass to vary a few GeV. This is motivated by the intrinsic theoretical uncertainties arising from missing higher order corrections, the experimental error of the top quark mass and parametric uncertainties from α_s [182]. Moreover, uncertainties arise due to differences in the spectrum calculators, for example, regarding the treatment of the RGE-running, the extraction of the top mass etc. [183]. For the spectrum calculator SPheno, which has been used for this analysis, an error of up to 2 % was estimated [184]. The second cut chooses the data points which agree with the experimentally determined relic density of Eq. (3.12) within a 5 σ confidence interval. As a third selection cut, we consider the inclusive branching ratio of the most sensitive B-meson decay, $b \to s\gamma$. The limits on the branching ratio correspond to a 3 σ confidence interval around the observed value of $\text{BR}(b \to s\gamma) = (3.55 \pm 0.26) \cdot 10^{-4}$ [185].

The second row of Fig. 6.3 shows the impact of the cut on the Higgs mass. In order to obtain the right ballpark of the Higgs mass, a large trilinear coupling is favoured, which is clearly visible in the plot showing the dependence on T_t. However, too large values of T_t are excluded in order to match the observed Higgs mass. This leads in particular to a cut on scenarios involving $t\,h^0$ final states with contributions up to 60 %. These large contributions have been achieved due to the significant impact of large T_t values on the Higgs-squark-squark coupling in the t-channel exchange.

Imposing the cut on the relic density, which is depicted in the third row of Fig. 6.3, two observations are especially striking. First, the correlated shape of the bino mass
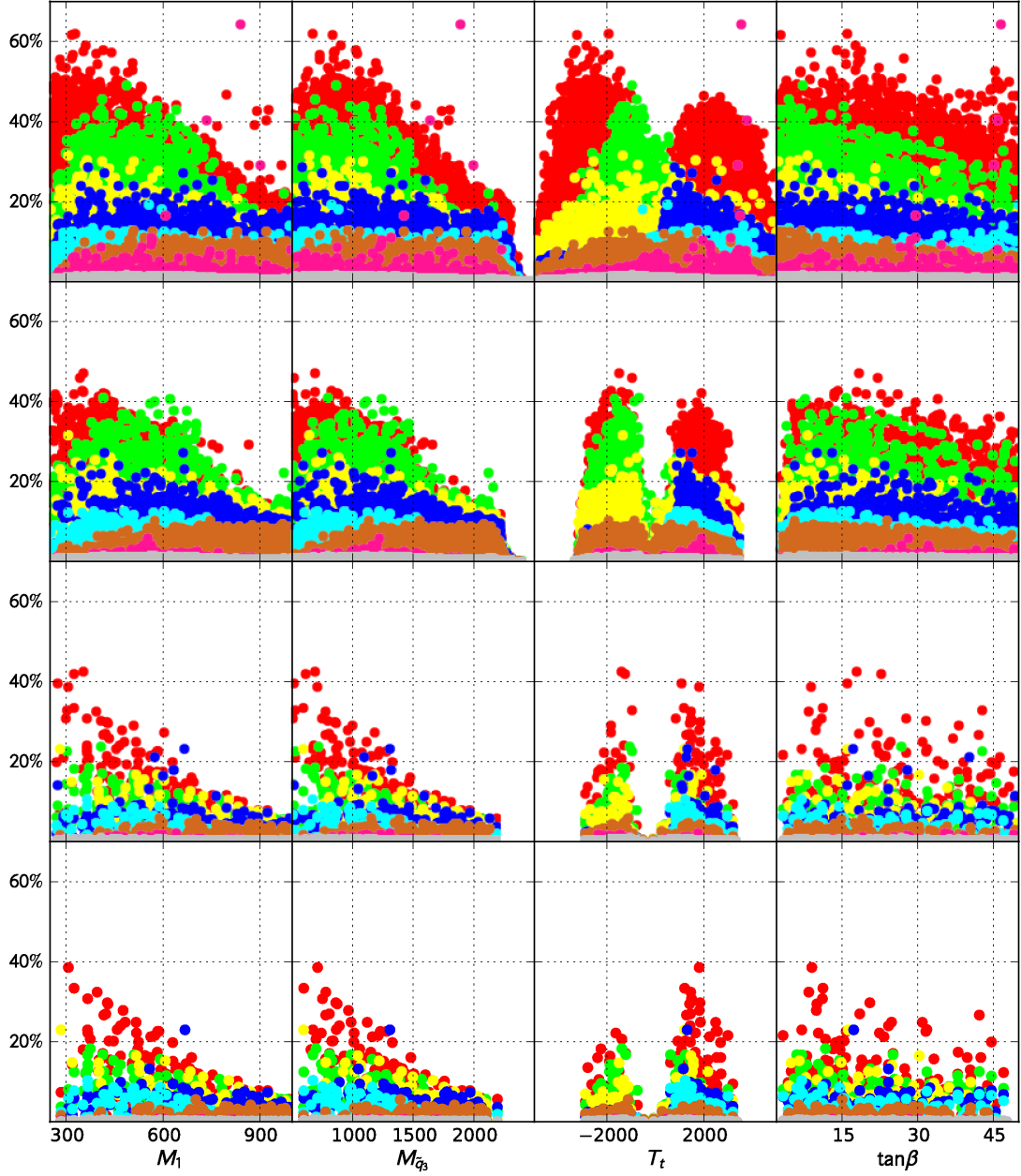
Figure 6.3: Relative contributions of the neutralino-stop coannihilation channels for the generated parameter points as a function of the input parameters M_1, $M_{\tilde{q}_3}$, T_t, and $\tan\beta$. The contributions of all eight final states are depicted: th^0 (red), tg (green), tZ^0 (blue), tH^0 (yellow), bW^+ (cyan), tA^0 (brown), bH^+ (pink), and $t\gamma$ (grey). The results before applying any cuts (first row) as well as after cutting on the Higgs mass (second row), the relic density (third row) and $b \to s\gamma$ (last row) are shown. The parameters M_1, $M_{\tilde{q}_3}$, and T_t are given in GeV.

	M_1	$M_{\tilde{q}_{1,2}}$	$M_{\tilde{q}_3}$	$M_{\tilde{\ell}}$	T_t	m_A	μ	$\tan\beta$	$m_{\tilde{\chi}_1^0}$	$m_{\tilde{t}_1}$	m_{h^0}	m_{H^0}
I	306.9	2037.7	709.7	1499.3	1806.5	1495.6	2616.1	9.0	307.1	350.0	124.43	1530.72
II	470.6	1261.2	905.3	1963.2	1514.8	1343.1	725.9	18.3	467.3	509.4	124.06	1342.77
III	314.4	2870.5	763.6	2417.7	1877.5	386.0	2301.5	10.3	316.5	371.9	123.43	367.45

Table 6.2: Three example scenarios chosen in the pMSSM, which will be considered in this study. Given are the input parameters as described in the text, the lightest neutralino mass $m_{\tilde{\chi}_1^0}$, the lightest stop mass $m_{\tilde{t}_1}$, as well as the masses of the light and heavy CP-even Higgs bosons m_{h^0} and m_{H^0} calculated by `SPheno` (version `3.2.1`. All values except for $\tan\beta$ are given in GeV.

	$\Omega_\chi h^2$	th^0	tH^0	tA^0	bH^+	tZ^0	bW^+	$t\gamma$	tg	$\Sigma_{\phi+V}$	Σ_{total}
I	0.114	38.5%	–	–	–	3.4%	5.9%	0.2%	8.0%	48.0%	56.0%
II	0.116	24.6%	–	–	–	10.7%	3.4%	0.3%	9.1%	39.0%	48.1%
III	0.111	14.2%	20.7%	0.7%	0.2%	1.2%	2.1%	0.1%	2.9%	39.2%	42.1%

Table 6.3: Neutralino relic density and relative contributions of neutralino-stop coannihilation to the different final states for the example scenarios of Tab. 6.2. Σ_{total} gives the sum of all listed contributions, $\Sigma_{\phi+V}$ indicates the sum of all final states containing Higgs and electroweak vector bosons.

parameter M_1 and the third generation squark mass parameter $M_{\tilde{q}_3}$ gets even more prominent. The symmetric shape arises from the specific mass difference between the neutralino and the stop which is needed to feature neutralino-stop coannihilation. Especially smaller values are favoured in order to obtain the right order of magnitude for the coannihilation cross section. In the same context, a second feature can be explained. Scenarios with a too large or too small T_t parameter are excluded, because they feature too much contribution of stop-stop annihilation, or neutralino-neutralino annihilation, respectively (cf. Fig. 6.2).
In the last row of Fig. 6.3, the cut on the branching ratio of $b \to s\gamma$ has been applied. As large, negative values of T_t are disfavoured by this constraint [186], a significant reduction in this range of the trilinear coupling is visible.
Altogether, the cuts do not directly lead to a preferred range of $\tan\beta$. However, small values of $\tan\beta$ are slightly favoured by the constraint on $b \to s\gamma$.

6.3 Selected Example Scenarios

For demonstrating the impact of the one-loop calculation to the various final states, we have chosen three different scenarios in which different processes dominate the neutralino-stop coannihilation. An overview is given in Tab. 6.2.
All three scenarios are in good agreement with current constraints on the neutralino relic density, the Higgs mass and BR($b \to s\gamma$). The chosen scenarios feature a sizeable trilinear coupling. The first and second generation squarks are heavy in comparison to the stop, which is in agreement with the current LHC bounds. The mass difference between the lightest neutralino and the stop lies around 40-55 GeV, which is

sufficiently small to give rise to dominant contribution of neutralino-stop coannihilation. However, the different scenarios also show significant differences, for example, regarding the values of $M_{\tilde{q}_{1,2}}$, m_A and μ, which lead to different dominating subchannels.

The relative contributions of the different final states to each scenario are given in Tab. 6.3. The relative contribution of all coannihilation processes to the total (co)annihilation cross section is indicated by Σ_{total}. With a contribution of $40-60$ % the importance of neutralino-stop coannihilation is clearly visible. As we study in Chap. 10 the impact of the one-loop corrections with respect to the Higgs and electroweak vector bosons in the final state, $\Sigma_{\phi+V}$ gives the corresponding sum of these contributions.

In the following, we work out the key features which will be interesting for the discussion of the loop effects for each scenario. Throughout the thesis especially the impact of the Higgs final states and the gluon will be covered, as these have been addressed particularly by the author.

Scenario I. Scenario I shows the highest contribution of neutralino-stop coannihilation with up to almost 60 %. The final state with the lightest Higgs boson dominates with 38.5% by far. The electroweak vector bosons and the gluon contribute to a much lesser extent.

To study the scenario further, Fig. 6.4 shows the contribution of the squared diagrams and their interference terms to the tree-level cross section for selected processes. The grey area indicates the thermal distribution of $\langle \sigma v \rangle$ in arbitrary units, which is convoluted with the corresponding cross section times velocity. For more details we refer to its derivation in Sec. 4.1.3. It can be taken as a measure for the relevant range of centre-of-mass momentum within the calculation of the relic density.

The upper left subfigure shows the contributing matrix elements for the process $\tilde{\chi}_1^0 \tilde{t}_1 \rightarrow t\,h$ of Scenario I. As already discussed above, the Higgs-squark-squark coupling is significantly enhanced due to a high value of T_t, which causes a dominating contribution of the squared matrix element tt, and leads to a sizeable st interference term. The ss-matrix element contributes only little. With the neutralino-neutralino-Higgs coupling being the only one which does not contain a trilinear coupling, the contribution of the u-channel is completely negligible in comparison to the others, and thus not shown in Fig. 6.4.

Scenario II. Although in Scenario II the final state with the lightest Higgs boson shows the highest individual contribution, this scenario is in contrast to the previous one. In this case, also the electroweak bosons feature a striking impact with 10.7 % for the Z^0-boson and 3.4 % for the W^+-boson. The gluon has a sizeable relative contribution of 9.1 %. The differences are based on a smaller μ parameter and a higher value for $\tan\beta$. Moreover, it has a slightly lower trilinear coupling parameter,
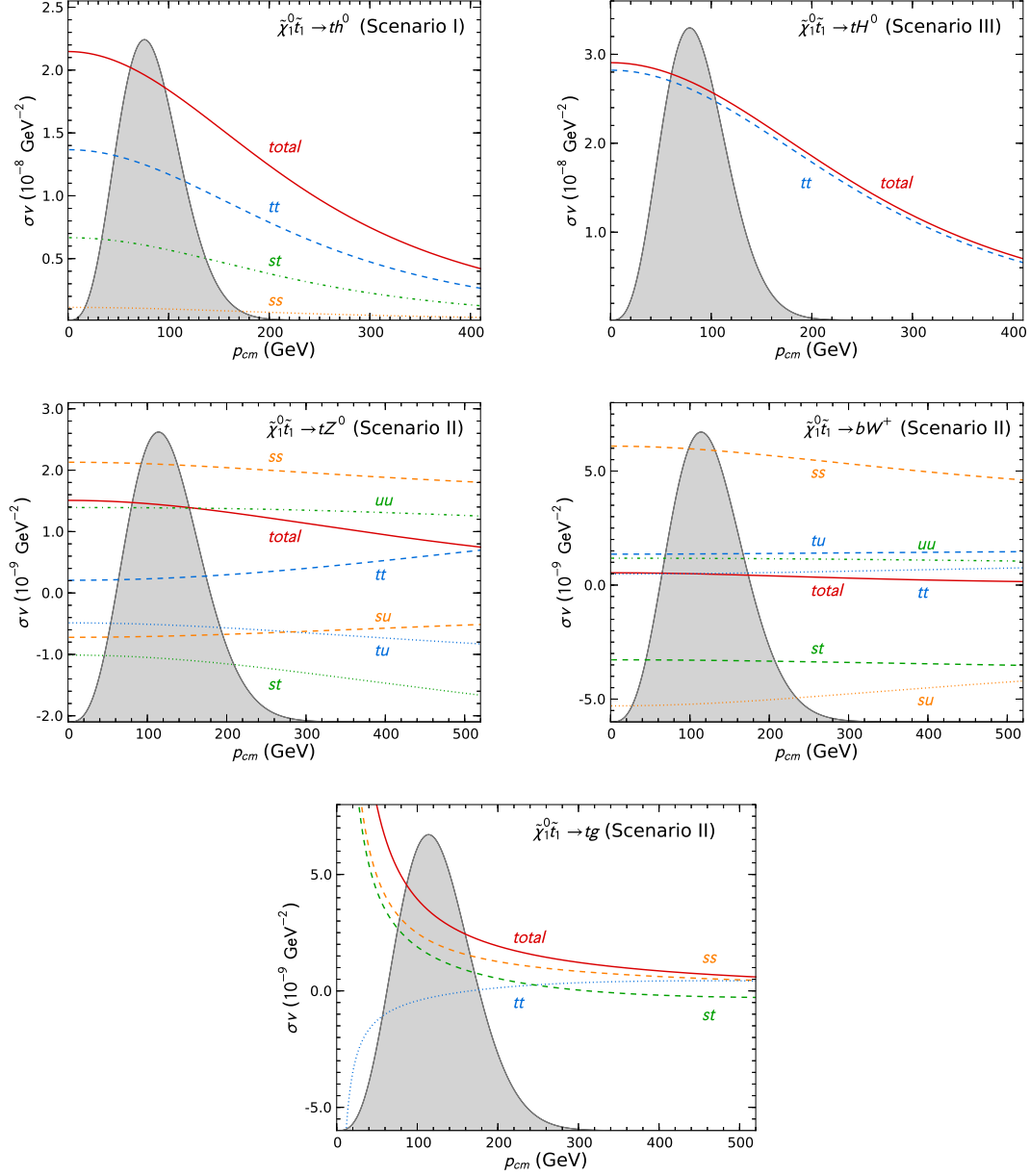
Figure 6.4: Contribution of the different diagrams (s-, t-, and u-channel) to selected processes of the different scenarios. The tree-level cross section as well as the most relevant contributions of the different squared diagrams (ss, tt, uu) and the interference terms (st, su, tu) are depicted.

and a slightly heavier third generation squark and bino mass parameter. The plots in the middle of Fig. 6.4 show the contributing squared diagrams and interference terms for the Z^0- and W^+-boson. In contrast to Scenario I, the tt matrix element shows only a small impact on the cross section. The dominating channel for the electroweak vector bosons is the ss-channel. Its contribution is even larger for the bW^+ final state than for tZ^0, due to a larger phase space. However, large destructive interferences of this diagram with the sub-leading t- and u-channels decrease its cross section such that the total value is almost an order of magnitude smaller than for the Z-boson. The lower subfigure shows a similar plot for a gluon in the final state. It features the highest cross section in comparison to the other final states. Due to the chosen gauge, an unphysical behaviour is observable for the tt element.

Scenario III. Scenario III is interesting especially in comparison to Scenario I. Both scenarios show a large contribution of the lightest Higgs final state, however, in Scenario III the heavy Higgs bosons also contributes. This is due to a pseudoscalar Higgs boson with a light pole mass of $m_{A^0} = 386$ GeV. With the other heavy Higgs bosons lying in the same ballpark, processes with heavy Higgs bosons in the final state are now accessible. Considering the upper right plot of Fig. 6.4, the cross section is dominated by the t-channel contribution, which is similar to the process with the lightest Higgs boson in the final state. The dominance of the tt-matrix element is even stronger than for the lightest Higgs, such that the ss- and st-contributions are negligible. This behaviour is caused by the modified mixing in the Higgs sector due to a smaller mass difference between h^0 and H^0. Neutralino-stop coannihilation into electroweak vector bosons is less important in this scenario.

Conclusions. We can conclude that neutralino-stop coannihilation plays an important role in the context of achieving the right value for the neutralino relic density, and obeying the experimental constraints at the same time. Due to its large contribution to the total (co)annihilation cross section, the impact of the full one-loop $\mathcal{O}(\alpha_s)$ supersymmetric QCD corrections is interesting to investigate. This is especially an important issue in order to match the experimental precision of PLANCK.
In the next three chapters 10, 8, and 9, we will theoretically discuss the performed one-loop calculation in detail, in order to study the impact of these corrections on the scenarios which have been just introduced in Chap. 10.

7 Virtual Corrections

In the following, we focus on the calculation of the full next-to-leading order (NLO) $\mathcal{O}(\alpha_s)$ corrections to neutralino-stop coannihilation into all final states. An overview of the corresponding tree-level diagrams for the process $\tilde{\chi}_i^0 \tilde{q}_j \rightarrow q_j X$, with $X = h^0, H^0, A^0, H^\pm, W^\pm, Z, \gamma, g$, has been already given in Fig. 6.1.

In order to obtain a full NLO calculation, we have to take into account all virtual and real contributions which contribute in $\mathcal{O}(\alpha_s)$. In the following, we focus on the virtual part, the real contributions will be addressed in a later chapter.

Virtual corrections have the same initial and final state particles as the corresponding tree-level diagrams, but feature additional, internal exchange particles. Thus, it possesses the same kinematics and phase space as the tree-level processes. We can distinguish three different kinds of virtual corrections: self-energies (2-point functions), vertex corrections (3-point functions) and box diagrams (4-point functions), which we will consider in the following.

The corresponding one-loop diagrams for the different studied final states are given in Figs. 7.7 to 7.10. Considering SUSY-QCD corrections implies that only quarks, squarks, gluons and gluinos can contribute as additional internal particles in the loops.

7.1 Regularization and Dimensional Reduction

All loop diagrams have one thing in common. They contain a virtual, unconstrained momentum q which has to be integrated over the whole phase space (cf. Fig. 7.1). Due to this, the propagator momentum q can become infinite, and thus, give rise to a divergence. Although the full calculation will be finite in the end, for the handling of separate contributions these divergences have to be extracted. One possible approach is introducing a cut off in order to prevent infinite momenta. However, this method violates translation and gauge invariance. Therefore, other methods have been proposed like, for instance, the Pauli-Villars regularization [187] or dimensional regularization (DReg or DR), see e.g. Ref. [188].

Dimensional Regularization. In the dimensional regularization approach, the divergences are isolated by calculating in D dimensions. The idea behind this method, becomes clearer in the following simple example. For instance, the divergence of a simple integral $\int_a^\infty \frac{1}{r^2} d^3 r$, which is linearly divergent, can be reduced by lowering the integration dimension. The integral $\int_a^\infty \frac{1}{r^2} d^2 r$ is only logarithmic divergent. By

lowering dimensions further $\int_a^\infty \frac{1}{r^2} dr$ the integral becomes convergent.

If we want to calculate an integral which is divergent in four dimensions, we can reformulate it in a convergent D-dimensional one, similar to the aforementioned example. When performing the limes to 4 dimensions, the divergence becomes visible as pole and makes these integrals manageable. A big advantage is moreover that dimensional regularization maintains Lorentz invariance, gauge invariance and unitarity.
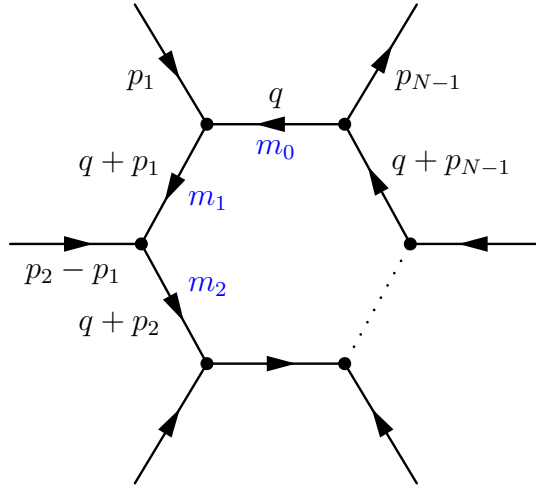
Figure 7.1: General N-loop diagram. All kinematics can be fixed by external momenta except one unconstrained momentum q.

Extraction of Ultraviolet and Infrared Divergences.   Based on a simple example we point out the strategy of dimensional regularization and demonstrate the extraction of infrared and ultraviolet poles.

In 4 dimensions the integral

$$\int d^4q \frac{1}{(q^2)^\alpha}, \tag{7.1}$$

which could arise due to a massless virtual particle in the propagator, is for all ranges of α divergent. Divergences which arise when $4 \geq 2\alpha$ are called ultraviolet (UV) divergent, poles which occur with $4 \leq 2\alpha$ are known as infrared (IR) divergent. To extract the poles, we reformulate this integral in D dimensions. Further, we can perform a Wick-rotation and reformulate the integral in Euclidean coordinates

$$\int d^D q \frac{1}{(q^2)^\alpha} = i(-1)^\alpha \Omega_D \int_0^\infty dq_E^2 \frac{1}{2} \left(q_E^2\right)^{\frac{D}{2}-1-\alpha} \tag{7.2}$$

with $\Omega_D = \pi^{\frac{D}{2}}/\Gamma(\frac{D}{2})$ being the solid angle. This integral is infrared divergent for $D < 2\alpha$ and ultraviolet divergent for $D > 2\alpha$. Thus, we split now the integral in two parts, the infrared part with $q_E^2 < \Lambda^2$ and the ultraviolet with $q_E^2 > \Lambda^2$

$$\int d^D q \frac{1}{(q^2)^\alpha} = i(-1)^\alpha \frac{\pi^{\frac{D}{2}}}{\Gamma(\frac{D}{2})} \left(\int_0^{\Lambda^2} dq_E^2 \frac{1}{2} (q_E^2)^{\frac{D}{2}-1-\alpha} + \int_{\Lambda^2}^\infty dq_E^2 \frac{1}{2} (q_E^2)^{\frac{D}{2}-1-\alpha} \right). \quad (7.3)$$

In order to distinguish between the two kinds of divergences, we introduce a variable $D' > 2\alpha$ for the infrared divergent integral and a second variable $D < 2\alpha$ for the ultraviolet divergent one. Thus we obtain the following expression

$$\int d^D q \frac{1}{(q^2)^\alpha} = i(-1)^\alpha \frac{2\pi^{\frac{D}{2}}}{\Gamma(\frac{D}{2})} \left(\frac{\Lambda^{D'-2\alpha}}{D'-2\alpha} - \frac{\Lambda^{D-2\alpha}}{D-2\alpha} \right). \quad (7.4)$$

If we set $\alpha = 2$, we arrive at the loop integral of the lowest order which features infrared and ultraviolet divergences. This integral, which we will be later able to identify with B(0,0,0), arises in our calculation for example in the gluon self energy with an internal gluon (see Fig.8.3). In this specific case, we obtain the following expression

$$\int d^D \frac{1}{(q^2)^2} = i \frac{2\pi^{\frac{D}{2}}}{\Gamma(\frac{D}{2})} \left(\frac{\Lambda^{D'-4}}{D'-4} - \frac{\Lambda^{D-4}}{D-4} \right) = i \frac{\pi^{2-\varepsilon}}{\Gamma(2-\varepsilon)} \left(\frac{\Lambda^{-2\varepsilon_{UV}}}{\varepsilon_{UV}} - \frac{\Lambda^{-2\varepsilon_{IR}}}{\varepsilon_{IR}} \right), \quad (7.5)$$

where we can easily see that we can nicely separate the infrared and ultraviolet divergences. In the limit of $D, D' \to 4$ we see how the poles arise, which nicely behave in D dimensions. In the last step, we have set

$$\varepsilon = \frac{4-D}{2}. \quad (7.6)$$

In our calculation we clearly distinguish between infrared $\frac{1}{\varepsilon_{IR}}$ and ultraviolet $\frac{1}{\varepsilon_{UV}}$ divergences. Especially for cross-checks in the final implementation of our DM@NLO code, keeping the distinction between both kinds of divergences, enables us to perform powerful cross-checks. However, one could also treat them undistinguishable and set both to $\frac{1}{\varepsilon}$. In this case, the example integral of Eq. (7.5) converges to zero. Working in D dimensions requires also to consistently adapt four-vectors to D-vectors and continuing the metric tensor so that e.g. $g_\mu^\mu = D$. Thus, the relation for the Dirac matrices reads now $\gamma^\mu \gamma_\mu = D$, whereas the anticommutator relation $\{\gamma^\mu \gamma^\nu\} = 2g^{\mu\nu}\mathbf{1}$ remains unchanged even in D dimensions.

Dimensional Reduction (DRed). Although dimensional regularization is a well established method to extract poles in Standard Model calculations, it poses a problem for loop calculations within Supersymmetry. This was explicitly shown in

Ref. [189, 190]. In D dimensions, vector fields would be now also D-dimensional with correspondingly adjusted degrees of freedom. Thus, a common superfield with its fermionic superpartner would not be possible anymore. This means, that Supersymmetry is not preserved within dimensional regularization.

Therefore, another kind of regularization scheme was introduced by Ref. [190], the so-called dimensional reduction (DRed). Within this scheme, the divergent integrals are treated similarly to DReg by calculating them in D dimensions. However, all tensors connected to vector fields are kept in 4 dimensions within the calculation. At one-loop level, differences between both schemes only appear as additional finite parts in DReg in comparison to DRed.

As we calculate SUSY-QCD loop corrections, we use in the following the dimensional reduction scheme.

7.2 Introduction to Loop Integrals

The occurring integrals within a one-loop calculation are well known for a long time, see for example Refs. [191, 192]. All N-loop diagrams of Fig. 7.1 can be reduced to the form of

$$I_n(\Upsilon) = \int d^D q \frac{1}{(q^2 - \Upsilon + i\epsilon)^n}, \tag{7.7}$$

where Υ is a function of masses and external momenta. This integral can be solved in D dimensions after performing a Wick-rotation and changing to Euclidean coordinates. Thus, we obtain the following expression

$$I_n(\Upsilon) = i(-1)^n \pi^{D/2} \frac{\Gamma(n - D/2)}{\Gamma(n)} (\Upsilon - i\epsilon)^{D/2-n}. \tag{7.8}$$

We clearly see that the term $\frac{\Gamma(n-D/2)}{\Gamma(n)}$ causes the divergences in the the loop integrals.

Example of Loop Integral Formalism: $A_0(m^2)$. To quote an example, we have a look at the easiest case of a loop integral, the scalar loop integral A_0. This is defined to be the integral $I_n(\Upsilon)$ with $n = 1$:

$$A_0(m^2) = \frac{(2\pi\mu)^{4-D}}{i\pi^2} \int d^D q \frac{1}{q^2 - m^2 + i\epsilon}. \tag{7.9}$$

Here, the prefactor is set by convention. The variable μ, which has the dimension of a mass, retains the correct dimension of the D-dimensional integral as it would have in four dimensions. We will later identify this variable as renormalization scale.

Without the need of performing any Feynman parametrization for this simple example, we immediately see that we can identify the integral $A_0(m^2)$ with the above
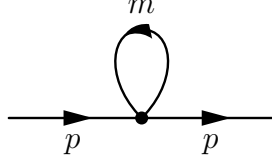
Figure 7.2: Generic $A_0(m^2)$ loop integral.

introduced integral $I_1(\Upsilon)$ by setting $\Upsilon = m^2$

$$A_0(m^2) = \frac{(2\pi\mu)^{4-D}}{i\pi^2} I_1(m^2) \tag{7.10}$$

such that we obtain by using Eq. (7.8)

$$A_0(m^2) = - \left(4\pi\mu^2\right)^{\frac{4-D}{2}} \Gamma(\frac{2-D}{2})(m^2 - i\epsilon)^{D/2-1} \tag{7.11}$$

$$= -(m^2 - i\epsilon) \left(\frac{m^2 - i\epsilon}{4\pi\mu^2}\right)^{-\varepsilon} \Gamma(\varepsilon - 1), \tag{7.12}$$

where in the last step $D = 4 - 2\varepsilon$ was used. We can perform a Taylor series for the ε-dependent terms

$$\left(\frac{m^2 - i\epsilon}{4\pi\mu^2}\right)^{-\varepsilon} = 1 - \varepsilon \ln\left(\frac{m^2 - i\epsilon}{4\pi\mu^2}\right) + \mathcal{O}(\varepsilon^2) \tag{7.13}$$

$$\Gamma(\varepsilon - 1) = -\frac{1}{\varepsilon} - \Gamma(1) - \Gamma'(1) + \mathcal{O}(\varepsilon) \tag{7.14}$$

$$= -\frac{1}{\varepsilon} - 1 + \gamma_E + \mathcal{O}(\varepsilon),$$

with using the definition of the Euler-Mascheroni constant $\gamma_E = -\Gamma'(1)$. Thus, we finally arrive at

$$A_0(m^2) = m^2 \left(\frac{1}{\varepsilon_{UV}} - \gamma_E + \ln 4\pi - \ln\left(\frac{m^2 - i\epsilon}{\mu^2}\right) + 1 + \mathcal{O}(\varepsilon)\right), \tag{7.15}$$

where we could extract an ultraviolet divergence $\frac{1}{\varepsilon_{UV}}$. It is common to introduce an abbreviation for the term

$$\Delta_{UV} = \left(\frac{1}{\varepsilon_{UV}} - \gamma_E + \ln 4\pi\right). \tag{7.16}$$

The reason for that will become clearer in Chap. 8.1.

Example of Loop Integral Formalism: $\mathbf{B_0(p_1^2, m_0^2, m_1^2)}$. Similarly, we can treat the scalar integral B_0.

$$B_0(p_1^2, m_0^2, m_1^2) = \frac{(2\pi\mu)^{4-D}}{i\pi^2} \int d^D q \frac{1}{[q^2 - m_0^2 + i\epsilon][(q+p_1)^2 - m_1^2 + i\epsilon]}, \quad (7.17)$$

It arises from a 2-point function of a generic self energy diagram like in Fig. 7.3. However, in order to obtain an integral of the form Eq. (7.7), we have to identify the argument Υ. Thus, we use the Feynman parametrization

$$\frac{1}{ab} = \int_0^1 dx \frac{a}{[a(1-x) + bx]^2} \quad (7.18)$$

and can rewrite Eq. (7.17) as

$$B_0(p_1^2, m_0^2, m_1^2) =$$
$$\frac{(2\pi\mu)^{4-D}}{i\pi^2} \int_0^1 dx \int d^D q \frac{1}{[(q+xp_1)^2 - x^2 p_1^2 + x(p_1^2 - m_1^2 + m_0^2) - m_0^2 + i\epsilon]^2}.$$
$$(7.19)$$

Substituting $q' \equiv q + xp_1$ and $dq' \equiv dq$, we can reformulate $B_0(p_1^2, m_0^2, m_1^2)$ in terms of the integral $I_n(\Upsilon)$ as

$$B_0(p_1^2, m_0^2, m_1^2) = \frac{(2\pi\mu)^{4-D}}{i\pi^2} \int_0^1 dx \, I_2(\Upsilon), \quad (7.20)$$

where $\Upsilon(x) = x^2 p_1^2 - x(p_1^2 - m_1^2 + m_0^2) + m_0^2$. This brings us to

$$B_0(p_1^2, m_0^2, m_1^2) = \frac{1}{\varepsilon_{UV}} - \gamma_E + \ln 4\pi - \int_0^1 dx \ln \left(\frac{x^2 p_1^2 - x(p_1^2 - m_1^2 + m_0^2) + m_0^2 - i\epsilon}{\mu^2} \right),$$
$$(7.21)$$

where we made use of Eq. (7.8).

Finally, we managed to isolate the ultraviolet divergence of the scalar 2-point function, which is a general feature independent of all arguments. At this point, it becomes clear, why a careful treatment of specific argument sets is important. The remaining integral can be performed further, however, for specific configurations of p_1^2, m_1^2 and m_2^2, the argument of the logarithm can become negative, and thus leads to complex values of the logarithm. Also, as already seen in the previous section, the specific loop function $B(0,0,0) = \frac{1}{\epsilon_{UV}} - \frac{1}{\epsilon_{IR}}$ features also an infrared divergence. Therefore, it is advised to perform this integral, and in general all loop integrals, for the specific argument sets separately. However, this has been done already extensively in the literature.
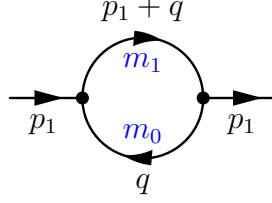
Figure 7.3: Generic $B_0(p_1^2, m_0^2, m_1^2)$ loop integral.

Tensor Reduction. We have shown the derivation of two loop integrals $A_0(m^2)$ and $B_0(p_1^2, m_0^2, m_1^2)$. However, when performing a one-loop calculation we also need loop integrals arising from 3-point and 4-point-functions. Continuing the naming convention they are defined as $C_0(p_1^2, (p_1 - p_2)^2, p_2^2, m_0^2, m_1^2, m_2^2)$ and $D_0(p_1^2, (p_2 - p_1)^2, (p_3 - p_2)^2, p_3^2, p_2^2, (p_1 - p_3)^2, m_0^2, m_1^2, m_2^2, m_3^2)$, respectively.

However, so far, we have only considered scalar particles within the loop. But we can also imagine having a fermionic propagator $\frac{i(\slashed{q}+m)}{q^2-m^2}$ in the loop of Fig. 7.1. Thus we get a tensor structure for the loop integrals like [193]

$$T_{\mu_1,...,\mu_M}^N(p_1,...,p_{N-1}; m_0,...,m_{N-1}) = \frac{(2\pi\mu)^{4-D}}{i\pi^2} \int d^D q \frac{q_{\mu_1}...q_{\mu_M}}{D_0 D_1 ... D_{N-1}} \qquad (7.22)$$

with

$$D_0 = q^2 - m_0^2 + i\epsilon, \quad D_i = (q + p_i)^2 - m_i + i\epsilon, \quad i = 1, ..., N-1, \qquad (7.23)$$

with $T^1 = A$, $T^2 = B$, $T^3 = C$, and $T^4 = D$, etc.

Passarino and Veltman developed for a way to treat these tensor integrals efficiently [192]. With the help of the so-called Passarino-Veltman reduction these integrals can be reduced in their tensorial rank and decomposed down to pure scalar integrals. Let us have a quick look at one quite frequently used tensor loop function. For instance, the tensor 2-point functions are given by

$$B^\mu = p_1^\mu B_1 \qquad (7.24)$$
$$B^{\mu\nu} = g^{\mu\nu} B_{00} + p_1^\mu p_1^\nu B_{11}. \qquad (7.25)$$

When multiplying both sides of Eq. 7.24 with the external momentum p_1 we arrive at

$$p_1^\mu B_\mu = \frac{(2\pi\mu)^{4-D}}{i\pi^2} \int d^D q \frac{p_1 \cdot q}{[q^2 - m_0^2 + i\epsilon][(q+p_1)^2 - m_1^2 + i\epsilon]} = p_1^2 B_1. \qquad (7.26)$$

Now, we can use a trick, and expand the product $p_1.q$ in terms of the denominator's factors

$$p_1.q = \frac{1}{2}\big([(q+p_1)^2 - m_i^2 + i\epsilon] - [q^2 - m_0^2 + i\epsilon] - [p_1^2 - m_i^2 + m_0^2]\big). \qquad (7.27)$$

Combining Eqs. (7.26) and (7.27) we can rewrite the tensor 2-point function in terms of pure scalar loop function A_0 and B_0:

$$p_1^2 B_1 = \frac{(2\pi\mu)^{4-D}}{i\pi^2}\frac{1}{2}\left(\int d^D q \frac{1}{q^2 - m_0^2 + i\epsilon}\right. \qquad (7.28)$$

$$- \int d^D q \frac{1}{(q+p_1)^2 - m_1^2 + i\epsilon}$$

$$\left. - (p_1^2 - m_1^2 + m_0^2)\int d^D q \frac{1}{[q^2 - m_0^2 + i\epsilon][(q+p_1)^2 - m_1^2 + i\epsilon]}\right)$$

$$= \frac{1}{2}\left[A_0(m_0^2) - A_0(m_1^2) - (p_1^2 - m_1^2 + m_0^2)B_0(p_1^2, m_0^2, m_1^2)\right]$$

$$\Rightarrow B_1 = \frac{1}{2\,p_1^2}\left[A_0(m_0^2) - A_0(m_1^2) - (p_1^2 - m_1^2 + m_0^2)B_0(p_1^2, m_0^2, m_1^2)\right] \qquad (7.29)$$

Similar is possible for the coefficients B_{00} and B_{11} of Eq. (7.25). We obtain

$$
\begin{aligned}
B_{00} &= \tfrac{1}{2(D-1)} && [A_0(m_1^2) + 2\,m_0^2\,B_0(p_1^2, m_0^2, m_1^2) \\
& && + (p_1^2 - m_1^2 + m_0^2)\,B_1(p_1^2, m_0^2, m_1^2)] && (7.30) \\
B_{11} &= \tfrac{1}{2(D-1)p_1^2} && [(D-2)\,A_0(m_1^2) - 2\,m_0^2\,B_0(p_1^2, m_0^2, m_1^2) \\
& && -D\,(p_1^2 - m_1^2 + m_0^2)\,B_1(p_1^2, m_0^2, m_1^2)] && (7.31)
\end{aligned}
$$

This method can be applied similarly to all loop integrals of all ranks. Thus, we are able to reduce the occurring loop integrals to few commonly used ones. Their analytic expressions with their divergence structure is well known and can be found in different literature [191–194].

Summary of Frequently Used Divergent Loop Integrals. As discussed before the calculation of loop functions give rise to ultraviolet and infrared divergences. As we could see on the example of the loop integral B_0, different argument sets can give rise to different divergent behaviour. Therefore, we give in the following an overview of the most frequently used divergent loop integrals in this calculation, in order to obtain a feeling for their divergence structure.

These loop integrals will be later set in the context of the cancellation of the virtual and real contributions (see Figs. 9.5, 9.6, 9.7 and 9.9). For further interest on

loop integral	$1/\epsilon_{UV}$	$1/\epsilon_{IR}$	$1/\epsilon_{IR}^2$
$A_0(m^2)$	✓	-	-
$B_0(p_1^2, m_0^2, m_1^2)$	✓	-	-
$B_0(0,0,0)$	✓	✓	-
$B_1(p_1^2, m_0^2, m_1^2)$	✓	-	-
$B_{00}(p_1^2, m_0^2, m_1^2)$	✓	-	-
$B_{11}(p_1^2, m_0^2, m_1^2)$	✓	-	-
$\dot{B}_0(m^2, m^2, 0)$	-	✓	-
$\dot{B}_1(m^2, m^2, 0)$	-	✓	-
$\dot{B}_{00}(p_1^2, m_0^2, m_1^2)$	✓	-	-
$C_0(m_1^2, s, m_2^2, 0, m_1^2, m_2^2)$	-	✓	-
$C_0(m^2, s, 0, 0, m^2, 0)$	-	-	✓
$C_{00}(p_1^2, (p_1 - p_2)^2, p_2^2, m_0^2, m_1^2, m_2^2)$	✓	-	-
$D_0(m_2^2, m_1^2, 0, m_3^2, s, u, 0, m_2^2, m^2, m_3^2)$	-	✓	-
$D_0(m_3^2, m_1^2, m_2^2, 0, t, s, 0, m_1^2, m_2^2, 0)$	-	-	✓

Table 7.1: Loop integrals with their leading divergence.

the divergent structure of different loop integrals, we refer the interested reader to Refs. [195–197].

7.3 Calculation of Virtual Corrections

For the calculation of the full one-loop SUSY-QCD corrections, we have to take different contributions into account. As we consider only corrections up to $\mathcal{O}(\alpha_s)$, the occurring contributions are vertex corrections $\Delta_{1,2}^{\mathrm{vert}}$, propagator corrections Δ^{prop}, and box contributions Δ^{box}. A schematic picture is shown in Fig. 7.4. Altogether they contribute to the full virtual corrections

$$\Delta_{\mathrm{virtual}}^{\mathrm{corr}} = \Delta_1^{\mathrm{vert}} + \Delta^{\mathrm{prop}} + \Delta_2^{\mathrm{vert}} + \Delta^{\mathrm{box}} \tag{7.32}$$

These corrections have to be calculated for all channels and final states depicted in Fig. 6.1.

In order to provide a powerful tool for the full SUSY-QCD one-loop calculation, we have chosen a generic and extendible structure for calculating the matrix elements of the propagator corrections, vertex corrections, boxes and counterterms for all final states. Due to the different structure in their calculation, we have divided the calculation into three parts: the Higgs boson final states, the electroweak vector boson final states and the gluon final state. As the author of this thesis has been in charge of the Higgs boson final states, and performed most of the parts for the gluon final state, this work focuses mainly on these five of the total eight processes. In the
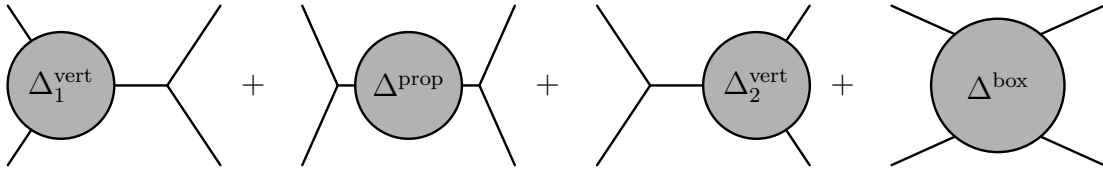
Figure 7.4: Contributions to the $\mathcal{O}(\alpha_s)$ corrections, consisting of vertex corrections $\Delta_{1,2}^{\text{vert}}$, propagator corrections Δ^{prop} and box contribution Δ^{box}.

following we want to demonstrate our calculation in particular on the example of the Higgs final states.

7.3.1 Processes with a Higgs Boson in the Final State

The four different Higgs boson final states can be treated in a common way. With a clever choice, we can construct generic amplitudes, which can be used for the tree-level calculation, as well as for the vertex corrections and propagator corrections. As the contributions arising from counterterms will be discussed in more detail in a later section, we only want to mention that also all matrix elements containing counterterms can be calculated based on this structure.

As an example we want to have a closer look at the corrections arising from a fermion
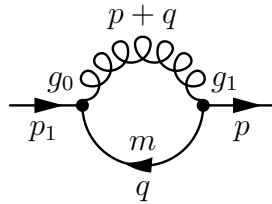
Figure 7.5: Derivation of the generic loop correction structure.

propagator, which is shown in Fig. 7.5. Assuming a general left/right structure for the couplings g_0 and g_1, we can calculate the corrections (with neglecting the external

legs so far) as follows

$$
\begin{aligned}
\frac{\mu^{4-D}}{(2\pi)^D} &\int dq^D i[g_{0_L} P_L + g_{0_R} P_R] T^a \gamma^\mu i \frac{(\slashed{q} + \slashed{q}_1) + m}{(q+q_1)^2 - m^2} i [g_{1_L} P_L + g_{1_R} P_R] T^a \gamma^\mu i \frac{-g^{\mu\nu}}{q^2} \\
&= -C_F \frac{\mu^{4-D}}{(2\pi)^D} \int dq^D \frac{[g_{0_L} g_{1_L} P_L + g_{0_R} g_{1_L} P_R](2-D)(\slashed{q} + \slashed{q}_1)}{[q^2][(q+q_1)^2 - m^2]} \\
&\quad - C_F \frac{\mu^{4-D}}{(2\pi)^D} \int dq^D \frac{[g_{0_L} g_{1_R} P_L + g_{0_R} g_{1_R} P_R] D m}{[q^2][(q+q_1)^2 - m^2]} \\
&= -\frac{C_F}{16\pi^2} \left\{ 4m[g_{0_L} g_{1_L} P_L + g_{0_R} g_{1_L} P_R] B_0(q_1^2, 0, m^2) \right. \\
&\quad \left. -2[g_{0_L} g_{1_L} P_L + g_{0_R} g_{1_L} P_R] \left(B_0(q_1^2, 0, m^2) + B_1(q_1^2, 0, m^2) \right) \slashed{q}_1 \right\}
\end{aligned}
\tag{7.33}
$$

Comparing with the last two lines of Eq. (7.33), we obtain a generic structure according to

$$
i[(Z_L^s P_L + Z_R^s P_R) + (Z_L^v P_L + Z_R^v P_R) \slashed{q}_1],
\tag{7.34}
$$

with q_1 being the propagator momentum. Furthermore, the parameters Z_L^s and Z_R^s account for the left and right chiral scalar coefficient, respectively. The left and right handed vectorial form factors are denoted by Z_L^v and Z_R^v. This structure is typical for all propagator and vertex corrections which include a fermion line, as well as for corresponding box diagrams. Based on this structure we can construct the necessary matrix elements.

s-channel contribution. In the s-channel diagram all vertex corrections and propagator corrections contain fermionic contributions, see Fig. 7.6. Thus, we can use the above derived general expression for all arising corrections such that the amplitude $\mathcal{M}_s$ shows the most general structure

$$
\begin{aligned}
\mathcal{M}_s = \quad &\bar{u}(p_3) \quad i\left[(F_L^s P_L + F_R^s P_R) + (F_L^v P_L + F_R^v P_R) \slashed{q}_1\right] \\
&i \frac{(\slashed{q}_1 + m_{q_1})}{q_1^2 - m_{q_1}^2} i\left[(Z_L^s P_L + Z_R^s P_R) + (Z_L^v P_L + Z_R^v P_R) \slashed{q}_1\right] \qquad i \frac{(\slashed{q}_1 + m_{q_1})}{q_1^2 - m_{q_1}^2} \\
&i\left[(A_{1\,L}^s P_L + A_{1\,R}^s P_R) + (A_{1\,L}^v P_L + A_{1\,R}^v P_R) \slashed{q}_1\right] \quad u(p_1).
\end{aligned}
\tag{7.35}
$$

The form factors $A_{1\,L,R}^{s,v}$ are introduced to model the corrections Δ_1^{vert} arising from the coupling $\hat{A}_{in}^{qg}$. The contributing loop diagrams are depicted in Fig. 7.7(c). Similarly, the form factors $F_{L,R}^{s,v}$ result from the coupling $\hat{F}_\phi^{qg}$ and lead to the corrections Δ_2^{vert} (cf. Fig. 7.4). Their contributing vertex corrections are shown in Fig. 7.8(a). The fermionic propagator which is contained in the s-channel diagram, leads to the above derived form factors $Z_{L,R}^{s,v}$. The two corresponding loop diagrams, which contribute to the propagator correction Δ^{prop} are depicted in Fig. 7.7(a). All corre-
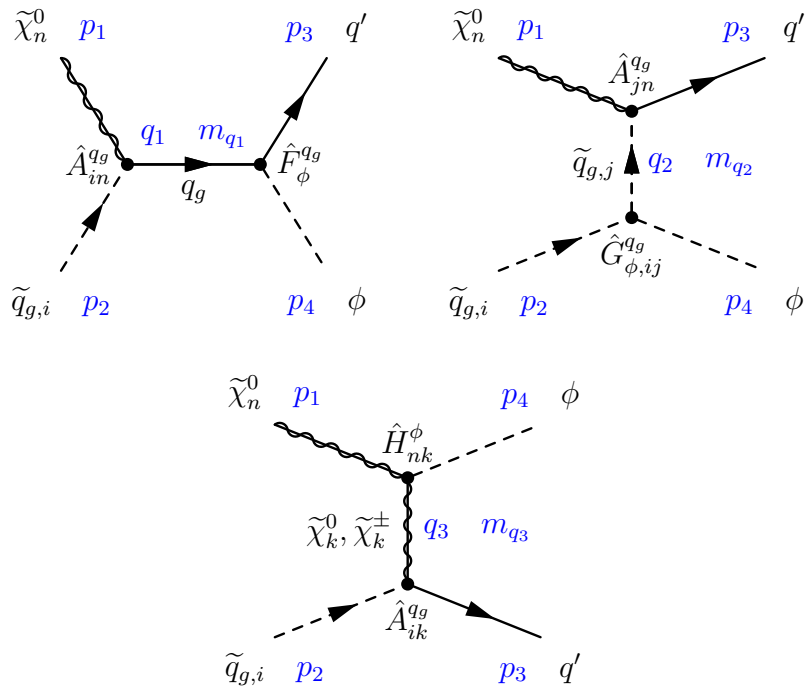
Figure 7.6: Definitions which have been used for the generic amplitudes with a Higgs boson in the final state ($\Phi = h^0, H^0, A^0, H^\pm$). S-, t- and u-channel are depicted.

sponding analytical expressions can be found in Appendix A–D.

However, we also want to recover the tree-level expression with this generic structure. In contrast to the tree-level expression, two propagator terms $\frac{(\slashed{q}_1 + m_{q_1})}{q_1^2 - m_{q_1}^2}$ enter the amplitude due to the loop corrected fermion propagator (cf. Eq. (7.35)). Therefore we have to perform a little trick in order to obtain the tree-level expression. Contracting the two fermionic propagators and the terms arising from the loop corrections to the propagator, we obtain

$$
\begin{aligned}
\mathcal{M}_s = \quad & \bar{u}(p_3) \quad i\left[(F_L^s P_L + F_R^s P_R) + (F_L^v P_L + F_R^v P_R)\,\slashed{q}_1\right] \\
& \frac{1}{q_1^2 - m_{q_1}^2} \quad i\left[(P_L^s P_L + P_R^s P_R) + (P_L^v P_L + P_R^v P_R)\,\slashed{q}_1\right] \\
& i\left[(A_{1\,L}^s P_L + A_{1\,R}^s P_R) + (A_{1\,L}^v P_L + A_{1\,R}^v P_R)\,\slashed{q}_1\right] u(p_1),
\end{aligned}
\tag{7.36}
$$

where the newly introduced form factors $P_{L,R}^{s,v}$ are connected to $Z_{L,R}^{s,v}$ as follows

$$
P_L^s = -\left[Z_L^s\, m_{q_1}^2 + Z_R^s\, q_1^2 + (Z_L^v + Z_R^v)\, m_{q_1}\, q_1^2\right]/(q_1^2 - m_{q_1}^2)
\tag{7.37}
$$

$$
P_R^s = -\left[Z_L^s\, q_1^2 + Z_R^s\, m_{q_1}^2 + (Z_L^v + Z_R^v)\, m_{q_1}\, q_1^2\right]/(q_1^2 - m_{q_1}^2)
\tag{7.38}
$$

$$
P_L^v = -\left[(Z_L^s + Z_R^s)\, m_{q_1} + Z_L^v\, m_{q_1}^2 + Z_R^v\, q_1^2\right] \quad /(q_1^2 - m_{q_1}^2)
\tag{7.39}
$$

$$
P_R^v = -\left[(Z_L^s + Z_R^s)\, m_{q_1} + Z_L^v\, q_1^2 + Z_R^v\, m_{q_1}^2\right] \quad /(q_1^2 - m_{q_1}^2).
\tag{7.40}
$$

Hereby, the coefficients $Z_{L,R}^{s,v}$ are again those which directly arise from the quark self energies, the momentum q_1 describes the propagator momentum and m_{q_1} the corresponding fermion mass. It is clearly visible, that we have absorbed the additional propagator denominator and the two additional complex i, which arise in contrast to the tree-level expressions.

Altogether, we can now use the above introduced expression (7.36) for all necessary corrections (and counterterms) as well as for recovering the tree level.

The tree level is obtained by setting all vectorial form factors to zero ($A_{1\,L,R}^v = F_{L,R}^v = 0$). For the scalar form factors, we can put in the usual tree-level couplings ($A_{1\,L,R}^s = A_{ij}^{q_g\,L,R}$, and $F_{L,R}^s = F_\Phi^{q_g\,L,R}$). They can be found in more detail in Appendix A. To reduce the propagator expression of Eq. 7.36 to the tree level, we have to put $P_L^v = P_R^v = 1$ and $P_L^s = P_R^s = m_{q_1}$, where m_{q_1} is the corresponding propagator mass.

If we want to account for the loop corrected version of the generic amplitude, we keep all form factors the same as for the tree-level case, except setting one of the vertices or the propagator to their loop corrected values in order to obtain Δ_1^{vert}, Δ_2^{vert}, or Δ^{prop}. The necessary form factors and couplings can be found in detail in Appendix A–D.

Of course, for calculating the whole squared matrix element, also the complex conjugated amplitude has to be considered. Addressing a one-loop calculation of $\mathcal{O}(\alpha_s)$, we have to consider all relevant interferences between the one-loop correction diagrams and their corresponding tree-level channels for each final state. Products of

loop-diagrams with themselves do not have to be considered, as these contributions are already beyond next-to-leading order level.

Therefore, it is sufficient to use a pure tree-level structure for the complex conjugated case

$$\mathcal{M}_s^\dagger = -\bar{u}(p_1)\, i\, [(A_{1\,R}^* P_L + A_{1\,L}^* P_R)]\, i\, \frac{\slashed{q}_1 + m}{q_1^2 - m_{q_1}^2}\, i\, [(F_R^* P_L + F_L^* P_R)]\, u(p_3)\,. \quad (7.41)$$

Hereby, it is not needed to distinguish between scalar and vectorial form factors. The basic naming convention is again similar to Eq. (7.35), and we can set the coefficients to the complex conjugated tree-level couplings $A_{1\,L,R}^* = A_{ij}^{q_g\,L,R*}$ and $F_{L,R}^* = F_\Phi^{q_g\,L,R}$.

t-channel contribution. A similar generic structure can be derived for the t-channel of Fig. 7.6 and is given by

$$\mathcal{M}_t = \bar{u}(p_3)\, i\, [(A_{2\,L}^s P_L + A_{2\,R}^s P_R) + (A_{2\,L}^v P_L + A_{2\,R}^v P_R)\, \slashed{q}_2] \quad (7.42)$$

$$\times\, \frac{i}{q_2^2 - m_{q_2}^2}\, i\, P_s\, \frac{i}{q_2^2 - m_{q_2}^2}\, i\, G\, u(p_1)\,. \quad (7.43)$$

With the coupling $\hat{G}_{\phi,ij}^{q_g}$ and the t-channel propagator being scalar, the structure is much more simplified than in the s-channel case, as only scalar corrections are expected for those. In order to be able to easily recover the tree-level structure we make again use of a small trick, such that we arrive at

$$\mathcal{M}_t = \bar{u}(p_3)\, i\, [(A_{2\,L}^s P_L + A_{2\,R}^s P_R) + (A_{2\,L}^v P_L + A_{2\,R}^v P_R)\, \slashed{q}_2]\, \frac{i\, P^2}{q_2^2 - m_{q_2}^2}\, i\, G\, u(p_1)\,,$$
$$(7.44)$$

with the following expression accounting for the propagator correction

$$P = -P_s/(q_2^2 - m_{q_2}^2)\,. \quad (7.45)$$

By setting $P = 1$ and $G = G_{\Phi,ij}^{q_g}$ we retain the tree-level expression. The loop contributions arising from the propagator are obtained by putting in the propagator corrections P_s (cp. Appendix C) of the squark self energy which are depicted in Fig. 7.7(b). The diagrams contributing to the radiative corrections of $G_{\Phi,ij}^{q_g}$ are depicted in Fig. 7.8(b), the corresponding form factors G are given in Appendix D. The loop corrections to the coupling $\hat{A}_{jn}^{q_g}$ are similar for all three channels, and are shown in Fig. 7.7(c).

Also in this case, we can assume for the complex conjugated amplitude a pure tree-level structure, which is given by

$$\mathcal{M}_t^\dagger = -\bar{u}(p_1)\, i\, G^*\, \frac{i}{q_2^2 - m_{q_2}^2}\, i\, [(A_{2\,R}^* P_L + A_{2\,L}^* P_R)]\, u(p_3)\,. \quad (7.46)$$

u-channel contribution. The last generic amplitude concerns the u-channel, which features the simplest generic structure:

$$\mathcal{M}_u = \bar{u}(p_3)\, i\, [(A^s_{3\,L}\, P_L + A^s_{3\,R}\, P_R) + (A^v_{3\,L}\, P_L + A^v_{3\,R}\, P_R)\, \slashed{q}_3]$$
$$\times\, i\, \frac{(\slashed{q}_3 + m_{q_3})}{q_3^2 - m_{q_3}^2}\, i\, [H^s_L P_L + H^s_R P_R]\, u(p_1). \tag{7.47}$$

With a neutralino or a chargino in the propagator, no propagator corrections arise, due to taking into account only SUSY-QCD corrections. Also the neutralino-neutralino-Higgs, and the neutralino-chargino-charged Higgs coupling, respectively, give no rise to SUSY-QCD corrections. Therefore, we have to address only corrections arising from the vertex $\hat{A}^{q_g}_{i,k}$.

For the corresponding complex conjugated amplitude we can write

$$\mathcal{M}^\dagger_u = \bar{u}(p_1)\, i\, [H^*_L P_L + H^*_R P_R]\, i\, \frac{(\slashed{q}_3 + m_{q_3})}{q_3^2 - m_{q_3}^2}\, i\, [(A^*_{3\,R} P_L + A^*_{3\,L} P_R)]\, u(p_3). \tag{7.48}$$

Again, no generic correction structure has to be taken into account.

Full matrix element. Bringing all expressions described above together, we arrive at the full matrix element for the tree level

$$|\mathcal{M}|^2_{\text{tree}} = \mathcal{M}^{\text{tree}}_s \mathcal{M}^{\text{tree}*}_s + \mathcal{M}^{\text{tree}}_t \mathcal{M}^{\text{tree}*}_t + \mathcal{M}^{\text{tree}}_u \mathcal{M}^{\text{tree}*}_u$$
$$+ 2\text{Re}(\mathcal{M}^{\text{tree}}_s \mathcal{M}^{\text{tree}*}_t) + 2\text{Re}(\mathcal{M}^{\text{tree}}_s \mathcal{M}^{\text{tree}*}_u) + 2\text{Re}(\mathcal{M}^{\text{tree}}_t \mathcal{M}^{\text{tree}*}_u) \tag{7.49}$$

and the following squared matrix element for the virtual corrections

$$\begin{aligned}
|\mathcal{M}|^2_{\text{virtual}} = &\ \mathcal{M}^{\text{A}_1}_s \mathcal{M}^{\text{tree}*}_s + 2\text{Re}(\mathcal{M}^{\text{A}_1}_s \mathcal{M}^{\text{tree}*}_t) + 2\text{Re}(\mathcal{M}^{\text{A}_1}_s \mathcal{M}^{\text{tree}*}_u) \\
&+ \mathcal{M}^{\text{F}}_s \mathcal{M}^{\text{tree}*}_s\ + 2\text{Re}(\mathcal{M}^{\text{F}}_s \mathcal{M}^{\text{tree}*}_t)\ + 2\text{Re}(\mathcal{M}^{\text{F}}_s \mathcal{M}^{\text{tree}*}_u) \\
&+ \mathcal{M}^{\text{P}}_s \mathcal{M}^{\text{tree}*}_s\ + 2\text{Re}(\mathcal{M}^{\text{P}}_s \mathcal{M}^{\text{tree}*}_t)\ + 2\text{Re}(\mathcal{M}^{\text{P}}_s \mathcal{M}^{\text{tree}*}_u) \\
&+ \mathcal{M}^{\text{A}_2}_t \mathcal{M}^{\text{tree}*}_t + 2\text{Re}(\mathcal{M}^{\text{A}_2}_t \mathcal{M}^{\text{tree}*}_s) + 2\text{Re}(\mathcal{M}^{\text{A}_2}_t \mathcal{M}^{\text{tree}*}_u) \\
&+ \mathcal{M}^{\text{G}}_t \mathcal{M}^{\text{tree}*}_t\ + 2\text{Re}(\mathcal{M}^{\text{G}}_t \mathcal{M}^{\text{tree}*}_s)\ + 2\text{Re}(\mathcal{M}^{\text{G}}_t \mathcal{M}^{\text{tree}*}_u) \\
&+ \mathcal{M}^{\text{P}}_t \mathcal{M}^{\text{tree}*}_t\ + 2\text{Re}(\mathcal{M}^{\text{P}}_t \mathcal{M}^{\text{tree}*}_s)\ + 2\text{Re}(\mathcal{M}^{\text{P}}_t \mathcal{M}^{\text{tree}*}_u) \\
&+ \mathcal{M}^{\text{A}_3}_u \mathcal{M}^{\text{tree}*}_u + 2\text{Re}(\mathcal{M}^{\text{A}_3}_u \mathcal{M}^{\text{tree}*}_s) + 2\text{Re}(\mathcal{M}^{\text{A}_3}_u \mathcal{M}^{\text{tree}*}_t),
\end{aligned} \tag{7.50}$$

where the conjugated elements are always set to the tree-level amplitude and the unconjugated terms account for all possibilities: tree level, vertex corrections, propagator corrections. The supscripts indicate the corrected amplitude according to the aforementioned introduced naming convention.

Thus, we have finally treated almost all virtual contributions

$$\sigma^{\text{full}} = \sigma^{\text{tree}} + \sigma^{\Delta^{\text{vert}}} + \sigma^{\Delta^{\text{prop}}}. \qquad (7.51)$$

However, the calculation of the box diagrams $\sigma^{\Delta^{\text{box}}}$ has still to be addressed.

Box contributions. The only missing piece of the virtual contributions arise from the box diagrams, depicted in Fig. 7.8(c). Also the boxes can be written in the same generic form as described above, such that we end up with the following generic expression for the box amplitude

$$\mathcal{M}_{\text{box}} = \bar{u}(p_3)\, i\, [(B_L^s\, P_L + B_R^s\, P_R) + (B_L^v\, P_L + B_R^v\, P_R)\, \slashed{p}_2]\, u(p_1), \qquad (7.52)$$

where $B_{L,R}^s$ denote the corresponding scalar form factors of the contributing boxes, and $B_{L,R}^v$ indicate the vectorial ones in dependence on the chosen momentum p_2. The full analytic expressions of the form factors are given in Appendix E.
The full squared matrix element for the box contributions reads

$$|\mathcal{M}|^2_{\text{box}} = \mathcal{M}_{\text{box}}\mathcal{M}_s^* + \mathcal{M}_{\text{box}}\mathcal{M}_t^* + \mathcal{M}_{\text{box}}\mathcal{M}_u^*, \qquad (7.53)$$

where the complex conjugated terms correspond to the above introduced expressions Eqs. (7.41),(7.46), and (7.48). Thus, we finally have calculated all parts

$$\sigma^{\text{full}} = \sigma^{\text{tree}} + \sigma^{\Delta^{\text{vert}}} + \sigma^{\Delta^{\text{prop}}} + \sigma^{\Delta^{\text{prop}}} \qquad (7.54)$$

contributing to the virtual corrections.
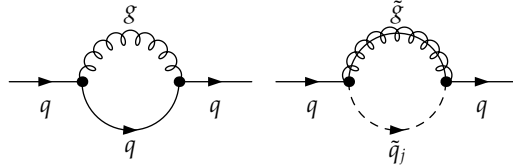
(a) Quark self energies at one-loop level contributing to $\mathcal{O}(\alpha_s)$. Their corresponding scalar and vectorial form factors $Z_{L,R}^{s,v}$ are given in Appendix C.
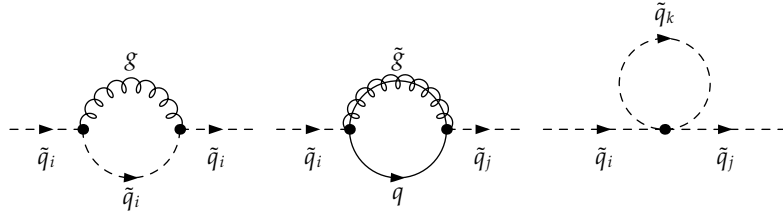
(b) Squark self energies at one-loop level contributing to $\mathcal{O}(\alpha_s)$. They give rise to the pure scalar corrections P_s, given in the Appendix C .
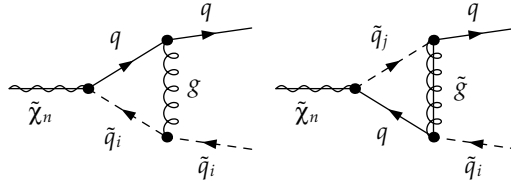
(c) Vertex corrections to the gaugino-squark-quark coupling $\hat{A}_{in}^{q_g}$, which contributes to all processes and channels. The form factors $A_{L,R}^{s,v}$ are given in Appendix D.

Figure 7.7: One-loop corrections which are common for all final states. Shown are the contributions arising from the quark and squark propagator, as well as from the gaugino-squark-quark coupling.
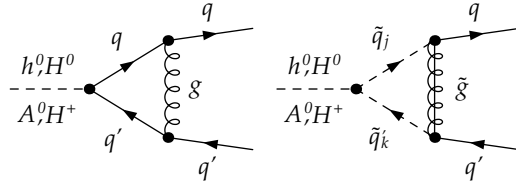
(a) Contributing vertex corrections to the Higgs-quark-quark coupling $\hat{F}_\phi^{q_g}$, which appears in the s-channel. The corresponding form factors $F_{L,R}^{s,v}$ are given in Appendix D.
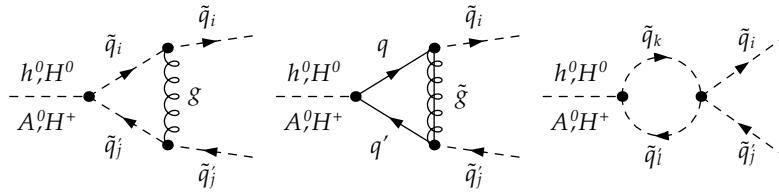
(b) Contributing vertex corrections to the Higgs-squark-squark coupling $\hat{G}_{\phi,ij}^{q_g}$, which occurs in the t-channel. The pure scalar form factors G are given in Appendix D.
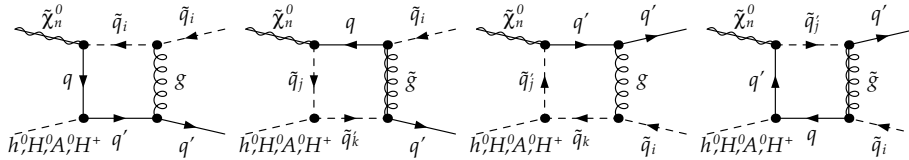
(c) All contributing box diagrams for the Higgs final state. Their form factors $B_{L,R}^{s,v}$ are given in Appendix E.

Figure 7.8: Specific virtual corrections in case of a Higgs boson in the final state.

7.3.2 Processes with a Gluon in the Final State

The process with the gluon in the final state receives the largest number of vertex corrections and box diagrams (cf. Fig. 7.10). Thus, we do not give all single form factors in detail as for the Higgs final state. This would exceed by far the scope of this document. Therefore, we show in the following only the generic structure of the amplitudes and the contributing diagrams.

In contrast to the Higgs final states, the gluon contributes only via an *s*-channel and *t*-channel diagram. The naming convention which was used for the calculation is shown in Fig. 7.9.
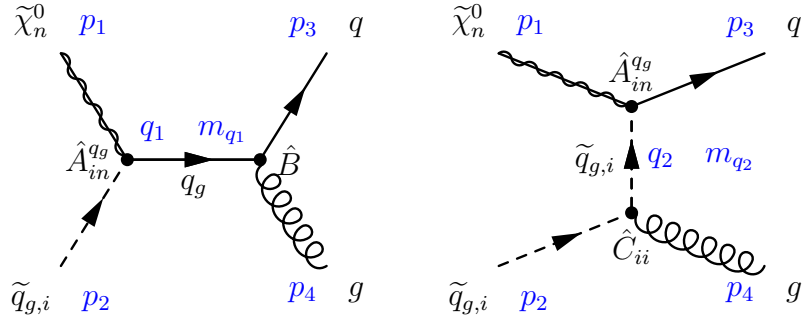
Figure 7.9: Definitions which have been used for the generic amplitudes with a gluon in the final state. The contributing *s*- and *t*-channel exchange is depicted.

As the $\hat{B}$-coupling involves two fermions and one vector boson, it leads to a quite complex structure for the loop corrected vertex diagrams such that we arrive at

$$
\begin{aligned}
\mathcal{M}_s =& \bar{u}(p_3)\, \epsilon_\mu^*(p_4) i \left[\ \gamma^\mu (B_{0\,L}^s P_L + B_{0\,R}^s P_R) + (q_1 + p_3)^\mu (B_{1\,L}^s P_L + B_{1\,R}^s P_R)\right. \\
&+ (q_1 - p_3)^\mu (B_{2\,L}^s P_L + B_{2\,R}^s P_R) + \left(\gamma^\mu (B_{0\,L}^v P_L + B_{0\,R}^v P_R)\right. \\
&\left.+ (q_1 + p_3)^\mu (B_{1\,L}^v P_L + B_{1\,R}^v P_R) + (q_1 + p_3)^\mu (B_{2\,L}^v P_L + B_{2\,R}^v P_R)\right)(\slashed{q}_1 - m_{q_1})\Big] \\
&\times \frac{1}{q_1^2 - m_{q_1}^2}\, i\left[(P_L^s P_L + P_R^s P_R) + (P_L^v P_L + P_R^v P_R)\, \slashed{q}_1\right] \\
&\times i\left[(A_{1\,L}^s\, P_L + A_{1\,R}^s\, P_R) + (A_{1\,L}^v\, P_L + A_{1\,R}^v\, P_R)\, \slashed{q}_1\right] u(p_1) \tag{7.55}
\end{aligned}
$$

for the generic amplitude of the *s*-channel diagram. The form factors $A_{1,L,R}^{s,v}$ for the neutralino-squark-quark coupling and the coefficients $P_{L,R}^{s,v}$ of the loop corrected fermionic propagator are the same as in the case of a Higgs boson in the final state. The only new loop corrected coupling concerns the $\hat{B}$-coupling. The contributing loop diagrams, which give rise to the form factors $B_{0,\,L,R}^{s,v}$, $B_{1,\,L,R}^{s,v}$, and $B_{2,\,L,R}^{s,v}$ are depicted in Fig. 7.10(a).

The complex conjugated matrix element $\mathcal{M}_s^\dagger$ has to retain only the tree level, and can be written in the following simpler form

$$\mathcal{M}_s^\dagger = -\bar{u}(p_1)\, i\, [(A_{1\,R}^* P_L + A_{1\,L}^* P_R)]\, i\, \frac{\slashed{q}_1 + m}{q_1^2 - m_{q_1}^2}\, i\, [(B_R^* P_L + B_L^* P_R)]\, u(p_3)\, \epsilon_\nu(p_4) \tag{7.56}$$

The necessary tree-level couplings $A_{1\,L,R}^* = A_{ij}^{q_g\,L,R*}$ and $B_{L,R}^* = B^*$ are given in the Appendix A.

The correction to the $\hat{C}_{ii}$-coupling is in contrast to the $\hat{B}$-coupling not that complex, because in this case two scalars are involved instead of two fermions. Therefore, the topology of the form factors reduces to a simple form. The generic structure of the t-channel can thus be written as

$$\begin{aligned}\mathcal{M}_t =&\bar{u}(p_3)\, \epsilon_\mu^*(p_4) i\, [(A_{2\,L}^s\, P_L + A_{2\,R}^s\, P_R) + (A_{2\,L}^v\, P_L + A_{2\,R}^v\, P_R)\, \slashed{q}_2]\\ &\times \frac{i\,P}{q_2^2 - m_{q_2}^2}\, i\, [C^1(p_2 + q_2)^\mu + C^2(p_2 - q_2)^\mu]\, u(p_1).\end{aligned} \tag{7.57}$$

Again, the form factors $A_{2,L,R}^{s,v}$ and the propagator correction P are the same as for the Higgs final state. The contributing diagrams to the $\hat{C}_{ii}$-coupling are shown in Fig. 7.10(b).

The complex conjugated amplitude can be written similarly to the Higgs final state

$$\mathcal{M}_t^\dagger = -\bar{u}(p_1)\, i\, C^*\, \frac{i}{q_2^2 - m_{q_2}^2}\, i\, [A_{2\,R}^* P_L + A_{2\,L}^* P_R]\, u(p_3) \epsilon_\nu(p_4), \tag{7.58}$$

with $A_{2\,L,R}^* = A_{in}^{q_g\,L,R*}$ and $C^* = C_{ij}^*$.

The squared matrix elements are obtained by multiplying the above introduced conjugated and unconjugated amplitudes with each other.

The tree-level contribution as given in Eq. (7.49) can be again recovered from the generic structure. To this end, we set all vectorial form factors arising from couplings to. The scalar form factors are substituted for $A_{1\,L,R}^s = A_{ij}^{q_g\,L,R}$, and $B_{0\,L,R}^s = B$. The propagator form factors are set to $P_L^v = P_R^v = 1$ and $P_L^s = P_R^s = m_{q_1}$ in the s-channel. The tree level in the t-channel is retained by setting $A_{2\,L,R}^s = A_{in}^{q_g\,L,R}$, $C^1 = C_{ij}$ and $P = 1$, whereas the remaining coefficients are set to zero.

The squared matrix element containing all propagator and vertex corrections to the gluon final state, is obtained as given in Eq. (7.50) by plugging in the corresponding form factors. Throughout the whole calculation we used unitary gauge, such that the polarization sum reads $\sum_{polarization} \epsilon_\mu^*(p_4) \epsilon_\nu(p_4) = -g_{\mu\nu} + x_v p_4^\mu p_4^\nu$, with $x_v = 0$ for massless vector bosons and $x_v = 1/m_4^2$ for massive vector bosons.

The last remaining piece concerns the box diagrams. In total, seven different boxes contribute in case of the gluon final state. They are depicted in Fig. 7.10(c). Because of the vector boson in the final state we arrive at a complex structure for the box
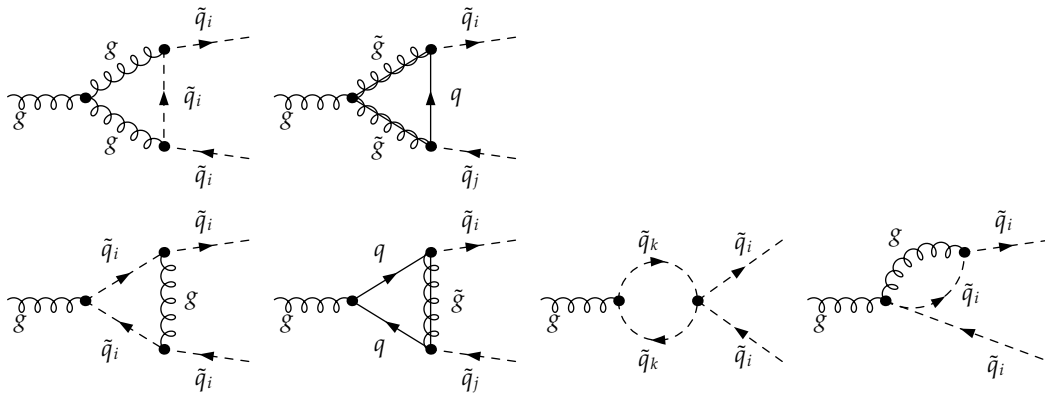
diagrams

$$
\begin{aligned}
\mathcal{M}_{\text{box}} =& \bar{u}(p_3)\, \epsilon_\mu^*(p_4) i \left[\gamma^\mu (B_{0\,L}'^s + B_{0\,L}'^v \not{p}_2) P_L + \gamma^\mu (B_{0\,R}'^s + B_{0\,R}'^v \not{p}_2) P_R \right. \\
& + p_1{}^\mu (B_{1\,L}'^s + B_{1\,L}'^v \not{p}_2) P_L + p_1{}^\mu (B_{1\,R}'^s + B_{1\,R}'^v \not{p}_2) P_R \\
& + p_2{}^\mu (B_{2\,L}'^s + B_{2\,L}'^v \not{p}_2) P_L + p_2{}^\mu (B_{2\,R}'^s + B_{2\,R}'^v \not{p}_2) P_R \\
& \left. + p_3{}^\mu (B_{3\,L}'^s + B_{3\,L}'^v \not{p}_2) P_L + p_3{}^\mu (B_{3\,R}'^s + B_{3\,R}'^v \not{p}_2) P_R \right] u(p_1),
\end{aligned} \tag{7.59}
$$

where we formulate everything in dependence on the momentum p_2, similar to the Higgs case. The whole squared matrix element is obtained according to Eq. (7.53).
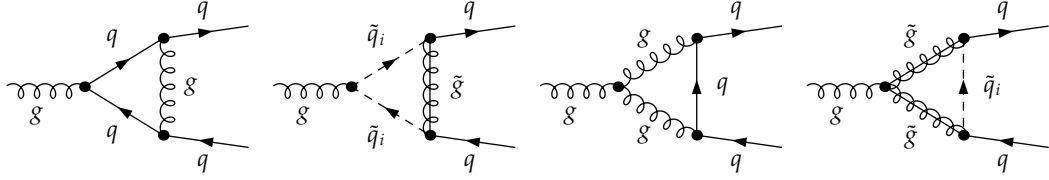
(a) Contributing vertex corrections to the gluon-quark-quark coupling $\hat{B}$, which appears in the s-channel. They give rise to the corresponding form factors $B_{0,\,L,R}^{s,v}$, $B_{1,\,L,R}^{s,v}$, and $B_{2,\,L,R}^{s,v}$.

(b) Contributing vertex corrections to the gluon-squark-squark coupling $\hat{C}_{ii}$, which occurs in the t-channel. The form factors are called C^1 and C^2.
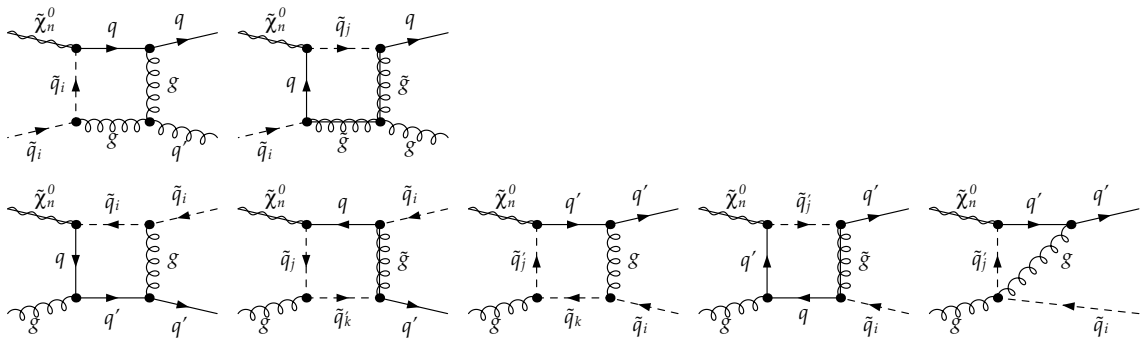
(c) All contributing box diagrams for a gluon in the final state, which give rise to the form factors $B_{0,\,L,R}^{\prime s,v}$, $B_{1,\,L,R}^{\prime s,v}$, $B_{2,\,L,R}^{\prime s,v}$, and $B_{3,\,L,R}^{\prime s,v}$.

Figure 7.10: Specific virtual corrections in case of a gluon in the final state.

7.3.3 Processes with an Electroweak Vector Boson in the Final State

Although the processes with the electroweak vector bosons have not been a dedicated part of this thesis, we want to mention them for completeness. Fig. 7.11 shows the naming convention which has been used for the calculation. In contrast to the processes with a gluon in the final state, also a u-channel exchange is possible for the Z^0 and $W^\pm$ boson. However, the u-channel is absent for the process involving a photon.
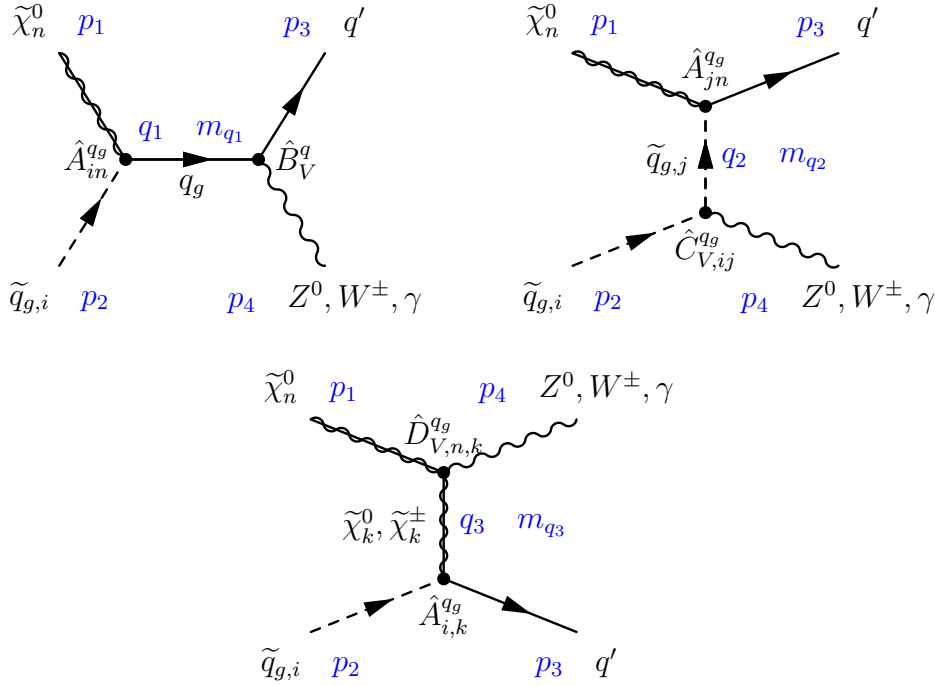
Figure 7.11: Definitions which have been used for the generic amplitudes with an electroweak vector boson in the final state. The contributing s-, t- and u-channel exchange is depicted. The u-channel exchange is absent in case of a photon in the final state.

As the generic loop structure for the electroweak vector bosons is the same as for the gluon in case of the s- and t-channel, we do not quote it again. The expressions can be taken over from Eqs. (7.55) to (7.58) of the previous section. The corresponding loop diagrams which give rise to the form factors are depicted in Fig. 7.12(a) and 7.12(b).

The additional amplitude of the u-channel can be be written as follows

$$
\begin{aligned}
\mathcal{M}_u =& \bar{u}(p_3)\,\epsilon_\mu^*(p_4) i \left[(A_{3\,L}^s\,P_L + A_{3\,R}^s\,P_R) + (A_{3\,L}^v\,P_L + A_{3\,R}^v\,P_R)\,\slashed{q}_3 \right] \\
& \times i\,\frac{(\slashed{q}_3 + m_{q_3})}{q_3^2 - m_{q_3}^2}\,i\,[D_L^s P_L + D_R^s P_R]\,u(p_1).
\end{aligned}
\tag{7.60}
$$

With a neutralino and a chargino, respectively, in the u-channel propagator, no SUSY-QCD propagator corrections arise. Also the neutralino-neutralino-Z^0 boson and neutralino-chargino-$W^\pm$-boson coupling, do not lead to radiative corrections. Therefore, only corrections to the vertex $\hat{A}_{i,k}^{q_g}$ have to be taken into account.
The corresponding complex conjugated amplitude can be written as

$$
\mathcal{M}_u^\dagger = \bar{u}(p_1)\,i\,[D_L^* P_L + D_R^* P_R]\,i\,\frac{(\slashed{q}_3 + m_{q_3})}{q_3^2 - m_{q_3}^2}\,i\,[(A_{3\,R}^* P_L + A_{3\,L}^* P_R)]\,u(p_3)\epsilon_\nu(p_4). \tag{7.61}
$$

Following the same principle as explained for the corrections to the processes involving a Higgs boson or a gluon, we can recover the tree level and calculate all propagator and vertex corrected matrix elements on the basis of this conventions.
All occurring box diagrams are depicted in Fig. 7.12(c). With the same underlying topology they can be calculated by the generic structure of Eq. (7.59).

Conclusions.   Altogether, we have finally obtained all virtual corrections including propagator corrections, vertex corrections and boxes. All permutations of generic amplitudes have been obtained by using `FORM` [198]. The form factors have been calculated and checked by using tools like `FeynCalc` [199] and `FormCalc` [200]. Independent cross checks ensure the viability of the implemented expressions in the code. The tree-level expressions have been additionally cross checked by comparing with the build-in `CalcHEP` version of `micrOMEGAs` [201].
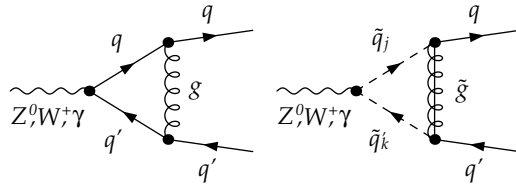
(a) Contributing vertex corrections to the quark-quark-electroweak vector boson coupling $\hat{B}_V^q$, which appears in the s-channel. They give rise to the corresponding form factors $B_{0,\,L,R}^{s,v}$, $B_{1,\,L,R}^{s,v}$, and $B_{2,\,L,R}^{s,v}$.
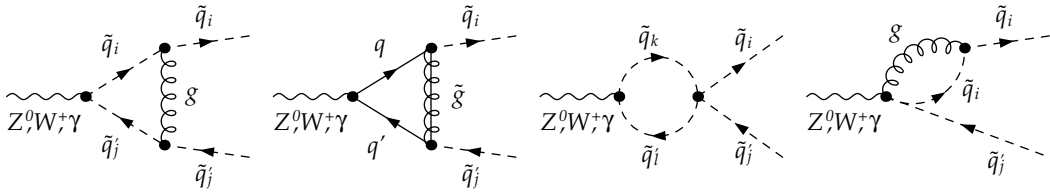
(b) Contributing vertex corrections to the squark-squark-electroweak vector boson coupling $\hat{C}_{V,ij}^{q_g}$, which occurs in the t-channel. The form factors are called C^1 and C^2.
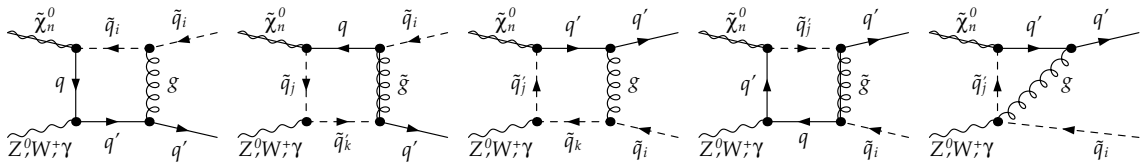
(c) Box diagrams in case of a Z boson, $W^\pm$ boson or photon in the final state.

Figure 7.12: Virtual corrections in case of an electroweak vector boson in the final state.

8 Renormalization

By working in D dimensions we have achieved to regularize all divergences in the one-loop corrections. However, for the final total cross section, we expect a finite result in the end. In order to give a physical meaning to the regularized loop contributions, renormalization is used, which absorbs the divergences into fields and parameters of the Lagrangian.

8.1 Principle of Renormalization

A common method is the multiplicative renormalization method, which is also used in this work. Basic introduction to renormalization can be found in Refs. [202, 203], further details are given in Refs. [204, 205]. As an introductory example we look at the scalar ϕ^4-theory

$$\mathcal{L}_{bare} = \frac{1}{2}\partial^\mu\phi_0\partial_\mu\phi_0 - \frac{m_0^2}{2}\phi_0^2 - \frac{\lambda_0}{4!}\phi_0^4. \tag{8.1}$$

In four dimensions the scalar field carries the mass dimension $[\phi_0] = 1$ and the quartic coupling $[\lambda_0] = 0$. Due to dimensional regularization we assume a D-dimensional Lagrangian such that the scalar field has dimension $[\phi_0] = \frac{D-2}{2}$. Thus, the coupling would now also be dependent on the dimension D with $[\lambda_0] = \frac{4-D}{2}$. In order to retain a dimensionless coupling, the parameter μ is introduced

$$\lambda_0 \rightarrow \lambda_0\mu^{\frac{4-D}{2}}. \tag{8.2}$$

This parameter is the so-called renormalization scale and was already introduced to retain the mass dimension of the loop integrals (cf. Eq. (7.9)).
Applying now multiplicative renormalization, we can absorb by rescaling the divergences which occurred in the calculation of the loop integrals in renormalization constants. These renormalization constants are used to rescale all bare fields, couplings and masses in the Lagrangian. For our example of Eq. (8.1), we can define

$$\phi_0 = \sqrt{Z_\phi}\,\phi \tag{8.3}$$
$$\lambda_0 = Z_\lambda\,\lambda \tag{8.4}$$
$$m_0^2 = Z_m\,m^2, \tag{8.5}$$

$$\longrightarrow \quad = \frac{i}{p^2 - m^2 + i\epsilon} \qquad \longrightarrow\!\!\times\!\!\longrightarrow \quad = i[(p^2 - m^2)\delta Z_\phi - m^2 \delta Z_m]$$

$$\times \quad = -i\lambda \qquad \times\!\!\!* \quad = -i(\delta Z_\lambda + 2\delta Z_\phi)$$

Figure 8.1: Overview of the Feynman rules for the ϕ^4-theory. On the left side the usual Feynman rules, on the right side the corresponding counterterm Feynman rules.

where Z_i are the multiplicative renormalization factors. In perturbation theory we can write

$$\phi_0 = (1 + \frac{1}{2}\delta Z_\phi)\,\phi \tag{8.6}$$

$$\lambda_0 = (1 + \frac{1}{2}\delta Z_\lambda)\,\lambda \tag{8.7}$$

$$m_0^2 = (1 + \delta Z_m)\,m^2 \equiv= 1 + \delta m^2. \tag{8.8}$$

Putting this in the bare Lagrangian of Eq. (8.1), we arrive at

$$\mathcal{L}_{bare} = \frac{1}{2}\partial^\mu\phi\partial_\mu\phi - \frac{m^2}{2}\phi^2 - \frac{\lambda}{4!}\phi^4 \tag{8.9}$$

$$+ \frac{1}{2}\delta Z_\phi\partial^\mu\phi\partial_\mu\phi - (\delta Z_m + \delta Z_\phi)\frac{m^2}{2}\phi^2 - (\delta Z_\lambda + 2\delta Z_\phi)\frac{\lambda}{4!}\phi^4 + \mathcal{O}(\delta Z^2)$$

$$= \mathcal{L}_{ren} + \mathcal{L}_{ct}, \tag{8.10}$$

where the first three terms belong to the renormalized Lagrangian and the remainder to the counterterm Lagrangian which absorbs the divergences. Within a one-loop calculation, we do not have to consider terms proportional to $\mathcal{O}(\delta Z^2)$.

We can see that the counterterm Lagrangian gives rise to similar Feynman rules like the original Lagrangian. They are depicted in Fig. 8.1. However, the occurring counterterms are not uniquely defined. Therefore, different approaches for their determination exist in literature. In the following, we want to mention two conceptionally different ones: the $\overline{\text{DR}}$ and the on-shell renormalization scheme.

$\overline{\text{DR}}$ **Renormalization Scheme.** To work out the differences between, the $\overline{\text{DR}}$ renormalization scheme and the on-shell renormalization scheme, we focus on the following example: the derivation of the mass counterterm δZ_m of the above introduced ϕ^4-Lagrangian. To this end, we consider the corrections to the propagator. Fig. 8.2 shows the different parts contributing to the one-loop corrected propagator: the leading order propagator, the one-loop correction and the corresponding counterterm contribution.
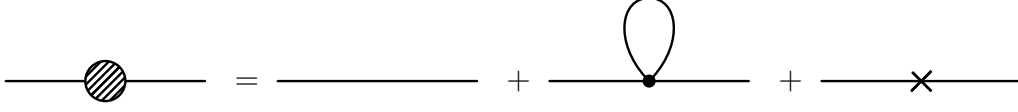
Figure 8.2: Contributions to the full next-to-leading order propagator: Leading order propagator, one-loop correction and counterterm contribution.

Thus, we arrive at one-loop level at

$$\frac{i}{p^2 - m^2} + \frac{i}{p^2 - m^2}\left(-i\Sigma(p^2)\right)\frac{i}{p^2 - m^2} = \frac{i}{p^2 - m^2}\left(1 + \frac{\Sigma(p^2)}{p^2 - m^2}\right) \qquad (8.11)$$

with $\Sigma(p^2)$ being the mass correction consisting of the one-loop correction and the corresponding counterterm:

$$-i\Sigma(p^2) = -i\frac{\lambda}{2}\frac{1}{16\pi^2}A_0(m^2) + i\Big[(p^2 - m^2)\delta Z_\phi - m^2\delta Z_m\Big]. \qquad (8.12)$$

The scalar self energy is given by the loop function A_0. The counterterm we can read off Eq. (8.10) or take it directly from Fig. 8.1. As the scalar loop integral is independent of the momentum p, we can set $\delta Z_\phi = 0$ without violating generality. This is a special feature of the ϕ^4 theory.

Considering the definition of A_0 in Eq. (7.15) we obtain the following expression

$$-i\Sigma(p^2) = -i\frac{\lambda}{2}\frac{m^2}{16\pi^2}\left[\frac{1}{\varepsilon} - \gamma_E + \ln 4\pi - \ln\left(\frac{m^2 - i\epsilon}{\mu^2} + 1\right)\right] - im^2\delta Z_m. \qquad (8.13)$$

In the dimensional reduction scheme the counterterm is defined to subtract only the pure divergence without any finite terms. Therefore, we can directly read off the DR mass counterterm from Eq. (8.13). The DR counterterm and the corresponding mass correction are given by

$$\Rightarrow \delta Z_m^{\text{DR}} = -\frac{\lambda}{32\pi^2}\frac{1}{\varepsilon} \quad \Rightarrow \quad \Sigma(p^2) = \frac{\lambda m^2}{32\pi^2}\left[-\gamma_E + \ln 4\pi + 1 - \ln\left(\frac{m^2 - i\epsilon}{\mu^2}\right)\right]. \qquad (8.14)$$

The $\overline{\text{DR}}$ counterterm, however, does not substract only the pure divergence, but the whole Δ_{UV}-term as defined in Eq. (7.16). Thus, the counterterm and the corresponding mass correction in the $\overline{\text{DR}}$ scheme can be expressed as

$$\Rightarrow \delta Z_m^{\overline{\text{DR}}} = -\frac{\lambda}{32\pi^2}\Delta \quad \Rightarrow \quad \Sigma(p^2) = \frac{\lambda m^2}{32\pi^2}\left[1 - \ln\left(\frac{m^2 - i\epsilon}{\mu^2}\right)\right]. \qquad (8.15)$$

For both kinds of counterterms, we see that the corrected mass is dependent on the renormalization scale μ. For dimensional regularization, the corresponding scheme is called `MS`- or $\overline{\text{MS}}$ renormalization scheme (minimal subtraction).

On-shell Renormalization Scheme.   Another approach of renormalization is the so-called on-shell scheme. Especially for particles, which are directly measurable like the top quark, this method is often used. The key ansatz is that the renormalized mass should be the physical mass such that it does not obtain any mass corrections. To this end, the following two renormalization conditions have to be fulfilled

$$\left. \text{Re}\, \Sigma(p^2) \right|_{p^2=m^2} = 0 \tag{8.16}$$

$$\lim_{p^2 \to m^2} \frac{1}{p^2 - m^2} \Sigma(p^2) = 1. \tag{8.17}$$

The first condition requires the renormalized mass to be the physical mass, i.e. the real part of the propagator's pole. The second condition asks for the residuum to be one. Performing a Taylor series of the mass correction around the pole mass

$$\Sigma(p^2) = \left. \Sigma(p^2) \right|_{p^2=m^2} + \left. \frac{d^2}{dp^2} \Sigma(p^2) \right|_{p^2=m^2} (p^2 - m^2) + \ldots, \tag{8.18}$$

and considering the first renormalization condition of Eq. (8.17) we get another condition

$$\left. \frac{d^2}{dp^2} \Sigma(p^2) \right|_{p^2=m^2} = 0. \tag{8.19}$$

However, as our example in the simple ϕ^4-theory is momentum independent, the on-shell mass counterterm is merely defined by Eq. (8.16) such that the corresponding on-shell mass counterterm reads

$$\Rightarrow \delta Z_m^{OS} = -\frac{\lambda}{32\pi^2} \left[\Delta + 1 - \ln\left(\frac{m^2 - i\epsilon}{\mu^2} \right) \right] \quad \Rightarrow \quad \Sigma(p^2) = 0. \tag{8.20}$$

Within this renormalization scheme, the renormalized mass corresponds exactly to the physical mass, and receives no mass corrections. In contrast to the `DR` scheme, the mass counterterm contains besides the divergence also finite terms.

8.2 Choice of Renormalization Scheme

Having the building blocks of renormalization in mind, we can think of a proper renormalization scheme for our studied processes. As we aim to provide the one-loop calculation of neutralino-squark coannihilation together with the other possible (co)annihilation processes as one common package which can be linked to public dark matter tools, we have to guarantee the viability of the renormalization scheme over a large region of the MSSM parameter space.

However, it is difficult to define a renormalization scheme for both, the bottom (s)quark sector and the top (s)quark sector at the same time that behaves well for the whole parameter space.

As the physical mass of the top quark is directly measurable in experiments and does not form bound states like the bottom quark, it seems appropriate to use its physical (on-shell) mass in the calculations and renormalize it in the on-shell scheme. The bottom quark, however, cannot be measured directly and forms hadrons such that we treat it in the $\overline{\text{DR}}$ scheme.

Because of having top squarks (and potentially bottom squarks) as external particles, the on-shell scheme is applied for the squark sector. A careful treatment is in particular needed for the trilinear coupling of the bottom quark A_b. This issue has been already discussed in literature, see for instance Refs. [206–209]. Using an on-shell renormalization scheme for A_b, we end up with the following renormalization constant δA_b

$$\delta A_b = \frac{1}{m_b}\Big[-(A_b - \mu^* \tan\beta)\,\delta m_b + \dots\Big]. \tag{8.21}$$

It is obvious that for parameter regions with $\mu \tan\beta \gg A_b$, the counterterm receives a large shift and thus, give rise to large corrections of A_b (see e.g. Ref. [207]). This results also in huge corrections to the lightest Higgs mass, which was shown in Ref. [206]. Therefore, we define the counterterms of the trilinear couplings in the $\overline{\text{DR}}$ scheme. With the Higgs-squark-squark coupling playing an important role in the coannihilation process with a Higgs boson in the final state, we define the trilinear couplings further as input parameters.

Altogether, we use a hybrid on-shell/$\overline{\text{DR}}$ renormalization scheme, which is set up in such a way that it minimizes potential problems with sensitive parameters. Similar renormalization schemes for the quark and squark sectors of the MSSM were already discussed and studied in Refs. [207, 210]. Compared to those approaches, however, our renormalization scheme differs significantly in the treatment of the squark mixing angles θ_t and θ_b, which will be discussed later in more detail. But still, our scheme shares some important features with the RS2 scheme which was introduced in Ref. [207].

In the following, we discuss in more detail the used hybrid on-shell/$\overline{\text{DR}}$ renormalization scheme with the renormalization and factorization scales set to $\mu = \sqrt{m_{\tilde{t}_1} m_{\tilde{t}_2}}$.

Starting with the quark sector, we discuss then the squark sector to close with the discussion of the α_s counterterm, which occur in the vertex counterterms of the gluon final state.

8.3 Quark Sector

8.3.1 Wave Function Renormalization Constants and Mass Counterterms

First, we focus on the renormalization of the quark sector, where we take into account mixing for the time being. The parameters to be renormalized are the quark fields and masses. To do so, we consider the bare Lagrangian

$$\mathcal{L}_0 = \bar{q}_{0,j}\delta_{ij}(i\slashed{\partial} - m_{0,q_i})q_{0,i} \tag{8.22}$$

and can substitute as discussed before, the unrenormalized fields and masses by their renormalized expressions and their corresponding counterterms

$$q_{0,i} \to (\delta_{ij} + \frac{1}{2}\delta Z_{ij}^L P_L + \frac{1}{2}\delta Z_{ij}^R P_R)q_j \tag{8.23}$$

$$m_{0,q_i} \to m_{q_i} + \delta m_{q_i}, \tag{8.24}$$

with $\delta Z_{ij}^{L,R}$ being the quark wave function renormalization constants and δm_{q_i} the quark mass counterterm. The renormalized one-particle irreducible two-point function of the quark is given by

$$\hat{\Gamma}_{ij} = \delta_{ij}(\slashed{k} - m_{q_i}) + \hat{\Pi}_{ij}(k^2) \tag{8.25}$$

$$\mathcal{M} = i\bar{u}_i(k)\hat{\Gamma}_{ij}u_j(k), \tag{8.26}$$

with $\hat{\Pi}_{ij}(k)$ being the renormalized self-energy and $\mathcal{M}$ defining its matrix element. The physical propagator is obtained by inverting the two-point Green's function $i(\hat{\Gamma}_{ij})^{-1}$. According to the usual fermionic propagator structure the renormalized self-energy can be written in the following generic form

$$\hat{\Pi}_{ij}(k^2) = \slashed{k}P_L\hat{\Pi}_{ij}^L(k^2) + \slashed{k}P_R\hat{\Pi}_{ij}^R(k^2) + P_L\hat{\Pi}_{ij}^{S,L}(k^2) + P_R\hat{\Pi}_{ij}^{S,R}(k^2), \tag{8.27}$$

where $\hat{\Pi}^{L,R}(k^2)$ and $\hat{\Pi}^{SL,SR}(k^2)$ stand for the vector and the scalar parts of the two-point Green's function. Again, the hat on the the self energy contributions marks

the parameters containing renormalized parameters and their counterterms

$$\hat{\Pi}_{ij}^{L/R} = \Pi_{ij}^{L/R} + \frac{1}{2}\left(\delta Z_{ij}^{L/R} + \delta Z_{ji}^{L/R\dagger}\right) \tag{8.28}$$

$$\hat{\Pi}_{ij}^{S,L/R} = \Pi_{ij}^{S,L/R} - \frac{1}{2}\left(m_{q_i}\delta Z_{ij}^{L/R} + m_{q_j}\delta Z_{ji}^{R/L\dagger}\right) - \delta_{ij}\delta m_{q_i}. \tag{8.29}$$

The two on-shell conditions read

$$\left.\mathrm{Re}\,\hat{\Pi}_{ij}(k^2)u_j(k)\right|_{k^2=m_{q_j}^2} = 0 \tag{8.30}$$

$$\lim_{k^2\to m_{q_i}^2}\frac{1}{\slashed{k}^2 - m_{q_i}^2}\mathrm{Re}\,\hat{\Pi}_{ii}(k^2)u_i(k) = u_i(k). \tag{8.31}$$

The first condition ensures that the pole mass corresponds to the particle's physical mass such that it does not obtain any loop corrections. Thus, it fixes the off-diagonal elements and the mass counterterm. The second condition, however, fixes the diagonal elements and care for a proper normalization by requiring the residuum to be one.

Applying these conditions on Eq. (8.27) together with considering Eqs. (8.29), we obtain the following expressions for the quark wave function renormalization constants and the mass counterterm.

$$\delta Z_{ij}^{L/R} = \frac{2}{m_{q_i}^2 - m_{q_j}^2}\mathrm{Re}\,\left\{m_{q_j}^2\Pi_{ij}^{L/R}(m_{q_j}^2) + m_{q_i}m_{q_j}\Pi_{ij}^{S,L/R}(m_{q_j}^2)\right.$$
$$\left. + m_{q_j}\Pi_{ij}^{S,R/L} + m_{q_i}\Pi_{ij}^{S,L/R}\right\}, i \neq j \tag{8.32}$$

$$\delta Z_{ii}^{L/R} = \mathrm{Re}\,\left\{-\Pi_{ii}^{L/R}(m_{q_i}^2) + \frac{1}{2m_{q_i}}\left[\Pi_{ii}^{S,L/R}(m_{q_i}^2) - \Pi_{ii}^{S,R/L}(m_{q_i}^2)\right]\right.$$
$$\left.\left. - m_{q_i}\frac{\partial}{\partial k^2}\left[m_{q_i}\left(\Pi_{ii}^{L/R}(k^2) + \Pi_{ii}^{R/L}(k^2)\right) + \Pi_{ii}^{S,L/R}(k^2) + \Pi_{ii}^{S,R/L}(k^2)\right]\right\}\right|_{k^2=m_{q_i}^2} \tag{8.33}$$

$$\delta m_{q_i} = \frac{1}{2}\mathrm{Re}\,\left\{m_{q_i}\left[\Pi_{ii}^L(m_{q_i}^2) + \Pi_{ii}^R(m_{q_i}^2)\right] + \Pi_{ii}^{S,L}(m_{q_i}^2) + \Pi_{ii}^{S,R}(m_{q_i}^2)\right\} \tag{8.34}$$

As we consider in our work only third generation quarks, quark mixing does not have to be considered. Thus, we set $i = j$ and neglect the indices in the following. For each chirality eigenstate of the quark we obtain one counterterm $\delta Z_{L,R}$

$$\begin{pmatrix} q_L \\ q_R \end{pmatrix} \to \begin{pmatrix} 1 + \frac{1}{2}\delta Z_L & 0 \\ 0 & 1 + \frac{1}{2}\delta Z_R \end{pmatrix}\begin{pmatrix} q_L \\ q_R \end{pmatrix}, \tag{8.35}$$

with $\delta Z_{L,R}$ given by Eq. (8.33) with $q = t, b$.

As the top quark mass is physically directly measurable and does not form any

bound states we renormalize it in the on-shell scheme such that the top quark mass counterterm is according to Eq. (8.34) given by

$$\delta m_t^{\mathtt{OS}} = \frac{1}{2} \mathrm{Re} \Big\{ m_t \Big[\Pi^L(m_t^2) + \Pi^R(m_t^2) \Big] + \Pi^{SL}(m_t^2) + \Pi^{SR}(m_t^2) \Big\} . \qquad (8.36)$$

In our calculation we use the physical (on-shell) top quark mass of $m_t = 173.1$ GeV.

8.3.2 Specific Treatment of the Bottom Mass

Due to the aforementioned reasons, in contrast to the top quark mass, we do not renormalize the bottom quark mass within the on-shell renormalization scheme, but use the $\overline{\mathrm{DR}}$ scheme. As the bottom quark mass is not directly experimentally accessible, the mass parameter $m_b(m_b)$ is extracted in the $\overline{\mathrm{MS}}$ renormalization scheme from Standard Model analysis of the Υ sum rules (for more details see, e.g. Ref. [211–214]). In order to obtain the bottom quark mass in the $\overline{\mathrm{DR}}$ renormalization scheme within the MSSM, some recalculation steps have to be performed. An overview is depicted in Eq. (8.37).

$$m_b^{\overline{\mathrm{MS}},\,\mathtt{SM}}(m_b) \xrightarrow[\text{running}]{\text{SM NNLO}} m_b^{\overline{\mathrm{MS}},\,\mathtt{SM}}(Q) \xrightarrow{\text{conversion}} m_b^{\overline{\mathrm{DR}},\,\mathtt{SM}}(Q) \xrightarrow[\text{corrections}]{\text{threshold}} m_b^{\overline{\mathrm{DR}},\,\mathtt{MSSM}}(Q) \quad (8.37)$$

Starting with the bottom mass at its own mass scale $m_b(m_b)$, we use the Standard Model next-to-next-to-leading order (NNLO) renormalization group running to obtain the bottom quark mass at an arbitrary scale Q [215]. The so obtained mass $m_b^{\overline{\mathrm{MS}},\,\mathtt{SM}}(Q)$ can then be recalculated in the $\overline{\mathrm{DR}}$ scheme [215]. As a last step, we then take account for threshold corrections Δm_b, which the mass receives when going from the SM to the MSSM.

$$m_b^{\overline{\mathrm{DR}},\,\mathtt{MSSM}}(Q) = m_b^{\overline{\mathrm{DR}},\,\mathtt{SM}}(Q) - \Delta m_b . \qquad (8.38)$$

Having calculated the $\overline{\mathrm{DR}}$ mass of the bottom quark, we can write its corresponding counterterm as

$$\delta m_b^{\overline{\mathrm{DR}}} = (-2) \frac{\alpha_s C_F}{4\pi} m_b^{\overline{\mathrm{DR}}} \Delta . \qquad (8.39)$$

8.3.3 Resummed Corrections to the Higgs-Quark-Quark Yukawa Coupling

A prominent place where quark masses enter our calculation is through the Yukawa coupling of the Higgs bosons to quarks. Especially, the Yukawa couplings to the bottom quarks were precisely studied through Standard Model decays of Higgs bosons into massive bottom quarks. QCD and top quark induced corrections to the Yukawa coupling were calculated up to $\mathcal{O}(\alpha_s^4)$ [216–218] and can be used in terms of an

effective Yukawa coupling for each neutral Higgs boson $\Phi = h^0, H^0, A^0$ defined as

$$\left[h_b^{\overline{\text{MS}},\text{QCD},\Phi}(Q)\right]^2 = \left[h_b^{\overline{\text{MS}},\Phi}(Q)\right]^2 \left[1 + \Delta_{\text{QCD}} + \Delta_t^\Phi\right]. \tag{8.40}$$

The usual $\overline{\text{MS}}$-Yukawa coupling of a Higgs boson to bottom quarks is denoted by $\left(h_b^{\overline{\text{MS}},\Phi}\right)(Q)$ and is corrected by the QCD corrections Δ_{QCD} and the top quark induced corrections Δ_t^Φ. The QCD corrections Δ_{QCD} are explicitly given by

$$
\begin{aligned}
\Delta_{\text{QCD}} \quad &= \frac{\alpha_s(Q)}{\pi} C_F \frac{17}{4} + \frac{\alpha_s^2(Q)}{\pi^2}\left[35.94 - 1.359\, n_f\right] \\
&+ \frac{\alpha_s^3(Q)}{\pi^3}\left[164.14 - 25.77\, n_f + 0.259\, n_f^2\right] \\
&+ \frac{\alpha_s^4(Q)}{\pi^4}\left[39.34 - 220.9\, n_f + 9.685\, n_f^2 - 0.0205\, n_f^3\right],
\end{aligned}
\tag{8.41}
$$

where n_f accounts for the number of flavours which are taken into account. The top-quark induced corrections Δ_t^Φ for each Higgs boson Φ read

$$\Delta_t^h = c_h(Q)\left[1.57 - \frac{2}{3}\log\frac{Q^2}{m_t^2} + \frac{1}{9}\log^2\frac{m_b^2(Q)}{Q^2}\right], \tag{8.42}$$

$$\Delta_t^H = c_H(Q)\left[1.57 - \frac{2}{3}\log\frac{Q^2}{m_t^2} + \frac{1}{9}\log^2\frac{m_b^2(Q)}{Q^2}\right], \tag{8.43}$$

$$\Delta_t^A = c_A(Q)\left[\frac{23}{6} - \log\frac{Q^2}{m_t^2} + \frac{1}{6}\log^2\frac{m_b^2(Q)}{Q^2}\right], \tag{8.44}$$

with

$$\left\{c_h(Q), c_H(Q), c_A(Q)\right\} = \frac{\alpha_s^2(Q)}{\pi^2}\left\{\frac{1}{\tan\alpha\tan\beta}, \frac{\tan\alpha}{\tan\beta}, \frac{1}{\tan^2\beta}\right\} \tag{8.45}$$

defining the prefactor of each correction.

So far we have only considered corrections arising within the Standard Model. However, also in the MSSM the Higgs-bottom quark coupling can receive large corrections for large $\tan\beta$ or large A_b even beyond next-to-leading order. As these known effects can affect our performed analysis, we include also these corrections that can be resummed to all orders of perturbation theory in our calculation [219, 220]. With Δ_b being the resummable part we can redefine the already corrected Yukawa coupling

$h_b^{\overline{\text{MS}},\text{QCD},\Phi}(Q)$ of Eq. (8.40) by

$$h_b^{\text{MSSM},h}(Q) = \frac{h_b^{\overline{\text{MS}},\text{QCD},h}(Q)}{1 + \Delta_b}\left[1 - \frac{\Delta_b}{\tan\alpha\tan\beta}\right], \qquad (8.46)$$

$$h_b^{\text{MSSM},H}(Q) = \frac{h_b^{\overline{\text{MS}},\text{QCD},H}(Q)}{1 + \Delta_b}\left[1 + \Delta_b\frac{\tan\alpha}{\tan\beta}\right], \qquad (8.47)$$

$$h_b^{\text{MSSM},A}(Q) = \frac{h_b^{\overline{\text{MS}},\text{QCD},A}(Q)}{1 + \Delta_b}\left[1 - \frac{\Delta_b}{\tan^2\beta}\right]. \qquad (8.48)$$

For our calculation we use the above defined resummed Yukawa couplings. However, as we already provide a full next-leading-order calculation we exclude all QCD and SUSY-QCD corrections arising from one-loop order, as they are already present in our calculation.

As already mentioned, `MicrOMEGAs` takes into account some effective couplings in the calculation of the (co)annihilation cross sections. The above introduced effective Higgs-bottom quark couplings of Eqs. 8.46–8.48 are according to Ref. [134] the only corrected parameters with direct impact on the cross section, which are implemented within `MicrOMEGAs` so far. Loop corrected sparticle masses and their corresponding mixing matrix elements are taken over from a chosen mass spectrum calculator, like `SPheno`, `Suspect`, `Isajet` or `SOFTSUSY`.

8.4 Squark Sector

After having discussed the renormalization of the quark sector, we focus now on the corresponding supersymmetric sector. Similarly to the fermionic case we can derive the wave function renormalization constants for the squarks. Again, we constrain ourselves to the third generation, i.e. to stops and sbottoms.

To derive the squark wave function renormalization constants we start from the scalar bare Lagrangian

$$\mathcal{L}_0 = \bar{\tilde{q}}_{0,j}\delta_{ij}(i\slashed{\partial} - m_{\tilde{q}_{0,i}})\tilde{q}_{0,i} \qquad (8.49)$$

and substitute the bare fields and masses by their renormalized parameters and the corresponding counterterms

$$\tilde{q}_{0,i} \rightarrow (\delta_{ij} + \frac{1}{2}\delta Z_{ij})\tilde{q}_j \qquad (8.50)$$

$$m_{\tilde{q}_{0,i}} \rightarrow m_{\tilde{q}_i} + \delta m_{\tilde{q}_i}, \qquad (8.51)$$

with δZ_{ij} being the squark wave function renormalization constant and $\delta m_{\tilde{q}_i}$ denot-

ing the mass counterterm. Hereby, we work in the mass eigenstate basis indicated by the indices i, j. Again, we define an one-particle irreducible two-point function $\hat{\Gamma}_{ij}$ as

$$\hat{\Gamma}_{ij} = \delta_{ij}(k^2 - m_{\tilde{q}_i}^2) + \hat{\Pi}_{ij}(k^2) \tag{8.52}$$

$$\mathcal{M} = i\hat{\Gamma}_{ij} \tag{8.53}$$

with its corresponding matrix element $\mathcal{M}$. The one-loop corrected self energy $\hat{\Pi}_{ij}(k^2)$ can be written as

$$\hat{\Pi}_{ij}(k^2) = \Pi_{ij}(k^2) + \frac{1}{2}(k^2 - m_{\tilde{q}_i}^2)\delta Z_{ij} + \frac{1}{2}(k^2 - m_{\tilde{q}_j}^2)\delta Z_{ji}^* - \delta_{ij}\delta m_{\tilde{q}_i}^2, \tag{8.54}$$

where $\Pi_{ij}(k^2)$ depicts the renormalized self energy and the remainder the corresponding counterterms. Considering the usual on-shell renormalization conditions

$$\operatorname{Re}\hat{\Pi}_{ij}(k)\Big|_{k^2=m_{\tilde{q}_j}^2} = 0 \tag{8.55}$$

$$\lim_{k^2 \to m_{\tilde{q}_i}^2} \frac{1}{k^2 - m_{q_i}^2}\operatorname{Re}\hat{\Pi}_{ii}(k) = 1, \tag{8.56}$$

we obtain the following expression for the squark counterterms

$$\delta Z_{ij} = \frac{2}{m_{\tilde{q}_i}^2 - m_{\tilde{q}_j}^2}\operatorname{Re}\Pi_{ij}(m_{\tilde{q}_j}^2), i \neq j \tag{8.57}$$

$$\delta Z_{ii} = -\operatorname{Re}\frac{\partial}{\partial k^2}\Pi_{ii}(k^2)\Big|_{k^2=m_{\tilde{q}_i}^2} \tag{8.58}$$

$$(\delta m_{\tilde{q}_i}^2)^{\mathsf{OS}} = \operatorname{Re}\Pi_{ii}(m_{\tilde{q}_i}^2). \tag{8.59}$$

However, the renormalization of the squark masses and connected parameters is more complicated than discussed until now, as the gauge eigenstates of the third generation squarks mix. At tree level the squark masses $m_{\tilde{q}_i}^2$ in the mass eigenstate basis are obtained by diagonalization of the squark mixing matrix

$$\begin{pmatrix} m_{\tilde{q}_1}^2 & 0 \\ 0 & m_{\tilde{q}_2}^2 \end{pmatrix} = \tag{8.60}$$

$$U^{\tilde{q}}\begin{pmatrix} M_{\tilde{Q}}^2 + (I_q^{3L} - e_q\,s_W^2)\cos 2\beta\,m_Z^2 + m_q^2 & m_q\big(A_q - \mu\,(\tan\beta)^{-2I_q^{3L}}\big) \\ m_q\big(A_q - \mu\,(\tan\beta)^{-2I_q^{3L}}\big) & M_{\{\tilde{U},\tilde{D}\}}^2 + e_q\,s_W^2\cos 2\beta\,m_Z^2 + m_q^2 \end{pmatrix}(U^{\tilde{q}})^{\dagger},$$

where e_q is the fractional charge of the squark in units of e, s_W is the sine of the weak mixing angle, and I_q^{3L} is the weak isospin of the squark. The squark mixing matrix is given by $U^{\tilde{q}}$, the soft breaking parameter are $M_{\tilde{Q}}^2, M_{\tilde{U}}^2, M_{\tilde{D}}^2$, and the trilinear couplings are denoted by A_t, A_b. Due to the $SU(2)$ symmetry the stop and

sbottom sector is connected through the common breaking parameter $M_{\tilde{Q}}^2$ such that it has to be renormalized together.

Considering the relation of Eq. (8.60), we end up with in total eleven free parameters $(M_{\tilde{Q}}^2, M_{\tilde{U}}^2, M_{\tilde{D}}^2, A_t, A_b, \theta_{\tilde{t}}, \theta_{\tilde{b}}, m_{\tilde{t}_1}^2, m_{\tilde{t}_2}^2, m_{\tilde{b}_1}^2, m_{\tilde{b}_2}^2)$, where five of those are completely independent. In order to fix the renormalization of the squark sector we have to select five independent input parameters. For this choice it is important that the renormalization scheme is applicable not only for the case of neutralino-stop coannihilation, but also for all the other annihilation and coannihilation processes which should be covered by our package `DM@NLO`.

As neutralino-stop coannihilation is extremely sensitive to the lightest stop mass $m_{\tilde{t}_1}^2$ and this mass plays also an important role in the t-channel exchange of neutralino annihilations (cf. [157]) it is quite obvious that the lightest stop mass is chosen as input-parameter and is treated on-shell. Furthermore, we treat also $m_{\tilde{b}_1}^2$ and $m_{\tilde{b}_2}^2$ as input parameter. By contrast, the heaviest squark mass $m_{\tilde{t}_2}^2$, which is less prone to receive large corrections, we treat as dependent parameter.

As already mentioned before, the trilinear couplings A_t, A_b play a crucial role in the neutralino-stop coannihilation processes with a Higgs boson in the final state. Therefore, it is quite natural to treat them also as input parameters. Due to huge shifts, which can appear when treating the trilinear coupling A_b on-shell (see Eq. (8.21)), we choose to define both, A_t and A_b in the $\overline{\text{DR}}$ scheme [206–209]. Another approach would be to define these parameters in the on-shell scheme, e.g. through the decay process of a squark into squark and a Higgs boson as done in [210]. This, however, would require a dedicated treatment of the infrared divergences arising in such a calculation.

To summarize, we have chosen in our hybrid on-shell-$\overline{\text{DR}}$ renormalization scheme the following parameters as input parameters

$$(m_{\tilde{t}_1}^2)^{\text{OS}}, (m_{\tilde{b}_1}^2)^{\text{OS}}, (m_{\tilde{b}_2}^2)^{\text{OS}}, A_t^{\overline{\text{DR}}}, A_b^{\overline{\text{DR}}}, \tag{8.61}$$

whereas

$$m_{\tilde{t}_2}^2, \theta_{\tilde{t}}, \theta_{\tilde{b}}, M_{\tilde{Q}}^2, M_{\tilde{U}}^2, M_{\tilde{D}}^2 \tag{8.62}$$

are dependent parameters.

As a next step we have to specify the counterterms of the input parameters. The counterterms for the on-shell masses $(m_{\tilde{t}_1}^2)^{\text{OS}}, (m_{\tilde{b}_1}^2)^{\text{OS}}, (m_{\tilde{b}_2}^2)^{\text{OS}}$ are defined according to Eq. (8.59) as follows

$$(\delta m_{\tilde{q}_i}^2)^{\text{OS}} = \text{Re}\Pi_{ii}(m_{\tilde{q}_i}^2), \quad \text{with} \quad \tilde{q}_i = \tilde{t}_1, \tilde{b}_1, \tilde{b}_2. \tag{8.63}$$

The corresponding $\overline{\text{DR}}$ counterterm of the trilinear couplings can be written as

$$\delta A_{\tilde{q}}^{\overline{\text{DR}}} = \frac{1}{m_q} \left[U_{11}^{\tilde{q}} U_{12}^{\tilde{q}} (\delta m_{\tilde{q}_1}^2)^{\overline{\text{DR}}} + U_{21}^{\tilde{q}} U_{22}^{\tilde{q}} (\delta m_{\tilde{q}_2}^2)^{\overline{\text{DR}}} \right.$$
$$+ \left(U_{21}^{\tilde{q}} U_{12}^{\tilde{q}} + U_{11}^{\tilde{q}} U_{22}^{\tilde{q}} \right) \left(m_{\tilde{q}_1}^2 - m_{\tilde{q}_2}^2 \right) \delta\theta_{\tilde{q}}^{\overline{\text{DR}}}$$
$$\left. - \frac{\delta m_q^{\overline{\text{DR}}}}{m_q} \left(U_{11}^{\tilde{q}} U_{12}^{\tilde{q}} m_{\tilde{q}_1}^2 + U_{21}^{\tilde{q}} U_{22}^{\tilde{q}} m_{\tilde{q}_2}^2 \right) \right], \tag{8.64}$$

with the necessary $\overline{\text{DR}}$ counterterms of the squark masses and their mixing angles defined by

$$(\delta m_{\tilde{q}_i}^2)^{\overline{\text{DR}}} = \frac{\alpha_s C_F}{4\pi} \Delta \left[\left((U_{i1}^{\tilde{q}})^2 - (U_{i2}^{\tilde{q}})^2 \right)^2 m_{\tilde{q}_i}^2 - m_{\tilde{q}_i}^2 + \left(U_{21}^{\tilde{q}} U_{11}^{\tilde{q}} - U_{22}^{\tilde{q}} U_{12}^{\tilde{q}} \right)^2 m_{\tilde{q}_j}^2 \right.$$
$$\left. + 8 m_q m_{\tilde{g}} U_{i1}^{\tilde{q}} U_{i2}^{\tilde{q}} - 4 m_{\tilde{g}}^2 - 4 m_q^2 \right], \tag{8.65}$$

$$\delta\theta_{\tilde{q}}^{\overline{\text{DR}}} = \frac{\alpha_s C_F}{4\pi} \Delta \frac{1}{(m_{\tilde{q}_1}^2 - m_{\tilde{q}_2}^2)} \left[\left(U_{21}^{\tilde{q}} U_{11}^{\tilde{q}} - U_{22}^{\tilde{q}} U_{12}^{\tilde{q}} \right) \left(\left((U_{11}^{\tilde{q}})^2 - (U_{12}^{\tilde{q}})^2 \right)^2 m_{\tilde{q}_1}^2 \right. \right.$$
$$\left. \left. + \left((U_{21}^{\tilde{q}})^2 - (U_{22}^{\tilde{q}})^2 \right)^2 m_{\tilde{q}_2}^2 \right) + 4 m_{\tilde{g}} m_q \left(U_{11}^{\tilde{q}} U_{22}^{\tilde{q}} + U_{12}^{\tilde{q}} U_{21}^{\tilde{q}} \right) \right]. \tag{8.66}$$

The necessary $\overline{\text{DR}}$ quark counterterms are defined according to Eq. (8.39).

In a second step we have to take care for the counterterms of the dependent parameters. To this end, we can use again relation (8.60). We can calculate the trace and the determinant for both, stops and sbottoms, on both sides of the equation. By requiring the corresponding values of both sides to be the same, we can express the three soft breaking parameters $M_{\tilde{Q}}^2, M_{\tilde{U}}^2, M_{\tilde{D}}^2$ in dependence of the input parameters. Having determined the soft breaking mass parameters, the mass eigenvalues of the stops and sbottoms can be calculated by diagonalizing the right hand side of Eq. (8.60). The obtained eigenvalues are then defined to be the three chosen on-shell masses $(m_{\tilde{t}_1}^2)^{\text{OS}}, (m_{\tilde{b}_1}^2)^{\text{OS}}, (m_{\tilde{b}_2}^2)^{\text{OS}}$, as well as the dependent stop mass $m_{\tilde{t}_2}^2$. Further, the mixing angles $\theta_{\tilde{t}}, \theta_{\tilde{b}}$ can be derived as dependent parameters.

The only missing piece, are now the counterterms of the dependent parameters $m_{\tilde{t}_2}^2, \theta_{\tilde{t}}, \theta_{\tilde{b}}$. As the counterterms of the soft breaking parameters never appear explicitly in any vertex, we do not have to calculate them. First, we can derive the counterterm for the squark mixing angles $\delta\theta_{\tilde{t}}$ and $\delta\theta_{\tilde{b}}$. Considering again Eq. (8.60),

we can express them according to

$$\delta\theta_{\tilde{q}} = \frac{\delta m_q\big(A_q - \mu\,(\tan\beta)^{-2I_q^{3L}}\big) + m_q\,\delta A_q - U_{11}^{\tilde{q}}U_{12}^{\tilde{q}}\big(\delta m_{\tilde{q}_1}^2 - \delta m_{\tilde{q}_2}^2\big)}{\big(U_{21}^{\tilde{q}}U_{12}^{\tilde{q}} + U_{11}^{\tilde{q}}U_{22}^{\tilde{q}}\big)\big(m_{\tilde{q}_1}^2 - m_{\tilde{q}_2}^2\big)}\,, \qquad (8.67)$$

in dependence of the counterterms of the input parameters. In other renormalization schemes, where the mixing angles belong to the set of input parameters, they can be expressed in terms of the wave-function renormalization constants (cf. [221]). The last remaining piece concerns the counterterm of the heavy stop mass $m_{\tilde{t}_2}^2$. This one can be also calculated by considering again the relations of Eq. (8.60)

$$\begin{aligned}
\delta m_{\tilde{t}_2}^2 = \frac{1}{U_{21}^{\tilde{t}}U_{12}^{\tilde{t}}}\Bigg[& \big(U_{21}^{\tilde{t}}U_{12}^{\tilde{t}} + U_{11}^{\tilde{t}}U_{22}^{\tilde{t}}\big)\Big((U_{11}^{\tilde{b}})^2\delta m_{\tilde{b}_1}^2 + (U_{21}^{\tilde{b}})^2\delta m_{\tilde{b}_2}^2 \\
& + 2U_{11}^{\tilde{b}}U_{21}^{\tilde{b}}\big(m_{\tilde{b}_1}^2 - m_{\tilde{b}_2}^2\big)\delta\theta_{\tilde{b}} - 2m_b\delta m_b - (U_{11}^{\tilde{t}})^2\delta m_{\tilde{t}_1}^2 + 2m_t\delta m_t\Big) \\
& - 2U_{11}^{\tilde{t}}U_{21}^{\tilde{t}}\Big(\delta m_t\big(A_t - \mu/\tan\beta\big) + m_t\,\delta A_t - U_{11}^{\tilde{t}}U_{12}^{\tilde{t}}\delta m_{\tilde{t}_1}^2\Big)\Bigg] \quad (8.68)
\end{aligned}$$

It depends on the other squark mass counterterms, the trilinear coupling counterterm as well as the above introduced mixing angle counterterm.

Altogether, we arrive at a stage, where we can fully renormalize all processes with electroweak vector bosons or Higgs bosons in the final state. However, in order to obtain a fully renormalized theory also in the case of a gluon in the final state, we have to treat the gluon wave function renormalization constants and the α_s counterterm, additionally. This we will do in the following section.

8.5 Gluon Sector

8.5.1 Wave Function Renormalization Constant

For the case of a gluon in the final state, we also have to derive the gluon wave function renormalization constant. To this end, we start again with the bare Lagrangian

$$\mathcal{L}_0 = -\frac{1}{4}\left(\partial_\mu G_{0\,\mu}^a - \partial_\nu G_{0\,\nu}^a\right)^2, \qquad (8.69)$$

where we can substitute according to the multiplicative renormalization the bare field with the following renormalized expression

$$G_{0\,\mu}^a \rightarrow (1 + \frac{1}{2}\delta Z^g)G_\mu^a\,, \qquad (8.70)$$

with δZ^g being the gluon wave function renormalization constant. As the gluon is renormalized on-shell, it remains after renormalization massless and thus does not obtain a mass counterterm. For calculating the renormalization constant we again write down the one-particle irreducible two-point function

$$\hat{\Gamma}_{\mu\nu}(k^2) = -g_{\mu\nu}k^2 - \hat{\Pi}_{\mu\nu}(k^2) \tag{8.71}$$

$$\mathcal{M} = -i\epsilon^{\mu}(k)\hat{\Gamma}_{\mu\nu}\epsilon^{*\,\nu}(k), \tag{8.72}$$

with its matrix element $\mathcal{M}$. The parameter $\hat{\Pi}_{\mu\nu}(k^2)$ indicates the gluon self energy and can be split into two parts: the transversal component $\hat{\Pi}_T(k^2)$ and the longitudinal component $\hat{\Pi}_L(k^2)$

$$\hat{\Pi}_{\mu\nu}(k^2) = \left(g_{\mu\nu} - \frac{k_{\mu}k_{\nu}}{k^2} \right) \hat{\Pi}_T(k^2) + \frac{k_{\mu}k_{\nu}}{k^2}\hat{\Pi}_L(k^2). \tag{8.73}$$

Considering the renormalization conditions

$$\left. \mathrm{Re}\hat{\Pi}_{ij}(k)\epsilon^{\nu}(k)\right|_{k^2=m_g^2} = 0 \tag{8.74}$$

$$\lim_{k^2 \to m_g^2} \frac{1}{k^2 - m_g^2}\mathrm{Re}\hat{\Pi}_{ii}(k)\epsilon^{\nu}(k) = -\epsilon^{\mu}(k), \tag{8.75}$$

and the relation $k_{\mu}\epsilon^{\mu} = 0$ we can neglect the longitudinal part for deriving the counterterm. Therefore, the loop corrected self energy can be written as

$$\hat{\Pi}_T(k^2) = \Pi_T(k^2) + k^2\delta Z^g, \tag{8.76}$$

with $\Pi_T(k^2)$ being the renormalized self energy and $k^2\delta Z^g$ its counterpart. By applying the on-shell renormalization conditions of Eqs. (8.74) and (8.75), we obtain finally the gluon wave function renormalization constant as

$$\delta Z^g = -\mathrm{Re}\frac{\partial}{\partial k^2}\Pi_T(k^2)\Big|_{k^2=m_g^2=0}, \tag{8.77}$$

which is dependent on the transversal component of the gluon self energy. The different contributions to the gluon self energy are depicted in Fig. 8.3. All seven diagrams, containing quarks, squarks, gluons, ghosts or gluinos, have to be taken into account. At this point it is interesting to mention that in contrast to the wave function renormalization constants of quark and squarks, also collinear infrared divergences occur. The three diagrams of Fig. 8.3 which contain a gluon, a ghost or light squarks give rise to the loop function $B_0(0,0,0) \propto \frac{1}{\varepsilon_{UV}} - \frac{1}{\varepsilon_{IR}}$ that contain a collinear divergence. This infrared divergence will be handled by the hard and collinear approximation that will be discussed in more detail in Section 9.3.2.
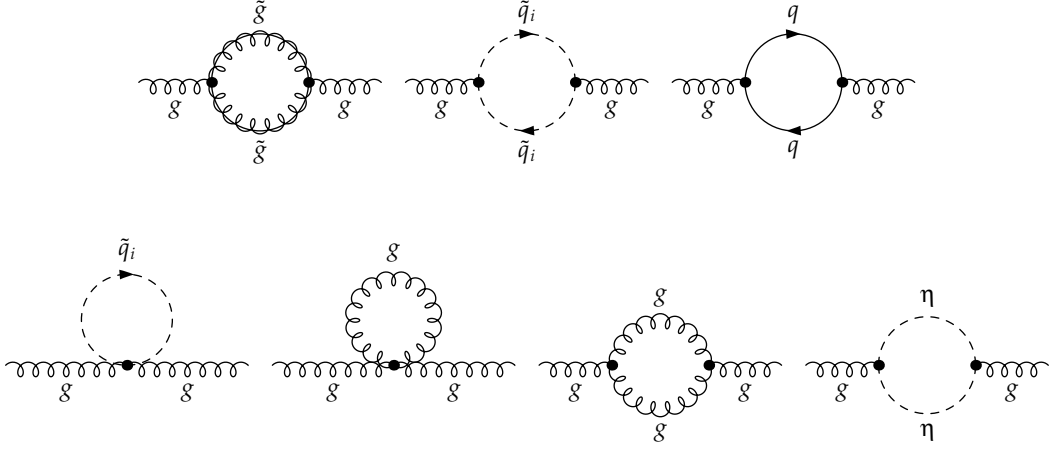
Figure 8.3: Gluon self energies, which contribute to the determination of the gluon wave function renormalization constant dZ^g.

8.5.2 Renormalization of $\alpha_\mathbf{s}$

The last basic ingredient which has to be derived is the counterterm for the strong coupling constant g_s, or the fine-structure constant α_s, respectively. Hereby, we follow the procedure of Ref. [222].

In order to fix the α_s counterterm we consider the decay of an off-shell gluon into a quark-antiquark pair. The corresponding Lagrangian looks like

$$\mathcal{L}_0 = -g_s \epsilon_0^{a\,\mu}(p)\bar{u}_{0\,s}(k_1) T_{st}^a \gamma_\mu v_{0\,t}(k_2). \tag{8.78}$$

We renormalize the bare Lagrangian by substituting the following expressions

$$v_{0\,t}(k_2) = (1 + \frac{1}{2}\delta Z_L^q P_L + \frac{1}{2}\delta Z_R^q P_R)\, v_t(k_2) \tag{8.79}$$

$$\bar{u}_{0\,s}(k_1) = \bar{u}_s(k_1)\,(1 + \frac{1}{2}\delta Z_L^q P_L + \frac{1}{2}\delta Z_R^q P_R) \tag{8.80}$$

$$\epsilon_0^{a\,\mu}(p) = (1 + \delta Z^{g\prime})\,\epsilon^{a\,\mu}(p), \tag{8.81}$$

where we consider the previously introduced quark wave function renormalization constants $Z_{L,R}^q$. Further, we apply the off-shell defined gluon wave function renormalization constant

$$\delta Z^{g\prime} = -\frac{1}{2}\frac{\mathrm{Re}\,(\Pi_T(p^2))}{p^2}. \tag{8.82}$$

In order to determine the counterterm of the strong coupling constant, we compare the UV-divergent terms arising from the vertex corrections to the gluon decay into a quark-antiquark pair with the corresponding counterterms obtained by Eqs. (8.79) to (8.81). As only terms proportional to γ_μ of the vertex corrections are of interest we can write the following simplified expression (see Ref. [222])

$$(1 + \frac{\delta g_s}{g_s})(1 + \frac{\delta Z^{g\,\prime}}{2})(1 + \frac{\delta Z_L^q}{2}P_L + \frac{\delta Z_R^q}{2}P_R)\gamma_\mu(1 + \frac{\delta Z_L^q}{2}P_L + \frac{\delta Z_R^q}{2}P_R)$$
$$= \gamma_\mu(1 - \Lambda - \Lambda_A\gamma_5) + \ldots, \tag{8.83}$$

where the term on the left hand side arises from the counterterm contributions. The expression on the right hand side indicates the terms linear in γ_μ which arise from the vertex corrections to the decay. Here we distinguish additionally between the terms linear in γ_μ named Λ and those linear in $\gamma_\mu\gamma_5$ denoted by Λ_A. All terms proportional to $\gamma_\mu\gamma_5$ have to cancel each other and are UV-finite.

Therefore, we end up with the following relation for determining the counterterm δg_s

$$\frac{\delta g_s}{g_s} = -\Lambda - \frac{1}{2}(\delta Z^{g\,\prime} + \delta Z_L^q + \delta Z_R^q). \tag{8.84}$$

In total four different diagrams contribute to the vertex correction of the quark-quark-gluon vertex. This vertex corresponds to the vertex $\hat{B}$ introduced in the previous chapter. The contributing UV divergent diagrams are depicted in Fig. 8.4. From the already calculated vertex corrections we are able to extract all terms Δ which are UV-divergent and linear in γ_μ. Furthermore, we can distinguish between contributions arising from the pure SM vertex corrections $\Lambda^{\text{SM},\overline{\text{DR}}}$ and the pure supersymmetric ones $\Lambda^{\text{SUSY},\overline{\text{DR}}}$.

Similar to extracting the UV-divergent terms out of the necessary vertex corrections, we can do the same for the wave function renormalization constants of the gluons and quarks. The contributing diagrams are depicted in Fig. 8.4, respectively.

Finally, we arrive at the following SM contributions to Eq. (8.84)

$$\delta Z^{g\,\prime\,\text{SM},\overline{\text{DR}}} = \frac{\alpha_s}{4\pi}\Delta\left(-\frac{2}{3}n_f + \frac{5}{3}C_A\right) \tag{8.85}$$

$$\delta Z_L^{q\,\text{SM},\overline{\text{DR}}} = \delta Z_R^{q\,\text{SM},\overline{\text{DR}}} = \frac{\alpha_s}{4\pi}\Delta\left(-C_F\right) \tag{8.86}$$

$$\Lambda^{\text{SM},\overline{\text{DR}}} = \frac{\alpha_s}{4\pi}\Delta\left(C_F + C_A\right), \tag{8.87}$$

where $n_f = 6$ indicates the number of flavors arising from the sum over the quark loop. The color factors are given as $C_F = \frac{4}{3}$ and $C_A = 3$. The corresponding super-
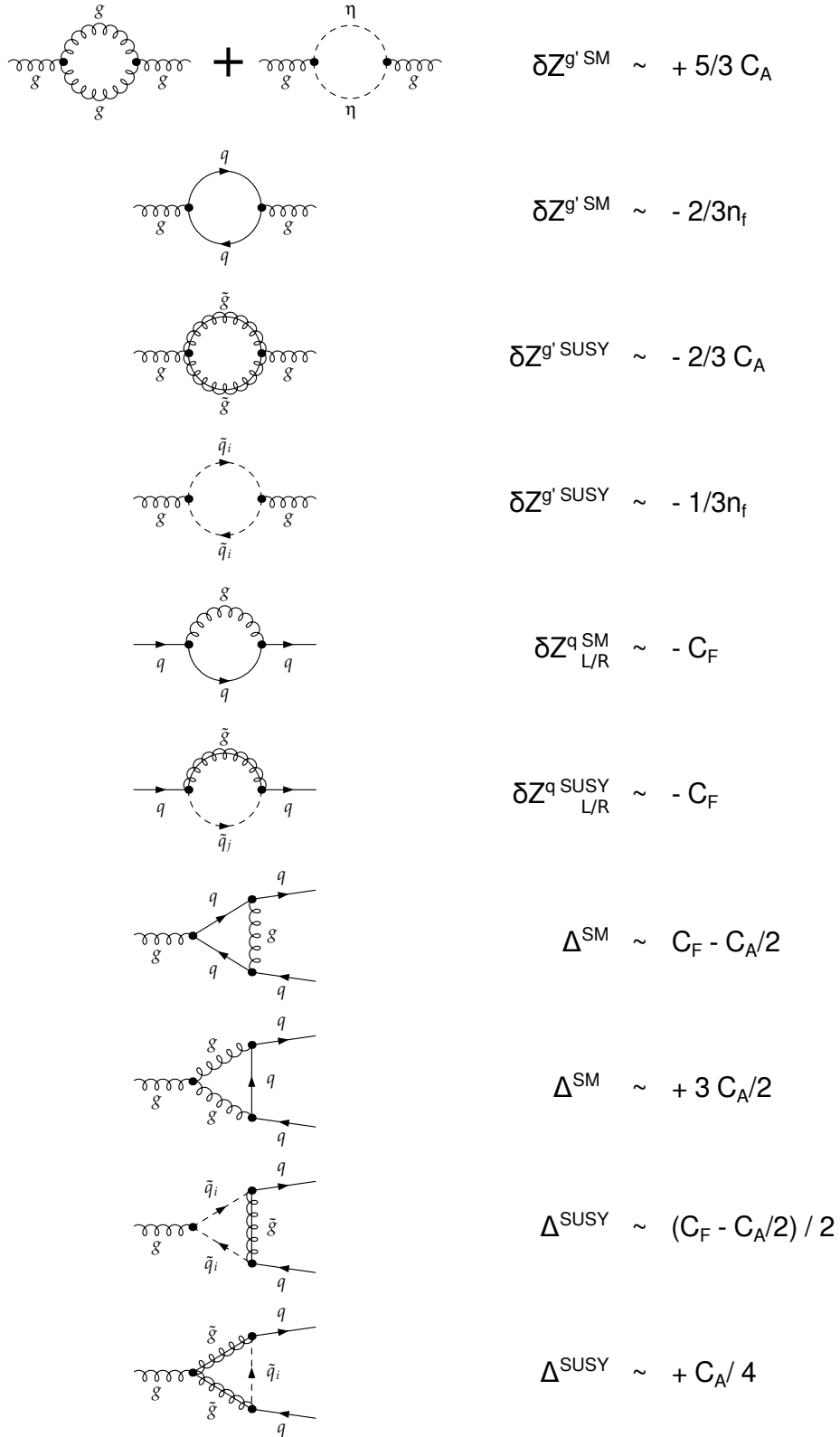
Figure 8.4: Overview of the diagrams which contribute to the α_s counterterm. All necessary expressions linear in $\frac{\alpha_s}{4\pi}\Delta$ are given.

symmetric terms are given by

$$\delta Z^{g\,\prime\,\text{SUSY},\overline{\text{DR}}} = \frac{\alpha_s}{4\pi}\,\Delta\,\left(-\frac{1}{3}n_f - \frac{2}{3}C_A\right) \tag{8.88}$$

$$\delta Z_L^{q\,\text{SUSY},\overline{\text{DR}}} = \delta Z_R^{q\,\text{SUSY},\overline{\text{DR}}} = \frac{\alpha_s}{4\pi}\,\Delta\,(-C_F) \tag{8.89}$$

$$\Lambda^{\text{SUSY},\overline{\text{DR}}} = \frac{\alpha_s}{4\pi}\,\Delta\,C_F, \tag{8.90}$$

where $n_f = 6$ comes from the sum over the squark loop. Putting all necessary pieces together we obtain the δg_s counterterms

$$\left(\frac{\delta g_s}{g_s}\right)^{\text{SM},\overline{\text{DR}}} = \frac{\alpha_s}{8\pi}\,\Delta\,\left(\frac{2}{3}n_f - \frac{11}{3}C_A\right) \tag{8.91}$$

$$\left(\frac{\delta g_s}{g_s}\right)^{\text{SUSY},\overline{\text{DR}}} = \frac{\alpha_s}{8\pi}\,\Delta\,\left(\frac{1}{3}n_f + \frac{2}{3}C_A\right), \tag{8.92}$$

where the first indicates the pure standard model counterterm, the second the supersymmetric one. Both together result in the final MSSM counterterm

$$\left(\frac{\delta g_s}{g_s}\right)^{\overline{\text{DR}}} = \frac{\alpha_s}{8\pi}\,\Delta\,(n_f - 3C_A). \tag{8.93}$$

As numerical input value for α_s we use so far the typical Standard Model value $\alpha_s^{\overline{\text{MS}},\text{SM}}(M_Z)$ with $n_f = 5$. However, principally $\alpha_s^{\overline{\text{DR}},\text{MSSM}}(Q)$ with $n_f = 6$ should be used within the MSSM, which is work in progress. An appropriate treatment of the running of α_s in the MSSM can be found in Ref. [223].

Having precisely deduced the source of every single contribution of the δg_s counterterm, it allows us to carefully check the UV-divergences in our code for every single contribution against each other. Thus, we have a powerful tool to validate different parts of our code. We have successfully checked that our code is UV-convergent for all possible final states.

8.6 Vertex Counterterms

Having derived all necessary counterterms for masses, mixing angles, and the strong coupling constant as well as the needed wave function renormalization constants, we are now able to construct the vertex counterterms for all corrected couplings. As an example we focus on the vertex counterterm to the coupling $\hat{A}_{j,n}^{q_g}$, which is present for all channels and all final states.

On the basis of the tree-level coupling

$$\hat{A}_{ij}^{q_g} = i\,[A_{ij}^{q_g\,L}P_L + A_{ij}^{q_g\,R}P_R], \tag{8.94}$$

with coefficients given by

$$A_{ij}^{u_g\,R} = -\frac{g_2 m_{u_g}}{\sin\theta_W\sqrt{2}M_W\sin\beta}N_{j\,4}U_{i2}^{u_g} \tag{8.95}$$

$$-\sqrt{2}\frac{g_2}{\sin\theta_W}\left((q_u - I_{3_u})\frac{\sin\theta_W}{\cos\theta_W}N_{j\,1} + I_{3_u}N_{j\,2}\right)U_{i1}^{u_g}$$

$$A_{ij}^{u_g\,L} = -g_2\frac{m_{u_g}}{\sin\theta_W\sqrt{2}M_W\sin\beta}N_{j\,4}^*U_{i1}^{u_g} \tag{8.96}$$

$$+\sqrt{2}g_2\frac{q_u}{\cos\theta_W}N_{j\,1}^*U_{i2}^{u_g}$$

we can derive the corresponding counterterm, which features the same generic structure

$$\delta\hat{A}_{ij}^{q_g} = i\,[\delta A_{ij}^{q_g\,L}P_L + \delta A_{ij}^{q_g\,R}P_R]. \tag{8.97}$$

In order to derive the coefficients of the counterterm, we have to consider all parameters of the original coupling which are connected to the strong coupling sector, and substitute those by their corresponding counterterms. In the following example, this applies for the quark mass counterterm δm_{u_g}, and the counterterm of the mixing matrix $\delta U_{i2}^{u_g}$:

$$\delta A_{ij}^{u_g\,R} = -\frac{g_2\,m_{u_g}}{\sin\theta_W\,\sqrt{2}M_W\,\sin\beta}N_{j\,4}U_{i2}^{u_g}\left(\frac{\delta m_{u_g}}{m_{u_g}} + \frac{\delta U_{i2}^{u_g}}{U_{i2}^{u_g}}\right) \tag{8.98}$$

$$-\frac{\sqrt{2}g_2}{\sin\theta_W}\left((q_u - I_{3_u})\frac{\sin\theta_W}{\cos\theta_W}N_{j\,1} + I_{3_u}N_{j\,2}\right)\delta U_{i1}^{u_g}$$

$$+ A_{1j}^{u_g\,R}\frac{1}{2}\delta Z_{1i}^{u_g} + A_{2j}^{u_g\,R}\frac{1}{2}\delta Z_{2i}^{u_g} + A_{ij}^{u_g\,R}\frac{1}{2}\delta Z_L^{*\,u_g}$$

$$\delta A_{ij}^{u_g\,L} = -\frac{g_2\,m_{u_g}}{\sin\theta_W\,\sqrt{2}M_W\,\sin\beta}N_{j\,4}^*U_{i1}^{u_g}\left(\frac{\delta m_{u_g}}{m_{u_g}} + \frac{\delta U_{i1}^{u_g}}{U_{i1}^{u_g}}\right) \tag{8.99}$$

$$+\frac{\sqrt{2}g_2 q_u}{\cos\theta_W}N_{j\,1}^*\delta U_{i2}^{u_g}$$

$$+ A_{1j}^{u_g\,L}\frac{1}{2}\delta Z_{1i}^{u_g} + A_{2j}^{u_g\,L}\frac{1}{2}\delta Z_{2i}^{u_g} + A_{ij}^{u_g\,L}\frac{1}{2}\delta Z_R^{*\,u_g}.$$

Also the corresponding wave function renormalization constants for the quark and squark legs of the coupling have to be considered.

With this approach, we are able to construct all vertex counterterms which are needed within the calculation. The derived vertex counterterms for the couplings which are involved in the processes with a Higgs boson in the final state are given in Appendix B.

With the generic structure introduced in Section 7.3, we can now also easily obtain the full squared matrix element that considers all counterterms. Similar to Eq. (7.50),

we can write the generic structure in case of a Higgs boson in the final state according to

$$
\begin{aligned}
|\mathcal{M}|^2_{\mathrm{counter}} = \; & \mathcal{M}^{\delta \mathrm{A}_1}_s \mathcal{M}^{\mathrm{tree}*}_s && + 2\mathrm{Re}(\mathcal{M}^{\delta \mathrm{A}_1}_s \mathcal{M}^{\delta \mathrm{tree}*}_t) && + 2\mathrm{Re}(\mathcal{M}^{\delta \mathrm{A}_1}_s \mathcal{M}^{\mathrm{tree}*}_u) \\
& + \mathcal{M}^{\delta \mathrm{F}}_s \mathcal{M}^{\delta \mathrm{tree}*}_s && + 2\mathrm{Re}(\mathcal{M}^{\delta \mathrm{F}}_s \mathcal{M}^{\mathrm{tree}*}_t) && + 2\mathrm{Re}(\mathcal{M}^{\delta \mathrm{F}}_s \mathcal{M}^{\mathrm{tree}*}_u) \\
& + \mathcal{M}^{\delta \mathrm{P}}_s \mathcal{M}^{\delta \mathrm{tree}*}_s && + 2\mathrm{Re}(\mathcal{M}^{\delta \mathrm{P}}_s \mathcal{M}^{\mathrm{tree}*}_t) && + 2\mathrm{Re}(\mathcal{M}^{\delta \mathrm{P}}_s \mathcal{M}^{\mathrm{tree}*}_u) \\
& + \mathcal{M}^{\delta \mathrm{A}_2}_t \mathcal{M}^{\delta \mathrm{tree}*}_t && + 2\mathrm{Re}(\mathcal{M}^{\delta \mathrm{A}_2}_t \mathcal{M}^{\mathrm{tree}*}_s) && + 2\mathrm{Re}(\mathcal{M}^{\delta \mathrm{A}_2}_t \mathcal{M}^{\mathrm{tree}*}_u) \\
& + \mathcal{M}^{\delta \mathrm{G}}_t \mathcal{M}^{\delta \mathrm{tree}*}_t && + 2\mathrm{Re}(\mathcal{M}^{\delta \mathrm{G}}_t \mathcal{M}^{\mathrm{tree}*}_s) && + 2\mathrm{Re}(\mathcal{M}^{\delta \mathrm{G}}_t \mathcal{M}^{\mathrm{tree}*}_u) \\
& + \mathcal{M}^{\delta \mathrm{P}}_t \mathcal{M}^{\delta \mathrm{tree}*}_t && + 2\mathrm{Re}(\mathcal{M}^{\delta \mathrm{P}}_t \mathcal{M}^{\mathrm{tree}*}_s) && + 2\mathrm{Re}(\mathcal{M}^{\delta \mathrm{P}}_t \mathcal{M}^{\mathrm{tree}*}_u) \\
& + \mathcal{M}^{\delta \mathrm{A}_3}_u \mathcal{M}^{\delta \mathrm{tree}*}_u && + 2\mathrm{Re}(\mathcal{M}^{\delta \mathrm{A}_3}_u \mathcal{M}^{\mathrm{tree}*}_s) && + 2\mathrm{Re}(\mathcal{M}^{\delta \mathrm{A}_3}_u \mathcal{M}^{\mathrm{tree}*}_t),
\end{aligned}
\tag{8.100}
$$

where we put the corresponding vertex counterterms ($\delta \mathrm{A}_{1,2,3}$, $\delta \mathrm{F}$, $\delta \mathrm{G}$) and propagator counterterms ($\delta \mathrm{P}$) according to the supscript of the amplitudes.

The same procedure can be performed for the neutralino-stop processes with a vector boson in the final state. We have derived all necessary counterterms, and have calculated the full squared matrix element by using the generic structure introduced in Section 7.3.

Conclusions. Finally, we have performed the full calculation of the virtual contributions. We have addressed the necessary propagator corrections, vertex corrections, and box diagrams. Due to a dedicated renormalization procedure, which has been introduced in this chapter, we managed to cancel all occurring UV divergences within the whole calculation. We have performed extensive UV-checks for all contributing processes of all final states, and can guarantee a full UV convergent calculation and implementation.

However, we are not yet completely at the end of the calculation. Still there are uncancelled infrared divergences, which occur, and have to be cancelled in a second, dedicated step. The corresponding treatment will be the topic of the following chapter.

9 Real Corrections

In this chapter we discuss the treatment of the remaining infrared divergences. After a brief introduction to infrared divergences in general and a motivation for including real emission diagrams, their calculation will be outlined. In a dedicated section we discuss the phase space slicing method for pure soft divergences, which occur in the processes with a Higgs or electroweak vector boson in the final state. As a second step, we focus on the treatment when both, soft and collinear divergences appear, which is the case for a gluon in the final state. For completeness, we address also difficulties that arise due to intermediate on-shell particles appearing in our matrix element.

9.1 Infrared Divergences

In order to get a finite result for the final full next-to-leading order calculation, one has also to treat carefully the infrared divergences (IR) arising from some virtual corrections in which at least one gluon is exchanged. These IR-divergences cancel against specific similar divergences of the real radiation diagrams where a gluon is emitted from one of the initial state squarks or final state quarks and gluons. In the total cross section, finally, all IR-divergences arising from virtual diagrams are cancelled exactly by the divergences of the real contributions which makes the full next-to-leading order result infrared safe, which was shown by the *Kinoshita-Lee-Nauenberg theorem*.

$$\sigma^{\mathrm{NLO}} = \int_{2\to3} d\sigma^{\mathrm{real}} + \int_{2\to2} d\sigma^{\mathrm{virtual}} = \text{finite} \tag{9.1}$$

However, the cancellation of these divergences is more involved than for the UV divergences. Whereas the IR divergences in the virtual diagrams arise due to virtual gluon exchange, the corresponding IR divergences in the real corrections occur only when integrating over the phase space of the external gluon (see Eq. (9.1)). The treatment of these infrared divergences is again in D dimensions possible, and should be worked out in the subsequent sections.

In order to understand the kinds of appearing infrared divergences, a generic real emission diagram is depicted in Fig. 9.1. The grey blob indicates the usual tree-level contribution $\mathcal{A}_0$ and has one outgoing leg of which a gluon is radiated off. It is the denominator of the intermediate propagator before the gluon emission which give
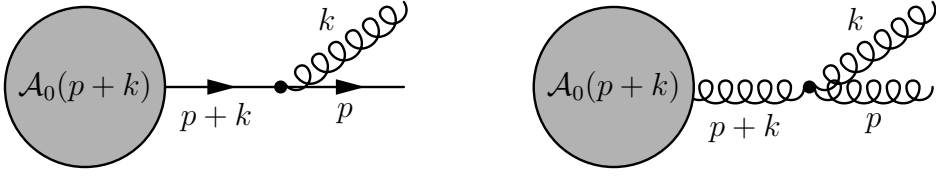
Figure 9.1: Schematic real emission diagram. The grey blob indicates for the absorbed contribution which is similar to the tree-level. The outgoing fermion / gluon line shows an exemplary leg of which a gluon is radiated off.

rise to two different kinds of infrared divergences:

$$\frac{1}{(p+k)^2 - m^2} = \frac{1}{2\,p\cdot k} = \frac{1}{\omega(E_p - |\vec{p}|\cos\theta)} \xrightarrow[m_p=0 \,\wedge\, \theta\to 0]{\omega\to 0 \,\vee} \infty, \qquad (9.2)$$

where $k = (\omega, \vec{k})$ is the D-momentum of the radiated gluon and $p = (E_p, \vec{p})$ of the second final state particle (see Fig. 9.1). If the momentum of the gluon becomes almost zero ($E_k \to 0$), a so-called *soft* divergence appears. Is the outgoing leg also a massless particle, like a gluon in our case, a *collinear* divergence can be caused if the angle between both outgoing particles is tiny ($\theta \to 0$).

9.2 Calculation of Real Emission Processes

In order to obtain a finite result for the total cross section, we have to take into account all possible real emission processes of all final states. Fig. 9.2 gives an overview over all processes in case of a Higgs or an electroweak vector boson in the final state. In Fig. 9.3 all diagrams involving a gluon in the final state are depicted. On the example of the Higgs final state, we give the amplitudes for all possible real emission processes. The matrix elements $\mathcal{M}_{si}$, $\mathcal{M}_{sp}$, and $\mathcal{M}_{sf}$ denote the amplitudes arising from gluon emission off the initial state squark, the quark propagator, and the final

state quark in the *s*-channel, respectively. They are given as follows

$$\mathcal{M}_{si} = \bar{u}(p_3)\, i\, [F_L^s P_L + F_R^s P_R]\, i\, \frac{\slashed{p}_3 + \slashed{p}_4 + m_{q_1}}{s_{34} - m_{q_1}^2}\, i\, [A_{1,\,L}^s P_L + A_{1,\,R}^s P_R]$$

$$\times\, \frac{i}{t_{25} - m_2^2}\, i\, g_0 (2 p_2^\mu - p_5^\mu)\, u(p_1)\, \epsilon_\mu^*(p_5) \tag{9.3}$$

$$\mathcal{M}_{sp} = \bar{u}(p_3)\, i\, [F_L^s P_L + F_R^s P_R]\, i\, \frac{\slashed{p}_3 + \slashed{p}_4 + m_{q_1}}{s_{34} - m_{q_1}^2}\, i\, g_1 \gamma^\mu\, i\, \frac{\slashed{p}_1 + \slashed{p}_2 + m_{q_1}}{s_{12} - m_{q_1}^2}$$

$$\times\, i\, [A_{1,\,L}^s P_L + A_{1,\,R}^s P_R]\, u(p_1)\, \epsilon_\mu^*(p_5) \tag{9.4}$$

$$\mathcal{M}_{sf} = \bar{u}(p_3)\, i\, g_1 \gamma^\mu\, i\, \frac{\slashed{p}_3 + \slashed{p}_5 + m_3}{s_{35} - m_3^2}\, i\, [F_L^s P_L + F_R^s P_R]\, i\, \frac{\slashed{p}_1 + \slashed{p}_2 + m_{q_1}}{s_{12} - m_{q_1}^2}$$

$$\times\, i\, [A_{1,\,L}^s P_L + A_{1,\,R}^s P_R]\, u(p_1)\, \epsilon_\mu^*(p_5). \tag{9.5}$$

The same naming convention is used for the corresponding real radiation in case of the *t*-channel diagrams

$$\mathcal{M}_{ti} = \bar{u}(p_3)\, i\, [A_{2,\,L}^s P_L + A_{2,\,R}^s P_R]\, u(p_1)\, \frac{i}{t_{31} - m_{q_2}^2}\, i G\, \frac{i}{t_{25} - m_2^2}\, i\, g_0 (2 p_2^\mu - p_5^\mu)\, \epsilon_\mu^*(p_5) \tag{9.6}$$

$$\mathcal{M}_{tp} = \bar{u}(p_3)\, i\, [A_{2,\,L}^s P_L + A_{2,\,R}^s P_R]\, u(p_1)\, \frac{i}{t_{31} - m_{q_2}^2}\, i\, g_0 (p_2^\mu - p_4^\mu + p_3^\mu - p_1^\mu)$$

$$\times\, \frac{i}{t_{24} - m_{q_2}^2}\, i G\, \epsilon_\mu^*(p_5) \tag{9.7}$$

$$\mathcal{M}_{tf} = \bar{u}(p_3)\, i\, g_1 \gamma^\mu\, i\, \frac{\slashed{p}_3 + \slashed{p}_5 + m_3}{s_{35} - m_3^2}\, i\, [A_{2,\,L}^s P_L + A_{2,\,R}^s P_R]\, u(p_1)\, \frac{i}{t_{24} - m_{q_2}^2}\, i G\, \epsilon_\mu^*(p_5), \tag{9.8}$$

as well as for the *u*-channel. However, in the latter case no gluon emission of the propagator is possible

$$\mathcal{M}_{ui} = \bar{u}(p_3)\, i\, [A_{3,\,L}^s P_L + A_{3,\,R}^s P_R]\, \frac{i}{t_{25} - m_2^2}\, i\, g_0 (2 p_2^\mu - p_5^\mu)\, i\, \frac{\slashed{p}_1 - \slashed{p}_4 + m_{q_3}}{t_{14} - m_{q_3}^2}$$

$$\times\, i\, [H_L^s P_L + H_R^s P_R]\, u(p_1)\, \epsilon_\mu^*(p_5) \tag{9.9}$$

$$\mathcal{M}_{uf} = \bar{u}(p_3)\, i\, g_1 \gamma^\mu\, i\, \frac{\slashed{p}_3 + \slashed{p}_5 + m_3}{s_{35} - m_3^2}\, i\, [A_{3,\,L}^s P_L + A_{3,\,R}^s P_R]\, i\, \frac{\slashed{p}_3 - \slashed{p}_4 + m_{q_3}}{t_{14} - m_{q_3}^2}$$

$$\times\, i\, [H_L^s P_L + H_R^s P_R]\, u(p_1)\, \epsilon_\mu^*(p_5). \tag{9.10}$$

In the above introduced matrix elements, the same conventions regarding the naming of the couplings, external and internal momenta, masses etc. have been used as introduced in Sec. 7.3. The additional gluon momentum is denoted as p_5. The

Mandelstam variables s_{ij} and t_{ij} are defined as

$$s_{ij} = (p_i + p_j)^2 \tag{9.11}$$
$$t_{ij} = (p_i - p_j)^2. \tag{9.12}$$

Moreover we substituted for simplification the following to couplings

$$-ig_s T^a (p_{in} + p_{out})^\mu = ig_0 (p_{in} + p_{out})^\mu \tag{9.13}$$
$$-ig_s T^b \gamma^\mu = ig_1 \gamma^\mu. \tag{9.14}$$

The full squared matrix element

$$|\mathcal{M}|^2_{real} = \sum_x \sum_y \mathcal{M}_x \mathcal{M}^*_y, \tag{9.15}$$

with $x, y = si, sp, sf, ti, tp, tf, ui, uf$ is obtained by considering all permutations of the above introduced single amplitudes. This was performed by using `FORM`.

Specific contributions to the full squared matrix element are now supposed to cancel against the infrared poles of the virtual contributions. However, the cancellation between the infrared divergences arising from the virtual contributions and those of the real contributions is not that straightforward as for the cancellation of the UV divergences within the virtual part. This is due to the fact that the divergences in the real contributions appear only by integrating over the gluon momentum. In the following we want to focus on one method which can be applied to address this problem, and is used within the `DM@NLO` code.
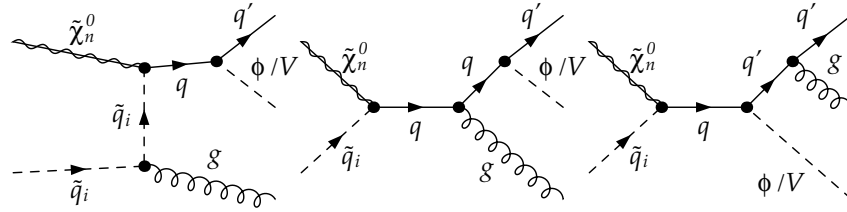
(a) Real emission from the *s*-channel diagram.
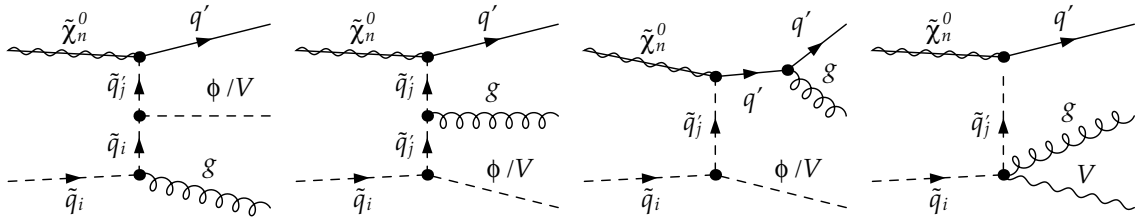
(b) Real emission from the *t*-channel diagram. Specific for an electroweak vector boson is the last diagram in the row, as an corresponding coupling is absent for a Higgs boson in the final state.
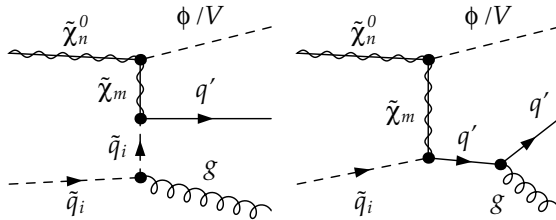
(c) Real emission from the *u*-channel diagram. There is no emission possible from the propagator.

Figure 9.2: Real emission diagrams in case of a Higgs (ϕ) or an electroweak vector boson (V) in the final state. From left to right, gluon emission from the initial state squark, the propagator, and the final state quark is depicted. Only the last diagram of Fig. 9.2(b) is special in case of an electroweak vector boson in the final state.
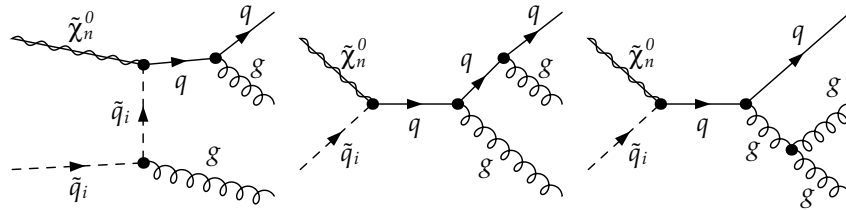
(a) Real emission from the s-channel diagram. The emission from the quark propagator and the external quark leg lead to the same undistinguishable process.
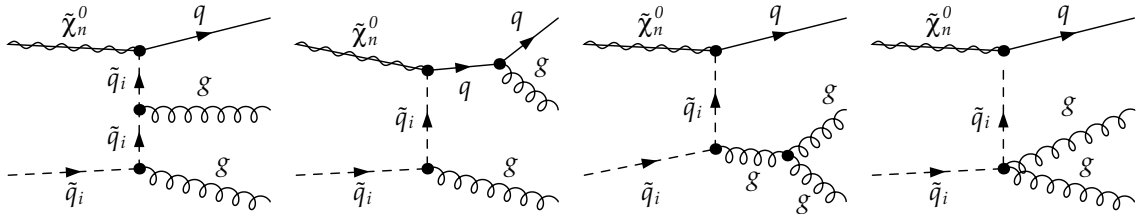
(b) Real emission from the t-channel diagram. The emission from the external squark leg and the squark propagator lead to the same undistinguishable process.
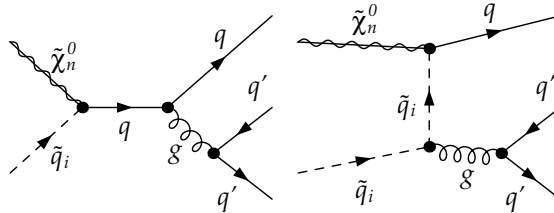
(c) Real emission of two light quarks from the external gluon leg. These processes are necessary to ensure total IR finiteness.

Figure 9.3: Real emission diagrams in case of a gluon in the final state. From left to right, gluon emission from the initial state squark as well as from the final state quark and gluon is depicted. The diagrams of Fig. 9.3(c) are specific for this final state.

9.3 Phase Space Slicing

The infrared divergences arising in the virtual contributions can be isolated by working in D dimensions as discussed in Sec. 7.1. However, in case of the infrared divergences occurring within the real emission processes an additional, special treatment is necessary. This is due to the fact, that divergences in the $2 \to 3$ processes arise, when integrating over the gluon phase space. To address this problem the so-called *phase space slicing* method is a possible method.

Within this approach the phase space is sliced into a soft part (σ^{soft}) and a hard part σ^{hard} (see Eq. (9.16))

$$\sigma^{\mathrm{real}} = \sigma^{\mathrm{soft}}(\Delta E) + \sigma^{\mathrm{hard}}(\Delta E) \tag{9.16}$$

$$= \sigma^{\mathrm{soft}}(\Delta E) + \sigma^{\mathrm{hard}}_{\mathrm{coll}}(\Delta E, \Delta\theta) + \sigma^{\mathrm{hard}}_{\mathrm{non-coll}}(\Delta E, \Delta\theta). \tag{9.17}$$

When also collinear divergences can arise like in case of a gluon in the final state, we cut the hard part again into two pieces, a hard and collinear $\sigma^{\mathrm{hard}}_{\mathrm{coll}}$, and a hard and non-collinear part $\sigma^{\mathrm{hard}}_{\mathrm{non-coll}}$ (see Eq. (9.17)). Fig. 9.4 shows an illustration of the sliced phase space.

We will see that the amplitudes factorize in their soft and collinear limit in terms of the $2 \to 2$ phase space. This factorization makes an easy cancellation of the real and virtual infrared poles possible.

In the following we focus first on the soft gluon approximation when a Higgs or a vector boson is in the final state. In a second step we discuss the special case involving a gluon in the final state. Here, one has to take care also for collinear divergences such that a special treatment is necessary.
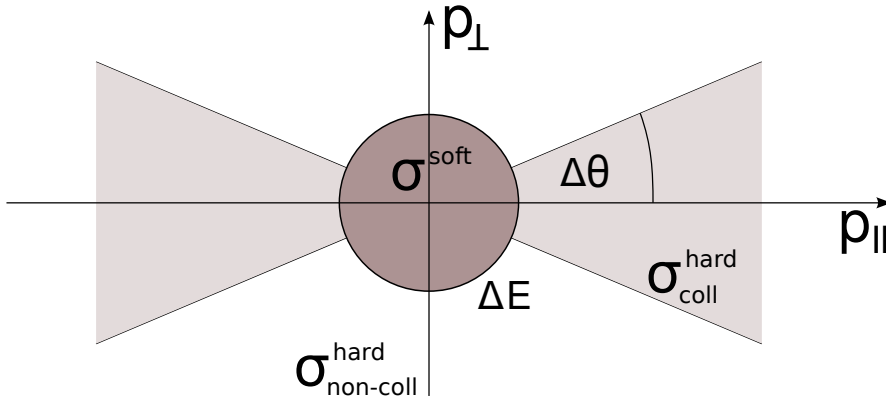
Figure 9.4: Schematic overview over the regions of the parameter space which have to be treated separately. We distinguish between the soft (soft and collinear) part σ^{soft}, the hard and collinear part $\sigma^{\mathrm{hard}}_{\mathrm{coll}}$, as well as the hard and non-collinear part $\sigma^{\mathrm{hard}}_{\mathrm{non-coll}}$.

9.3.1 Processes with a Higgs or an Electroweak Vector Boson in the Final State

Treatment of Soft Divergences

With the gluon being emitted from massive particles, the processes with a Higgs or a vector boson in the final state give only rise to soft divergences. Considering the contributing $2 \to 3$ processes shown in Fig. 9.2, only diagrams with a gluon radiated of an initial state squark, or a final state quark feature a divergence. Real emission off the propagator does not lead to a divergence, as both propagators are independent of the gluon momentum (cf. Eqs. (9.4), and (9.7)).

In order to cancel the soft divergences arising from these diagrams with the corresponding contributions of the virtual corrections (see Figs. 9.5 and 9.6) we would like to factorize the divergent part in terms of the $2 \to 2$ phase space. Considering Fig. 9.1, we can phrase the $2 \to 3$ process dependent on an amplitude $\mathcal{A}_0$ which is similar to the tree-level, but with an outgoing fermion carrying the momentum $p + k$. From this outgoing leg the gluon with momentum k is radiated off. Thus we can write

$$\mathcal{M} = \mathcal{A}_0(p + k)\frac{i(\not{p} + \not{k} + m)}{(p + k)^2 - m^2}(-ig_s T^a \gamma^\mu)\overline{u}(p)\varepsilon_\mu^*(k). \tag{9.18}$$

Assuming the soft limit $k^\mu \to 0$, we can write the above equation as

$$\mathcal{M} = \mathcal{A}_0(p)\overline{u}(p)\frac{p \cdot \varepsilon^*}{p \cdot k}(g_s T^a). \tag{9.19}$$

Thus, in the soft gluon approximation (often also called eikonal approximation), we are able factorize the real emission amplitude in terms of the tree-level amplitude, a term which contains the divergence, and a factor arising from the process specific coupling.

The same expression can be also derived in the case a gluon is radiated off an ingoing sfermion. Finally, the most general expression is given by

$$\mathcal{M} = \mathcal{M}_0 \sum_i \pm\frac{p_i \cdot \varepsilon^*}{p_i \cdot k}(-g_s T^a), \tag{9.20}$$

where $+$ is valid for an outgoing particle or incoming antiparticle, and $-$ for an incoming particle or an outgoing antiparticle.

Thus, we can write the squared matrix element of all real radiation diagrams for each specific process $\tilde{\chi}_1^0 \tilde{t}_1 \to t\phi, V$ with $\phi = h^0, H^0, A^0, H^\pm$ and $Z^0, W^\pm, \gamma$ (see Fig. 9.2) in the soft limit by using the eikonal approximation as follows

$$\mathcal{M}^2 = |\mathcal{M}_0|^2 \times (-g_s^2 C_F)\left[\frac{p_2^2}{(p_2 \cdot k)^2} + \frac{p_3^2}{(p_3 \cdot k)^2} - \frac{2p_2 \cdot p_3}{(p_2 \cdot k)(k \cdot p_3)}\right]. \tag{9.21}$$

The first term arises from the squared initial state radiation contribution, the second one from the squared final state radiation diagram, and the third expression denotes their interference terms.

Having managed to factorize the squared matrix element of the real emission in terms of the tree level contribution, we now have to separate also the phase space. Therefore, we concentrate now on the integration over the $2 \to 3$ phase space in dimensional regularization with $D > 4$. We can write the partial cross section as

$$d\sigma = \frac{1}{\Phi} \int \frac{d^{D-1}p_3}{(2\pi)^{D-1}2E_3} \frac{d^{D-1}p_4}{(2\pi)^{D-1}2E_4} \frac{d^{D-1}k}{(2\pi)^{D-1}2\omega} (2\pi)^D \delta^{(D)}(p_1 + p_2 - p_3 - p_4 - k)\overline{|\mathcal{M}|^2},$$
(9.22)

where Φ indicates the flux factor. Due to the soft gluon approximation we can assume the momentum of the gluon being negligible in the delta function $k^\mu = 0$ such that we can separate the integration over the gluon phase space from the two-body phase space

$$d\Gamma_3\big|_{\text{soft}} = \left[\frac{d^{D-1}p_3}{(2\pi)^{D-1}2E_3} \frac{d^{D-1}p_4}{(2\pi)^{D-1}2E_4} (2\pi)^D \delta^{(D)}(p_1 + p_2 - p_3 - p_4) \right] \frac{d^{D-1}k}{(2\pi)^{D-1}2\omega},$$
(9.23)

with

$$\frac{d^{D-1}p_3}{(2\pi)^{D-1}2E_3} \frac{d^{D-1}p_4}{(2\pi)^{D-1}2E_4} (2\pi)^D \delta^{(D)}(p_1 + p_2 - p_3 - p_4) = d\Gamma_2$$
(9.24)

being the usual two-body phase space in D dimensions. Taking into account Eq. (9.21) and Eq. (9.23) we can express Eq. (9.22) as

$$\left(\frac{d\sigma}{d\Gamma_2} \right) = -\left(\frac{d\sigma}{d\Gamma_2} \right)_0 \times \frac{g_s^2 C_F \mu^{4-D}}{8\pi^3} \int_{|\vec{k}| \leq \delta_s} \frac{d^{D-1}k}{(2\pi)^{D-4}} \frac{1}{2\omega}$$
$$\times \left[\frac{p_2^2}{(p_2 \cdot k)^2} + \frac{p_3^2}{(p_3 \cdot k)^2} - \frac{2p_2 \cdot p_3}{(p_2 \cdot k)(k \cdot p_3)} \right],$$
(9.25)

where μ denotes the renormalization scale. This gives us the factorized form of the phase space we aimed for, which is valid in the soft limit $|\vec{k}| \leq \delta_s$.

However, we now have to isolate the infrared divergence of the remaining integration over the D-momentum of the gluon. Thus, we focus on the following integral, which

is a generic form of the appearing expressions in Eq. (9.25)

$$I'_{ab} = (a \cdot b) \, I_{ab} \tag{9.26}$$

$$I_{ab} = \mu^{4-D} \int_{|\vec{k}| \leq \delta_s} \frac{d^{D-1}k}{(2\pi)^{D-4}} \frac{1}{2\omega} \frac{2}{(a \cdot k)(b \cdot k)}, \tag{9.27}$$

where a and b denote the D-momenta of the particles from which the gluon k is radiated off. This integral has been extensively studied in the literature, see e.g. Refs. [194, 224], which we will follow for the subsequent derivation.

First, the integration over the D-momentum can be reformulated into an integration over the gluon's absolute momentum and the spatial angle θ

$$\int d^{D-1}k = \int d|\vec{k}| \, |\vec{k}|^{D-2} \int d\Omega_{D-2} = 2 \frac{\pi^{(D-2)/2}}{\Gamma(\frac{D-2}{2})} \int d|\vec{k}| \, |\vec{k}|^{D-2} \int_0^\pi d\theta \sin^{D-3}\theta. \tag{9.28}$$

In a second step we re-express the product of the scalar products. To this end, we introduce the new momenta p and q which are related to the momenta a and b as follows

$$p = \alpha a \quad \text{and} \quad q = b \quad \text{with} \quad (p-q)^2 = 0. \tag{9.29}$$

The variable α is hereby fixed due to the condition $(p-q)^2 = 0$ and has to fulfil $\frac{\alpha a^0 - b^0}{b^0} > 0$. After reformulating the scalar products, we make use of the Feynman parametrization and can write the denominator in dependence of $P = q + (p-q)x$:

$$\frac{1}{(a \cdot k)(b \cdot k)} = \frac{\alpha}{(p \cdot k)(q \cdot k)} = \int_0^1 dx \frac{\alpha}{[(q \cdot k)(1-x) + (p \cdot k)x]^2} = \int_0^1 dx \frac{\alpha}{(P \cdot k)^2}. \tag{9.30}$$

Inserting Eq. (9.28) and Eq. (9.30) in Eq. (9.27) we arrive at the following expression

$$I_{ab} = 2\alpha \frac{\mu^{4-D}}{(2\pi)^{D-4}} \frac{\pi^{(D-2)/2}}{\Gamma(\frac{D-2}{2})} \int_0^{\delta_s} dk \, k^{D-3} \int_{-1}^1 (d\cos\theta) \sin^{D-4}\theta \int_0^1 dx \frac{1}{k^2(P^0 - |\vec{P}|\cos\theta)^2}, \tag{9.31}$$

where we have taken into account the relation $k \equiv |\vec{k}| = k^0 = \omega$ which is valid due to the light-like D-momentum of the gluon. This we can also use in order to reformulate the scalar product $P \cdot k = k^2(P^0 - |\vec{P}|\cos\theta)^2$ in dependence of the angle θ. Considering all momenta k appearing in Eq. (9.31), we can extract the arising

soft infrared divergence

$$\int_0^{\delta_s} dk \; k^{D-5} = \frac{\delta_s^{(D-4)}}{D-4} = -\frac{\delta_s^{(D-4)}}{2\varepsilon}, \tag{9.32}$$

where $D = 4 - 2\varepsilon$. Using the relation of Eq. (9.32) we can further write

$$I_{ab} = \alpha \frac{2}{D-4} \frac{\pi^{(D-2)/2}}{(2\pi)^{D-4}} \frac{1}{\Gamma(\frac{D-2}{2})} \frac{\delta_s^{(D-4)}}{\mu^{D-4}} \int_{-1}^1 dy \int_0^1 dx \frac{(1-y^2)^{(D-4)/2}}{(P^0 - |\vec{P}|y)^2}, \tag{9.33}$$

where we substituted the integration variable according to $y = \cos\theta$. In comparison to Eq. (9.31) we rearranged the prefactors in such a way that we can expand them easily up to orders $\mathcal{O}(\varepsilon)$. After the expansion of all terms depending on ε and the multiplication with the infrared pole $-1/\varepsilon$ we can write Eq. (9.33) as follows

$$I_{ab} = \alpha\pi \int_0^1 dx \int_{-1}^1 dy \frac{-\frac{1}{\varepsilon} - \log 4\pi + \gamma_E + \log\frac{\delta_s^2}{\mu^2}}{(P^0 - |\vec{P}|y)^2} + \frac{\log(1-y^2)}{(P^0 - |\vec{P}|y)^2}, \tag{9.34}$$

where we applied the definition of the Euler–Mascheroni constant $\Gamma'(1) = -\gamma_E$. Moreover, we split the integrand into two terms, which is useful for the remaining integration over y. At this point, we do not want to go into too much detail as the following integration is quite lengthy. For more details we refer to Refs. [194, 224]. The result is given by

$$I_{ab} = 2\pi\alpha \int_0^1 dx \frac{1}{P^2} \left\{ -\frac{1}{\varepsilon} - \log 4\pi + \gamma_E + \log\frac{4\delta_s^2}{\mu^2} + \frac{P^0}{|\vec{P}|}\log\left(\frac{P^0 - |\vec{P}|}{P^0 + |\vec{P}|}\right) \right\}, \tag{9.35}$$

where we have assumed that $P^0 > |\vec{P}|^2$. Performing the very last integration over x we arrive at our final expression for the integral I_{ab} which we need to finally calculate Eq. (9.25).

$$I'_{ab} = \frac{4\pi\alpha(a.b)}{(\alpha a)^2 - b^2} \left\{ \frac{1}{2} \left(-\frac{1}{\varepsilon} - \log 4\pi + \gamma_E + \log\frac{4\delta_s^2}{\mu^2} \right) \ln\frac{(\alpha a)^2}{b^2} \right.$$
$$\left. + \left[\frac{1}{4}\ln^2\left(\frac{P^0 - |\vec{P}|}{P^0 + |\vec{P}|}\right) + \text{Li}_2\left(1 - \frac{P^0 - |\vec{P}|}{\frac{\alpha^2 a^2 - b^2}{2(\alpha a^0 - b^0)}}\right) + \text{Li}_2\left(1 - \frac{P^0 + |\vec{P}|}{\frac{\alpha^2 a^2 - b^2}{2(\alpha a^0 - b^0)}}\right) \right]_{P=b}^{P=\alpha a} \right\}. \tag{9.36}$$

Hereby, we reintroduced again our starting variables a and b, see Eq. (9.29).
The special case of the integral I_{a^2}, where the D-momenta a and b are equal, can be directly obtained from Eq. (9.34), as we do not need to perform a Feynman parametrization and the additional integration over x in this case. Therefore, we

obtain the following expression

$$I'_{a^2} = 2\pi \left\{ -\frac{1}{\varepsilon} - \log 4\pi + \gamma_E + \log\frac{4\delta_s^2}{\mu^2} + \frac{a^0}{|\vec{a}|}\ln\left(\frac{a^0 - |\vec{a}|}{a^0 + |\vec{a}|}\right) \right\}. \tag{9.37}$$

Finally, we have derived the integrals needed for calculating Eq. (9.25). Thus we are able to explicitly isolate the soft divergence which arise due to the integration over the gluon phase space, and managed to factorize this in dependence of the two-body phase space of the corresponding tree level.

Fixing the kinematics of the processes in the centre of mass (CMS) system of the incoming particles we can express the D-momenta of the participating particles as follows

$$p_1 = \frac{\sqrt{s}}{2}\left(\frac{2E_1}{\sqrt{s}}, ..., 0, 0, \beta_1\right) \tag{9.38}$$

$$p_2 = \frac{\sqrt{s}}{2}\left(\frac{2E_2}{\sqrt{s}}, ..., 0, 0, -\beta_1\right) \tag{9.39}$$

$$p_3 = \frac{\sqrt{s}}{2}\left(\frac{2E_3}{\sqrt{s}}, ..., 0, \beta_2\sin\theta, \beta_2\cos\theta\right) \tag{9.40}$$

$$p_4 = \frac{\sqrt{s}}{2}\left(\frac{2E_4}{\sqrt{s}}, ..., 0, -\beta_2\sin\theta, -\beta_2\cos\theta\right), \tag{9.41}$$

where their energies and $\beta_{i=1,2}$ are given by

$$E_1 = \frac{s + m_1^2 - m_2^2}{2\sqrt{s}} \quad E_2 = \frac{s + m_2^2 - m_1^2}{2\sqrt{s}} \quad \beta_1 = \frac{\lambda^{1/2}(s, m_1^2, m_2^2)}{s} \tag{9.42}$$

$$E_3 = \frac{s + m_3^2 - m_4^2}{2\sqrt{s}} \quad E_4 = \frac{s + m_4^2 - m_3^2}{2\sqrt{s}} \quad \beta_2 = \frac{\lambda^{1/2}(s, m_3^2, m_4^2)}{s}, \tag{9.43}$$

with

$$\lambda(x, y, z) = x^2 + y^2 + z^2 - 2xy - 2xz - 2yz \tag{9.44}$$

being the so-called Källén function. With the above defined D-momenta, we can express the studied real radiation diagrams in the soft limit with Eq. (9.36) and Eq. (9.37).

The final expression for the considered real radiation diagrams in the soft limit is given by

$$\left(\frac{d\sigma}{d\Gamma_2}\right) = -\left(\frac{d\sigma}{d\Gamma_2}\right)_0 \times \frac{g_s^2 C_F}{16\pi^3}\left[I'_{p_2^2}(\delta_s) + I'_{p_3^2}(\delta_s) - 2I'_{p_2 p_3}(\delta_s)\right]. \tag{9.45}$$
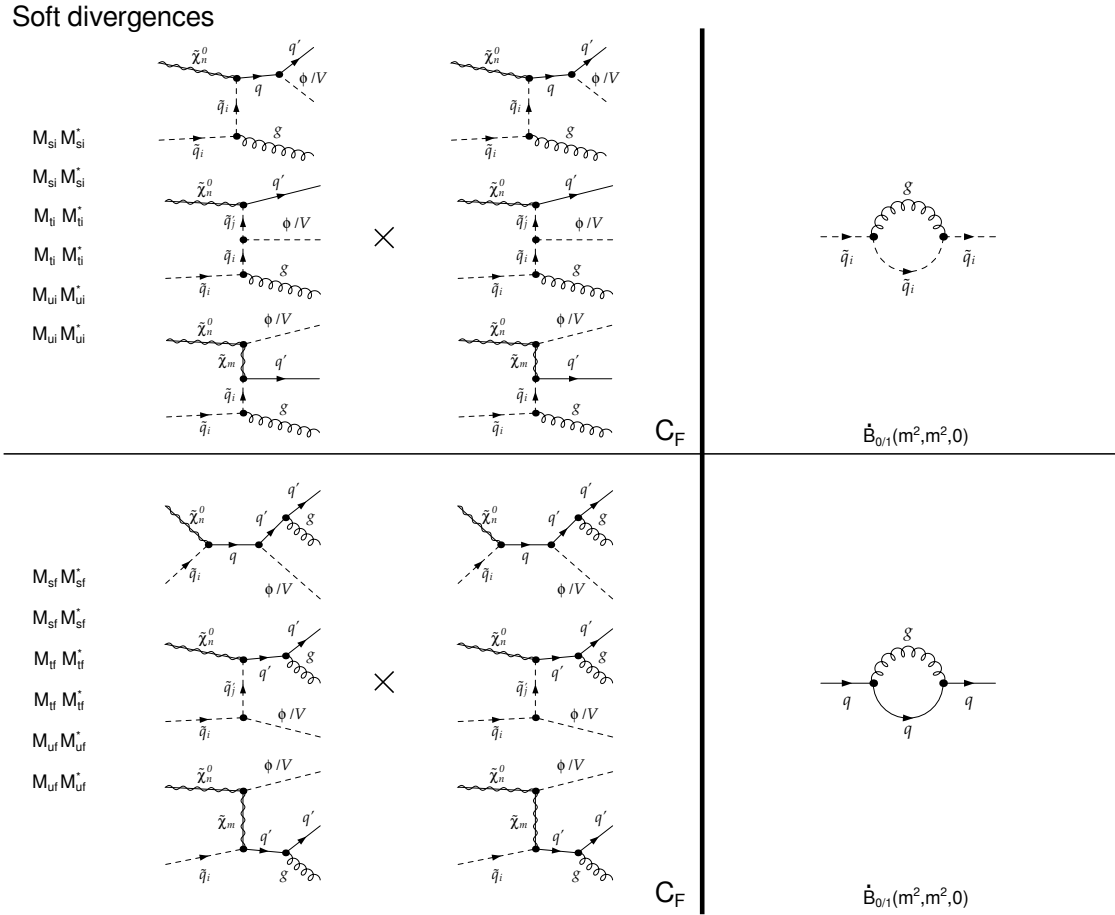
Figure 9.5: Overview (part I) of the soft diagrams of the real (left) and virtual part (right) which cancel each other. Besides the colour factor, also the corresponding infrared divergent loop integrals are given.

Soft divergences

Figure 9.6: Overview (part II) of the soft diagrams of the real (left) and virtual part (right) which cancel each other. Besides the colour factor, also the corresponding infrared divergent loop integrals are given.

Conclusions. Having derived the soft limit of the necessary real radiation diagrams in terms of the tree-level matrix element, we are able to cancel easily the corresponding infrared divergences of the virtual and real corrections. This we have checked in our `DM@NLO` implementation diagram by diagram, and can guarantee infrared convergence for all processes. Figs. 9.5 and 9.6 show the corresponding soft diagrams which are cancelled between the real and virtual part. Additionally, the infrared divergent loop diagrams are given.

Especially interesting is the last row in Fig. 9.6. It shows the only infrared divergent vertex correction in case of a Higgs or electroweak vector boson in the final state. It arises only in processes featuring an u-channel, and is thus absent for a photon in the final state.

Another powerful check is the test concerning the cutoff independence. When performing the real emission computation, the real radiation diagrams are evaluated according to the soft gluon approximation until the cutoff δ_s (see Eq. (9.45)). For values larger than the cutoff, the usual real radiation calculation as described in Sec. 9.2 is performed. However, the whole calculation should be independent of the cutoff in the end. The cutoff behaviour has been intensively studied such that we can ensure cutoff independence for a reasonable cutoff range.

9.3.2 Processes with a Gluon in the Final State
Treatment of Soft and Collinear Divergences

Up to now we have only considered processes, where a gluon was radiated off a massive particle. However, in the case of a gluon in the final state, we have to consider additionally gluon emission off a gluon. This gives rise not only to soft, but also to collinear divergences, which have to be treated carefully. To this end, basically two approaches exist to extend the phase space slicing algorithm to these purposes: the *one cutoff* and the *two cutoff* method. A comparison of both is performed for instance in Ref. [225], where it has been shown, that both methods agree within their systematic and statistic errors.

In contrast to the two cutoff method, the single cutoff approach introduces only one condition to distinguish between the finite and divergent part of the phase space. The infrared divergent part of the phase space is defined as the region where the final state particle i and the emitted particle j are not longer resolvable. Thus, the divergent region is defined by the requirement $s_{ij} = 2p_i p_j < s_{cut}$, with s_{cut} being a small value. Further details on the one cutoff method can be found in Refs. [226, 227].

In this work, however, we follow the two-cutoff approach, introduced by Ref. [228]. According to Eq. (9.17) we can slice the phase space with an additional cutoff parameter δ_c into three different regions: the soft (and eventually also collinear) part, the hard and collinear region and the pure hard and non-collinear phase space. Such, we can define the hard and collinear phase space region by requir-

ing $\omega > \delta_s \wedge (1 - \cos\theta_{pk}) \leqq \delta_c$. In contrast to the pure massive initial and final states of the previous section, also the soft part $\omega \leqq \delta_s$ can become collinear now. As the introduced general integrals of the previous section (see Eqs. (9.36) and (9.37)) do not take into account collinear divergences and thus possible double poles, we have to develop new expressions for the correct treatment of the soft and collinear case. Hereby, we follow the procedure of the two-cutoff method described in Ref. [228].

Soft and collinear. First, we start with the treatment of the processes which can become soft and collinear in the soft limit of the phase space $\omega \leqq \delta_s$. Such behaviour occurs when a diagram with gluon emission from a final state gluon interferes with real radiation from an initial state squark or a final state quark, respectively. The corresponding diagrams are depicted in Fig. 9.3. Similar to the previous case, we can perform also for the non-abelian cases an eikonal approximation, which has been shown in detail in Refs. [229–231]. Thus, we arrive at

$$|\mathcal{M}|^2 = \sum_{spin} |\mathcal{M}_0|^2 \times \frac{-C_A}{2} \left[-\frac{2p_2 \cdot p_4}{(p_2 \cdot k)(p_4 \cdot k)} - \frac{2p_3 \cdot p_4}{(p_3 \cdot k)(p_4 \cdot k)} \right]. \tag{9.46}$$

Due to the soft gluon approximation $k^\mu \to 0$, the 3-body phase space $d\Gamma_3$ (cf. Eq. (9.22)) factorizes in terms of the 2-body phase space Γ_2, such that we can write in D dimensions

$$d\Gamma_3\big|_{soft} = d\Gamma_2 \frac{d^{D-1}k}{(2\pi)^{D-1}2\omega} = d\Gamma_2 \frac{dk\, k^{D-2}}{(2\pi)^{D-1}2k} \, d\theta_1 \sin^{D-3}\theta_1 \, d\theta_2 \sin^{D-4}\theta_2 \, \Omega_{D-4}, \tag{9.47}$$

with θ_1 being the polar and θ_2 the azimuthal angle. The solid angle Ω_{D-4} can be rewritten according to

$$\Omega_{D-4} = \frac{2\pi^{\frac{D-3}{2}}}{\Gamma\left(\frac{D-3}{2}\right)} = \frac{2\pi^{\frac{1-2\varepsilon}{2}}\Gamma(1-\varepsilon)}{\sqrt{\pi}2^{2\varepsilon}\Gamma(1-2\varepsilon)}, \tag{9.48}$$

such that Eq. (9.47) can be reformulated

$$d\Gamma_3\big|_{soft} = d\Gamma_2 \frac{\pi^\varepsilon\, \Gamma(1-\varepsilon)}{(2\pi)^3\, \Gamma(1-2\varepsilon)} \, dk k^{D-3} \, d\theta_1 \sin^{D-3}\theta_1 \, d\theta_2 \sin^{D-4}\theta_2. \tag{9.49}$$

The corresponding differential cross section $(d\sigma/d\Gamma_2)$ in terms of the differential cross section of the tree-level $(d\sigma/d\Gamma_2)_0$ and the phase space integration over the

emitted gluon D-momentum is obtained as

$$
\left(\frac{d\sigma}{d\Gamma_2}\right) = -\left(\frac{d\sigma}{d\Gamma_2}\right)_0 \times \frac{g_s^2}{8\pi^3}\frac{\mu^{4-D}\pi^\varepsilon\,\Gamma(1-\varepsilon)}{\Gamma(1-2\varepsilon)}\int_0^{\delta_s} dk\,k^{D-3}\int_0^\pi d\theta_1\sin^{D-3}\theta_1
$$
$$
\times \int_0^\pi d\theta_2\sin^{D-4}\theta_2\frac{-C_A}{2}\left[-\frac{2p_2\cdot p_4}{(p_2\cdot k)(p_4\cdot k)} - \frac{2p_3\cdot p_4}{(p_3\cdot k)(p_4\cdot k)}\right],
\tag{9.50}
$$

with C_A being the color factor. Up to corrections of $\mathcal{O}(\delta_s)$ we can express the D-momentum of the emitted gluon in the CMS-system of the incoming particles as

$$
k = k\,(1,...,0,\sin\theta_1\sin\theta_2,\sin\theta_1\cos\theta_2,\cos\theta_1)\,.
\tag{9.51}
$$

Thus, we get for the necessary scalar products of Eq. (9.50) the following expressions

$$
(p_2\cdot k) = \frac{k\sqrt{s}}{2}x_{p_2k} = \frac{k\sqrt{s}}{2}\left(\frac{2E_2}{\sqrt{s}} + \beta_1\cos\theta_1\right)
\tag{9.52}
$$

$$
(p_3\cdot k) = \frac{k\sqrt{s}}{2}x_{p_3k} = \frac{k\sqrt{s}}{2}\left(\frac{2E_3}{\sqrt{s}} - \beta_2\sin\theta\sin\theta_1\cos\theta_2 - \beta_2\cos\theta\cos\theta_1\right)
\tag{9.53}
$$

$$
(p_4\cdot k) = \frac{k\sqrt{s}}{2}x_{p_4k} = \frac{k\sqrt{s}}{2}\left(\frac{2E_4}{\sqrt{s}} + \beta_2\sin\theta\sin\theta_1\cos\theta_2 + \beta_2\cos\theta\cos\theta_1\right),
\tag{9.54}
$$

where we introduced the short-hand notation x_{p_ik} for the terms that are independent of the radiated gluon's energy. Bringing everything together we end up with

$$
\left(\frac{d\sigma}{d\Gamma_2}\right) = \left(\frac{d\sigma}{d\Gamma_2}\right)_0 \times \frac{g_s^2 C_A}{16\pi^3}\frac{\mu^{4-D}\pi^\varepsilon\,\Gamma(1-\varepsilon)}{\Gamma(1-2\varepsilon)}\int_0^{\delta_s} dk\,k^{D-3}\int_0^\pi d\theta_1\sin^{D-3}\theta_1
$$
$$
\times \int_0^\pi d\theta_2\sin^{D-4}\theta_2\left[-\frac{4(m_2^2-t)}{k^2s\,x_{p_2k}\,x_{p_4k}} - \frac{4(s-m_3^2)}{k^2s\,x_{p_3k}\,x_{p_4k}}\right].
\tag{9.55}
$$

With a little trick we can now re-express the second term of the scalar products which will be helpful for the final integration in the next step.

$$
\left(\frac{d\sigma}{d\Gamma_2}\right) = \left(\frac{d\sigma}{d\Gamma_2}\right)_0 \times \frac{g_s^2 C_A}{16\pi^3}\frac{\mu^{4-D}\pi^\varepsilon\,\Gamma(1-\varepsilon)}{\Gamma(1-2\varepsilon)}\frac{1}{s}\int_0^{\delta_s} dk\,k^{D-5}\int_0^\pi d\theta_1\sin^{D-3}\theta_1
$$
$$
\times \int_0^\pi d\theta_2\sin^{D-4}\theta_2\left[-\frac{4(m_2^2-t)}{x_{p_2k}\,x_{p_4k}} - \frac{2(s-m_3^2)}{x_{p_3k}} - \frac{2(s-m_3^2)}{x_{p_4k}}\right].
\tag{9.56}
$$

Furthermore, we can identify the soft divergence arising from the integration over the energy of the emitted gluon

$$\int_0^{\delta_s} dk \; k^{D-5} = \frac{\delta_s^{(D-4)}}{D-4} = -\frac{\delta_s^{(D-4)}}{2\varepsilon}. \tag{9.57}$$

Having been able to isolate the first infrared divergence, we now have to extract the second, collinear divergence, which is hidden within the integration over both angles, the polar angle θ_1, and the azimuthal θ_2. In the following we use again the definition $D = 4 - 2\varepsilon$. The remaining integration can be expressed in the following generic form

$$I_\varepsilon^{(l,m)} = \int_0^\pi d\theta_1 \sin^{1-2\varepsilon}\theta_1 \int_0^\pi d\theta_2 \sin^{-2\varepsilon}\theta_2 \frac{(a + b\cos\theta_1)^{-l}}{(A + B\cos\theta_1 + C\sin\theta_1\cos\theta_2)^m}, \tag{9.58}$$

where one factor depends on both, θ_1 and θ_2, the other, however, only on the polar angle θ_1. Thanks to our little trick in Eq. (9.56) we achieved also for the second summand of Eq. (9.55) this parametrization.

These kind of integrals are well known and tabulated in dedicated literature [226, 232–234]. For our cases we need two different cases. The first one $I_\varepsilon^{(0,1)}(x_{p3k})$ can be expressed only in terms of one of the two factors of Eq. (9.58) with the coefficients fulfilling the condition $A^2 \neq B^2 + C^2$ and is taken from [234]

$$\begin{aligned}
I_\varepsilon^{(0,1)} &= Y + \varepsilon Z \\
&= \frac{\pi}{\sqrt{B^2 + C^2}} \left\{ \ln\frac{A + \sqrt{B^2 + C^2}}{A - \sqrt{B^2 + C^2}} \right. \tag{9.59} \\
&+ 2\varepsilon \left[\mathrm{Li}_2\left(\frac{2\sqrt{B^2 + C^2}}{A + \sqrt{B^2 + C^2}} + \frac{1}{4}\ln^2\frac{A + \sqrt{B^2 + C^2}}{A - \sqrt{B^2 + C^2}} \right) \right] + \mathcal{O}(\varepsilon^2) \left. \right\}.
\end{aligned}$$

For later use, we introduce a short-hand notation. The variable Y denotes the term independent of ε, the parameter Z indicates the expression linear in ε. As we can see, no divergence is caused by this integral.

The other two cases $I_\varepsilon^{(1,1)}(x_{p2k}\, x_{p4k})$ and $I_\varepsilon^{(1,1)}(x_{p4k})$ fulfil the conditions $a^2 \neq b^2$ and $A^2 = B^2 + C^2$. As we expect the occurrence of a double pole in our final solution, we have to take into account all terms up to $\mathcal{O}(\varepsilon)$. However, as this is not given in the usual literature, we take a similar integral of Ref. [235] and recalculated on

permutation relations the needed case. Thus, we end up with

$$
\begin{aligned}
I_\varepsilon^{(1,1)} &= \frac{1}{\varepsilon} X + Y + \varepsilon Z \\
&= \pi \frac{1}{aA - bB} \left\{ -\frac{1}{\varepsilon} + \ln \frac{(aA - bB)^2}{(a^2 - b^2)A^2} - \varepsilon \left[\ln^2 \left(\frac{(a - b)A}{Aa - bB} \right) - \frac{1}{2} \ln^2 \left(\frac{a + b}{a - b} \right) \right. \right. \\
&\quad \left. \left. + 2\mathrm{Li}_2 \left(\frac{b(B - A)}{A(a - b)} \right) - 2\mathrm{Li}_2 \left(\frac{-b(A + B)}{Aa - bB} \right) \right] + \mathcal{O}(\varepsilon^2) \right\}.
\end{aligned}
\tag{9.60}
$$

Again, the parameter Y denotes the summand that is independent of ε, whereas the summand Z is linearly dependent. The term which give rise to a divergence, however, is indicated by X. Comparing now the coefficients A, B, C, a, b and their indices l, m with the corresponding coefficients of the scalar products of Eq. (9.54) we can make the following identifications:

First term $I_\varepsilon^{(1,1)}(x_{p_2 k}, x_{p_4 k})$:

$a =$	$\frac{2E_2}{\sqrt{s}}$	$A =$	$\frac{2E_4}{\sqrt{s}} = \frac{s - m_3^2}{s}$
$b =$	β_1	$B =$	$\beta_2 \sin\theta$
$l =$	1	$C =$	$\beta_2 \cos\theta$
		$m =$	1
$\mathbf{a^2}$	$\neq \mathbf{b^2}$	$\mathbf{A^2} =$	$\mathbf{B^2 + C^2}$

Second term $I_\varepsilon^{(0,1)}(x_{p_3 k})$:

$A =$	$\frac{2E_3}{\sqrt{s}} = \frac{s + m_3^2}{s}$
$B =$	$-\beta_2 \sin\theta$
$C =$	$-\beta_2 \cos\theta$
$m =$	1
$\mathbf{A^2} \neq$	$\mathbf{B^2 + C^2}$

Third term $I_\varepsilon^{(1,1)}(x_{p_4 k})$:

$a =$	1	$A =$	$\frac{2E_4}{\sqrt{s}} = \frac{s - m_3^2}{s}$
$b =$	0	$B =$	$\beta_2 \sin\theta$
$l =$	1	$C =$	$\beta_2 \cos\theta$
		$m =$	1
$\mathbf{a^2}$	$\neq \mathbf{b^2}$	$\mathbf{A^2} =$	$\mathbf{B^2 + C^2}$

Finally, we end up with the following integrated expression:

$$
\begin{aligned}
\left(\frac{d\sigma}{d\Gamma_2} \right) &= - \left(\frac{d\sigma}{d\Gamma_2} \right)_0 \times \frac{g_s^2 C_A}{16\pi^3 s} \frac{\pi^\varepsilon}{\Gamma(1 - 2\varepsilon)} \left(-\frac{1}{2\varepsilon} \right) \left(\frac{\mu^2}{\delta_s^2} \right)^\varepsilon \\
&\quad \times \left[4(m_2^2 - t) I_\varepsilon^{(1,1)}(x_{p_2 k} \, x_{p_4 k}) + 2(s - m_3^2) I_\varepsilon^{(0,1)}(x_{p_3 k}) \right. \\
&\quad \left. + 2(s - m_3^2) I_\varepsilon^{(1,1)}(x_{p_4 k}) \right].
\end{aligned}
\tag{9.61}
$$

Now all terms dependent on ε have to be expanded properly. They result from the solid angle expression of Eq. (9.49), the integration of the gluon's energy (cf. Eq. (9.57)) and the angular integration (cf. Eq. (9.56) with Eqs. (9.59) and (9.60)). Such we end up with the following relation

$$
\begin{aligned}
I_\varepsilon'^{(i,j)} &= \left(-\frac{1}{2\varepsilon}\right)\left(\frac{\mu^2}{\delta_s^2}\right)^\varepsilon \frac{\pi^\varepsilon\,\Gamma(1-\varepsilon)}{\Gamma(1-2\varepsilon)}\left(\frac{1}{\varepsilon}X + Y + \varepsilon Z\right) = \\
&= \frac{1}{2}\left\{-\frac{1}{\varepsilon^2}X + \frac{1}{\varepsilon}\left[-Y + \left(-\ln 4\pi + \gamma_E + \ln\frac{4\delta_s^2}{\mu^2}\right)X\right]\right.\\
&\quad -Z + \left(-\ln 4\pi + \gamma_E + \ln\frac{4\delta_s^2}{\mu^2}\right)Y \\
&\quad \left. + \frac{1}{4}\left[\pi^2 - 2(\gamma_E - \ln\pi)^2 - \ln\frac{\delta_s^2}{\mu^2}\left(4\gamma_E + 2\ln\frac{\delta_s}{\pi^2\mu^2}\right)\right] + \mathcal{O}(\varepsilon)\right\}. \qquad (9.62)
\end{aligned}
$$

Altogether, we arrive finally at the following expression in the soft limit

$$
\begin{aligned}
\left(\frac{d\sigma}{d\Gamma_2}\right) &= -\left(\frac{d\sigma}{d\Gamma_2}\right)_0 \times \frac{g_s^2 C_A}{16\pi^3 s}\left[4(m_2^2 - t)I_\varepsilon'^{(1,1)}(x_{p_2 k}\,x_{p_4 k}) + 2(s - m_3^2)I_\varepsilon'^{(0,1)}(x_{p_3 k})\right.\\
&\qquad\qquad \left. + 2(s - m_3^2)I_\varepsilon'^{(1,1)}(x_{p_4 k})\right], \qquad (9.63)
\end{aligned}
$$

which takes care for the arising soft and collinear divergences in the interference terms of gluon emission off a final state gluon with the gluon emission off an initial state squark or a final state quark, respectively. We can see that we get besides single poles, also the expected double poles.

Fig. 9.7 shows schematically how the soft-collinear matrix elements of the virtual and real contributions are connected. The above derived expression cancels the soft-collinear divergences which arise in the box and vertex corrections containing two internal gluons. The corresponding infrared divergent loop integrals are given additionally.

Hard and collinear. In the next step, we discuss the treatment of the processes which give rise to single poles in the hard and collinear limit ($\omega > \delta_s \wedge 0 \leqq s_{45} \leqq \delta_c$). This is the case for all squared matrix elements containing gluon emission off a gluon as well as for the matrix element involving the final state gluon splitting into two massless quarks.

In the collinear limit, the leading pole approximation is valid and we can factorize again the relevant $2 \to 3$ processes as a product of the tree-level and a factor containing the single poles with logarithms of δ_s and δ_c. Terms of order $\delta_s \delta_c$ can be neglected. To find the necessary expressions for the occurring processes we follow closely the procedure of Ref. [228].

Fig. 9.8 shows an example process of a gluon that is emitted of the final state gluon.

Soft-collinear divergences
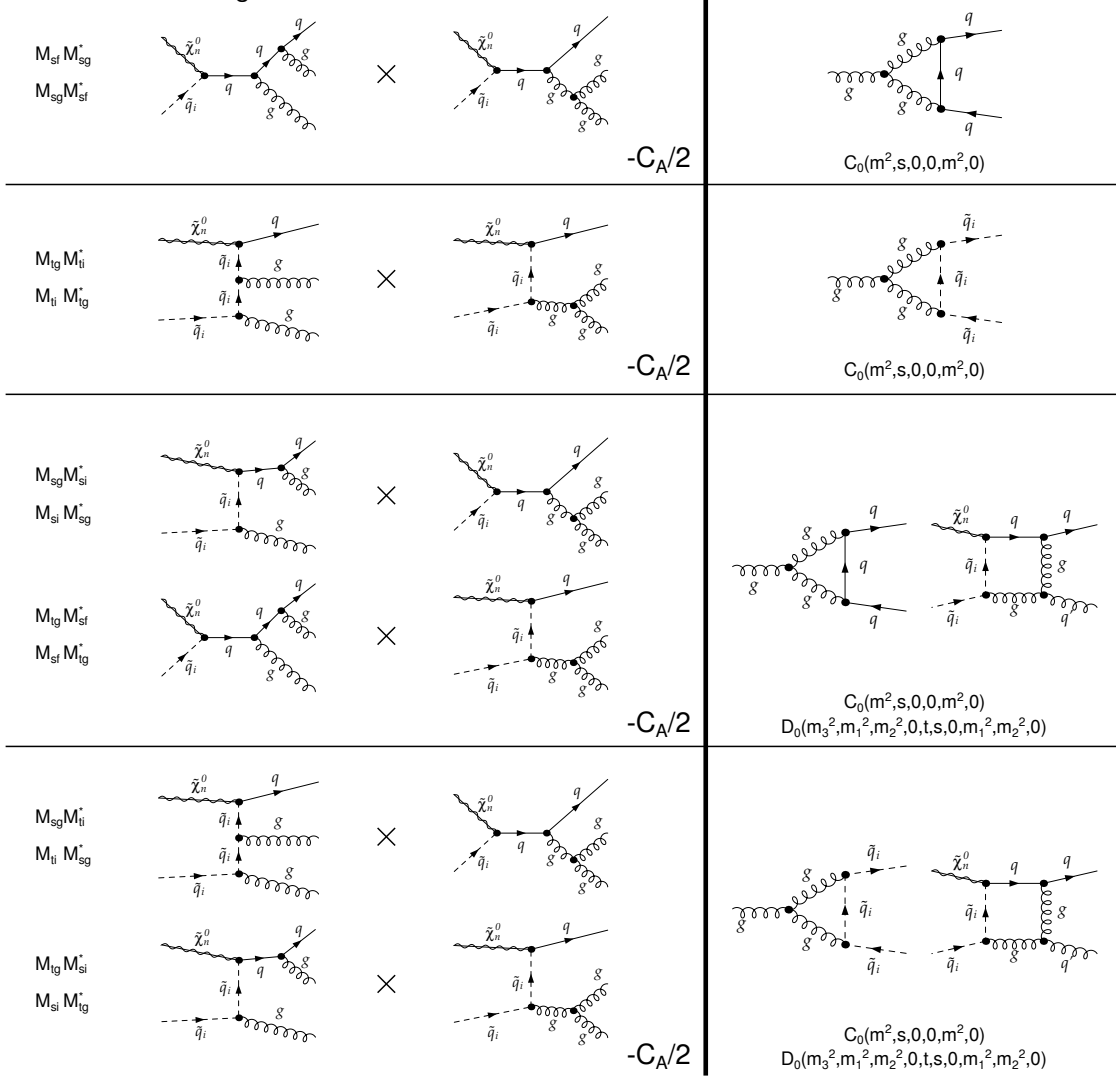
Figure 9.7: Correspondence of real (left) and virtual (right) soft-collinear diagrams. These processes arise only for a gluon in the final state. In the left column the occurring colour factor is indicated, in the right column also the corresponding infrared divergent loop integrals are given.
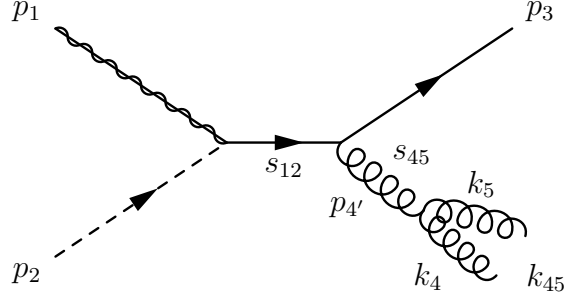
Figure 9.8: Naming convention of momenta and mandelstam variables for the derivation of the collinear approximation. The example diagram shows the radiation of a gluon off the final state gluon, which give rise to a collinear divergence.

It defines the naming convention of the momenta for the derivation of the hard and collinear approximation. In the collinear limit $\vec{k}_t^2 \ll (zk)^2$, we can express the outgoing momenta k_4 and k_5 in terms of their effective momentum $k_{45} = k_4 + k_5 + \mathcal{O}(k_t^2)$ in the following way

$$k_{45} = (k, 0, 0, k) \tag{9.64}$$

$$k_4 \simeq \left(zk + \frac{k_t^2}{2zk}, \vec{k}_t, zk \right) \tag{9.65}$$

$$k_5 \simeq \left((1-z)k + \frac{k_t^2}{2(1-z)k}, -\vec{k}_t, (1-z)k \right), \tag{9.66}$$

where $\vec{k}_t$ indicates the transverse component of particle 4, and $-\vec{k}_t$ for particle 5 in the centre-of-mass system. Hereby z denotes the momentum fraction of particle k_4 with respect to the merged D-momentum k_{45}, and $(1-z)$ the complementary fraction of particle k_5 in the direction of the z-axis. Their corresponding energies result from a Taylor series in k_t^2.

In the collinear limit, the relation $k_{45} = k_4 + k_5$ is valid, such that we can write $d^{D-1}k_{45} = d^{D-1}k_4$ assuming a fixed k_5. Thus, the 3-body phase space in D-dimensions can be written as

$$d\Gamma_3\big|_{coll} = \left[\frac{d^{D-1}p_3}{(2\pi)^{D-1}2E_3} \frac{d^{D-1}k_{45}}{(2\pi)^{D-1}2E_{45}} (2\pi)^D \delta^{(D)}(p_1 + p_2 - p_3 - p_{45}) \right] \frac{d^{D-1}k_5}{(2\pi)^{D-1}2E_5} \frac{E_{45}}{E_4}, \tag{9.67}$$

where we have used a trick, and expanded the relation with E_{45}/E_{45}. This allows us to factorize the 3-body phase space differential into a 2-body phase space differential and a factor carrying the integration over the gluon or light quark momentum that give rise to an infrared divergence. With the short-hand notation for the 2-body

phase space $d\Gamma_2$, we obtain the short expression

$$d\Gamma_3\big|_{coll} = d\Gamma_2 \frac{d^{D-1}k_5}{(2\pi)^{D-1}2E_5} \frac{E_{45}}{E_4}. \tag{9.68}$$

With the momenta definition of Eq. (9.66) we obtain the mandelstam variable s_{45} as follows

$$s_{45} = 2k_4 \cdot k_5 \simeq \frac{k_t^2}{z(1-z)}. \tag{9.69}$$

In order to rewrite the integration over the D-momentum k_5 we make use of the relation $dk_t^2 = z(1-z)ds_{45}$ and $d^{D-2}k_5 = dk_5 k_5^{D-3} d\Omega_{D-3}$ such that we arrive at

$$d\Gamma_3\big|_{coll} = d\Gamma_2 \frac{d^{D-1}k_5}{(2\pi)^{D-1}2E_5} \frac{E_{45}}{E_4} = d\Gamma_2 \frac{(4\pi)^\varepsilon \Gamma(1-\varepsilon)}{16\pi^2 \Gamma(1-2\varepsilon)} \frac{dz\, ds_{45}}{[s_{45}z(1-z)]^\varepsilon}, \tag{9.70}$$

where we have used $d\Omega_{D-3} = \frac{2\pi^{1-\varepsilon}}{\Gamma(1-\varepsilon)}$.

After having achieved to reformulate the 3-body phase space integration such that it factorizes in the 2-body integration, the similar has to be obtained for the squared matrix elements. This is accomplished by imposing collinear kinematics to the expressions of the squared $2 \to 3$ matrix elements which are proportional to the leading collinear singularity. This method is called *collinear* or *leading pole approximation*. Due to the factorization theorem the squared matrix element can then be basically written in terms of a leading order squared matrix element and an appropriate splitting kernel [236–239]. Finally, the squared $2 \to 3$ matrix elements can be written in the collinear limit as

$$\overline{\sum}|M_{1+2\to3+4+5}|^2 \simeq \overline{\sum}|M_{1+2\to3+4'}|^2 P_{44'}(z,\varepsilon) g_s^2 \mu^{2\varepsilon} \frac{2}{s_{45}}, \tag{9.71}$$

where $P_{i,j}(z,\varepsilon)$ denotes the unregulated ($z < 1$) splitting functions in D-dimensions based on the usual Altarelli-Parisi splitting kernels [240]. These splitting functions account for the probability that particle i is separated off a particle j.

Thus, the differential cross section can be written in the collinear limit ($E_{4,5} > \delta_s \wedge 0 \leqq s_{45} \leqq \delta_c$) as follows

$$\left(\frac{d\sigma}{d\Gamma_2}\right) = \left(\frac{d\sigma}{d\Gamma_2}\right)_0 \times \frac{g_s^2(4\pi\mu^2)^\varepsilon \, \Gamma(1-\varepsilon)}{8\pi^2\Gamma(1-2\varepsilon)} \int_0^{\delta_c} \frac{ds_{45}}{s_{45}^{\varepsilon+1}} \int dz \frac{P_{44'}(z,\varepsilon)}{(z(1-z))^\varepsilon}, \tag{9.72}$$

where we have considered Eq. (9.70) and Eq. (9.71). As the calculation has to be performed in dimensional regularization, we need the corresponding splitting functions

in D-dimensions. Due to the relation

$$P_{ij}(z, \varepsilon) = P_{ij}(z) + \varepsilon P'_{ij}(z), \tag{9.73}$$

the unregulated D-dimensional splitting functions can be written in terms of the usual splitting kernels in four dimensions. The relevant Altarelli-Parisi splitting functions can be found in dedicated literature, for instance in Refs. [228, 240]. For the cases studied in this work, we have to account for gluon emission off a gluon and the splitting of a light quark off a gluon. Therefore we need the following splitting kernels

$$P_{gg}(z) = 2N \left[\frac{z}{1-z} + \frac{1+z}{z} + z(1-z) \right] \qquad\qquad P'_{gg}(z) = 0 \tag{9.74}$$

$$P_{qg}(z) = \frac{1}{2} \left[z^2 + (1-z)^2 \right] \qquad\qquad P'_{qg}(z) = -z(1-z), \tag{9.75}$$

with $N = 3$ and $C_F = 4/3$.

However, until now we have not considered the integration bounds for the integral over the splitting kernels. As no soft divergence appear in case of the real emission diagram containing a $g \to q\bar{q}$ splitting, the corresponding diagrams are hard over the whole phase space. Therefore, the splitting functions are integrated over the full region of $0 \le z \le 1$.

This is in contrast to the case of a diagram involving a $g \to gg$ splitting. Here, also soft divergences can occur such that one has to ensure that both external gluons have to fulfil the hard condition

$$\delta_s \le E_{4,5} \le \frac{\sqrt{s_{12}}}{2}. \tag{9.76}$$

In the rest frame of p_1 and p_2 the energy conservation relation $(p_1 + p_2)^2 - 2k_5 \cdot (p_1 + p_2) = (p_3 + p_4)^2$ can be reformulated to $s_{12} - 2E_5\sqrt{s_{12}} = s_{34}$ such that the energies E_4 and E_5 can be expressed as

$$E_5 = \frac{s_{12} - s_{34}}{2\sqrt{s_{12}}} \quad \text{and} \quad E_4 = \frac{s_{12} - s_{35}}{2\sqrt{s_{12}}}, \tag{9.77}$$

where similar follows for particle 4. Putting Eq. (9.77) in the hard condition of Eq. (9.76) and assuming the approximations

$$s_{12} = (p_3 + k_{45})^2 \simeq m_3^2 + 2p_3 \cdot k_{45}$$
$$s_{34} = (p_3 + k_4)^2 = m_3^2 + 2p_3 \cdot k_4 \simeq m_3^2 + z(2p_3 \cdot k_{45}) \simeq m_3^2 + z(s_{12} - m_3^2)$$
$$s_{35} = (p_3 + k_5)^2 = m_3^2 + 2p_3 \cdot k_5 \simeq m_3^2 + (1-z)(2p_3 \cdot k_{45}) \simeq m_3^2 + (1-z)(s_{12} - m_3^2)$$
$$\tag{9.78}$$

the final integrations bounds are obtained

$$\frac{2\delta_s}{\sqrt{s_{12}} - \frac{m_3^2}{\sqrt{s_{12}}}} \leq z \leq 1 - \frac{2\delta_s}{\sqrt{s_{12}} - \frac{m_3^2}{\sqrt{s_{12}}}}. \tag{9.79}$$

Now we can expand all remaining factors of Eq. (9.72) that dependent on ε, and identify the collinear divergence

$$\int_0^{\delta_c} \frac{ds_{45}}{s_{45}^{\varepsilon+1}} = \left(-\frac{1}{\varepsilon}\right)\delta_c^{-\varepsilon}. \tag{9.80}$$

When now the integration is performed according to the bounds which we have derived above, we obtain the final expression for the differential cross section in the collinear limit

$$\left(\frac{d\sigma}{d\Gamma_2}\right) = \left(\frac{d\sigma}{d\Gamma_2}\right)_0 \times \frac{g_s^2}{8\pi^2}\left[\left(\frac{1}{\varepsilon} + \ln 4\pi - \gamma_E + \ln\mu^2\right)\left(A_\varepsilon^{g\to gg} + A_\varepsilon^{g\to q\bar{q}}\right)\right.$$
$$\left. + \left(A_0^{g\to gg} + A_0^{g\to q\bar{q}}\right)\right]. \tag{9.81}$$

The parameters $A_{\varepsilon,0}^{i\to jk}$ result from the integration over the splitting functions and are given by

$$A_\varepsilon^{g\to gg} = N\left[\frac{11}{6} + \ln 4\delta_s^2 - 2\ln(\sqrt{s_{12}} - \frac{m_3^2}{\sqrt{s_{12}}})\right] \tag{9.82}$$

$$A_0^{g\to gg} = N\left[\frac{67}{18} - \frac{\pi^2}{3} - \left(\ln 2\delta_s - \ln(\sqrt{s_{12}} - \frac{m_3^2}{\sqrt{s_{12}}})\right)^2\right.$$
$$\left. - \ln\delta_c\left(\frac{11}{6} + \ln 4\delta_s^2 - 2\ln(\sqrt{s_{12}} - \frac{m_3^2}{\sqrt{s_{12}}})\right)\right] \tag{9.83}$$

$$A_\varepsilon^{g\to q\bar{q}} = -\frac{n_f}{3} \tag{9.84}$$

$$A_0^{g\to q\bar{q}} = \frac{n_f}{3}\left[\ln\delta_c - \frac{5}{3}\right], \tag{9.85}$$

where $N = 3$ and n_f indicates the number of flavours. In our considered case we take $n_f = 4$, to cancel exactly the divergence which arise from the gluon self energy containing the four light quarks.

In Fig. 9.9 we show the corresponding matrix elements which cancel each other in the hard-collinear limit. The squared amplitude where a gluon is emitted off a gluon, cancels the divergent contributions, which arise due to a gluon and a ghost loop within the gluon wave function renormalization constant. The squared amplitude

Hard-collinear divergences
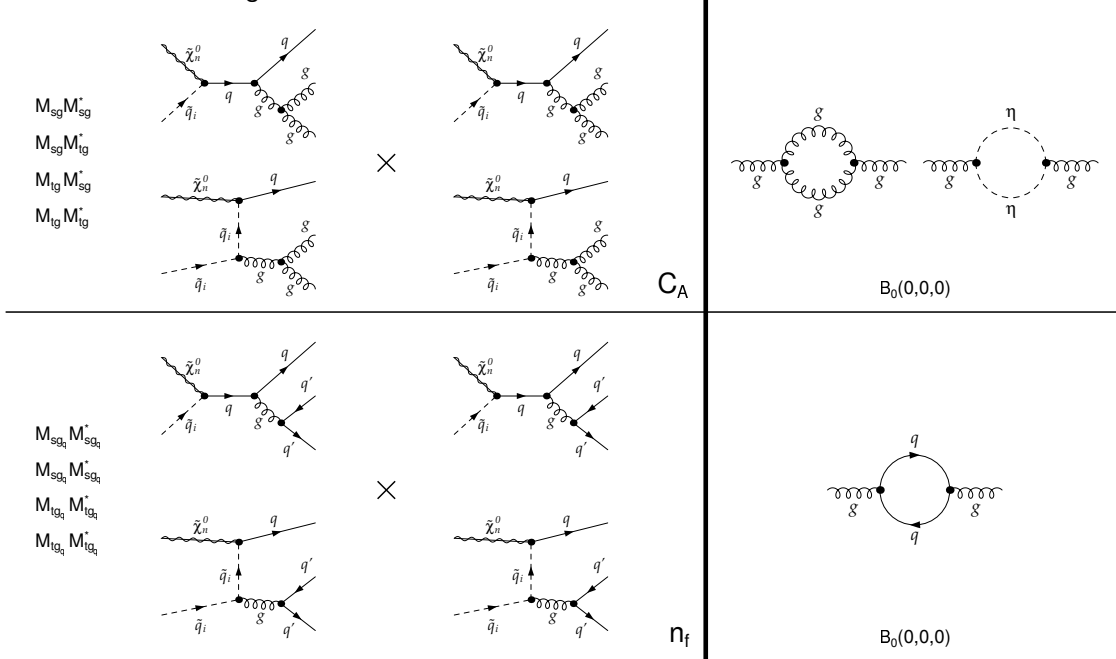
Figure 9.9: Correspondence of real (left) and virtual (right) hard-collinear diagrams. These processes arise only for a gluon in the final state. In the left column the occurring colour factor is indicated, in the right column the corresponding infrared divergent loop integrals are also given.

of emitted n_f light squarks is cancelled by the light quark loop of the gluon wave function renormalization constant.

9.3.3 Processes with a Photon in the Final State
Additional Soft Divergence

So far we have only addressed cases, where the infrared divergences were caused by the radiating gluon. However, in case of real emission of a gluon off a process with a photon in the final state $\tilde{\chi}_1^0 \tilde{t} \to t\gamma g$, also the photon can become soft in certain regions of phase space. As this would lead to numerical instabilities, we have to carefully treat the possibility of such a soft photon. Thus, we introduce similar to the treatment of a soft gluon (see Sec. 9.3.1) another cutoff and subtract the soft parts. We can formulate the soft photon expression similar to the terms we have already derived

$$\left(\frac{d\sigma}{d\Gamma_2}\right) = -\left(\frac{d\sigma}{d\Gamma_2}\right)_0 \times \frac{e^2\,q^2}{16\pi^3}\left[I'_{p_2^2}(\delta_s) + I'_{p_3^2}(\delta_s) - 2I'_{p_2p_3}(\delta_s)\right], \qquad (9.86)$$

where e denotes the electric charge and q the charge of interacting particle. In our studied case a photon that can become soft is radiated off a stop or a top such that we have $q = 2/3$. The integrals I'_{ab} are given in Eqs. (9.36) and (9.37).

As we address in our work only corrections of $\mathcal{O}(\alpha_s)$, the artificially introduced cutoff dependence cannot vanish. For a cutoff independent formulation one would have to take into account also elctroweak corrections, which is beyond the scope of this work. As the photon final state in general contributes marginally to the total coannihilation cross section in the studied scenarios (cf. Sec. 6.3), the error caused due to this kind of treatment is negligible.

9.3.4 Alternative Approach: Subtraction Methods

Besides phase space slicing, another well established approach to treat infrared divergences exists in literature: the so-called *subtraction method*. In contrast to phase space slicing, the subtraction method does not depend on any cutoff parameters, but introduces similar to the ansatz of the UV-treatment a kind of counterterm. An often used approach is the *Catani-Seymour dipole subtraction* method, see e.g. Refs. [241, 242]. When applying this method, one can write the full finite cross section as follows

$$\sigma_{NLO} = \int_{m+1} \left[\left(d\sigma^R\right)_{\varepsilon=0} - \left(d\sigma^A\right)_{\varepsilon=0} \right] + \int_m \left[d\sigma^V + \int_1 d\sigma^A \right]_{\varepsilon=0}, \qquad (9.87)$$

where $d\sigma^R$ indicates the partial cross section arising from the real contributions in $2 \rightarrow 3$ phase space, and $d\sigma^V$ denotes the virtual contributions in $2 \rightarrow 2$ phase space. In order to regularize the arising infrared divergences, an auxiliary partial cross section $d\sigma^A$ is introduced. It is a local counterterm of $d\sigma^R$ in D dimensions and cancels pointwise its singular behaviour. Hereby, the auxiliary term $d\sigma^A$ has to be chosen in such a way that at the same time also an analytical integration over the one-particle phase space in D dimensions is possible. This ensures that this term also cancels locally the infrared divergences arising from the virtual corrections and makes an integration in $D = 4$ possible.

For deriving the local counterterm $d\sigma^A$ a special factorization formula is used, which is called *dipole factorization*, and gives this method its name. In a symbolic notation it can be written as

$$d\sigma^A = \sum_{dipoles} d\sigma^B \otimes dV_{dipole}, \qquad (9.88)$$

where $d\sigma^B$ indicates a process dependent term which implies spin and color information. The expression dV_{dipole}, however, is the process independent dipole factor which takes care for the infrared behaviour and can be calculated generally for generic cases. Both is summed in spin and color and convoluted over the phase space, which is denoted by the symbol $\otimes$.

Whereas first only massless initial and final state particles have been considered for deriving the dipoles [241, 242], it has been extended to the case of massive particles and also to some specific configurations of supersymmetric particles in the initial or final state [243–245].

In a follow-up work, we plan to treat the infrared divergences also by using the Catani-Seymour approach. However, because of expected analytical subtleties we have focused first on the phase space slicing method. Having implemented both in the DM@NLO code, this will offer us an interesting possibility to compare the capability of both, the dipole subtraction method and the phase space slicing procedure. Moreover, it provides an additional powerful possibility of cross-checking. Considering previous comparisons of both approaches, for instance those performed in Ref. [246], we expect a more efficient and accurate behaviour when using the dipole subtraction method.

For completeness also other subtraction methods should be mentioned. Frequently used methods are for example the so-called *antenna subtraction* (see e.g. Refs. [247–249]), which uses a generalization of the Catani-Seymour dipole functions, or the *Frixione-Kunszt-Signer subtraction* (FKS) (see e.g. Refs. [238, 250]).

9.4 Intermediate On-shell States

Another subtlety can appear when calculating real emission contributions. In two of the real radiation diagrams of Fig. 9.2 and Fig. 9.3 intermediate on-shell states can occur. Fig. 9.10 shows the relevant cases.

When a gluon is radiated off an initial state stop (left diagram) or the propagating top quark (right diagram) in the s-channel diagram of the Wb final state, the internal top propagator can become on-shell. This leads to an extra unphysical enhancement of these processes. With $m_t > m_b + m_W$, such an enhancement can arise as soon as $\sqrt{s} > m_t$ is fulfilled and the radiating gluon carries enough energy.

When considering Fig. 9.10, one can see that these states can also be understood
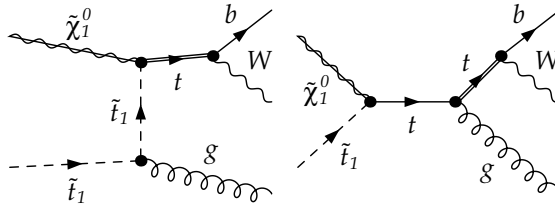
Figure 9.10: Real gluon emission off the initial state squark (left) or the propagating quark (right) with a W^+b final state. In these two cases the internal top propagator can become on-shell, as indicated by a double line.

as the corresponding tree level process $\tilde{\chi}_1^0 \tilde{t}_1 \to tg$, where the top decays further $t \to bW^+$. However, the corresponding tree level process has been already accounted

for in the calculation of the leading order processes. Considering that this process can arise from these two different sources, the LO process which decays further and the NLO contribution with an on-shell top, this would result in double counting. As for the intermediate on-shell states huge cross sections are expected for the real emission contributions, also the prediction of the neutralino relic density would be distorted, such that we cannot neglect this problem and have to treat it carefully.

Different approaches exist in literature to treat this problem. One possible method is a kind of slicing method, where the phase space region in which the top could become on-shell is cut away [251]. Requiring $|M_{bW^+} - m_t| > \delta\,\Gamma_T$ with M_{bW^+} being the invariant mass of the bottom quark and the W-boson, Γ_T the width of the top quark and δ a regulator, the relevant phase space where the top can become on-shell, is excluded. However, this approach is not independent of the chosen cutoff and also interference terms with diagrams without any intermediate on-shell states are neglected.

A second approach is the *diagram removal* (DR-I) scheme [252]. If one distinguishes the matrix elements between these contributions which can become resonant $\mathcal{M}_{res}$ and those which are non-resonant (remnant) $\mathcal{M}_{rem}$, the full matrix element can be written as

$$|\mathcal{M}|^2 = |\mathcal{M}_{res}|^2 + 2Re(\mathcal{M}_{res}^*\mathcal{M}_{rem}) + |\mathcal{M}_{rem}|^2. \tag{9.89}$$

In the diagram removal method the resonant matrix element $\mathcal{M}_{res}$ is set to zero. This means that also interference terms with non-resonant contributions are neglected. As these terms can become sizeable, this can cause uncertainties and is thus a disadvantage of this method.

Therefore a second kind of *diagram removal* (DR-II) has been introduced, where only the squared resonant matrix element $|\mathcal{M}_{res}|^2$ is set to zero. In this case interference terms are retained [253]. Both diagram removal methods have in common that they break gauge invariance and lead thus to arbitrary results, as it is not guaranteed that the neglected contributions are small [254].

Another possibility is the so-called *local on-shell subtraction* (DS), which retains gauge invariance and keeps also the interference terms of resonant and non-resonant contributions. As firstly introduced in Ref. [255], it is also called the PROSPINO-*approach* and is quite frequently used until today (cf. Refs. [254–257]). Due to its obvious advantages we apply it also in our case.

Within this approach, the problematic propagator is regularized by substituting for a Breit-Wigner propagator in the amplitudes of the two resonant diagrams

$$\frac{1}{p^2 - m^2} \longrightarrow \frac{1}{p^2 - m^2 + im\Gamma} \tag{9.90}$$

with a finite width Γ. However, the width has not to be the physical width of the propagator particle. It is sufficient to introduce a small mathematical regulator to

stabilize the integration as the calculation will not depend on it.

In order to solve the problem regarding double counting, a kind of counterterm ($|\mathcal{M}_{res}^{sub}|^2$) is introduced.

$$|\mathcal{M}|^2 = |\mathcal{M}_{res}|^2 - |\mathcal{M}_{res}^{sub}|^2 + 2Re(\mathcal{M}_{res}^*\mathcal{M}_{rem}) + |\mathcal{M}_{rem}|^2. \qquad (9.91)$$

This counterterm is defined as

$$|\mathcal{M}_{res}^{sub}|^2 = \frac{m_t^2\Gamma_t^2}{(p_t^2 - m_t^2)^2 + m_t^2\Gamma_t^2}\,|\mathcal{M}_{res}|_{p_t^2=m_t^2}^2. \qquad (9.92)$$

The $2 \rightarrow 3$-matrix element, which is set exactly on-shell, is multiplied with a Breit-Wigner distribution, with the momentum p_t not being fixed on-shell. When the top-quark gets on-shell, the subtraction term is equal to the full $2 \rightarrow 3$ matrix element, while it decreases as a Breit-Wigner distribution when the top moves away from its pole.

Thus we managed to remove locally the resonant terms, but retain at the same time possible interference terms, which can give rise to significant contributions.

We have checked that the total cross section after subtraction is independent of the top width.

10 Impact of the One-Loop Corrections

Having implemented the full one-loop calculation in the `DM@NLO` code, a precise analysis of the impact of these corrections on the cross section and the neutralino relic density is possible. To do so, we study the effect of the corrections based on the scenarios introduced in Sec. 6.3. As they feature different dominant final states, it allows us to discuss several interesting aspects of the phenomenology.

In the following, the main focus lies on the discussion of the corrections involving a Higgs boson, additionally, key features of the electroweak vector bosons are addressed.[1]

10.1 Impact on the Total Cross Section

Before discussing the effect of the supersymmetric QCD corrections on the neutralino relic density, we investigate the direct impact of the one-loop calculation on the total coannihilation cross section.

To get an idea of the interplay of the different calculated loop corrections, Fig. 10.1 shows a break down of the total next-to-leading order correction (without the tree-level) into individual UV-finite contributions. This overview is shown for the two processes $\tilde{\chi}_1^0 \tilde{t}_1 \to t h^0$ (Scenario I) and $\tilde{\chi}_1^0 \tilde{t}_1 \to t Z^0$ (Scenario II). The contributions arising from the virtual part of the calculation including propagators, vertices and boxes, as well as the real contribution is depicted. Although each individual contribution is UV-finite due to the renormalization procedure, the vertex, box and the real part still contain IR-divergent expressions. This leads to a certain ambiguity in their exact definition. Each contribution contains an uncancelled pole together with an uncancelled logarithm of the large factorization scale. Within the calculation these relics of the infrared treatment are absorbed by the real part, which consists of the soft part calculated by using the eikonal approximation and the hard radiation. Due to the large logarithms, the box contribution gets artificially large and leads to a negative correction of the real emission part in order to ensure a complete absorption. Therefore, no quantitative statement on these corrections is possible. However, we are able to make a qualitative comparison between the corrections of both final states depicted in Fig. 10.1.

For the Higgs final state, the contributions of the propagator and the box is enhanced

---

[1] As a last numerical cross-check regarding the soft-collinear contributing diagrams of the gluon final state could not been finalized until the thesis was to be finished, we take into account only the Higgs and electroweak vector bosons for the subsequent study.
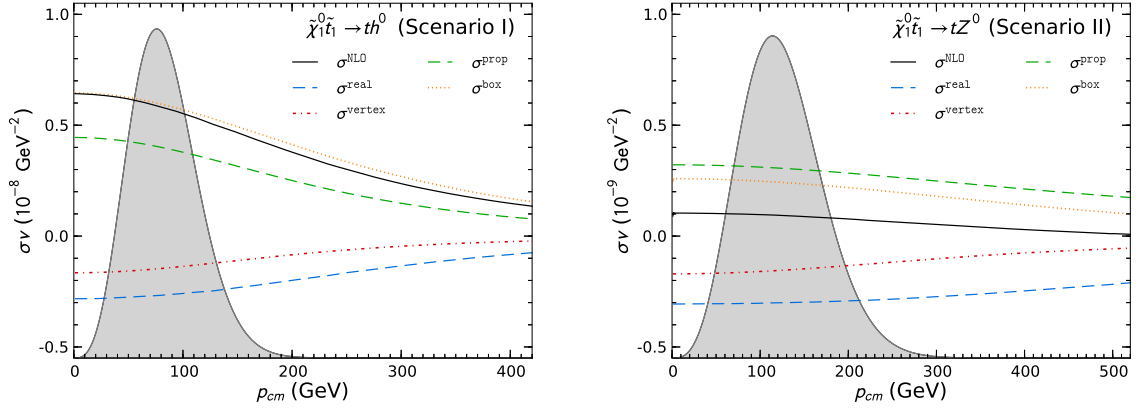
Figure 10.1: Absolute contribution of the different corrections to the total next-to-leading order correction for the case of coannihilation into th^0 (Scenario I) and into tZ^0 (Scenario II). The tree-level contribution is not contained in σ^{NLO}. The grey area indicates the thermal distribution (in arbitrary units).

in contrast to the Z-boson final state. This is caused by the significant contribution of the t-channel exchange in case of a Higgs boson in the final state, which driven by the large trilinear coupling. The t-channel diagram receives a correction to the stop propagator and the box diagram where a gluon is exchanged between the final state quark and the initial state squark. This leads to enhanced box and propagator corrections, and lead to a large overall NLO correction in the case of coannihilation with a Higgs boson in the final state.

After studying the individual contributions of the one-loop corrected result, we focus now on the quantitative correction to the cross section. To this end, Fig. 10.2 shows for different final states of each scenario the impact of the full next-to-leading order calculation. The total cross section is depicted in dependence of the center-of-mass momentum for the effective tree-level computation of `MicrOMEGAs` (orange solid line), the tree-level calculation as implemented in `DM@NLO` (black dashed line), and the full one-loop result (blue solid line). The grey shape, which gives the thermal distribution in arbitrary units according to Eq. (4.28), allows one to estimate the range of center-of-mass momentum which is relevant for the relic density calculation. The lower panel of each plot depicts the ratio of the aforementioned cross sections.

The upper left subfigure of Fig. 10.2 shows the results for the process $\tilde{\chi}_1^0 \tilde{t}_1 \to th^0$ of Scenario I. We clearly see that both tree-level computations, the one performed by `MicrOMEGAs` and the one computed by our `DM@NLO` implementation are in perfect agreement. Furthermore, the full one-loop contribution is depicted. Through the SUSY-QCD corrections the cross section is enhanced by about 30 %. This is caused by the large contribution from the box diagrams and propagator corrections as discussed before.
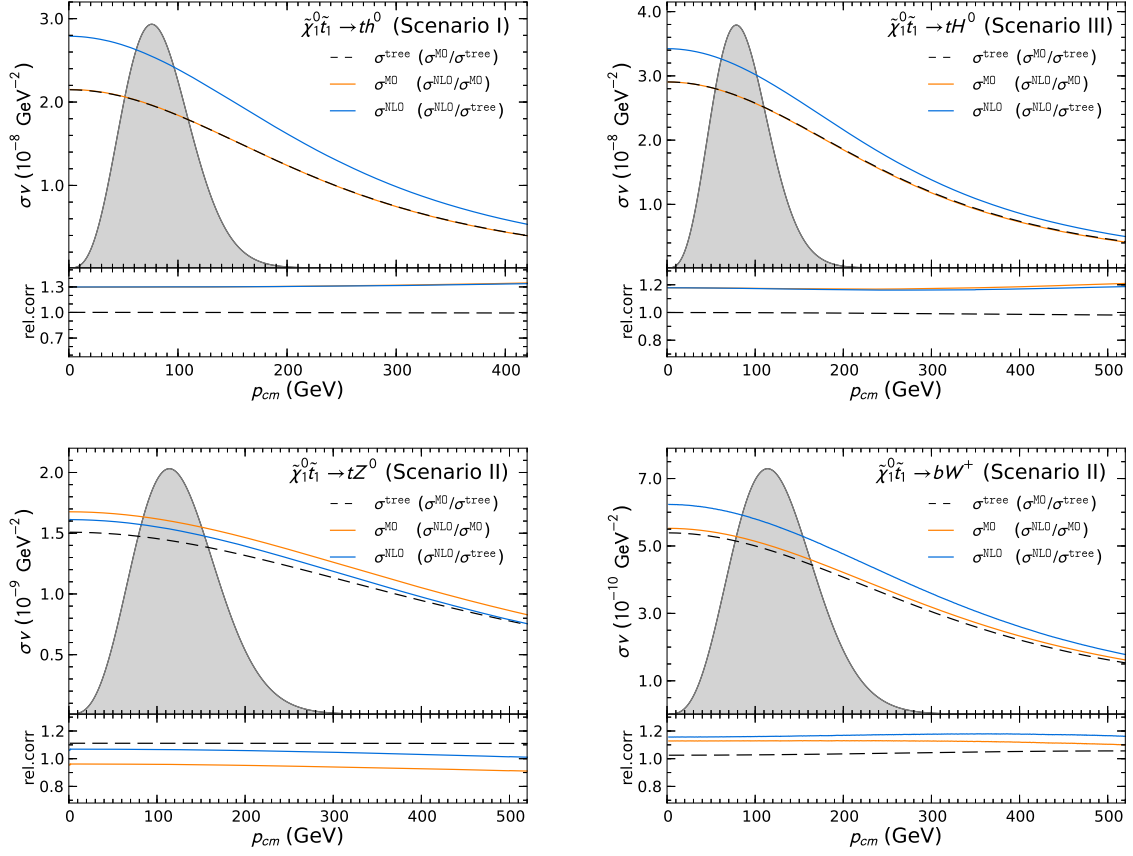
Figure 10.2: Tree-level (black dashed line), full one-loop (blue solid line) and `MicrOMEGAs` (orange solid line) cross sections for selected coannihilation channels of the scenarios of Tab. 6.2. The upper part of each plot shows the absolute value of σv and the thermal distribution (grey, in arbitrary units), whereas the lower part shows the corresponding relative shifts (second item in the legend).

Similar behaviour is observed for Scenario III, where the final state with a heavy Higgs boson H^0 plays an important role. The same explanation as for the lightest Higgs final state accounts here. For this case, the one-loop cross section lies about $18 - 20$ % above the tree-level contribution. Both tree-level calculations, the one implemented in `DM@NLO` and the one of `MicrOMEGAs` are again in very good agreement to each other.

Those observations are in contrast to the results shown for the processes $\tilde{\chi}_1^0 \tilde{t}_1 \to t Z^0$ and $\tilde{\chi}_1^0 \tilde{t}_1 \to b W^\pm$ of Scenario II. In these scenarios, a significant shift of about 10 % between the two tree-level calculations is visible. However, this behaviour is well understood, and arises due to our choice of the renormalization scheme. It is caused by the different definition of the squark mixing angles, which enter the calculation through different interactions between squarks and quarks. The processes containing a Higgs in the final state are dominated by the t-channel diagram. In this diagram two of these interactions appear. The mixing angle $\theta_{\tilde{t}}$ enters the neutralino-squark-quark vertex as well as the squark-squark-Higgs coupling. As the internal propagator has to be summed over the two possible squark mass eigenstates, $\tilde{t}_1$ and $\tilde{t}_2$, the result gets less sensitive to the exact value of the mixing angle. This is in contrast to the diagram with a Z^0-boson in the final state, where the s-channel dominates the cross section. In this case, only the neutralino-squark-quark vertex contains an interaction between squarks and quarks, and the squark eigenstate is fixed due to the initial state quark. Therefore, the processes with an electroweak vector boson in the final state are much more sensitive than the diagrams containing a Higgs boson.

We have checked this behaviour numerically and are able to recover the original `MicrOMEGAs` tree-level value by changing our definition of the mixing angles. An additional flag is implemented for changing between these two definitions, which enables an easy comparison of the tree-level cross section calculated by `MicrOMEGAs` and `DM@NLO`.

10.2 Impact on the Neutralino Relic Density

After having discussed the impact of the calculated one-loop corrections on the cross section for specific processes, we concentrate now on their impact on the neutralino relic density. As the three different scenarios, introduced in Sec. 6.3, feature different dominant and subdominant final states, we are able to investigate the interplay of their individual one-loop corrections.

First, we discuss the change of the relic density $\Omega_{\mathrm{CDM}} h^2$ when a single input parameter is varied. In Fig. 10.3 this is studied for Scenario I by varying the bino mass parameter M_1 (left panel), and the trilinear coupling T_t (right panel), respectively. Again, the same colour code is used as in the previous figures: The default `MicrOMEGAs` tree level is depicted as an orange solid line, the `DM@NLO` tree level as a black dashed line, and our full one-loop corrected result as blue solid line. A
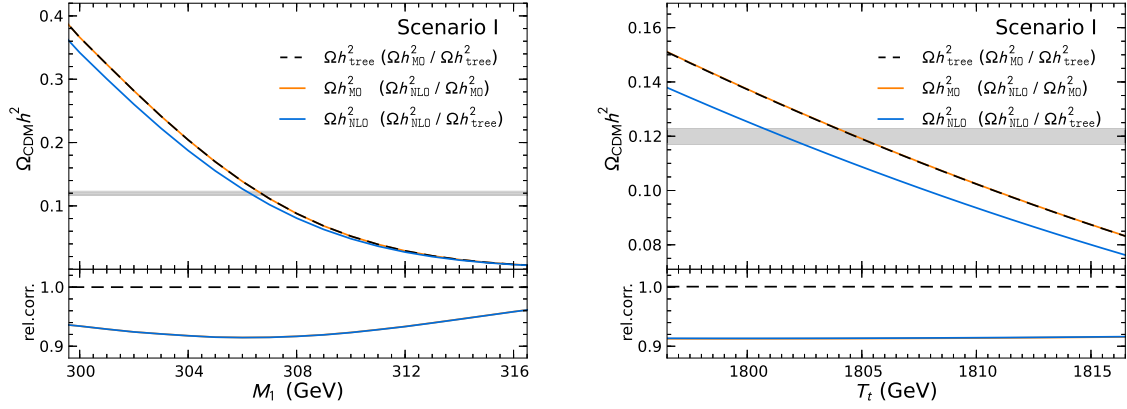
Figure 10.3: The neutralino relic density $\Omega_{CDM}h^2$ as a function of M_1 (left) and T_t (right) calculated by using different coannihilation cross sections: default `MicrOMEGAs` (orange solid line), and `DM@NLO` tree level (black dashed line), as well as the full one loop (blue solid line). The grey band indicates the PLANCK favoured range of the relic density according to Eq. (3.12). The lower part shows the relative impact of the one-loop correction on the relic density compared to the tree-level calculation.

grey band shows the PLANCK favoured range of the neutralino relic density (cf. Eq. (3.12)).

The left subfigure shows that the relic density is highly sensitive to variations in the bino mass parameter. This is due to reasons which have been already discussed in Sec. 6.1. By tuning M_1 to higher values, the mass gap between the lightest neutralino and the stop becomes smaller and thus stop-stop annihilation is enhanced. Due to the large cross section of stop-stop annihilation, this leads to a significant smaller value for the relic density, which is not any longer in agreement with the range favoured by PLANCK. However, when the value of M_1 decreases, the mass gap gets enlarged. Thus, neutralino-stop coannihilation and stop-stop annihilation gets much less important in favour of neutralino-neutralino annihilation. As the latter features a quite small cross section, the predicted relic density becomes quickly too large.

The left subfigure of Fig. 10.3 allows us also to make a quantitative comparison of the differently calculated relic density predictions. Our tree level result is very well in agreement with the relic density computed by `MicrOMEGAs`. However, within the PLANCK favoured range a significant shift is visible between the relic density calculated by default `MicrOMEGAs` and the one computed by using our full next-to-leading order correction.

In the lower part of the plot, the ratios of the differently evaluated relic density are depicted. In blue the ratio of the full NLO calculation and the tree-level calculation is shown. The SUSY-QCD corrections result in a relative correction of around 9 %

to the relic density evaluated on the basis of the tree level cross section. For Scenario I, this can be explained due to the dominance of the lightest Higgs in the final state, which contributes around 38.5 % (cf. Tab. 6.3) to the total (co)annihilation cross section with a corresponding correction of around 30% (cf. Fig. 10.2).

A similar plot is given in the right subfigure of Fig. 10.3. Here, the trilinear coupling parameter is slightly varied around the input value of Scenario I, $T_t = 1806.5$ GeV. Higher values for T_t enlarge the stop mass splitting, which results in a smaller mass gap for a fixed neutralino mass and thus leads to enhanced stop-stop annihilation. Smaller values for T_t reduce the mass splitting such that neutralino annihilation is dominant. The observed shift of the predicted relic density corresponds roughly to a shift of 3 GeV in the trilinear coupling parameter.

For an even better estimate of the impact of the loop corrections, a closer look to the parameter space is interesting. Therefore, we performed for each scenario 2-dimensional scans in dependence of the third generation squark mass parameter $M_{\tilde{q}_3}$ and the bino mass parameter M_1 (left column) as well as in dependence of the trilinear coupling parameter T_t and the bino parameter M_1 (right column). The corresponding plots are depicted in Fig. 10.4.

In all subfigures the PLANCK-favoured region of parameter space within an 1σ interval is marked as a band. In orange we show the cosmologically favoured region based on the default `MicrOMEGAs` calculation, in blue based on our full one-loop calculation. A clear separation of the two bands is visible for all scenarios, which indicates that the resulting corrections are larger than the current experimental uncertainties. Therefore, they have to be considered in order to obtain realistic estimations on the cosmologically favoured region of parameter space.

First, we concentrate on the plots of Fig. 10.4 with respect to Scenario I. For this scenario, the separation of the two relic density bands is most significant. This is due to the clear dominance of the process with the lightest Higgs in the final state which contributes with 38.5 % to the total cross section. As already discussed before, it achieves corrections up to 9 % and thus leads to a significant shift of the cosmologically favoured region of parameter space. In black lines the relative impact of the one-loop corrections for the whole $(M_{\tilde{q}_3}, M_1)$ plane is shown. With greater distance from the relic density bands, also the impact of the studied corrections decrease. This is due to less contribution of neutralino-stop processes to the total cross section, which are the only processes we correct within this analysis.

It also attracts attention that the PLANCK-favoured band follows a straight line in the $(M_1, M_{\tilde{q}_3})$ plane, which corresponds to a constant mass difference between the lightest neutralino and the lightest stop of about 40 GeV. Above the cosmologically allowed band the neutralino becomes heavier and the mass difference decreases. As a consequence, stop-stop annihilation becomes dominant. As stop-stop annihilation has typically a significantly higher cross section than the coannihilation processes, this leads to a too small neutralino relic density. For large values of M_1 (grey area in
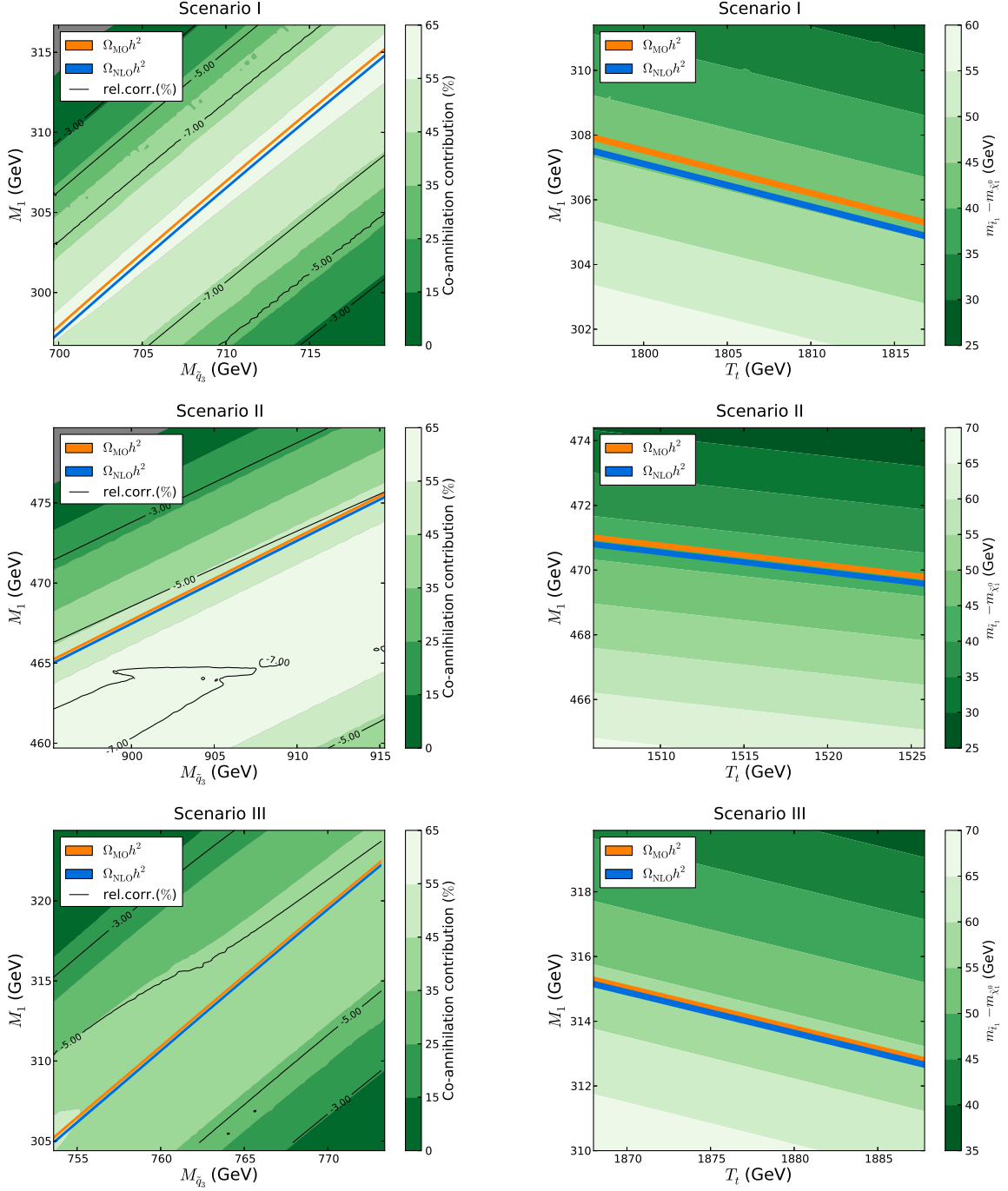
Figure 10.4: PLANCK-compatible relic density bands from default `MicrOMEGAs` calculation (orange) and our one-loop calculation for coannihilation (blue) in the $(M_{\tilde{q}_3}, M_1)$ (left) and (T_t, M_1) (right) planes. In the plots on the left hand side the relative contribution of coannihilation processes is shown in green contour, and the relative impact of the one-loop corrections on the relic density in black lines. The plots on the right hand side show the LSP-NLSP mass difference in green contour.

the upper left corner) the stop becomes the lightest supersymmetric particle. This particle, however, is disfavoured as dark matter candidate because it carries electric and colour charge. Below the cosmologically allowed band, the mass difference gets larger and thus the neutralino-stop and stop-stop (co)annihilation becomes more and more Boltzmann suppressed. The neutralino annihilation, which has a lower cross section, becomes now dominant, which results in a too large relic density. The relative contribution of neutralino-stop coannihilation is depicted in shades of green. On the right hand side of Fig. 10.4, the (T_t, M_1) plane is shown. Again, a clear separation of the two relic density bands is visible, together with a moderate dependence on the trilinear coupling parameter T_t (see discussion of Fig. 10.3). In different green colours the mass difference between the lightest and next-to-lightest supersymmetric particle is depicted. It confirms the statement that the PLANCK-favoured region follows a line of a constant mass difference of around $40 - 45$ GeV.

We can conclude that the impact of the studied one-loop corrections on the dark matter relic density is larger than the current experimental uncertainties by PLANCK. In the second row we show the similar 2-dimensional plots for Scenario II, in which in particular two processes dominate the cross section, namely the $t\,h^0$ final state with 24.6 % and the $t\,Z^0$ final state with 10.7 %. Whereas the Higgs final state receives large corrections, the correction to the process involving a Z-boson is quite small (cf. Fig. 10.2). Combining both processes, the correction of the total cross section is not as large as for Scenario I. This is due to a smaller contribution of the Higgs final state, and the much smaller correction of the $t\,Z^0$ final state (in comparison to `MicrOMEGAs` the correction of the $t\,Z^0$ final state even differs in sign with respect to the corrections obtained for the other final states). Therefore, the loop corrections for Scenario II result only in a correction of about $5 - 6$ %. The PLANCK favoured relic density bands obtained by using the default `MicrOMEGAs` (orange) and our full one-loop corrections (blue) are not as significantly separated as for Scenario I.

Another interesting feature of Scenario II is visible in the left subfigure. For this scenario, the preferred PLANCK region lies outside the area of maximal contribution of neutralino-stop coannihilation. This effect arises from the importance of the coannihilation process involving a Z-boson. With the process $\tilde{\chi}_1^0\tilde{t}_1 \rightarrow t\,Z^0$ featuring a lower cross section, neutralino-stop coannihilation is not sufficient any more in order to achieve a total (co)annihilation cross section that results in a relic density which is in agreement with the PLANCK measurements. Thus, in this parameter region, stop-stop annihilation is needed to obtain the right value for the dark matter relic density. It is striking for Scenario II that coannihilation dominates for a comparable large mass difference between the stop and the lightest neutralino of about 70 GeV. However, this can be explained by having a closer look at Tab. 6.2. In comparison to the two other scenarios, the masses of the lightest neutralino and stop are much heavier. As the freeze-out temperature is proportional to the mass of the dark matter particle $T_F = m_\chi x_F$ with $x_F \approx 27$, an increased neutralino mass leads also to an increased freeze-out temperature. This results in weaker Boltzmann suppression

in this scenario (cf. 4.21) such that the same suppression which is achieved for a mass difference of $40 - 45$ GeV in Scenario I, is obtained for a larger mass splitting of 70 GeV in Scenario II. Thus, neutralino-stop coannihilation is also possible for larger mass differences between the LSP and NLSP.

Finally, we study further the phenomenology of Scenario III, where the light CP-even Higgs boson dominates the neutralino-stop coannihilation with 20.7 %, followed by the process involving the lightest neutral Higgs boson with 14.2 %. As depicted in Fig. 10.2, the correction on neutralino-stop coannihilation with a CP-even Higgs boson in the final state accounts for 20 % to the cross section. This is not as large as for the process with the lightest neutral Higgs boson in the final state. Thus, the effect on the relic density is consequently smaller than for Scenario I. Nevertheless, an overall impact of $5 - 6$ % to the relic density is reached. This leads also in this scenario to a separation of the PLANCK favoured relic density band calculated by `micrOMEGAs` and the one calculated with the full one-loop SUSY-QCD corrections. Although the mass difference between the LSP and NLSP seems to be quite large with 55 GeV in this scenario, this is in perfect agreement with the other scenarios. As discussed above, the important key parameter is the value of $\Delta M = (m_{\tilde{t}_1} - m_{\tilde{\chi}_1})/m_{\tilde{\chi}_1}$ (see discussion in Sec.6.1), which is with $\Delta M = 0.18$ in a similar ball park as Scenario I with $\Delta M = 0.14$, for instance.

Conclusions. We have studied the impact of the supersymmetric QCD corrections on the (co)annihilation cross section as well as on the neutralino relic density. A clear separation of the cosmologically preferred region by PLANCK is visible. Thus, the one-loop corrections exceed the experimental uncertainties and are important to be taken into account in order to obtain a realistic estimation on the favoured regions of parameter space.

As the corrections will be publicly available within the package `DM@NLO`, it can be used in order to improve studies of parameter space and global fits.

11 Conclusions

Although the Standard Model of particle physics has demonstrated its success during the last decades, it has several shortcomings. For instance, it does not provide a particle which can account for the main component of dark matter. Therefore, we have discussed several dark matter candidates which could extend the Standard Model of particle physics. One example on which we have focused in this thesis is the MSSM with conserved R-parity. It provides naturally a good cold dark matter candidate, the lightest neutralino.

Due to measurements of the cosmic microwave background by WMAP and the Planck satellite, the value of the dark matter relic density is very precisely determined. We have studied in detail the derivation of the relic density calculation. One significant quantity which enters directly the theoretical prediction of the relic density is the cross section of annihilation and coannihilation processes. Besides neutralino pair annihilation, also coannihilation of the neutralino and the next-to-lightest supersymmetric particle can contribute significantly, when both particles are almost mass degenerate.

Based on an example scenario we have intensively studied the interplay between neutralino-pair annihilation, neutralino-stop coannihilation and stop-stop annihilation with respect to their impact on the relic density. We have demonstrated that besides neutralino-neutralino annihilation, neutralino-stop coannihilation is one important process in order to not overclose the universe. Thus, it should not be neglected for a precise computation of the relic density. Moreover, it has been shown that also in the context of the discovery of a 125 GeV Higgs boson neutralino-stop coannihilation is phenomenologically very well motivated.

In order to study the phenomenology of neutralino-stop coannihilation further, we have performed an extensive parameter study. We have been able to show that neutralino-stop coannihilation contributes significantly to the total coannihilation cross section, especially regarding the process with a lightest Higgs boson in the final state. Due to the demonstrated phenomenological importance we have performed the full supersymmetric next-to-leading order QCD corrections to neutralino-squark coannihilation. We have presented details of our calculation, and described our $\overline{\text{DR}}$/on-shell renormalization scheme. It has been chosen in order to ensure a stable calculation for wide regions of parameter space, also with respect to neutralino-pair annihilation. Further, we have discussed the treatment of the occurring infrared divergences. We have shown in detail the performed phase space slicing method, which has been used to isolate soft and collinear divergences. We have derived the neces-

sary terms for the cancellation of soft divergences in case of massive final states and have introduced the two-cutoff approach for a gluon in the final state. Further, we have pointed out the special treatment of intermediate on-shell states in case of a $W^{\pm}$ in the final state.

Taking everything together we have arrived at a fully convergent SUSY-QCD next-to-leading order calculation[1]. Based on three example scenarios we have studied the impact of the corrections on the total coannihilation cross section. Especially for the light Higgs boson in the final state, we have achieved corrections of around 30 %. This leads to an significant effect on the prediction of the relic density. We have reached corrections of around 10 %. As this effect is larger than the experimental uncertainties of the Planck satellite, a significant shift within the studied parameter space has been caused. Thus, it is important to take these corrections into account in order to obtain a precise theoretical relic density prediction.

Therefore, we have implemented the SUSY-QCD corrections in `DM@NLO`. This computing tool can be linked to existing software packages like `MicrOMEGAs` and `DarkSUSY`, which compute the relic density for a specific point in the MSSM parameter space. Making `DM@NLO` publicly available in the future, it can be of interest for everybody who includes the relic density constraint in a parameter study or a global fit.

For the future we plan to join the different subprojects of `DM@NLO` which we have introduced in Chapter 5. This will allow us to perform phenomenological studies in further regions of the parameter space and is expected to show a similar striking impact of SUSY-QCD corrections on the neutralino relic density prediction. Based on the work performed within this thesis, an extension to models beyond the MSSM would also be possible. Due to the generic implementation of our calculation, this can be achieved with a reasonable effort. One example for such an extension could be the NMSSM. Further, it would be interesting to consider Sommerfeld enhancement. This has been studied in the literature quite recently [258–260] and is also expected to have a non-negligible impact.

All in all, we have shown that the performed SUSY-QCD corrections have a significant impact on the neutralino relic density prediction. This topic connects many different fields of research, offers a broad phenomenology, and give rise to many interesting new questions.

---

[1] As a last final IR-convergence check regarding the gluon final state has not been finalized yet, we have restricted ourselves to studying only the processes with a Higgs or electroweak vector boson in the final state.

Acknowledgements

I would like to conclude with dedicating some lines to those people who made this work possible. In particular, I would like to thank
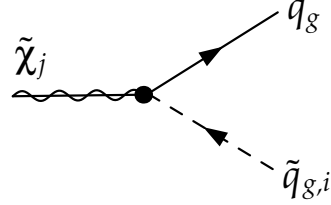
- all my colleagues, especially those from building 1b, but also the whole Theory group for the great working atmosphere. In particular, I would like to thank *Tomas Kasemets* for his encouraging words in moments of frustration. Thanks also to *Aoife Bharucha* who motivated me especially during the last weeks a lot! Last but not least, I would like to thank also *Frank Tackmann*, who has had always an open door for both, scientific discussions and personal advice.

- all the people from the LAPTh for welcoming me so warmly. Especially, thanks to *Andreas Goudelis*, *Diego Guadagnoli* and *Tiago Dinis da Fonseca*.

- all my friends who have always been understanding especially during the last months... In particular, I would like to thank *Nicole* and *Flo* for all the years of friendship, and my good friend *Patrick* for all the long night discussions about politics, computer science and personal topics.

- my *parents*, who have always believed in me. Thanks for your endless support, for motivating me in frustrating times and for encouraging me in going my way.

- *Bene* for sharing all the years with me, for all the great moments and for your support in bad times – thanks for just being you!

A Couplings

We present all necessary couplings with respect to neutralino-stop coannihilation. As mixing between generations is not taken into account, the generation index g is suppressed in the following.

A.1 Neutralino-Squark-Quark

$$\hat{A}^q_{ij} = i\left[A^{q\,L}_{ij}P_L + A^{q\,R}_{ij}P_R\right] \qquad \text{(A.1)}$$

Up-type squark/quark

$$A^{u\,R}_{ij} = -\frac{g_2 m_u}{\sin\theta_W \sqrt{2}M_W \sin\beta}N_{j\,4}U^u_{i2} \tag{A.2}$$
$$-\sqrt{2}\frac{g_2}{\sin\theta_W}\left((q_u - I_{3_u})\frac{\sin\theta_W}{\cos\theta_W}N_{j\,1} + I_{3_u}N_{j\,2}\right)U^u_{i1}$$
$$A^{u\,L}_{ij} = -g_2\frac{m_u}{\sin\theta_W \sqrt{2}M_W \sin\beta}N^*_{j\,4}U^u_{i1} \tag{A.3}$$
$$+\sqrt{2}g_2\frac{q_u}{\cos\theta_W}N^*_{j\,1}U^u_{i2}$$

Down-type squark/quark

$$A^{d\,R}_{ij} = -g_2\frac{m_d}{\sin\theta_W \sqrt{2}M_W \cos\beta}N_{j\,3}U^d_{i2} \tag{A.4}$$
$$-\sqrt{2}\frac{g_2}{\sin\theta_W}\left(I_{3_d}N_{j\,2} + (q_d - I_{3_d})\frac{\sin\theta_W}{\cos\theta_W}N_{j\,1}\right)U^d_{i1}$$
$$A^{d\,L}_{ij} = -g_2\frac{m_d}{\sin\theta_W \sqrt{2}M_W \cos\beta}N^*_{j\,3}U^d_{i1} \tag{A.5}$$
$$+\sqrt{2}g_2\frac{q_d}{\cos\theta_W}N^*_{j\,1}U^d_{i2}$$

A.2 Chargino-Squark-Quark

Up-type squark/quark

$$A_{ij}^{u\,L} = \frac{g_2 m_d}{\sin\theta_W \sqrt{2} M_W \cos\beta} W_{j\,2}^* U_{i1}^u \tag{A.6}$$

$$A_{ij}^{u\,R} = -\frac{g_2}{\sin\theta_W} V_{j\,1} U_{i1}^u + \frac{g_2 m_u}{\sin\theta_W \sqrt{2} M_W \sin\beta} V_{j\,2} U_{i2}^u$$

Down-type squark/quark

$$A_{ij}^{d\,L} = \frac{g_2 m_u}{\sin\theta_W \sqrt{2} M_W \sin\beta} V_{j\,2}^* U_{i1}^u \tag{A.7}$$

$$A_{ij}^{d\,R} = -\frac{g_2}{\sin\theta_W} W_{j\,1} U_{i1}^u + \frac{g_2 m_d}{\sin\theta_W \sqrt{2} M_W \cos\beta} W_{j\,2} U_{i2}^u$$

A.3 Quark-Quark-Higgs

$$\hat{F}_\Phi^q = i\left[F_\Phi^{q\,L} P_L + F_\Phi^{q\,R} P_R\right] \tag{A.8}$$
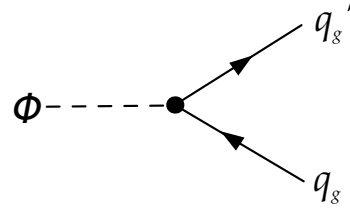
Up-type quark

$$F_{h^0}^{u\,L} = -\frac{g_2 m_u \cos\alpha}{\sin\theta_W 2 M_W \sin\beta}, \qquad F_{h^0}^{u\,R} = F_{h^0}^{u\,L} \tag{A.9}$$

$$F_{H^0}^{u\,L} = -\frac{g_2 m_u \sin\alpha}{\sin\theta_W 2 M_W \sin\beta} \qquad F_{H^0}^{u\,R} = F_{H^0}^{u\,L} \tag{A.10}$$

$$F_{A^0}^{u\,L} = -\frac{i g_2 m_u \cos\beta}{\sin\theta_W 2 M_W \sin\beta} \qquad F_{A^0}^{u\,R} = -F_{A^0}^{u\,L} \tag{A.11}$$

$$F_{H^+}^{u\,L} = \frac{g_2 m_d \sin\beta}{\sqrt{2} \sin\theta_W M_W \cos\beta} \tag{A.12}$$

$$F_{H^+}^{u\,R} = \frac{g_2 m_u \cos\beta}{\sqrt{2} \sin\theta_W M_W \sin\beta} \tag{A.13}$$

Down-type quark

$$F_{h^0}^{dL} = \frac{g_2 m_d \sin\alpha}{\sin\theta_W 2M_W \cos\beta} \qquad\qquad F_{h^0}^{dR} = F_{h^0}^{dL} \tag{A.14}$$

$$F_{H^0}^{dL} = -\frac{g_2 m_d \cos\alpha}{\sin\theta_W 2M_W \cos\beta} \qquad\qquad F_{H^0}^{dR} = F_{H^0}^{dL} \tag{A.15}$$

$$F_{A^0}^{dL} = -\frac{ig_2 m_d \sin\beta}{\sin\theta_W 2M_W \cos\beta} \qquad\qquad F_{A^0}^{dR} = -F_{A^0}^{dL} \tag{A.16}$$

$$F_{H^-}^{dL} = \frac{g_2 m_d \cos\beta}{\sqrt{2}\sin\theta_W M_W \sin\beta} \tag{A.17}$$

$$F_{H^-}^{dR} = \frac{g_2 m_d \sin\beta}{\sqrt{2}\sin\theta_W M_W \cos\beta} \tag{A.18}$$

A.4 Squark-Squark-Higgs

$$\hat{G}_{\Phi,ij}^q = i\,G_{\Phi,ij}^q \qquad\qquad \text{(A.19)}$$
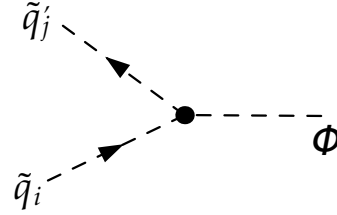
Neutral Higgs

$$G_{\Phi,ij}^q = \sum_{s,t} \tilde{G}_{\Phi,st}^q U_{js}^q U_{it}^q \tag{A.20}$$

Charged Higgs

$$G_{\Phi^+,ij}^u = \sum_{s,t} \tilde{G}_{\Phi^+,st}^u U_{js}^d U_{it}^u \tag{A.21}$$

$$G_{\Phi^+,ij}^d = \sum_{s,t} \tilde{G}_{\Phi^+,st}^d U_{js}^u U_{it}^d \tag{A.22}$$

Incoming up-type squark

$$\tilde{G}^u_{h^0,\,11} = - \frac{g_2 m_u}{M_W \sin\theta_W \sin\beta} m_u \cos\alpha \tag{A.23}$$

$$+ g_2 M_Z (I_{3_u} - q_u \sin^2\theta_W) \frac{\sin\alpha\cos\beta + \cos\alpha\sin\beta}{\sin\theta_W \cos\theta_W}$$

$$\tilde{G}^u_{h^0,\,22} = - \frac{g_2 m_u}{M_W \sin\theta_W \sin\beta} m_u \cos\alpha \tag{A.24}$$

$$+ g_2 M_Z q_u \sin^2\theta_W \frac{\sin\alpha\cos\beta + \cos\alpha\sin\beta}{\sin\theta_W \cos\theta_W}$$

$$\tilde{G}^u_{h^0,\,12} = - \frac{g_2 m_u}{2 M_W \sin\theta_W \sin\beta} (A_u \cos\alpha + \mu \sin\alpha) \tag{A.25}$$

$$\tilde{G}^u_{h^0,\,21} = \tilde{G}^u_{h^0,\,12} \tag{A.26}$$

$$\tilde{G}^u_{H^0,\,11} = - \frac{g_2 m_u}{M_W \sin\theta_W \sin\beta} m_u \sin\alpha \tag{A.27}$$

$$- g_2 M_Z (I_{3_u} - q_u \sin^2\theta_W) \frac{\cos\alpha\cos\beta - \sin\alpha\sin\beta}{\sin\theta_W \cos\theta_W}$$

$$\tilde{G}^u_{H^0,\,22} = - \frac{g_2 m_u}{M_W \sin\theta_W \sin\beta} m_u \sin\alpha \tag{A.28}$$

$$- g_2 M_Z q_u \sin^2\theta_W \frac{\cos\alpha\cos\beta - \sin\alpha\sin\beta}{\sin\theta_W \cos\theta_W}$$

$$\tilde{G}^u_{H^0,\,12} = - \frac{g_2 m_u}{2 M_W \sin\theta_W \sin\beta} (A_u \sin\alpha - \mu \cos\alpha) \tag{A.29}$$

$$\tilde{G}^u_{H^0,\,21} = \tilde{G}^u_{H^0,\,12} \tag{A.30}$$

$$\tilde{G}^u_{A^0,\,11} = 0 \tag{A.31}$$

$$\tilde{G}^u_{A^0,\,22} = 0 \tag{A.32}$$

$$\tilde{G}^u_{A^0,\,12} = \frac{i g_2 m_u}{2 M_W \sin\theta_W \sin\beta} (A_u \cos\beta + \mu \sin\beta) \tag{A.33}$$

$$\tilde{G}^u_{A^0,\,21} = - \tilde{G}^u_{A^0,\,12} \tag{A.34}$$

$$\tilde{G}^u_{H^+,11} = \frac{g_2 m_d}{\sqrt{2}M_W \sin\theta_W \cos\beta} m_d \sin\beta \tag{A.35}$$

$$+ \frac{g_2 m_u}{\sqrt{2}M_W \sin\theta_W \sin\beta} m_u \cos\beta - \frac{g_2 M_W}{\sqrt{2}\sin\theta_W}(2\tan\beta\cos^2\beta)$$
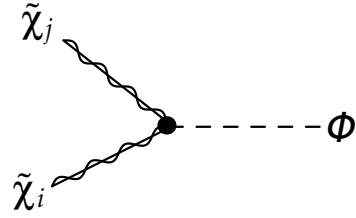
$$\tilde{G}^u_{H^+,22} = \frac{g_2 m_u}{\sqrt{2}M_W \sin\theta_W \sin\beta} m_d \cos\beta \tag{A.36}$$

$$+ \frac{g_2 m_d}{\sqrt{2}M_W \sin\theta_W \cos\beta} m_u \sin\beta$$

$$\tilde{G}^u_{H^+,12} = \frac{g_2 m_u}{\sqrt{2}M_W \sin\theta_W \sin\beta}(A_u \cos\beta + \mu\sin\beta) \tag{A.37}$$

$$\tilde{G}^u_{H^+,21} = \frac{g_2 m_d}{\sqrt{2}M_W \sin\theta_W \cos\beta}(A_d \sin\beta + \mu\cos\beta) \tag{A.38}$$

Incoming down-type squark

$$\tilde{G}^d_{h^0,11} = \frac{g_2 m_d}{M_W \sin\theta_W \cos\beta} m_d \sin\alpha \tag{A.39}$$

$$+ g_2 M_Z(I_{3_d} - q_d \sin^2\theta_W)\frac{\sin\alpha\cos\beta + \cos\alpha\sin\beta}{\sin\theta_W \cos\theta_W}$$

$$\tilde{G}^d_{h^0,22} = \frac{g_2 m_d}{M_W \sin\theta_W \cos\beta} m_d \sin\alpha \tag{A.40}$$

$$+ g_2 M_Z q_d \sin^2\theta_W \frac{\sin\alpha\cos\beta + \cos\alpha\sin\beta}{\sin\theta_W \cos\theta_W}$$

$$\tilde{G}^d_{h^0,12} = \frac{g_2 m_d}{2M_W \sin\theta_W \cos\beta}(A_d \sin\alpha + \mu\cos\alpha) \tag{A.41}$$

$$\tilde{G}^d_{h^0,21} = \tilde{G}^d_{h^0,12} \tag{A.42}$$

$$\tilde{G}^d_{H^0,11} = -\frac{g_2 m_d}{M_W \sin\theta_W \cos\beta} m_d \cos\alpha \tag{A.43}$$

$$- g_2 M_Z(I_{3_d} - q_d \sin^2\theta_W)\frac{\cos\alpha\cos\beta - \sin\alpha\sin\beta}{\sin\theta_W \cos\theta_W}$$

$$\tilde{G}^d_{H^0,22} = -\frac{g_2 m_d}{M_W \sin\theta_W \cos\beta} m_d \cos\alpha \tag{A.44}$$

$$- g_2 M_Z q_d \sin^2\theta_W \frac{\cos\alpha\cos\beta - \sin\alpha\sin\beta}{\sin\theta_W \cos\theta_W}$$

$$\tilde{G}^d_{H^0,12} = -\frac{g_2 m_d}{2M_W \sin\theta_W \cos\beta}(A_d \cos\alpha - \mu\sin\alpha) \tag{A.45}$$

$$\tilde{G}^d_{H^0,21} = \tilde{G}^d_{H^0,12} \tag{A.46}$$

$$\tilde{G}^d_{A^0,\,11} = 0 \tag{A.47}$$

$$\tilde{G}^d_{A^0,\,22} = 0 \tag{A.48}$$

$$\tilde{G}^d_{A^0,\,12} = \frac{ig_2 m_d}{2 M_W \sin\theta_W \cos\beta}(A_d \sin\beta + \mu \cos\beta) \tag{A.49}$$

$$\tilde{G}^d_{A^0,\,21} = -\,\tilde{G}^d_{A^0,\,12} \tag{A.50}$$

$$\tilde{G}^d_{H^-,\,11} = \frac{g_2 m_d}{\sqrt{2} M_W \sin\theta_W \cos\beta} m_d \sin\beta \tag{A.51}$$

$$+ \frac{g_2 m_u}{\sqrt{2} M_W \sin\theta_W \sin\beta} m_u \cos\beta - \frac{g_2 M_W}{\sqrt{2}\sin\theta_W}(2\tan\beta\cos^2\beta)$$

$$\tilde{G}^d_{H^-,\,22} = \frac{g_2 m_u}{\sqrt{2} M_W \sin\theta_W \sin\beta} m_d \cos\beta + \frac{g_2 m_d}{\sqrt{2} M_W \sin\theta_W \cos\beta} m_u \sin\beta \tag{A.52}$$

$$\tilde{G}^d_{H^-,\,12} = \frac{g_2 m_d}{\sqrt{2} M_W \sin\theta_W \cos\beta}(A_d \sin\beta + \mu \cos\beta) \tag{A.53}$$

$$\tilde{G}^d_{H^-,\,21} = \frac{g_2 m_u}{\sqrt{2} M_W \sin\theta_W \sin\beta}(A_u \cos\beta + \mu \sin\beta) \tag{A.54}$$

A.5 Neutralino-Neutralino-Higgs

$$\hat{H}^\Phi_{ij} = i\left[H^{\Phi\,L}_{ij} P_L + H^{\Phi\,R}_{ij} P_R\right] \qquad \text{(A.55)}$$

$$H^{h^0\,L}_{ij} = -\frac{g_2}{2*\sin\theta_W}\Big((-\sin\alpha)(N^*_{j3}N^*_{i2} + N^*_{i3}N^*_{j2} - \frac{\sin\theta_W}{\cos\theta_W}(N^*_{j3}N^*_{i1} + N^*_{i3}N^*_{j1})) \tag{A.56}$$

$$-\cos\alpha(N^*_{j4}N^*_{i2} + N^*_{i4}N^*_{j2} - \frac{\sin\theta_W}{\cos\theta_W}(N^*_{j4}N^*_{i1} + N^*_{i4}N^*_{j1})))$$

$$H^{h^0\,R}_{ij} = -\frac{g_2}{2\sin\theta_W}\Big((-\sin\alpha)(N_{j3}N_{i2} + N_{i3}N_{j2} - \frac{\sin\theta_W}{\cos\theta_W}(N_{j3}N_{i1} + N_{i3}N_{j1})) \tag{A.57}$$

$$-\cos\alpha(N_{j4}N_{i2} + N_{i4}N_{j2} - \frac{\sin\theta_W}{\cos\theta_W}(N_{j4}N_{i1} + N_{i4}N_{j1})))$$

$$H_{ij}^{H^0\,L} = -\frac{g_2}{2\sin\theta_W}((+\cos\alpha)(N_{j3}^*N_{i2}^* + N_{i3}^*N_{j2}^* - \frac{\sin\theta_W}{\cos\theta_W}(N_{j3}^*N_{i1}^* + N_{i3}^*N_{j1}^*))$$

$$\text{(A.58)}$$

$$- \sin\alpha(N_{j4}^*N_{i2}^* + N_{i4}^*N_{j2}^* - \frac{\sin\theta_W}{\cos\theta_W}(N_{j4}^*N_{i1}^* + N_{i4}^*N_{j1}^*)))$$

$$H_{ij}^{H^0\,R} = -\frac{g_2}{2\sin\theta_W}((+\cos\alpha)(N_{j3}N_{i2} + N_{i3}N_{j2} - \frac{\sin\theta_W}{\cos\theta_W}(N_{j3}N_{i1} + N_{i3}N_{j1}))$$

$$\text{(A.59)}$$

$$- \sin\alpha(N_{j4}N_{i2} + N_{i4}N_{j2} - \frac{\sin\theta_W}{\cos\theta_W}(N_{j4}N_{i1} + N_{i4}N_{j1})))$$

$$H_{ij}^{A^0\,L} = -\frac{i\,g_2}{2\sin\theta_W}((-\sin\beta)(N_{j3}^*N_{i2}^* + N_{i3}^*N_{j2}^* - \frac{\sin\theta_W}{\cos\theta_W}(N_{j3}^*N_{i1}^* + N_{i3}^*N_{j1}^*))$$

$$\text{(A.60)}$$

$$+ \cos\beta(N_{j4}^*N_{i2}^* + N_{i4}^*N_{j2}^* - \frac{\sin\theta_W}{\cos\theta_W}(N_{j4}^*N_{i1}^* + N_{i4}^*N_{j1}^*)))$$

$$H_{ij}^{A^0\,R} = +\frac{i\,g_2}{2\sin\theta_W}((-\sin\beta)(N_{j3}N_{i2} + N_{i3}N_{j2} - \frac{\sin\theta_W}{\cos\theta_W}(N_{j3}N_{i1} + N_{i3}N_{j1}))$$

$$\text{(A.61)}$$

$$+ \cos\beta(N_{j4}N_{i2} + N_{i4}N_{j2} - \frac{\sin\theta_W}{\cos\theta_W}(N_{j4}N_{i1} + N_{i4}N_{j1})))$$

A.6 Neutralino-Chargino-Higgs

$$H_{ij}^{H^+\,L} = -\frac{g_2\cos\beta}{\sin\theta_W}(V_{j1}^*N_{i4}^* + \frac{1}{\sqrt{2}}(N_{i2}^* + \frac{\sin\theta_W}{\cos\theta_W}\,N_{i1}^*)V_{j2}^*) \qquad \text{(A.62)}$$
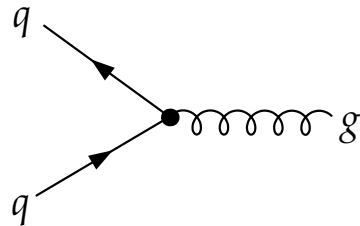
$$H_{ij}^{H^+\,R} = -\frac{g_2\sin\beta}{\sin\theta_W}(W_{j1}N_{i3} - \frac{1}{\sqrt{2}}(N_{i1} + \frac{\sin\theta_W}{\cos\theta_W}\,N_{i1})W_{j2}) \qquad \text{(A.63)}$$

A.7 Fermion-Fermion-Gluon

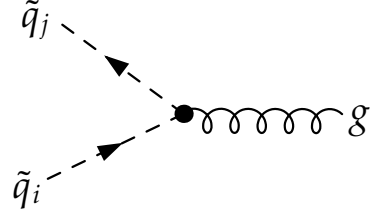$$\hat{B} = i\,B \qquad \text{(A.64)}$$

$$B = -g_s \qquad \text{(A.65)}$$

$$\text{(A.66)}$$

A.8 Sfermion-Sfermion-Gluon

$$\hat{C}_{ij} = i\,C_{ij} \qquad (A.67)$$
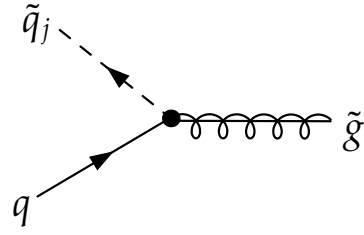
$$C_{ij} = g_s^2 \delta_{ij} \qquad (A.68)$$

A.9 Gluino-Squark-Quark

$$\hat{J}_j^q = i\,[J_j^{q\,L} P_L + J_j^{q\,R} P_R] \qquad (A.69)$$

$$J_j^{q\,L} = -g_s\sqrt{2}\,U_{j1}^u \qquad (A.70)$$

$$J_j^{q\,R} = g_s\sqrt{2}\,U_{j2}^u \qquad (A.71)$$

B Vertex Counterterms

B.1 Neutralino-Squark-Quark

$$\delta \hat{A}_{ij}^q = i \left[\delta A_{ij}^{q\,L} P_L + \delta A_{ij}^{q\,R} P_R \right] \tag{B.1}$$

Up-type squark/quark

$$\begin{aligned}
\delta A_{ij}^{u\,R} = &- \frac{g_2\, m_u}{\sin\theta_W\, \sqrt{2} M_W\, \sin\beta} N_{j\,4} U_{i2}^u \left(\frac{\delta m_u}{m_u} + \frac{\delta U_{i2}^u}{U_{i2}^u} \right) \\
&- \frac{\sqrt{2} g_2}{\sin\theta_W} \left((q_u - I_{3_u}) \frac{\sin\theta_W}{\cos\theta_W} N_{j\,1} + I_{3_u} N_{j\,2} \right) \delta U_{i1}^u \\
&+ A_{1j}^{u\,R} \frac{1}{2} \delta Z_{1\,i}^u + A_{2j}^{u\,R} \frac{1}{2} \delta Z_{2\,i}^u + A_{ij}^{u\,R} \frac{1}{2} \delta Z_L^{*\,u}
\end{aligned} \tag{B.2}$$

$$\begin{aligned}
\delta A_{ij}^{u\,L} = &- \frac{g_2\, m_u}{\sin\theta_W\, \sqrt{2} M_W\, \sin\beta} N_{j\,4}^* U_{i1}^u \left(\frac{\delta m_u}{m_u} + \frac{\delta U_{i1}^u}{U_{i1}^u} \right) \\
&+ \frac{\sqrt{2} g_2 q_u}{\cos\theta_W} N_{j\,1}^* \delta U_{i2}^u \\
&+ A_{1j}^{u\,L} \frac{1}{2} \delta Z_{1\,i}^u + A_{2j}^{u\,L} \frac{1}{2} \delta Z_{2\,i}^u + A_{ij}^{u\,L} \frac{1}{2} \delta Z_R^{*\,u}
\end{aligned} \tag{B.3}$$

Down-type squark/quark

$$\begin{aligned}
\delta A_{ij}^{d\,R} = &- \frac{g_2\, m_d}{\sin\theta_W\, \sqrt{2} M_W\, \cos\beta} N_{j\,3} U_{i2}^d \left(\delta \frac{\delta m_d}{m_d} + \frac{\delta U_{i2}^d}{U_{i2}^d} \right) \\
&- \frac{\sqrt{2} g_2}{\sin\theta_W} \left(I_{3_d} N_{j\,2} + (q_d - I_{3_d}) \frac{\sin\theta_W}{\cos\theta_W} N_{j\,1} \right) \delta U_{i1}^d \\
&+ A_{1j}^{d\,R} \frac{1}{2} \delta Z_{1\,i}^d + A_{2j}^{d\,R} \frac{1}{2} \delta Z_{2\,i}^d + A_{ij}^{d\,R} \frac{1}{2} \delta Z_L^{*\,d}
\end{aligned} \tag{B.4}$$

$$\begin{aligned}
\delta A_{ij}^{d\,L} = &- \frac{g_2\, m_d}{\sin\theta_W\, \sqrt{2} M_W\, \cos\beta} N_{j\,3}^* U_{i1}^d \left(\frac{\delta m_d}{m_d} + \frac{\delta U_{i1}^d}{U_{i1}^d} \right) \\
&+ \frac{\sqrt{2} g_2\, q_d}{\cos\theta_W} N_{j\,1}^* \delta U_{i2}^d
\end{aligned} \tag{B.5}$$

$$+ A_{1j}^{dL} \frac{1}{2} \delta Z_{1i}^d + A_{2j}^{dL} \frac{1}{2} \delta Z_{2i}^d + A_{ij}^{dL} \frac{1}{2} \delta Z_R^{*d}$$

B.2 Chargino-Squark-Quark

Up-type squark/quark

$$\delta A_{ij}^{uL} = \frac{g_2\, m_d}{\sin\theta_W\, \sqrt{2} M_W * \cos\beta} W_{j\,2}^* U_{i1}^u \left(\frac{\delta m_d}{m_d} + \frac{\delta U_{i1}^u}{U_{i1}^u} \right) \tag{B.6}$$
$$+ A_{1j}^{uL} \frac{1}{2} \delta Z_{1i}^u + A_{2j}^{uL} \frac{1}{2} \delta Z_{2i}^u + A_{ij}^{uL} \frac{1}{2} \delta Z_R^{*d}$$

$$\delta A_{ij}^{uR} = - \frac{g_2}{\sin\theta_W} V_{j\,1} \delta U_{i1}^u + \frac{g_2\, m_u}{\sin\theta_W * \sqrt{2} M_W * \sin\beta} V_{j\,2} U_{i2}^u \left(\frac{\delta m_u}{m_u} + \frac{\delta U_{i2}^u}{U_{i2}^u} \right) \tag{B.7}$$
$$+ A_{1j}^{uR} \frac{1}{2} \delta Z_{1i}^u + A_{2j}^{uR} \frac{1}{2} \delta Z_{2i}^u + A_{ij}^{uR} \frac{1}{2} \delta Z_L^{*d}$$

Down-type squark/quark

$$\delta A_{ij}^{dL} = \frac{g_2 * m_u}{\sin\theta_W * \sqrt{2} M_W * \sin\beta} V_{j\,2}^* U_{i1}^d \left(\frac{\delta m_u}{m_u} + \frac{\delta U_{i1}^d}{U_{i1}^d} \right) \tag{B.8}$$
$$+ A_{1j}^{dL} \frac{1}{2} \delta Z_{1i}^d + A_{2j}^{dL} \frac{1}{2} \delta Z_{2i}^d + A_{ij}^{dL} \frac{1}{2} \delta Z_R^{*d}$$

$$\delta A_{ij}^{dR} = - \frac{g_2}{\sin\theta_W} W_{j\,1} \delta U_{i1}^d + \frac{g_2\, m_d}{\sin\theta_W * \sqrt{2} M_W * \cos\beta} W_{j,2} U_{i2}^d \left(\frac{\delta m_d}{m_d} + \frac{\delta U_{i2}^d}{U_{i2}^d} \right) \tag{B.9}$$
$$+ A_{1j}^{dR} \frac{1}{2} \delta Z_{1i}^d + A_{2j}^{dR} \frac{1}{2} \delta Z_{2i}^d + A_{ij}^{dR} \frac{1}{2} \delta Z_L^{*d}$$

B.3 Quark-Quark-Higgs

$$\delta \hat{F}_\Phi^q = i \left[\delta F_\Phi^{qL} P_L + \delta F_\Phi^{qR} P_R \right] \tag{B.10}$$

for $\Phi = h^0, H^0, A^0, H^\pm$

Up-type quark

$$\delta F_\Phi^{uL} = F_\Phi^{uL} \left(\frac{\delta m_u}{m_u} + \frac{1}{2} \delta Z_R^u + \frac{1}{2} \delta Z_L^{*u} \right) \tag{B.11}$$

$$\delta F_\Phi^{uR} = F_\Phi^{uR} \left(\frac{\delta m_u}{m_u} + \frac{1}{2} \delta Z_L^u + \frac{1}{2} \delta Z_R^{*u} \right) \tag{B.12}$$

Down-type quark

$$\delta F_\Phi^{d\,L} = F_\Phi^{d\,L} \left(\frac{\delta m_d}{m_d} + \frac{1}{2}\,\delta Z_R^d + \frac{1}{2}\,\delta Z_L^{*\,d} \right) \tag{B.13}$$

$$\delta F_\Phi^{d\,R} = F_\Phi^{d\,L} \left(\frac{\delta m_d}{m_d} + \frac{1}{2}\,\delta Z_L^d + \frac{1}{2}\,\delta Z_R^{*\,d} \right) \tag{B.14}$$

B.4 Squark-Squark-Higgs

$$\delta \hat{G}_{\Phi,\,ij}^q = i\,\delta G_{\Phi,\,ij}^q \tag{B.15}$$

Neutral Higgs

$$
\begin{aligned}
G_{\Phi,\,ij}^q = \sum_t \Bigg[&\sum_s \left(\delta U_{it}^q \tilde{G}_{\Phi,\,st}^q U_{js}^q + U_{it}^q \delta \tilde{G}_{st}^q U_{js}^q + U_{it}^q \tilde{G}_{\Phi,\,st}^q \delta U_{js}^q \right) \\
&+ \frac{1}{2}\delta Z_{tj}^{q\,*} G_{\Phi\,it}^q + \frac{1}{2} Z_{ti}^q G_{\Phi,\,tj}^q \Bigg]
\end{aligned}
\tag{B.16}
$$

Charged Higgs

$$
\begin{aligned}
G_{\Phi,\,ij}^u = \sum_t \Bigg[&\sum_s \left(\delta U_{it}^u \tilde{G}_{\Phi,\,st}^u U_{js}^d + U_{it}^u \delta \tilde{G}_{st}^u U_{js}^d + U_{it}^u \tilde{G}_{\Phi,\,st}^u \delta U_{js}^d \right) \\
&+ \frac{1}{2}\delta Z_{tj}^{d\,*} G_{\Phi\,it}^q + \frac{1}{2} Z_{ti}^u G_{\Phi,\,tj}^q \Bigg]
\end{aligned}
\tag{B.17}
$$

$$
\begin{aligned}
G_{\Phi,\,ij}^d = \sum_t \Bigg[&\sum_s \left(\delta U_{it}^d \tilde{G}_{\Phi,\,st}^d U_{js}^u + U_{it}^d \delta \tilde{G}_{st}^d U_{js}^q + U_{it}^d \tilde{G}_{\Phi,\,st}^d \delta U_{js}^u \right) \\
&+ \frac{1}{2}\delta Z_{tj}^{u\,*} G_{\Phi\,it}^q + \frac{1}{2} Z_{ti}^d G_{\Phi,\,tj}^q \Bigg]
\end{aligned}
\tag{B.18}
$$

Up-type squark

$$\delta \tilde{G}_{h^0,\,11}^u = -\,\frac{g_2\,m_u^2\,\cos\alpha}{M_W\,\sin\theta_W\,\sin\beta}\frac{2\,\delta m_u}{m_u} \tag{B.19}$$

$$\delta \tilde{G}_{h^0,\,22}^u = -\,\frac{g_2\,m_u^2\,\cos\alpha}{M_W\,\sin\theta_W\,\sin\beta}\frac{2\,\delta m_u}{m_u} \tag{B.20}$$

$$\delta\tilde{G}^u_{h^0,12} = -\frac{g_2\, m_u \cos\alpha}{2\, M_W\, \sin\theta_W\, \sin\beta}\, A_u \left(\frac{\delta m_u}{m_u} + \frac{\delta A_u}{A_u}\right) \tag{B.21}$$
$$\qquad\qquad -\frac{g_2\, m_u \sin\alpha}{2\, M_W\, \sin\theta_W\, \sin\beta}\, \mu\frac{\delta m_u}{m_u}$$
$$\delta\tilde{G}^u_{h^0,21} = \delta\tilde{G}^u_{h^0,12} \tag{B.22}$$

$$\delta\tilde{G}^u_{H^0,11} = -\frac{g_2 m_u^2 \sin\alpha}{M_W\, \sin\theta_W\, \sin\beta}\, \frac{2\,\delta m_u}{m_u} \tag{B.23}$$

$$\delta\tilde{G}^u_{H^0,22} = -\frac{g_2 m_u^2 \sin\alpha}{M_W\, \sin\theta_W\, \sin\beta}\, \frac{2\,\delta m_u}{m_u} \tag{B.24}$$

$$\delta\tilde{G}^u_{H^0,12} = -\frac{g_2 m_u \sin\alpha}{2\, M_W\, \sin\theta_W\, \sin\beta}\, A_u \left(\frac{\delta m_u}{m_u} + \frac{\delta A_u}{A_u}\right) \tag{B.25}$$
$$\qquad\qquad +\frac{g_2 m_u \cos\alpha}{2\, M_W\, \sin\theta_W\, \sin\beta}\, \mu\frac{\delta m_u}{m_u}$$
$$\delta\tilde{G}^u_{H^0,21} = \delta\tilde{G}^u_{h^0,12} \tag{B.26}$$

$$\delta\tilde{G}^u_{A^0,11} = 0 \tag{B.27}$$
$$\delta\tilde{G}^u_{A^0,22} = 0 \tag{B.28}$$
$$\delta\tilde{G}^u_{A^0,12} = \frac{i\, g_2\, m_u \cos\beta}{2\, M_W\, \sin\theta_W\, \sin\beta}\, A_u \left(\frac{\delta m_u}{m_u} + \frac{\delta A_u}{A_u}\right) \tag{B.29}$$
$$\qquad\qquad +\frac{i\, g_2 m_u}{2\, M_W\, \sin\theta_W}\, \mu\frac{\delta m_u}{m_u}$$
$$\delta\tilde{G}^u_{A^0,21} = -\delta\tilde{G}^u_{A^0,12} \tag{B.30}$$

$$\delta\tilde{G}^u_{H^+,11} = \frac{g_2 m_d^2 \sin\beta}{\sqrt{2}\, M_W\, \sin\theta_W\, \cos\beta}\, \frac{2\,\delta m_d}{m_d} + \frac{g_2 m_u^2 \cos\beta}{\sqrt{2}\, M_W\, \sin\theta_W\, \sin\beta}\, \frac{2\,\delta m_u}{m_u} \tag{B.31}$$
$$\delta\tilde{G}^u_{H^+,22} = \left(\frac{g_2 m_u\, m_d \cos\beta}{\sqrt{2}\, M_W\, \sin\theta_W\, \sin\beta} + \frac{g_2 m_d\, m_u \sin\beta}{\sqrt{2}\, M_W\, \sin\theta_W\, \cos\beta}\right) \left(\frac{\delta m_u}{m_u} + \frac{\delta m_d}{m_d}\right) \tag{B.32}$$
$$\delta\tilde{G}^u_{H^+,12} = \frac{g_2 m_u \cos\beta}{\sqrt{2}\, M_W\, \sin\theta_W\, \sin\beta}\, A_u \left(\frac{\delta m_u}{m_u} + \frac{\delta A_u}{A_u}\right) \tag{B.33}$$
$$\qquad\qquad +\frac{g_2 m_u}{\sqrt{2}\, M_W\, \sin\theta_W}\, \mu\frac{\delta m_u}{m_u}$$

$$\delta \tilde{G}^u_{H^+,21} = \frac{g_2 m_d \sin\beta}{\sqrt{2}\, M_W\,\sin\theta_W\,\cos\beta} A_d \left(\frac{\delta m_d}{m_d} + \frac{\delta A_d}{A_d} \right) \tag{B.34}$$
$$+ \frac{g_2 m_d}{\sqrt{2}\, M_W\,\sin\theta_W} \mu \frac{\delta m_d}{m_d}$$

Down-type squark

$$\delta \tilde{G}^d_{h^0,11} = \frac{g_2 m_d^2 \sin\alpha}{M_W\,\sin\theta_W\,\cos\beta} \frac{2\,\delta m_d}{m_d} \tag{B.35}$$

$$\delta \tilde{G}^d_{h^0,22} = \frac{g_2 m_d^2 \sin\alpha}{M_W\,\sin\theta_W\,\cos\beta} \frac{2\,\delta m_d}{m_d} \tag{B.36}$$

$$\delta \tilde{G}^d_{h^0,12} = \frac{g_2 m_d \sin\alpha}{2\, M_W\,\sin\theta_W\,\cos\beta} A_d \left(\frac{\delta m_d}{m_d} + \frac{\delta A_d}{A_d} \right) + \frac{g_2 m_d \cos\alpha}{2\, M_W\,\sin\theta_W\,\cos\beta} \mu \frac{\delta m_d}{m_d} \tag{B.37}$$

$$\delta \tilde{G}^d_{h^0,21} = \delta \tilde{G}^d_{h^0,12} \tag{B.38}$$

$$\delta \tilde{G}^d_{H^0,11} = - \frac{g_2 m_d^2 \cos\alpha}{M_W\,\sin\theta_W\,\cos\beta} \frac{2\,\delta m_d}{m_d} \tag{B.39}$$

$$\delta \tilde{G}^d_{H^0,22} = - \frac{g_2 m_d^2 \cos\alpha}{M_W\,\sin\theta_W\,\cos\beta} \frac{2\,\delta m_d}{m_d} \tag{B.40}$$

$$\delta \tilde{G}^d_{H^0,12} = - \frac{g_2 m_d \cos\alpha}{2\, M_W\,\sin\theta_W\,\cos\beta} A_d \left(\frac{\delta m_d}{m_d} + \frac{\delta A_d}{A_d} \right) + \frac{g_2 m_d \sin\alpha}{2\, M_W\,\sin\theta_W\,\cos\beta} \mu \frac{\delta m_d}{m_d} \tag{B.41}$$

$$\delta \tilde{G}^d_{H^0,21} = \delta \tilde{G}^d_{H^0,12} \tag{B.42}$$

$$\delta \tilde{G}^d_{H^0,11} = 0 \tag{B.43}$$
$$\delta \tilde{G}^d_{H^0,22} = 0 \tag{B.44}$$
$$\delta \tilde{G}^d_{H^0,12} = \frac{i\, g_2 m_d \sin\beta}{M_W\,\sin\theta_W\,\cos\beta} A_d \left(\frac{\delta m_d}{m_d} + \frac{\delta A_d}{A_d} \right) + \frac{i\, g_2 m_d}{2\, M_W\,\sin\theta_W} \mu \frac{\delta m_d}{m_d} \tag{B.45}$$
$$\delta \tilde{G}^d_{H^0,21} = - \delta \tilde{G}^d_{H^0,12} \tag{B.46}$$

$$\delta \tilde{G}^d_{H^-,11} = \frac{g_2 m_d^2 \sin\beta}{\sqrt{2}\, M_W\,\sin\theta_W\,\cos\beta} \frac{2\,\delta m_d}{m_d} + \frac{g_2 m_{u_g^2} \cos\beta}{\sqrt{2}\, M_W\,\sin\theta_W\,\sin\beta} \frac{2\,\delta m_u}{m_u} \tag{B.47}$$

$$\delta\tilde{G}^d_{H^-,\,22} = \left(\frac{g_2 m_u\, m_d\,\cos\beta}{\sqrt{2}\, M_W\,\sin\theta_W\,\sin\beta} + \frac{g_2 m_d m_u\sin\beta}{\sqrt{2}\, M_W\,\sin\theta_W\,\cos\beta}\right)\left(\frac{\delta m_u}{m_u} + \frac{\delta m_d}{m_d}\right)$$

$$\tag{B.48}$$

$$\delta\tilde{G}^d_{H^-,\,12} = \frac{g_2 m_d\,\sin\beta}{\sqrt{2}\, M_W\,\sin\theta_W\,\cos\beta}\,A_d\left(\frac{\delta m_d}{m_d} + \frac{\delta A_d}{A_d}\right) + \frac{g_2 m_d}{\sqrt{2}\, M_W\,\sin\theta_W}\,\mu\frac{\delta m_d}{m_d}$$

$$\tag{B.49}$$

$$\delta\tilde{G}^d_{H^-,\,21} = \frac{g_2 m_u\cos\beta}{\sqrt{2}\, M_W\,\sin\theta_W\,\sin\beta}\,A_u\left(\frac{\delta m_u}{m_u} + \frac{\delta A_u}{A_u}\right) + \frac{g_2 m_u}{\sqrt{2}\, M_W\,\sin\theta_W}\,\mu\,\frac{\delta m_u}{m_u}$$

$$\tag{B.50}$$

B.5 Fermion-Fermion-Gluon

$$\delta\hat{B} = i\,\delta B \tag{B.51}$$

$$\delta B = -g_s\left(\frac{1}{2}(\delta Z_L + \delta Z_L^* + \delta Z^g) + \frac{\delta g_s}{g_s}\right) \tag{B.52}$$

B.6 Sfermion-Sfermion-Gluon

$$\delta\hat{C}_{ij} = i\,\delta C_{ij} \tag{B.53}$$

$$\delta C_{ij} = -g_s\left(\frac{1}{2}(\delta Z_{ij}^* + \delta Z_{ji} + \delta Z_{ij}^g) + \frac{\delta g_s}{g_s}\delta_{ij}\right) \tag{B.54}$$

C Propagator Corrections and Counterterms
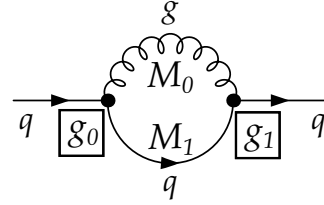
C.1 Corrections

C.1.1 Quark Self-Energies

Gluon contribution

$$g_0 = -g_s \qquad \text{(C.1)}$$
$$g_1 = -g_s \qquad \text{(C.2)}$$

$$M_0 = 0 \qquad \text{(C.3)}$$
$$M_1 = m_q \qquad \text{(C.4)}$$

$$B_0(s, 0, m_q^2) \qquad \text{(C.5)}$$

$$Z_L^s = \frac{C_F}{8\pi^2} g_0 g_1 m_q 2 B_0 \qquad \text{(C.6)}$$

$$Z_R^s = Z_L^s \qquad \text{(C.7)}$$

$$Z_L^v = \frac{C_F}{16\pi^2} g_0 g_1 \left(2 B_0 + 2 B_1\right) \qquad \text{(C.8)}$$

$$Z_R^v = Z_L^v \qquad \text{(C.9)}$$

Gluino contribution

$$g_{0_L} = J_j^{q\,L}, \qquad g_{0_R} = J_j^{q\,R} \qquad \text{(C.10)}$$
$$g_{1_L} = J_j^{q\,R} \qquad g_{1_R} = J_j^{q\,L} \qquad \text{(C.11)}$$

$$M_0 = m_{\tilde{g}} \qquad \text{(C.12)}$$
$$M_1 = m_{\tilde{q}_j} \qquad \text{(C.13)}$$

191
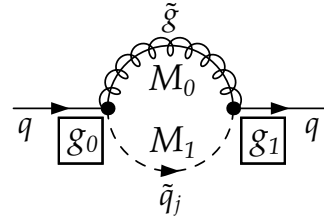
$$B_0(s, m_{\tilde{g}}^2, m_{\tilde{q}_j}^2) \tag{C.14}$$

$$Z_L^s = \sum_{j=1}^{2} \frac{C_F}{16\pi^2} g_{0_L} g_{1_L} m_{\tilde{g}} B_0 \tag{C.15}$$

$$Z_R^s = Z_L^s \tag{C.16}$$

$$Z_L^v = \sum_{j=1}^{2} -\frac{C_F}{16\pi^2} g_{0_R} g_{1_L} B_1 \tag{C.17}$$

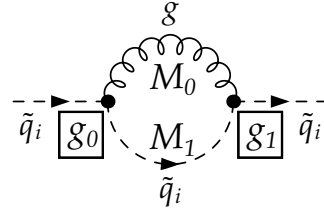$$Z_R^v = Z_L^v \tag{C.18}$$

C.1.2 Squark Self-Energies

Gluon contribution

$$g_0 = -g_s \tag{C.19}$$
$$g_1 = -g_s \tag{C.20}$$

$$M_0 = 0 \tag{C.21}$$
$$M_1 = m_{\tilde{q}_{g,i}} \tag{C.22}$$

$$A_0(m_{\tilde{q}_i}^2) \tag{C.23}$$
$$B_0(t, 0, m_{\tilde{q}_i}^2) \tag{C.24}$$

$$P_s = -\frac{C_F}{16\pi^2}\left(g_0 g_1\left(2(t + M_1^2)B_0 - A_0\right)\right) \tag{C.25}$$

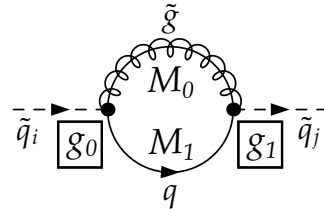**Gluino contribution**

$$g_{0_L} = J_j^{qR}, \qquad g_{0_R} = J_j^{qL} \tag{C.26}$$
$$g_{1_L} = J_j^{qL}, \qquad g_{1_R} = J_j^{qR} \tag{C.27}$$

$$M_0 = m_{\tilde{g}} \tag{C.28}$$
$$M_1 = m_q \tag{C.29}$$

$$B_0(t, m_{\tilde{g}}^2 m_q^2) \tag{C.30}$$

$$P_s = -\frac{C_F}{16\pi^2}((g_{0_L}g_{1_R} + g_{0_R}g_{1_L})(A_0(M_1) + A_0(M_0) + (M_0^2 + M_1^2 - t)B_0)$$
$$+ 2(g_{0_R}g_{1_R} + g_{0_L}g_{1_L})M_0M_1B_0) \qquad (C.31)$$

Squark contribution
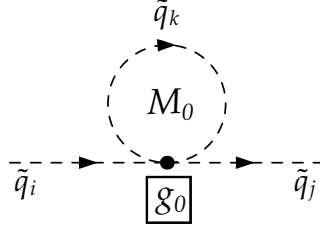
$$g_0 = -g_s^2(U_{l1}^q U_{i1}^q - U_{l2}^q U_{i2}^q)(U_{j1}^{q_g'} U_{k1}^{q_g'} - U_{j2}^{q_g'} U_{k2}^{q_g'}) \qquad (C.32)$$

$$M_0 = m_{\tilde{q}_{g,\,k}} \qquad (C.33)$$

$$P_s = \sum_{k=1}^{2} -\frac{C_F}{16\pi^2} g_0 A_0(M_0) \qquad (C.34)$$

C.2 Counterterms

C.2.1 Quark Self-Energies

In order to be consistent with the implementation within `DM@NLO`, we merge the conventions set due to renormalization with those of the generic amplitude structure in Eqs. C.35 and C.36.

$$\delta Z_R^v = \frac{1}{2}\left(\delta Z_L + \delta Z_L^\dagger\right) \tag{C.35}$$

$$\delta Z_L^v = \frac{1}{2}\left(\delta Z_R + \delta Z_R^\dagger\right) \tag{C.36}$$

$$\delta Z_L^s = -\frac{1}{2}\left(m_q \delta Z_L + m_q \delta Z_R^\dagger\right) - \delta m_q \tag{C.37}$$

$$\delta Z_R^s = -\frac{1}{2}\left(m_q \delta Z_R + m_q \delta Z_L^\dagger\right) - \delta m_q \tag{C.38}$$

$$\delta Z_L = \left\{-\Pi_{V,L}(m_q^2) - m_q\left[m_q\left(\dot{\Pi}_{V,L}(m_q^2) + \dot{\Pi}_{V,R}(m_q^2)\right) + \dot{\Pi}_{S,L}(m_q^2) + \dot{\Pi}_{S,R}(m_q^2)\right]\right\} \tag{C.39}$$

$$\delta Z_R = \left\{-\Pi_{V,R}(m_q^2) - m_q\left[m_q\left(\dot{\Pi}_{V,R}(m_q^2) + \dot{\Pi}_{V,L}(m_q^2)\right) + \dot{\Pi}_{S,R}(m_q^2) + \dot{\Pi}_{S,L}(m_q^2)\right]\right\} \tag{C.40}$$

Gluon Loop

$$B_0(p^2, M_1^2, M_0^2) \tag{C.41}$$

$$\Pi_{V,R} = Z_R^v \tag{C.42}$$

$$\Pi_{V,L} = Z_L^v \tag{C.43}$$

$$\dot{\Pi}_{S,R} = -\frac{C_F}{16\pi^2}4g_0 g_1 M_1 \dot{B}_0 \tag{C.44}$$

$$\dot{\Pi}_{S,L} = -\frac{C_F}{16\pi^2}4g_0 g_1 M_1 \dot{B}_0 \tag{C.45}$$

$$\dot{\Pi}_{V,R} = -\frac{C_F}{16\pi^2}2g_0 g_1 \dot{B}_1 \tag{C.46}$$

$$\dot{\Pi}_{V,L} = -\frac{C_F}{16\pi^2}2g_0 g_1 \dot{B}_1 \tag{C.47}$$

Gluino Loop

$$B_0(p^2, M_0^2, M_1^2) \tag{C.48}$$

$$\Pi_{V,R} = Z_R^v \tag{C.49}$$
$$\Pi_{V,L} = Z_L^v \tag{C.50}$$

$$\dot{\Pi}_{S,R} = +\frac{C_F}{16\pi^2}g_{0_R}g_{1_R}M_0\dot{B}_0 \tag{C.51}$$

$$\dot{\Pi}_{S,L} = +\frac{C_F}{16\pi^2}g_{0_L}g_{1_L}M_0\dot{B}_0 \tag{C.52}$$

$$\dot{\Pi}_{V,R} = -\frac{C_F}{16\pi^2}g_{0_R}g_{1_L}\dot{B}_1 \tag{C.53}$$

$$\dot{\Pi}_{V,L} = -\frac{C_F}{16\pi^2}g_{0_L}g_{1_R}\dot{B}_1 \tag{C.54}$$

C.2.2 Squark Self-Energies

$$\delta P_s(ij) = \hat{\Pi}_{ij}(k^2) = \frac{1}{2}(k^2 - m_{\tilde{q}_i}^2)\delta Z_{ij} + \frac{1}{2}(k^2 - m_{\tilde{q}_j}^2)\delta Z_{ji}^* - \delta_{ij}\delta m_{\tilde{q}_i}^2, \tag{C.55}$$

$$\delta Z_{ij} = \frac{2}{m_{\tilde{q}_i}^2 - m_{\tilde{q}_j}^2}\mathrm{Re}\Pi_{ij}(m_{\tilde{q}_j}^2), i \neq j \tag{C.56}$$

$$\delta Z_{ii} = -\mathrm{Re}\dot{\Pi}_{ii}(k^2)\Big|_{k^2 = m_{\tilde{q}_i}^2} \tag{C.57}$$

Gluon Loop

$$\Pi_{ij}(p^2) = -\frac{C_F}{16\pi^2}g_0g_1(2(M_1^2 + p^2)\dot{B}_0(p^2, M_0, M_1) + 2B_0(p^2, M_0, M_1)) \tag{C.58}$$

Gluino Loop

$$\Pi_{ij}(p^2) = = -\frac{C_F}{16\pi^2}(2(g_{0_L}g_{1_L} + g_{0_R}g_{1_R})M_0M_1\dot{B}_0(p^2, M_0, M_1)$$
$$+ (g_{0_R}g_{1_L} + g_{0_L}g_{1_R})((M_0^2 + M_1^2 - p^2)\dot{B}_0(p^2, M_0, M_1) - B_0(p^2, M_0, M_1))) \tag{C.59}$$

D Vertex Corrections

D.1 Neutralino-Sfermion-Fermion Coupling (A-Coupling)

D.1.1 Gluon Contribution
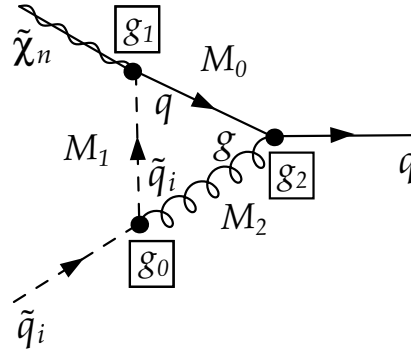
Correction to the S-Channel Diagram

$$g_0 \quad = -g_s \tag{D.1}$$

$$g_{1_L} = A_{in}^{q\,L}, \qquad g_{1_R} = A_{in}^{q\,R} \tag{D.2}$$

$$g_{2_L} = -g_s, \qquad g_{2_R} = -g_s \tag{D.3}$$

$$M_0 = m_q \tag{D.4}$$

$$M_1 = m_2 \tag{D.5}$$

$$M_2 = m_{\tilde{g}} \tag{D.6}$$

$$B_0(m_2^2, m_2^2, 0) \tag{D.7}$$

$$C_0(m_1^2, m_2^2, s, m_q^2, m_2^2, 0) \tag{D.8}$$

$$
\begin{aligned}
A_{1\,L}^s = \frac{C_F}{16\pi^2} \big[&-g_0 g_{1_R} g_{2_L} M_0 m_1 (2C_0 + C_1) \\
&+ g_0 g_{1_L} g_{2_L} (B_0 + M_0^2 C_0 + s C_2 + 2m_1^2 C_1 + 2m_1^2 C_2 - 2m_2^2 C_2) \big]
\end{aligned}
\tag{D.9}
$$

$$A_{1\,R}^s = A_{1\,L}^s (R \leftrightarrow L) \tag{D.10}$$

$$A_{1\,L}^v = \frac{C_F}{16\pi^2} \big[g_0 g_{1_R} g_{2_L} M_0 (C_0 - C_2) - g_0 g_{1_L} g_{2_L} m_1 (2C_2 + C_1) \big] \tag{D.11}$$

$$A_{1\,R}^v = A_{1\,L}^v (R \leftrightarrow L) \tag{D.12}$$

Correction to the T-Channel Diagram

$$M_0 = m_3 \tag{D.13}$$
$$M_1 = m_{\tilde{q}_i} \tag{D.14}$$
$$M_2 = 0 \tag{D.15}$$

$$B_0(t, m_{\tilde{q}_i}^2, 0) \tag{D.16}$$
$$C_0(m_1^2, t, m_3^2, m_3^2, m_{\tilde{q}_i}^2, 0) \tag{D.17}$$

$$\begin{aligned} A_{2\,L}^s = \frac{C_F}{16\pi^2} \big[& g_{0_L} g_{1_L} g_{2_L} (B_0 + M_0^2 C_0 - m_3^2 C_2 + 2m_1^2 C_1 + 2(m_1^2 + m_3^2 - t)C_2) \\ & - g_{0_R} g_{1_R} g_{2_R} m_1 m_3 (C_1 + 2C_2) - g_{0_L} g_{1_R} g_{2_L} M_0 m_1 (2C_0 + C_1) \\ & - g_{0_R} g_{1_L} g_{2_R} M_0 m_3 (C_0 - C_2) \big] \end{aligned} \tag{D.18}$$

$$A_{2\,R}^s = A_{2\,L}^s (R \leftrightarrow L) \tag{D.19}$$

Correction to the U-Channel Diagram

$$M_0 = m_3 \tag{D.20}$$
$$M_1 = m_{\tilde{q}_i} \tag{D.21}$$
$$M_2 = 0 \tag{D.22}$$

$$B_0(m_2^2, m_{\tilde{q}_i}^2, 0) \tag{D.23}$$
$$C_0(u, m_2^2, m_3^2, m_3^2, m_{\tilde{q}_i}^2, 0) \tag{D.24}$$

$$\begin{aligned} A_{3\,L}^s = \frac{C_F}{16\pi^2} \big[& g_{0_L} g_{1_L} g_{2_L} (B_0 + M_0^2 C_0 + 2uC_1 + (2u - 2m_2^2 + m_3^2)C_2) \\ & + g_{0_R} g_{1_L} g_{2_R} m_3 M_0 (C_0 - C_2) \big] \end{aligned} \tag{D.25}$$

$$A_{3\,R}^s = A_{3\,L}^s (R \leftrightarrow L) \tag{D.26}$$

$$A_{3\,L}^v = -\frac{C_F}{16\pi^2} \big[g_{0_L} g_{1_R} g_{2_L} M_0 (2C_0 + C_1) + g_{0_R} g_{1_R} g_{2_R} m_3 (C_1 + 2C_2) \big] \tag{D.27}$$

$$A_{3\,R}^v = A_{3\,L}^v (R \leftrightarrow L) \tag{D.28}$$

D.1.2 Gluino Contribution

Correction to the S-Channel Diagram

$$g_{0_L} = J_i^{q\,R\,*}, \qquad g_{0_R} = J_i^{q\,L\,*} \tag{D.29}$$
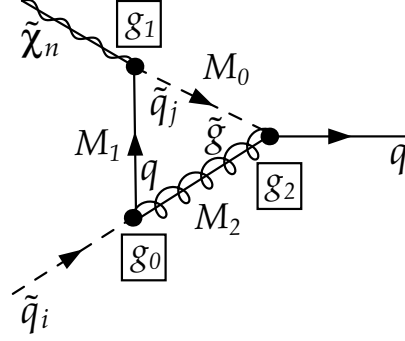
$$g_{1_L} = A_{jn}^{q\,R\,*}, \qquad g_{1_R} = A_{jn}^{q\,L\,*} \tag{D.30}$$

$$g_{2_L} = J_j^{q\,R\,*}, \qquad g_{2_R} = J_j^{q\,L\,*} \tag{D.31}$$

$$M_0 = m_{\tilde{q}_j} \tag{D.32}$$

$$M_1 = m_q \tag{D.33}$$

$$M_2 = m_{\tilde{g}} \tag{D.34}$$

$$B_0(m_2^2, m_q^2, m_{\tilde{g}}^2) \tag{D.35}$$

$$C_0(m_1^2, m_2^2, s, m_{\tilde{q}_j}^2, m_q^2, m_{\tilde{g}}^2) \tag{D.36}$$

$$A_{1\,L}^s = \sum_{j=1}^{2} -\frac{C_F}{16\pi^2} \left[(g_{0_L} g_{1_L} g_{2_L} M_1 M_2 + g_{0_L} g_{1_R} g_{2_L} M_2 m_1) C_0 + g_{0_R} g_{1_L} g_{2_L} (B_0 + M_0^2 C_0) \right.$$
$$\left. + g_{0_L} g_{1_R} g_{2_L} M_2 m_1 C_1 + g_{0_R} g_{1_R} g_{2_L} M_1 m_1 C_1 + g_{0_R} g_{1_L} g_{2_L} (m_1^2 C_1 + s C_2) \right] \tag{D.37}$$

$$A_{1\,L}^s = A_{1\,R}^s (R \leftrightarrow L) \tag{D.38}$$

$$A_{1\,R}^v = \sum_{j=1}^{2} -\frac{C_F}{16\pi^2} \left[(g_{0_R} g_{1_R} g_{2_L} M_1 + g_{0_R} g_{1_L} g_{2_L} m_1) C_0 + g_{0_L} g_{1_R} g_{2_L} M_2 C_2 \right.$$
$$\left. + g_{0_R} g_{1_R} g_{2_L} M_1 C_2 + g_{0_R} g_{1_L} g_{2_L} m_1 (C_1 + C_2) \right] \tag{D.39}$$

$$A_{1\,L}^s = A_{1\,R}^s (R \leftrightarrow L) \tag{D.40}$$

Correction to the T-Channel Diagram

$$M_0 = m_{\tilde{q}'_j} \tag{D.41}$$

$$M_1 = m_{q'} \tag{D.42}$$

$$M_2 = m_{\tilde{g}} \tag{D.43}$$

$$B_0(t, m_{q'}^2, m_{\tilde{g}}^2) \tag{D.44}$$

$$C_0(m_1^2, t, m_3^2, m_{\tilde{q}'_j}^2, m_{q'}^2, m_{\tilde{g}}^2) \tag{D.45}$$

$$
\begin{aligned}
A_{2\,L}^s = \sum_{j=1}^2 -\frac{C_F}{16\pi^2} \big[& g_{0_L} g_{1_L} g_{2_L} M_1 M_2 C_0 + g_{0_L} g_{1_R} g_{2_L} M_2 m_1 (C_0 + C_1) \\
+ \; & g_{0_L} g_{1_L} g_{2_R} M_1 m_3 (C_0 + C_2) + g_{0_L} g_{1_R} g_{2_R} m_1 m_3 (C_0 + C_1 + C_2) \\
+ \; & g_{0_R} g_{1_L} g_{2_R} M_2 m_3 C_2 + g_{0_R} g_{1_R} g_{2_L} M_1 m_1 C_1 \\
+ \; & g_{0_R} g_{1_L} g_{2_L} (B_0 + M_0^2 C_0 + m_1^2 C_1 + m_3^2 C_2) \big]
\end{aligned}
\tag{D.46}
$$

$$A_{2\,R}^s = A_{2\,L}^s(R \leftrightarrow L) \tag{D.47}$$

Correction to the U-Channel Diagram

$$M_0 = m_{\tilde{q}'_j} \tag{D.48}$$

$$M_1 = m_q \tag{D.49}$$

$$M_2 = m_{\tilde{g}} \tag{D.50}$$

$$B_0(m_2^2, m_q^2, m_{\tilde{g}}^2) \tag{D.51}$$

$$C_0(u, m_2^2, m_3^2, m_{\tilde{q}'_j}^2, m_q^2, m_{\tilde{g}}^2) \tag{D.52}$$

$$
\begin{aligned}
A_{3\,L}^s = -\frac{C_F}{16\pi^2} \sum_{j=1}^2 \big[& g_{0_L} g_{1_L} g_{2_L} M_1 M_2 C_0 + g_{0_L} g_{1_L} g_{2_R} M_1 m_3 (C_0 + C_2) \\
+ \quad & g_{0_R} g_{1_L} g_{2_R} M_2 m_3 C_2 + g_{0_R} g_{1_L} g_{2_L} (B_0 + M_0^2 C_0 + u C_1 + m_3^2 C_2) \big]
\end{aligned}
\tag{D.53}
$$

$$A_{3\,R}^s = A_{3\,L}^s(R \leftrightarrow L) \tag{D.54}$$

$$
\begin{aligned}
A_{3\,L}^v = -\frac{C_F}{16\pi^2} \sum_{j=1}^2 \big[& g_{0_R} g_{1_R} g_{2_L} M_1 C_1 + g_{0_L} g_{1_R} g_{2_L} M_2 (C_0 + C_1) \\
+ \quad & g_{0_L} g_{1_R} g_{2_R} m_3 (C_0 + C_1 + C_2) \big]
\end{aligned}
\tag{D.55}
$$

$$A_{3\,R}^v = A_{3\,L}^v(R \leftrightarrow L) \tag{D.56}$$

D.2 Higgs-Fermion-Fermion Coupling (F-Coupling)

D.2.1 Gluon Contribution

$$g_{0_L} = -g_s, \qquad g_{0_R} = -g_s \qquad (D.57)$$
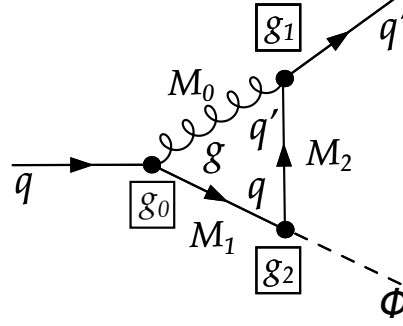
$$g_{1_L} = -g_s, \qquad g_{1_R} = -g_s \qquad (D.58)$$

$$g_{2_L} = F_\Phi^{q\,L}, \qquad g_{2_R} = F_\Phi^{q\,R} \qquad (D.59)$$

$$M_0 = 0 \qquad (D.60)$$

$$M_1 = m_q \qquad (D.61)$$

$$M_2 = m_3 \qquad (D.62)$$

$$B_0(m_4^2, m_q^2, m_3^2) \qquad (D.63)$$

$$C_0(s, m_4^2, m_3^2, 0, m_q^2, m_3^2) \qquad (D.64)$$

$$
\begin{aligned}
F_L^s = \frac{C_F}{8\pi^2} \big[& g_{0_R} g_{1_L} g_{2_L} (2B_0 + (s + m_3^2 - m_4^2 + 2M_0^2)C_0 \\
& + (3s + m_3^2 - m_4^2)C_1 + (s + 3m_3^2 - m_4^2)C_2) \\
& + g_{0_R} g_{1_R} g_{2_R} M_1 m_3 (-C_0 - C_2) + 2g_{0_R} g_{1_L} g_{2_R} M_1 M_2 C_0 \\
& - g_{0_R} g_{1_R} g_{2_L} M_2 m_3 C_2 \big]
\end{aligned}
\qquad (D.65)
$$

$$F_R^s = F_L^s (R \leftrightarrow L) \qquad (D.66)$$

$$F_L^s = -\frac{C_F}{8\pi^2} \big[g_{0_L} g_{1_L} g_{2_L} M_1 C_1 + g_{0_L} g_{1_L} g_{2_R} M_2 (C_0 + C_1) \big] \qquad (D.67)$$

$$F_R^v = F_L^v (R \leftrightarrow L) \qquad (D.68)$$

D.2.2 Gluino Contribution

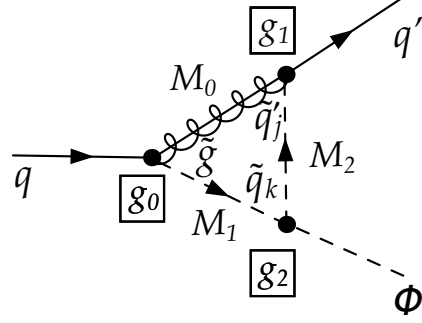$$g_{0_L} = J_k^{q\,L}, \qquad g_{0_R} = J_k^{q\,R} \qquad (\text{D.69})$$

$$g_{1_L} = J_j^{q'\,R*}, \qquad g_{1_R} = J_j^{q'\,L*} \qquad (\text{D.70})$$

$$g_2 = G_{\Phi,\,kj}^{q} \qquad (\text{D.71})$$

$$M_0 = m_{\tilde{g}} \qquad (\text{D.72})$$

$$M_1 = m_{\tilde{q}_k} \qquad (\text{D.73})$$

$$M_2 = m_{\tilde{q}'_j} \qquad (\text{D.74})$$

$$C_0(s, m_4^2, m_3^2, m_{\tilde{g}}^2, m_{\tilde{q}_k}^2, m_{\tilde{q}_j}^2) \qquad (\text{D.75})$$

$$F_L^s = -\frac{C_F}{16\pi^2} \sum_{j=1}^{2} \sum_{k=1}^{2} \left[g_{0_L} g_{1_L} g_2 M_0 C_0 - g_{0_L} g_{1_R} g_2 m_3 C_2 \right] \qquad (\text{D.76})$$

$$F_R^s = F_L^s(R \leftrightarrow L) \qquad (\text{D.77})$$

$$F_L^v = -\frac{C_F}{16\pi^2} \sum_{j=1}^{2} \sum_{k=1}^{2} \left[g_{0_R} g_{1_L} g_2 C_1 \right] \qquad (\text{D.78})$$

$$F_R^v = F_L^v(R \leftrightarrow L) \qquad (\text{D.79})$$

D.3 Higgs-Sfermion-Sfermion Coupling (G-Coupling)

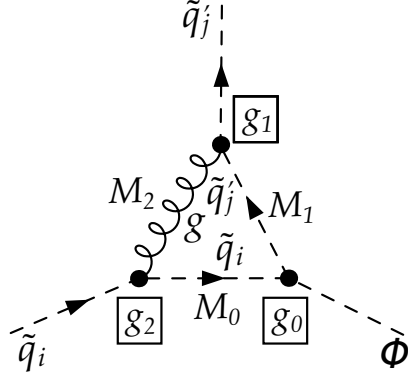## D.3.1 Gluon Contribution

$$g_0 \;= G^q_{\Phi,ij} \tag{D.80}$$

$$g_1 \;= -g_s \tag{D.81}$$

$$g_2 \;= -g_s \tag{D.82}$$

$$M_0 = m_2 \tag{D.83}$$

$$M_1 = m_{\tilde{q}'_j} \tag{D.84}$$

$$M_2 = 0 \tag{D.85}$$

$$B_0(t, m^2_{\tilde{q}'_j}, 0) \tag{D.86}$$

$$C_0(m^2_4, t, m^2_2, m^2_2, m^2_{\tilde{q}'_j}, 0) \tag{D.87}$$

$$G = \frac{C_F}{16\pi^2} g_0 g_1 g_2 \left[B_0 + (M_0^2 + t - m_4^2)C_0 + (t + m_4^2 - m_2^2)C_1 + (m_4^2 - m_2^2 - t)C_2 \right] \tag{D.88}$$

D.3.2 Gluino Contribution

$$g_{0_L} = F^{q\,L}_\Phi, \qquad g_{0_R} = F^{q\,R}_\Phi \tag{D.89}$$

$$g_{1_L} = J^{q'\,L}_j, \qquad g_{1_R} = J^{q'\,R}_j \tag{D.90}$$

$$g_{2_L} = J^{q\,R*}_i \qquad g_{2_R} = J^{q\,L*}_i \tag{D.91}$$

$$M_0 = m_q \tag{D.92}$$

$$M_1 = m_{q'} \tag{D.93}$$

$$M_2 = m_{\tilde{g}} \tag{D.94}$$

$$B_0(t, m^2_{q'}, m^2_{\tilde{g}}) \tag{D.95}$$

$$C_0(m^2_4, t, m^2_2, m^2_q, m^2_{q'}, m^2_{\tilde{g}}) \tag{D.96}$$
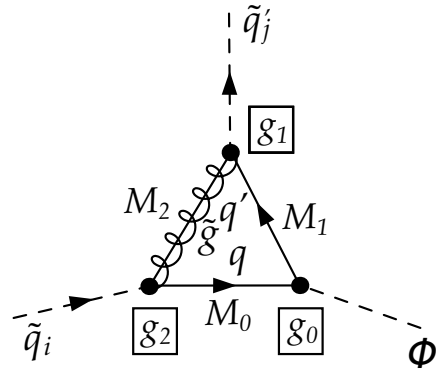
$$
\begin{aligned}
G = \frac{C_F}{16\pi^2} \big[& (g_{0_L} g_{1_L} g_{2_L} + g_{0_R} g_{1_R} g_{2_R}) 2M_0 M_1 M_2 C_0 \\
& + (g_{0_R} g_{1_R} g_{2_L} + g_{0_L} g_{1_L} g_{2_R}) M_1 (2(B_0 + M_0^2 C_0 + m_2^2 C_2) + (m_2^2 + m_4^2 - t)C_1)
\end{aligned}
$$

203

$$+ (g_{0_L} g_{1_R} g_{2_R} + g_{0_R} g_{1_L} g_{2_L}) M_2 (2(B_0 + M_0^2 C_0 + m_4^2 C_1) + (m_2^2 + m_4^2 - t) C_2)$$
$$+ (g_{0_L} g_{1_R} g_{2_L} + g_{0_R} g_{1_L} g_{2_R}) M_0 (2(B_0 + M_0^2 C_0 + m_4^2 C_1 + m_2^2 C_2)$$
$$+ (m_2^2 + m_4^2 - t)(C_0 + C_1 + C_2))\big] \tag{D.97}$$

D.3.3 Squark Contribution
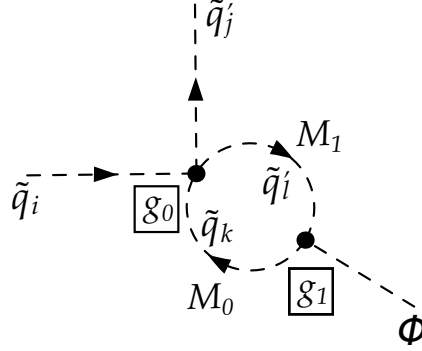
$$g_0 = -g_s^2 (U_{l1}^q U_{i1}^q - U_{l2}^q U_{i2}^q)(U_{j1}^{q'} U_{k1}^{q'} - U_{j2}^{q'} U_{k2}^{q'}) \tag{D.98}$$
$$g_1 = G_{\Phi, lk}^q \tag{D.99}$$

$$B_0(m_4^2, m_{\tilde{q}_k}^2, m_{\tilde{q}_l'}^2) \tag{D.100}$$

$$G = \sum_{l=1}^{2} \sum_{k=1}^{2} \frac{C_F}{16\pi^2} g_0 g_1 B_0 \tag{D.101}$$

E Box Contributions

E.1 S-Channel Box with Gluon

$$g_0 = -g_s \tag{E.1}$$

$$g_{1_L} = A_{in}^{q\,L}, \quad g_{1_R} = A_{in}^{q\,R} \tag{E.2}$$

$$g_{2_L} = F_\Phi^{q\,L}, \quad g_{2_R} = F_\Phi^{q\,R} \tag{E.3}$$

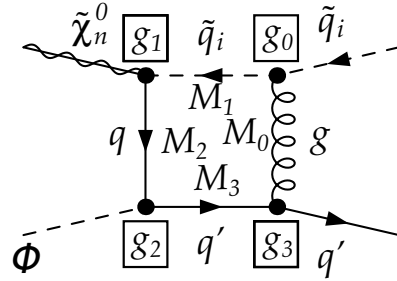$$g_3 = -g_s \tag{E.4}$$

$$M_0 = 0 \tag{E.5}$$

$$M_1 = m_2 \tag{E.6}$$

$$M_2 = m_q \tag{E.7}$$

$$M_3 = m_3 \tag{E.8}$$

$$C_0'(m_2^2, s, m_1^2, M_1^2, M_0^2, M_2^2) \tag{E.9}$$

$$C_0(m_1^2, m_4^2, u, M_1^2, M_2^2, M_3^2) \tag{E.10}$$

$$D_0(m_2^2, m_1^2, m_4^2, m_3^2, s, u, M_0^2, M_1^2, M_2^2, M_3^2) \tag{E.11}$$

$$
\begin{aligned}
B_{1\,L}^s = -\frac{C_F}{16\pi^2} \big[& g_0 g_3 (g_{1_L} (-(g_{2_R}(m_3 - M_3)(C_0 + M_0^2 D_0 + s D_2 + m_2^2(2D_0 + 3D_1 + 2D_2))) \\
& + g_{2_R}(-m_3 3 + 2m_3^2 M_3 + m_3 M_3^2 + 2m_2^2(-m_3 + M_3) - 2M_3 u) D_3 \\
& + g_{2_L} M_2 (C_0 + M_0^2 D_0 - 2u D_0 - u D_1 + m_1^2 D_2 - t D_2 - u D_2 + m_3 M_3 D_3 - 2u D_3 \\
& + m_2^2(2D_0 + 3(D_1 + D_2) + 2D_3) + m_3^2(2D_0 + D_1 + 2D_2 + 3D_3))) \\
& + g_{1_R} m_1 (g_{2_R} M_2(-m_3 + M_3) D_2 + g_{2_L} \\
& + \times(C_0 + C_2' + M_0^2 D_0 - 2u D_0 - u D_1 + (m_1^2 + M_3^2 - t) D_2 - 3u D_2 + m_3 M_3 D_3 \\
& - 2u D_3 + m_2^2(2D_0 + 3(D_1 + D_2) + 2D_3) + m_3^2(2D_0 + D_1 + 3(D_2 + D_3)))))\big]
\end{aligned}
\tag{E.12}
$$

$$B_{1\,R}^s = B_{1\,L}^s(R \leftrightarrow L) \tag{E.13}$$

$$B_{1\,L}^v = -\frac{C_F}{16\pi^2} \left[g_0 g_3 (g_{1_L} m_1 (2 g_{2_L} M_2 D_2 + g_{2_R}(-m_3 + M_3)(2D_0 + D_1 + 2D_2) \right.$$
$$- 2 g_{2_R} m_3 D_3) + g_{1_R}(g_{2_R} M_2((-m_3 + M_3)(2D_0 + D_1 + D_2) - 2m_3 D_3)$$
$$+ g_{2_L}(3C_0 - C_0' - C_1' + 3M_0^2 D_0 - 2uD_0 + M_3^2 D_1 - 3uD_1$$
$$+ (m_1^2 + M_3^2 + 2s - t)D_2 - 3uD_2 - m_3 M_3 D_3 - 2uD_3$$
$$\left. + m_2^2(2D_0 + 5D_1 + 3D_2 + 2D_3) + m_3^2(2D_0 + 2D_1 + 3D_2 + 5D_3))))\right] \qquad \text{(E.14)}$$

$$B_{1\,R}^v = B_{1\,L}^v (R \leftrightarrow L) \qquad \text{(E.15)}$$

E.2 T-Channel Box with Gluon

$$g_0 = -g_s \tag{E.16}$$

$$g_1 = -g_s \tag{E.17}$$

$$g_{2_L} = A_{jn}^{q'\,L}, \quad g_{2_R} = A_{jn}^{q'\,R} \tag{E.18}$$

$$g_3 = G_{\Phi,ij}^{q} \tag{E.19}$$

$$M_0 = 0 \tag{E.20}$$

$$M_1 = m_3 \tag{E.21}$$

$$M_2 = m_{\tilde{q}'_j} \tag{E.22}$$

$$M_3 = m_2 \tag{E.23}$$
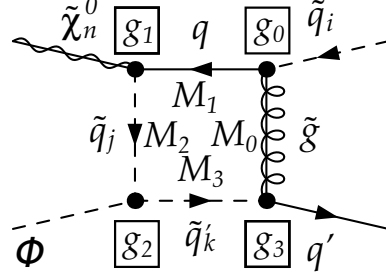
$$C_0(m_1^2, m_4^2, u, M_1^2, M_2^2, M_3^2) \tag{E.24}$$

$$D_0(m_3^2, m_1^2, m_4^2, m_2^2, t, u, M_0^2, M_1^2, M_2^2, M_3^2) \tag{E.25}$$

$$
\begin{aligned}
B_{2\,L}^{s} = -\frac{C_F}{16\pi^2} \sum_{j=1}^{2} \big[& g_0 g_1 g_3 (2 g_{2_L}(m_2^2 + m_3^2 - u) D_0 + g_{2_L}(C_0 + M_0^2 D_0) \\
& + g_{2_L}(2m_2^2 + m_3(3m_3 + M_1) - 2u) D_1 + g_{2_L}(3m_2^2 + m_3^2 - u) D_3 \\
& + (g_{2_R} m_1(m_3 - M_1) + g_{2_L}(-m_1^2 + 2m_2^2 + m_3(2m_3 + M_1) + t - 2u)) D_2 \big]
\end{aligned}
\tag{E.26}
$$

$$B_{2\,R}^{s} = B_{2\,L}^{s}(R \leftrightarrow L) \tag{E.27}$$

$$
\begin{aligned}
B_{2\,L}^{v} = -\frac{C_F}{16\pi^2} \sum_{j=1}^{2} \big[& g_0 g_1 g_3 (2 g_{2_R}(-m_3 + M_1) D_0 - 2 g_{2_R} m_3 D_1 \\
& - 2(g_{2_L} m_1 + g_{2_R} m_3) D_2 + g_{2_R}(-m_3 + M_1) D_3) \big]
\end{aligned}
\tag{E.28}
$$

$$B_{2\,R}^{v} = B_{2\,L}^{v}(R \leftrightarrow L) \tag{E.29}$$

E.3 S-Channel Box with Gluino

$$g_{0_L} = J_i^{q\,R\,*}, \quad g_{0_R} = J_i^{q\,L\,*} \qquad \text{(E.30)}$$

$$g_{1_L} = A_{jn}^{q\,R\,*} \quad g_{1_R} = A_{jn}^{q\,L\,*} \qquad \text{(E.31)}$$

$$g_2 \;\; = G_{\Phi,\,jk}^{q} \qquad\qquad\qquad \text{(E.32)}$$

$$g_{3_L} = J_k^{q'\,R\,*} \quad g_{3_R} = J_k^{q'\,L\,*} \qquad \text{(E.33)}$$

$$M_0 = m_{\tilde{g}} \qquad\qquad\qquad\qquad \text{(E.34)}$$

$$M_1 = m_q \qquad\qquad\qquad\qquad \text{(E.35)}$$

$$M_2 = m_{\tilde{q}_j} \qquad\qquad\qquad\qquad \text{(E.36)}$$

$$M_3 = m_{\tilde{q}_k'} \qquad\qquad\qquad\qquad \text{(E.37)}$$
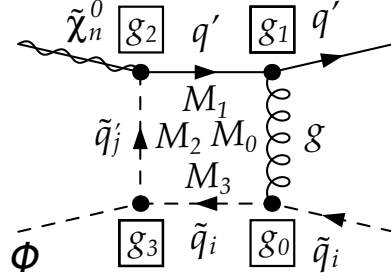
$$C_0(m_1^2, m_4^2, u, M_1^2, M_2^2, M_3^2) \qquad\qquad\qquad\qquad \text{(E.38)}$$

$$D_0(m_2^2, m_1^2, m_4^2, m_3^2, s, u, M_0^2, M_1^2, M_2^2, M_3^2) \qquad\qquad \text{(E.39)}$$

$$B_{3\,L}^s = \frac{C_F}{16\pi^2} \sum_{j=1}^{2} \sum_{k=1}^{2} \big[g_2(g_{0_L}g_{1_L}g_{3_L}M_0M_1D_0 + g_{0_R}g_{1_L}g_{3_L}(C_0 + M_0^2 D_0)$$

$$+ g_{0_R}g_{1_L}g_{3_L}m_2^2 D_1 - g_{3_L}(m_1(g_{0_R}g_{1_L}m_1 + g_{0_L}g_{1_R}M_0 + g_{0_R}g_{1_R}M_1) - g_{0_R}g_{1_L}s)D_2$$

$$- g_{1_L}g_{3_R}m_3(g_{0_R}M_0 + g_{0_L}M_1)D_3)\big] \qquad\qquad\qquad \text{(E.40)}$$

$$B_{3\,R}^s = B_{3\,L}^s (R \leftrightarrow L) \qquad\qquad\qquad\qquad\qquad \text{(E.41)}$$

$$B_{3\,L}^s = \frac{C_F}{16\pi^2} \sum_{j=1}^{2} \sum_{k=1}^{2} \big[g_2(-(g_{0_L}g_{1_R}g_{3_L}M_0D_0) - g_{1_R}g_{3_L}(g_{0_L}M_0 + g_{0_R}M_1)D_1$$

$$- g_{3_L}(g_{0_R}g_{1_L}m_1 + g_{0_L}g_{1_R}M_0 + g_{0_R}g_{1_R}M_1)D_2 + g_{0_L}g_{1_R}g_{3_R}m_3 D_3)\big] \qquad \text{(E.42)}$$

$$B_{3\,R}^v = B_{3\,L}^v (R \leftrightarrow L) \qquad\qquad\qquad\qquad\qquad \text{(E.43)}$$

E.4 T-Channel Box with Gluino

$$g_{0_L} = J_i^{q\,R\,*}, \quad g_{0_R} = J_i^{q\,L\,*} \tag{E.44}$$

$$g_{1_L} = J_j^{q'\,R\,*}, \quad g_{1_R} = J_j^{q'\,L\,*} \tag{E.45}$$

$$g_{2_L} = A_{jn}^{q'\,R\,*}, \quad g_{2_R} = A_{jn}^{q'\,L\,*} \tag{E.46}$$
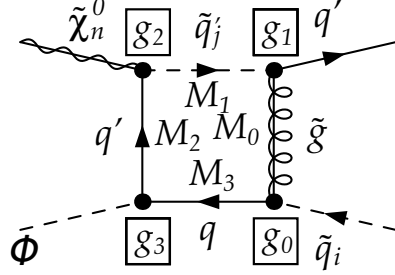
$$g_{3_L} = F_\Phi^{q\,L}, \quad g_{3_R} = F_\Phi^{q\,R} \tag{E.47}$$

$$M_0 = m_{\tilde{g}} \tag{E.48}$$

$$M_1 = m_{\tilde{q}'_j} \tag{E.49}$$

$$M_2 = m_{q'} \tag{E.50}$$

$$M_3 = m_q \tag{E.51}$$

$$C_0'(m_3^2, t, m_1^2, M_1^2, M_0^2, M_2^2) \tag{E.52}$$

$$C_0(m_1^2, m_4^2, u, M_1^2, M_2^2, M_3^2) \tag{E.53}$$

$$D_0(m_3^2, m_1^2, m_4^2, m_2^2, t, u, M_0^2, M_1^2, M_2^2, M_3^2) \tag{E.54}$$

$$
\begin{aligned}
B_{4\,L}^s = {} & \frac{C_F}{16\pi^2} \sum_{j=1}^2 [g_{0_R}(-(g_{1_R} m_3 M_0 (g_{2_R} g_{3_L} m_1 D_1 + g_{2_L}(g_{3_L} M_2(D_1 + D_2) \\
& + g_{3_R} M_3 (D_0 + D_1 + D_2)))) + g_{1_L}(g_{2_R} m_1(g_{3_R} M_2 M_3 D_2 + g_{3_L}(C_0 + C_2' + M_0^2 D_0 \\
& + (m_1^2 + m_2^2 + m_3^2 + M_3^2 - s - u)D_2 \\
& + m_2^2 D_3)) + g_{2_L}(g_{3_R} M_3(C_0 + M_0^2 D_0 + t D_2 + m_2^2 D_3 - u D_3 + m_3^2(D_1 + D_3)) \\
& + g_{3_L} M_2(C_0 + M_0^2 D_0 + m_1^2 D_2 - s D_2 + m_2^2(D_2 + D_3))))) \\
& + g_{0_L}(-(g_{1_R} m_3(g_{2_R} g_{3_L} m_1 M_3 D_1 + g_{2_L}(g_{3_L} M_2 M_3(D_1 + D_2) \\
& + g_{3_R}(C_0 - C_0' - C_1' + M_0^2 D_0 - u D_1 + m_1^2 D_2 - (s + u)D_2 + m_3^2(D_1 + D_2) \\
& + M_3^2(D_1 + D_2) + m_2^2(D_2 + D_3))))) \\
& + g_{1_L} M_0(g_{2_R} m_1(g_{3_R} M_2 D_2 + g_{3_L} M_3(D_0 + D_2)) \\
& + g_{2_L}(g_{3_L} M_2 M_3 D_0 + g_{3_R}(C_0 + M_0^2 D_0 - u D_0 - u D_1 + t D_2 - u D_2 - u D_3 \\
& + m_3^2(D_0 + 2D_1 + D_2 + D_3) + m_2^2(D_0 + D_1 + D_2 + 2D_3)))))] \tag{E.55}
\end{aligned}
$$

$$B_{4\,R}^s = B_{4\,L}^s(R \leftrightarrow L) \tag{E.56}$$

$$
B_{4\,L}^s = \frac{C_F}{16\pi^2} \sum_{j=1}^2 [-(g_{0_L}(g_{1_R} m_3(-(g_{3_R}(g_{2_L} m_1 D_1 + g_{2_R} M_2(D_1 + D_2))) + g_{2_R} g_{3_L} M_3 D_3)
$$

$$+ g_{1_L} M_0(g_{2_L} g_{3_R} m_1(D_0 + D_2 + D_3) + g_{2_R}(g_{3_L} M_3 D_3 + g_{3_R} M_2(D_0 + D_3)))))$$
$$+ g_{0_R}(-(g_{1_R} g_{2_R} g_{3_L} m_3 M_0(D_0 + D_1 + D_2 + D_3))$$
$$+ g_{1_L}(g_{2_L} m_1(g_{3_L} M_2 D_2 - g_{3_R} M_3 D_3) + g_{2_R}(-(g_{3_R} M_2 M_3 D_3)$$
$$+ g_{3_L}(C_0 + M_0^2 D_0 + m_3^2 D_1 + t D_2 + (m_2 - M_3)(m_2 + M_3)D_3)))) \big] \tag{E.57}$$

$$B_{4\,R}^s = B_{4\,L}^s(R \leftrightarrow L) \tag{E.58}$$

Bibliography

[1] J. Harz, B. Herrmann, et al., "Neutralino-stop coannihilation into electroweak gauge and Higgs bosons at one loop", Physical Review D **87**, 054031 (2013), arXiv: 1212.5241.

[2] J. Harz, B. Herrmann, et al., "Impact of SUSY-QCD corrections on neutralino-stop co-annihilation and the neutralino relic density", 15 (2013), arXiv: 1302.3525.

[3] G. Aad, A. T., et al., "Observation of a new particle in the search for the Standard Model Higgs boson with the ATLAS detector at the LHC", Physics Letters B **716**, 1–29 (2012), arXiv: 1207.7214.

[4] S. Chatrchyan, V. Khachatryan, et al., "Observation of a new boson at a mass of 125 GeV with the CMS experiment at the LHC", Physics Letters B **716**, 30–61 (2012), arXiv: 1207.7235.

[5] E. Gildener, "Gauge-symmetry hierarchies", Physical Review D **14**, 1667–1672 (1976).

[6] E. Gildener and S. Weinberg, "Symmetry breaking and scalar bosons", Physical Review D **13**, 3333–3341 (1976).

[7] S. Coleman and J. Mandula, "All Possible Symmetries of the S Matrix", Physical Review **159**, 1251–1256 (1967).

[8] R. Haag, J. T. Łopuszański, and M. Sohnius, "All possible generators of supersymmetries of the S-matrix", Nuclear Physics B **88**, 257–274 (1975).

[9] J. Wess and J. Bagger, *Supersymmetry and Supergravity* (Princeton University Press, 1992).

[10] S. Weinberg, *The Quantum Theory of Fields Vol. III* (Cambridge University Press).

[11] M. Drees, R. M. Godbole, and P. Roy, *Theory and Phenomenology of Sparticles* (World Scientific, 2004).

[12] M. Drees, "An Introduction to Supersymmetry", 42 (1996), arXiv: hep-ph/9611409.

[13] H. Müller-Kirsten and A. Wiedemann, *Introduction to Supersymmetry*, Vol. 80 (World Scientific Lecture Notes in Physics, 2010).

[14] S. P. Martin, "A Supersymmetry Primer", 152 (1997), arXiv: hep-ph/9709356.

[15] L. O'Raifeartaigh, "Spontaneous symmetry breaking for chirals scalar superfields", Nuclear Physics B **96**, 331–352 (1975).

[16] P. Fayet and J. Iliopoulos, "Spontaneously broken supergauge symmetries and goldstone spinors", Physics Letters B **51**, 461–464 (1974).

[17] A. H. Chamseddine, R. Arnowitt, and P. Nath, "Locally Supersymmetric Grand Unification", Physical Review Letters **49**, 970–974 (1982).

[18] M. Dine, W. Fischler, and M. Srednicki, "Supersymmetric technicolor", Nuclear Physics B **189**, 575–593 (1981).

[19] I. J. R. Aitchison, "Supersymmetry and the MSSM: An Elementary Introduction", 159 (2005), arXiv: hep-ph/0505105.

[20] J. Beringer, J. F. Arguin, et al., "Review of Particle Physics", Physical Review D **86**, 010001 (2012).

[21] A. Djouadi, J.-L. Kneur, and G. Moultaka, "SuSpect: A Fortran code for the Supersymmetric and Higgs particle spectrum in the MSSM", Computer Physics Communications **176**, 426–455 (2007), arXiv: hep-ph/0211331.

[22] C. F. Berger, J. S. Gainer, et al., "Supersymmetry without prejudice", Journal of High Energy Physics **2009**, 023–023 (2009), arXiv: 0812.0980.

[23] F. Zwicky, "Die Rotverschiebung von extragalaktischen Nebeln", Helvetica Physica Acta **6**, 110–127 (1933).

[24] J. Einasto, "Dark Matter", 31 (2009), arXiv: 0901.0632.

[25] V. Trimble, "Dark Matter: Past, Present, and Future", in *Neutrinos and explosive events in the universe* (Springer Netherlands, 2005), pp. 181–199.

[26] G. Bertone, D. Hooper, and J. Silk, "Particle dark matter: evidence, candidates and constraints", Physics Reports **405**, 279–390 (2005), arXiv: hep-ph/0404175.

[27] K. Garrett and G. Duda, "Dark Matter: A Primer", Advances in Astronomy **2011**, 1–22 (2011), arXiv: 1006.2483.

[28] K. G. Begeman, A. H. Broeils, and R. H. Sanders, "Extended rotation curves of spiral galaxies: Dark haloes and modified dynamics", Mon.Not.Roy.Astron.Soc. **249**, 523 (1991).

[29] D. Clowe, M. Bradač, et al., "A Direct Empirical Proof of the Existence of Dark Matter", The Astrophysical Journal **648**, L109–L113 (2006), arXiv: astro-ph/0608407.

[30] G. F. Smoot, C. Bennett, et al., "Structure in the COBE differential microwave radiometer first year maps", Astrophys.J. **396**, L1–L5 (1992).

[31] A. Kogut, J. Dunkley, et al., "Three-Year Wilkinson Microwave Anisotropy Probe (WMAP) Observations: Foreground Polarization", The Astrophysical Journal **665**, 355–362 (2007), arXiv: 0704.3991.

[32] J. Dunkley, E. Komatsu, et al., "Five-Year Wilkinson Microwave Anisotropy Probe (WMAP) Observations: Likelihoods and Parameters from the WMAP Data", The Astrophysical Journal Supplement Series **180**, 306–329 (2009), arXiv: 0803.0586.

[33] E. Komatsu, K. M. Smith, et al., "Seven-Year Wilkinson Microwave Anisotropy Probe (WMAP) Observations: Cosmological Interpretation", The Astrophysical Journal Supplement Series **192**, 18 (2011), arXiv: 1001.4538.

[34] G. Hinshaw, D. Larson, et al., "Nine-Year Wilkinson Microwave Anisotropy Probe (WMAP) Observations: Cosmological Parameter Results", (2012), arXiv: 1212.5226.

[35] W. Hu, N. Sugiyama, and J. Silk, "The physics of microwave background anisotropies", Nature **386**, 37–43 (1997), arXiv: astro-ph/9604166.

[36] T. Bringmann, "Lecture Notes: Dark Matter", 2011.

[37] Planck Collaboration, P. A. R. Ade, et al., "Planck 2013 results. XVI. Cosmological parameters", 67 (2013), arXiv: 1303.5076.

[38] W. Hu and S. Dodelson, "Cosmic Microwave Background Anisotropies", Annual Review of Astronomy and Astrophysics **40**, 171–216 (2002), arXiv: astro-ph/0110414.

[39] M. Taoso, G. Bertone, and A. Masiero, "Dark matter candidates: a ten-point test", Journal of Cosmology and Astroparticle Physics **2008**, 022 (2008), arXiv: 0711.4996.

[40] W. L. Freedman, B. F. Madore, et al., "Final Results from the Hubble Space Telescope Key Project to Measure the Hubble Constant", The Astrophysical Journal **553**, 47–72 (2000), arXiv: astro-ph/0012376.

[41] P. Natarajan, A. Loeb, et al., "Constraints on the Collisional Nature of the Dark Matter from Gravitational Lensing in the Cluster A2218", The Astrophysical Journal **580**, L17–L20 (2002), arXiv: astro-ph/0207045.

[42] R. Cyburt, B. Fields, et al., "Constraining strong baryon–dark-matter interactions with primordial nucleosynthesis and cosmic rays", Physical Review D **65**, 123503 (2002), arXiv: astro-ph/0203240.

[43] X. Chen, S. Hannestad, and R. Scherrer, "Cosmic microwave background and large scale structure limits on the interaction between dark matter and baryons", Physical Review D **65**, 123515 (2002), arXiv: astro-ph/0202496.

[44] E. Kolb and M. Turner, *The Early Universe* (Westview, 1994).

[45] J. R. Primack, "Whatever Happened to Hot Dark Matter?", SLAC Beam Line **31N3**, 50–57 (2001), arXiv: astro-ph/0112336.

[46] A. Klypin, A. V. Kravtsov, et al., "Where Are the Missing Galactic Satellites?", The Astrophysical Journal **522**, 82–92 (1999), arXiv: astro-ph/9901240.

[47] B. Moore, S. Ghigna, et al., "Dark Matter Substructure within Galactic Halos", The Astrophysical Journal **524**, L19–L22 (1999), arXiv: astro-ph/9907411.

[48] M. Viel, G. Becker, et al., "How Cold Is Cold Dark Matter? Small-Scales Constraints from the Flux Power Spectrum of the High-Redshift Lyman-α Forest", Physical Review Letters **100**, 041304 (2008), arXiv: 0709.0131.

[49] L. G. van den Aarssen, T. Bringmann, and C. Pfrommer, "Is Dark Matter with Long-Range Interactions a Solution to All Small-Scale Problems of Λ Cold Dark Matter Cosmology?", Physical Review Letters **109**, 231301 (2012), arXiv: 1205.5809.

[50] S. Hofmann, D. Schwarz, and H. Stöcker, "Damping scales of neutralino cold dark matter", Physical Review D **64**, 083507 (2001), arXiv: astro-ph/0104173.

[51] M. D. Weinberg and N. Katz, "Bar-driven Dark Halo Evolution: A Resolution of the Cusp-Core Controversy", The Astrophysical Journal **580**, 627–633 (2002), arXiv: astro-ph/0110632.

[52] K. A. Olive, G. Steigman, and T. P. Walker, "Primordial nucleosynthesis: theory and observations", Physics Reports **333-334**, 389–407 (2000), arXiv: astro-ph/9905320.

[53] R. H. Cyburt, B. D. Fields, et al., "New BBN limits on physics beyond the standard model from 4He", Astroparticle Physics **23**, 313–323 (2005), arXiv: astro-ph/0408033.

[54] R. Cyburt, J. Ellis, et al., "Updated nucleosynthesis constraints on unstable relic particles", Physical Review D **67**, 103521 (2003), arXiv: astro-ph/0211258.

[55] G. G. Raffelt, "Particle Physics from Stars", Annual Review of Nuclear and Particle Science **49**, 163–216 (1999), arXiv: hep-ph/9903472.

[56] M. Milgrom, "A modification of the Newtonian dynamics as a possible alternative to the hidden mass hypothesis", The Astrophysical Journal **270**, 365 (1983).

[57] M. Milgrom, "MOND–a pedagogical review", Acta Phys.Polon. **B32**, 3613 (2001), arXiv: astro-ph/0112069.

[58] R. H. Sanders, "The Virial Discrepancy in Clusters of Galaxies in the Context of Modified Newtonian Dynamics", The Astrophysical Journal **512**, L23–L26 (1999), arXiv: astro-ph/9807023.

[59] M. Milgrom, "MD or DM? Modified dynamics at low accelerations vs dark matter", Proceedings of Science **HRMS2010**, 033 (2010), arXiv: 1101.5122.

[60] B. J. Carr, "Recent developments in the search for baryonic dark matter", (2001), arXiv: astro-ph/0102389.

[61] S. Riemer-Sørensen, D. Parkinson, and T. M. Davis, "Combining Planck with Large Scale Structure gives strong neutrino mass constraint", (2013), arXiv: 1306.4153.

[62] S. Dodelson and L. M. Widrow, "Sterile Neutrinos as Dark Matter", Physical Review Letters **72**, 10 (1993), arXiv: hep-ph/9303287.

[63] L. Canetti, M. Drewes, et al., "Dark matter, baryogenesis and neutrino oscillations from right-handed neutrinos", Physical Review D **87**, 093006 (2013), arXiv: 1208.4607.

[64] L. Canetti, M. Drewes, and M. Shaposhnikov, "Sterile Neutrinos as the Origin of Dark and Baryonic Matter", Physical Review Letters **110**, 061801 (2013), arXiv: 1204.3902.

[65] M. Viel, J. Lesgourgues, et al., "Can Sterile Neutrinos Be Ruled Out as Warm Dark Matter Candidates?", Physical Review Letters **97**, 071301 (2006), arXiv: astro-ph/0605706.

[66] U. Seljak, A. Makarov, et al., "Can Sterile Neutrinos Be the Dark Matter?", Physical Review Letters **97**, 191303 (2006), arXiv: astro-ph/0602430.

[67] R. D. Peccei and H. R. Quinn, "Constraints imposed by CP conservation in the presence of pseudoparticles", Physical Review D **16**, 1791–1797 (1977).

[68] J. E. Kim, "A review on axions and the strong CP problem", 10 (2009), arXiv: 0909.3908.

[69] D. Cadamuro, "Cosmological limits on axions and axion-like particles", PhD thesis (Oct. 2012), p. 132, arXiv: 1210.3196.

[70] T. Falk, K. A. Olive, and M. Srednicki, "Heavy Sneutrinos as Dark Matter", Physics Letters B **339**, 7 (1994), arXiv: hep-ph/9409270.

[71] H.-S. Lee, K. Matchev, and S. Nasri, "Revival of the thermal sneutrino dark matter", Physical Review D **76**, 041302 (2007), arXiv: hep-ph/0702223.

[72] B. Dumont, G. Belanger, et al., "Mixed sneutrino dark matter in light of the 2011 XENON and LHC results", Journal of Cosmology and Astroparticle Physics **2012**, 38 (2012), arXiv: 1206.1521.

[73] F. D. Steffen, "Dark-matter candidates", The European Physical Journal C **59**, 557–588 (2009), arXiv: 0811.3347.

[74] Y. Santoso, "The Phenomenology of Gravitino Dark Matter Scenarios in Supergravity Models", in Dark matter in astrophysics and particle physics - proceedings of the 7th international heidelberg conference on dark 2009 (Mar. 2010), pp. 77–86, arXiv: 0903.2860.

[75] K.-Y. Choi, L. Covi, et al., "Axino cold dark matter revisited", Journal of High Energy Physics **2012**, 106 (2012), arXiv: 1108.2282.

[76] J. Feng and J. Kumar, "Dark-Matter Particles without Weak-Scale Masses or Weak Interactions", Physical Review Letters **101**, 231301 (2008), arXiv: 0803.4196.

[77] J. L. Feng, J. Kumar, et al., "Isospin-violating dark matter", Physics Letters B **703**, 124–127 (2011), arXiv: 1102.4331.

[78] K. R. Dienes and B. Thomas, "Dynamical dark matter. I. Theoretical overview", Physical Review D **85**, 083523 (2012), arXiv: 1106.4546.

[79] D. Hooper and S. Profumo, "Dark matter and collider phenomenology of universal extra dimensions", Physics Reports **453**, 29–115 (2007), arXiv: hep-ph/0701197.

[80] A. Goudelis, B. Herrmann, and O. Stål, "Dark matter in the Inert Doublet Model after the discovery of a Higgs-like boson at the LHC", 29 (2013), arXiv: 1303.3010.

[81] A. De Rújula, S. Glashow, and U. Sarid, "Charged dark matter", Nuclear Physics B **333**, 173–194 (1990).

[82] H. Ziaeepour, "A Decaying Ultra Heavy Dark Matter (WIMPZILLA): Review of Recent Progress", Grav.Cosmol.Suppl. **6**, 128–133 (2000), arXiv: astro-ph/0005299.

[83] L. Bergström, "Non-baryonic dark matter: observational evidence and detection methods", Reports on Progress in Physics **63**, 793–841 (2000), arXiv: hep-ph/0002126.

[84] P. Gondolo, "Introduction to Non-Baryonic Dark Matter", NATO Sci.Ser.II **187**, 279–333 (2005), arXiv: astro-ph/0403064.

[85] M. Cirelli, G. Corcella, et al., "PPPC 4 DM ID: a poor particle physicist cookbook for dark matter indirect detection", Journal of Cosmology and Astroparticle Physics **2011**, 051–051 (2011), arXiv: 1012.4515.

[86] M. Cirelli, "Indirect searches for dark matter", Pramana **79**, 1021–1043 (2012), arXiv: 1202.1454.

[87] M. Cirelli, M. Kadastik, et al., "Model-independent implications of the , cosmic ray spectra on properties of Dark Matter", Nuclear Physics B **813**, 1–21 (2009), arXiv: arXiv:0809.2409v4.

[88] M. Aguilar, G. Alberti, et al., "First Result from the Alpha Magnetic Spectrometer on the International Space Station: Precision Measurement of the Positron Fraction in Primary Cosmic Rays of 0.5–350 GeV", Phys.Rev.Lett. **110**, 141102 (2013).

[89] D. Hooper, P. Blasi, and P. D. Serpico, "Pulsars as the sources of high energy cosmic ray positrons", Journal of Cosmology and Astroparticle Physics **2009**, 025–025 (2009), arXiv: 0810.1527.

[90] T. Bringmann, X. Huang, et al., "Fermi LAT search for internal bremsstrahlung signatures from dark matter annihilation", Journal of Cosmology and Astroparticle Physics **2012**, 054–054 (2012), arXiv: 1203.1312.

[91] D. P. Finkbeiner, M. Su, and C. Weniger, "Is the 130 GeV line real? A search for systematics in the Fermi-LAT data", Journal of Cosmology and Astroparticle Physics **2013**, 029–029 (2013), arXiv: 1209.4562.

[92] C. Weniger, M. Su, et al., "Closing in on the Fermi Line with a New Observation Strategy", 21 (2013), arXiv: 1305.4710.

[93] R. Kappl and M. W. Winkler, "New limits on dark matter from Super-Kamiokande", Nuclear Physics B **850**, 505–521 (2011), arXiv: 1104.0679.

[94] M. G. Aartsen, R. Abbasi, et al., "Search for Dark Matter Annihilations in the Sun with the 79-String IceCube Detector", Physical Review Letters **110**, 131302 (2013), arXiv: 1212.4097.

[95] P. Salati, "Indirect and direct dark matter detection", in Cargèse summer school: cosmology and particle physics beyond the standard models (2007).

[96] L. Baudis, "Direct dark matter detection: The next decade", Physics of the Dark Universe **1**, 94–108 (2012), arXiv: 1211.7222.

[97] R. Mahapatra, "Review of dark matter direct detection experiments", Pramana **79**, 1045–1057 (2012).

[98] E. Aprile, M. Alfonsi, et al., "Limits on Spin-Dependent WIMP-Nucleon Cross Sections from 225 Live Days of XENON100 Data", Physical Review Letters **111**, 021301 (2013), arXiv: 1301.6620.

[99] S. Archambault, E. Behnke, et al., "Constraints on low-mass WIMP interactions on 19F from PICASSO", Physics Letters B **711**, 153–161 (2012), arXiv: 1202.1240.

[100] E. Behnke, J. Behnke, et al., "First dark matter search results from a 4-kg CF_3I bubble chamber operated in a deep underground site", Physical Review D **86**, 052001 (2012), arXiv: 1204.3094.

[101] M. Felizardo, T. A. Girard, et al., "Final Analysis and Results of the Phase II SIMPLE Dark Matter Search", Physical Review Letters **108**, 201302 (2012), arXiv: 1106.3014.

[102] E. Aprile, M. Alfonsi, et al., "Dark Matter Results from 225 Live Days of XENON100 Data", Physical Review Letters **109**, 181301 (2012), arXiv: 1207.5988.

[103] C. Savage, K. Freese, et al., "Compatibility of DAMA/LIBRA dark matter detection with other searches in light of new galactic rotation velocity measurements", Journal of Cosmology and Astroparticle Physics **2009**, 036–036 (2009), arXiv: 0901.2713.

[104] R. Bernabei, P. Belli, et al., "New results from DAMA/LIBRA", The European Physical Journal C **67**, 39–49 (2010), arXiv: 1002.1028.

[105] J. Cherwinka, R. Co, et al., "A search for the dark matter annual modulation in South Pole ice", Astroparticle Physics **35**, 749–754 (2012), arXiv: 1106.1156.

[106] G. Angloher, M. Bauer, et al., "Results from 730 kg days of the CRESST-II Dark Matter search", The European Physical Journal C **72**, 1971 (2012), arXiv: 1109.0702.

[107] L. Stodolsky, G. Angloher, et al., "The CRESST II Dark Matter Search", Journal of Physics: Conference Series **384**, 012013 (2012), arXiv: 1203.6835.

[108] CDMS Collaboration, R. Agnese, et al., "Dark Matter Search Results Using the Silicon Detectors of CDMS II", 5 (2013), arXiv: 1304.4279.

[109] *Resonaances - More mess with dark matter detection*, July 31, 2013.

[110] CDMS Collaboration, R. Agnese, et al., "Silicon Detector Results from the First Five-Tower Run of CDMS II", 5 (2013), arXiv: 1304.3706.

[111] C. E. Aalseth, P. S. Barbeau, et al., "Results from a Search for Light-Mass Dark Matter with a p-Type Point Contact Germanium Detector", Physical Review Letters **106**, 131301 (2011), arXiv: 1002.4703.

[112] C. E. Aalseth, P. S. Barbeau, et al., "CoGeNT: A search for low-mass dark matter using p-type point contact germanium detectors", Physical Review D **88**, 012002 (2013), arXiv: 1208.5737.

[113] P. J. Fox, R. Harnik, et al., "LEP shines light on dark matter", Physical Review D **84**, 014028 (2011), arXiv: 1103.0240.

[114] Y. Bai, P. J. Fox, and R. Harnik, "The Tevatron at the frontier of dark matter direct detection", Journal of High Energy Physics **2010**, 48 (2010), arXiv: 1005.3797.

[115] J. Goodman, M. Ibe, et al., "Constraints on light Majorana dark matter from colliders", Physics Letters B **695**, 185–188 (2011), arXiv: 1005.1286.

[116] J. Goodman, M. Ibe, et al., "Constraints on dark matter from colliders", Physical Review D **82**, 116010 (2010), arXiv: 1008.1783.

[117] H. Dreiner, D. Schmeier, and J. Tattersall, "Contact interactions probe effective dark-matter models at the LHC", EPL (Europhysics Letters) **102**, 51001 (2013), arXiv: 1303.3348.

[118] C. Bartels, M. Berggren, and J. List, "Characterising WIMPs at a future e^+e^- Linear Collider", The European Physical Journal C **72**, 2213 (2012), arXiv: 1206.6639.

[119] H. K. Dreiner, M. Huck, et al., "Illuminating dark matter at the ILC", Physical Review D **87**, 075015 (2013), arXiv: 1211.2254.

[120] G. Aad, T. Abajyan, et al., "Search for dark matter candidates and large extra dimensions in events with a jet and missing transverse momentum with the ATLAS detector", Journal of High Energy Physics **2013**, 75 (2013), arXiv: 1210.4491.

[121] S. Chatrchyan, V. Khachatryan, et al., "Search for dark matter and large extra dimensions in monojet events in pp collisions at $\sqrt{s} = 7\text{TeV}$", Journal of High Energy Physics **2012**, 94 (2012), arXiv: 1206.5663.

[122] L. G. van den Aarssen, T. Bringmann, and Y. C. Goedecke, "Thermal decoupling and the smallest subhalo mass in dark matter models with Sommerfeld-enhanced annihilation rates", Physical Review D **85**, 123512 (2012), arXiv: 1202.5456.

[123] P. Gondolo and G. B. Gelmini, "Cosmic abundances of stable particles: improved analysis", Nuclear Physics B **360**, 145–179 (1991).

[124] S. Dodelson, *Modern Cosmology* (Academic Press, 2003).

[125] E. Müller, "Hydrodynamik in der Astrophysik: Grundlagen, numerische Verfahren und Anwendungen", 2012.

[126] G. Jungman, M. Kamionkowski, and K. Griest, "Supersymmetric Dark Matter", Physics Reports **267**, 195–373 (1995), arXiv: hep-ph/9506380.

[127] K. Griest and D. Seckel, "Three exceptions", Physical Review D **43**, 3191–3203 (1991).

[128] J. Edsjö, "Neutralino relic density including coannihilations", Physical Review D **56**, 1879–1894 (1997), arXiv: hep-ph/9704361.

[129] J. Edsjo, "Aspects of Neutrino Detection of Neutralino Dark Matter", PhD thesis (Apr. 1997), p. 92, arXiv: hep-ph/9704384.

[130] P. Binétruy, G. Girardi, and P. Salati, "Constraints on a system of two neutral fermions from cosmology", Nuclear Physics B **237**, 285–306 (1984).

[131] P. Salati, "Heavy neutrinos: the heterodox strikes back", Physics Letters B **253**, 173–180 (1991).

[132] D. J. Fixsen, "The Temperature of the Cosmic Microwave Background", The Astrophysical Journal **707**, 916–920 (2009), arXiv: 0911.1955.

[133] G. Bélanger, F. Boudjema, et al., "micrOMEGAs: A program for calculating the relic density in the MSSM", Computer Physics Communications **149**, 103–120 (2002), arXiv: hep-ph/0112278.

[134] G. Bélanger, F. Boudjema, et al., "micrOMEGAs: Version 1.3", Computer Physics Communications **174**, 577–604 (2006), arXiv: hep-ph/0405253.

[135] G. Bélanger, F. Boudjema, et al., "Indirect search for dark matter with micrOMEGAs 2.4", Computer Physics Communications **182**, 842–856 (2011), arXiv: 1005.4133.

[136]   P. Gondolo, J. Edsjö, et al., "DarkSUSY: computing supersymmetric dark matter properties numerically", Journal of Cosmology and Astroparticle Physics **2004**, 008–008 (2004), arXiv: astro-ph/0406204.

[137]   A. Arbey and F. Mahmoudi, "SuperIso Relic: A program for calculating relic density and flavor physics observables in Supersymmetry", Computer Physics Communications **181**, 1277–1292 (2010), arXiv: 0906.0369.

[138]   J. Hamann, S. Hannestad, et al., "How robust are inflation model and dark matter constraints from cosmological data?", Physical Review D **75**, 023522 (2007), arXiv: astro-ph/0611582.

[139]   A. Arbey and F. Mahmoudi, "SUSY constraints from relic density: High sensitivity to pre-BBN expansion rate", Physics Letters B **669**, 46–51 (2008), arXiv: 0803.0741.

[140]   M. Hindmarsh and O. Philipsen, "Dark matter of weakly interacting massive particles and the QCD equation of state", Physical Review D **71**, 087302 (2005), arXiv: hep-ph/0501232.

[141]   S. Matsumoto and M. Yoshimura, "Temperature power law of equilibrium heavy particle density", Physical Review D **61**, 123508 (2000), arXiv: hep-ph/9910393.

[142]   T. Wizansky, "Finite temperature corrections to relic density calculations", Physical Review D **74**, 065007 (2006), arXiv: arXiv:hep-ph/0605179v2.

[143]   C. E. Yaguna, "Large contributions to dark matter annihilation from three-body final states", Physical Review D **81**, 075024 (2010), arXiv: 1003.2730.

[144]   T. Bringmann and F. Calore, "Significant Enhancement of Neutralino Dark Matter Annihilation", (2013), arXiv: 1308.1089.

[145]   W. Porod, "SPheno, a program for calculating supersymmetric spectra, SUSY particle decays and SUSY particle production at e^+e^- colliders", Computer Physics Communications **153**, 275–315 (2003), arXiv: hep-ph/0301101.

[146]   B. Allanach, "SOFTSUSY: A program for calculating supersymmetric spectra", Computer Physics Communications **143**, 305–331 (2002), arXiv: hep-ph/0104145.

[147]   H. Baer, F. E. Paige, et al., "ISAJET 7.69: A Monte Carlo Event Generator for pp, $\bar{p}p$, and $e^=e^-$ Reactions", 95 (2003), arXiv: hep-ph/0312045.

[148]   B. C. Allanach, S. Kraml, and W. Porod, "Theoretical uncertainties in sparticle mass predictions from computational tools", Journal of High Energy Physics **2003**, 22 (2003), arXiv: hep-ph/0302102.

[149]   B. Allanach, G. Belanger, et al., "Requirements on collider data to match the precision of WMAP on supersymmetric dark matter", Journal of High Energy Physics **2004**, 020–020 (2004), arXiv: hep-ph/0410091.

[150] B. C. Allanach, G. Bélanger, et al., "Uncertainties in the Prediction of the Relic Density of Supersymmetric Dark Matter", 4 (2004), arXiv: hep-ph/0410049.

[151] B. C. Allanach, G. Belanger, et al., "Uncertainties in Relic Density Calculations in mSUGRA", 6 (2004), arXiv: hep-ph/0402161.

[152] G. Bélanger, S. Kraml, and A. Pukhov, "Comparison of supersymmetric spectrum calculations and impact on the relic density constraints from WMAP", Physical Review D **72**, 015003 (2005), arXiv: hep-ph/0502079.

[153] A. Chatterjee, M. Drees, and S. Kulkarni, "Radiative Corrections to the Neutralino Dark Matter Relic Density - an Effective Coupling Approach", Physical Review D **86**, 37 (2012), arXiv: 1209.2328.

[154] N. Baro, F. Boudjema, and A. Semenov, "Full one-loop corrections to the relic density in the MSSM: A few examples", Physics Letters B **660**, 550–560 (2008), arXiv: 0710.1821.

[155] N. Baro, F. Boudjema, et al., "Relic density at one-loop with gauge boson pair production", Physical Review D **81**, 015005 (2010), arXiv: 0910.3293.

[156] B. Herrmann and M. Klasen, "Supersymmetric QCD corrections to dark matter annihilation in the Higgs funnel region", Physical Review D **76**, 117704 (2007), arXiv: 0709.0043.

[157] B. Herrmann, M. Klasen, and K. Kovařík, "Supersymmetric QCD effects on neutralino dark matter annihilation beyond scalar or gaugino mass unification", Physical Review D **80**, 085025 (2009), arXiv: 0907.0030.

[158] B. Herrmann, M. Klasen, and K. Kovařík, "Neutralino annihilation into massive quarks with supersymmetric QCD corrections", Physical Review D **79**, 061701 (2009), arXiv: 0901.0481.

[159] A. Freitas, "Radiative corrections to bino-stop co-annihilation", Physics Letters B **652**, 280–284 (2007), arXiv: 0705.4027.

[160] P. Skands, B. Allanach, et al., "SUSY Les Houches Accord: Interfacing SUSY Spectrum Calculators, Decay Packages, and Event Generators", Journal of High Energy Physics **2004**, 036–036 (2004), arXiv: hep-ph/0311123.

[161] B. Allanach, C. Balázs, et al., "SUSY Les Houches Accord 2", Computer Physics Communications **180**, 8–25 (2009), arXiv: 0801.0045.

[162] C. Boehm and A. Djouadi, "Light scalar top quarks and supersymmetric dark matter", Physical Review D **62**, 035012 (2000), arXiv: hep-ph/9911496.

[163] H. Baer, C. Balázs, and A. Belyaev, "Neutralino relic density in minimal supergravity with co-annihilations", Journal of High Energy Physics **2002**, 042–042 (2002), arXiv: hep-ph/0202076.

[164] J. Ellis, K. A. Olive, and Y. Santoso, "Calculations of neutralino-stop coannihilation in the CMSSM", Astroparticle Physics **18**, 395–432 (2003), arXiv: hep-ph/0112113.

[165] J. Edsjö, M. Schelke, et al., "Accurate relic densities with neutralino, chargino and sfermion coannihilations in mSUGRA", Journal of Cosmology and Astroparticle Physics **2003**, 001–001 (2003), arXiv: hep-ph/0301106.

[166] I. Gogoladze, S. Raza, and Q. Shafi, "Neutralino-sbottom coannihilation in SU(5)", Journal of High Energy Physics **2012**, 54 (2012), arXiv: 1111.6299.

[167] J. Ellis, T. Falk, and K. A. Olive, "Neutralino-stau coannihilation and the cosmological upper limit on the mass of the lightest supersymmetric particle", Physics Letters B **444**, 367–372 (1998), arXiv: hep-ph/9810360.

[168] D. Delepine, J.-M. Gérard, et al., "A light stop and electroweak baryogenesis", Physics Letters B **386**, 183–188 (1996), arXiv: hep-ph/9604440.

[169] M. Carena, G. Nardini, et al., "The effective theory of the light stop scenario", Journal of High Energy Physics **2008**, 062–062 (2008), arXiv: 0806.4297.

[170] M. Carena, G. Nardini, et al., "MSSM Electroweak Baryogenesis and LHC Data", Journal of High Energy Physics **2013**, 28 (2012), arXiv: 1207.6330.

[171] M. Papucci, J. T. Ruderman, and A. Weiler, "Natural SUSY endures", Journal of High Energy Physics **2012**, 35 (2012), arXiv: 1110.6926.

[172] Z.-H. Yu, X.-J. Bi, et al., "Detecting light stop pairs in coannihilation scenarios at the LHC", Physical Review D **87**, 055007 (2013), arXiv: 1211.2997.

[173] C. Kilic and B. Tweedie, "Cornering light stops with dileptonic m T2", Journal of High Energy Physics **2013**, 110 (2013), arXiv: 1211.6106.

[174] S. Heinemeyer, O. Stål, and G. Weiglein, "Interpreting the LHC Higgs search results in the MSSM", Physics Letters B **710**, 201–206 (2012), arXiv: 1112.3026.

[175] M. Badziak, E. Dudas, et al., "Inverted sfermion mass hierarchy and the Higgs boson mass in the MSSM", Journal of High Energy Physics **2012**, 155 (2012), arXiv: 1205.1675.

[176] M. Carena, S. Heinemeyer, et al., "MSSM Higgs Boson Searches at the LHC: Benchmark Scenarios after the Discovery of a Higgs-like Particle", 33 (2013), arXiv: 1302.7033.

[177] A. Arbey, M. Battaglia, et al., "An update of the constraints on the phenomenological MSSM from the new LHC Higgs results", Physics Letters B **720**, 153–160 (2013), arXiv: 1211.4004.

[178] H. E. Haber, R. Hempfling, and A. H. Hoang, "Approximating the radiatively corrected Higgs mass in the minimal supersymmetric model", Zeitschrift für Physik C Particles and Fields **75**, 539–554 (1997), arXiv: hep-ph/9609331.

[179]   A. Fowlie, K. Kowalska, et al., "Dark matter and collider signatures of the MSSM", 41 (2013), arXiv: 1306.1567.

[180]   J. A. Aguilar-Saavedra, A. Ali, et al., "Supersymmetry parameter analysis: SPA convention and project", The European Physical Journal C **46**, 43–60 (2006), arXiv: hep-ph/0511344.

[181]   T. A. Collaboration, "Measurements of the properties of the Higgs-like boson in the two photon decay channel with the ATLAS detector using 25 fb^{-1} of proton-proton collision data", (2013).

[182]   G. Degrassi, S. Heinemeyer, et al., "Towards high-precision predictions for the MSSM Higgs sector", The European Physical Journal C - Particles and Fields **28**, 133–143 (2003), arXiv: hep-ph/0212020.

[183]   J. L. Feng, P. Kant, et al., "3-Loop Corrections to the Higgs Boson Mass and Implications for Supersymmetry at the LHC", 4 (2013), arXiv: 1306.2318.

[184]   W. Porod and F. Staub, *SPheno 3.1: extensions including flavour, CP-phases and models beyond the MSSM (talk given at TOOLS 2012)*, 2012.

[185]   The Heavy Flavor Averaging Group, D. Asner, et al., "Averages of b-hadron, c-hadron, and tau-lepton Properties", 288 (2010), arXiv: 1010.1589.

[186]   K. Ishiwata, N. Nagata, and N. Yokozaki, "Natural supersymmetry and constraints", Physics Letters B **710**, 145–148 (2012), arXiv: 1112.1944.

[187]   W. Pauli and F. Villars, "On the Invariant Regularization in Relativistic Quantum Theory", Reviews of Modern Physics **21**, 434–444 (1949).

[188]   G. 't Hooft and M. Veltman, "Regularization and renormalization of gauge fields", Nuclear Physics B **44**, 189–213 (1972).

[189]   R. Delbourgo and V. B. Prasad, "Supersymmetry in the four-dimensional limit", Journal of Physics G: Nuclear Physics **1**, 377–380 (1975).

[190]   W. Siegel, "Supersymmetric dimensional regularization via dimensional reduction", Physics Letters B **84**, 193–196 (1979).

[191]   G. 't Hooft and M. Veltman, "Scalar one-loop integrals", Nuclear Physics B **153**, 365–401 (1979).

[192]   G. Passarino and M. Veltman, "One-loop corrections for e annihilation into $\mu^+\mu^-$ in the Weinberg model", Nuclear Physics B **160**, 151–207 (1979).

[193]   A. Denner, "Techniques for the calculation of electroweak radiative corrections at the one-loop level and results for W-physics at LEP200", Fortsch.Phys. **41**, 307–420 (1991), arXiv: 0709.1075.

[194]   K. Kovarik, *Hitchhiker's Guide To Renormalization* (Not yet published).

[195]   S. Dittmaier, "Separation of soft and collinear singularities from one-loop N-point integrals", Nuclear Physics B **675**, 447–466 (2003), arXiv: hep-ph/0308246.

[196] R. K. Ellis and G. Zanderighi, "Scalar one-loop integrals for QCD", Journal of High Energy Physics **2008**, 002–002 (2008), arXiv: 0712.1851.

[197] A. Denner and S. Dittmaier, "Scalar one-loop 4-point integrals", Nuclear Physics B **844**, 199–242 (2011), arXiv: 1005.2076.

[198] J. A. M. Vermaseren, "New features of FORM", (2000), arXiv: math-ph/0010025.

[199] R. Mertig, M. Böhm, and A. Denner, "Feyn Calc - Computer-algebraic calculation of Feynman amplitudes", Computer Physics Communications **64**, 345–359 (1991).

[200] T. Hahn, "FormCalc 6", Proceedings of Science **ACAT08**, 121 (2008), arXiv: 0901.1528.

[201] A. Pukhov, "CalcHEP 2.3: MSSM, structure functions, event generation, batchs, and generation of matrix elements for other packages", (2004), arXiv: hep-ph/0412191.

[202] M. Böhm, A. Denner, and H. Joos, *Gauge Theories of the Strong and Electroweak Interaction* (Vieweg Verlag, Friedr, & Sohn Verlagsgesellschaft mbH, 2001).

[203] M. E. A. Peskin and D. V. A. Schroeder, *An Introduction To Quantum Field Theory*, Advanced book classics (Addison-Wesley Publishing Company, 1995).

[204] T. Muta, *Foundations of Quantum Chromodynamics* (World Scientific Publishing Co. Pte. Ltd., 2010).

[205] J. C. Collins, *Renormalization: An Introduction to Renormalization, the Renormalization Group and the Operator-Product Expansion* (Cambridge University Press, 1984).

[206] S. Heinemeyer, W. Hollik, et al., "High-precision predictions for the MSSM Higgs sector at $\mathcal{O}(\alpha_b \alpha_s)$", The European Physical Journal C **39**, 465–481 (2005), arXiv: hep-ph/0411114.

[207] S. Heinemeyer, H. Rzehak, and C. Schappacher, "Proposals for Bottom Quark/Squark Renormalization in the Complex MSSM", Physical Review D **82**, 47 (2010), arXiv: 1007.0689.

[208] H. Eberl, K. Hidaka, et al., "Improved supersymmetric QCD corrections to Higgs boson decays into quarks and squarks", Physical Review D **62**, 055006 (2000), arXiv: hep-ph/9912463.

[209] C. Weber, K. Kovarik, et al., "Complete one-loop corrections to decays of charged and CP-even neutral Higgs bosons into sfermions", Nuclear Physics B **776**, 34 (2007), arXiv: hep-ph/0701134.

[210] N. Baro and F. Boudjema, "Automatized full one-loop renormalization of the MSSM. II. The chargino-neutralino sector, the sfermion sector, and some applications", Physical Review D **80**, 076010 (2009), arXiv: 0906.1665.

[211] K. Melnikov and A. Yelkhovsky, "The b quark low-scale running mass from Upsilon sum rules", Physical Review D **59**, 22 (1998), arXiv: hep-ph/9805270.

[212] A. H. Hoang, "1S and MSbar Bottom Quark Masses from Upsilon Sum Rules", Physical Review D **61**, 20 (1999), arXiv: hep-ph/9905550.

[213] M. Beneke and A. Signer, "The bottom $\overline{\text{MS}}$ quark mass from sum rules at next-to-next-to-leading order", Physics Letters B **471**, 14 (1999), arXiv: hep-ph/9906475.

[214] A. A. Penin and A. A. Pivovarov, "Bottom quark pole mass and $|V_{cb}|$ matrix element from $R(e^+e^- \to b\bar{b})$ and $\Gamma_{sl}(b \to cl\nu_l)$ in the next-to-next-to-leading order", Nuclear Physics B **549**, 217–241 (1998), arXiv: hep-ph/9807421.

[215] H. Baer, J. Ferrandis, et al., "Relating bottom quark mass in $\overline{\text{DR}}$ and $\overline{\text{MS}}$ regularization schemes", Physical Review D **66**, 074007 (2002), arXiv: hep-ph/0207126.

[216] K. G. Chetyrkin, "Correlator of the quark scalar currents and $\Gamma_{tot}(\text{H} \to$ hadrons) at $\text{O}(\alpha_s^3)$ in pQCD", Physics Letters B **390**, 11 (1996), arXiv: hep-ph/9608318.

[217] P. A. Baikov, K. G. Chetyrkin, and J. H. Kühn, "Scalar Correlator at $\text{O}(\alpha_s^4)$, Higgs Decay into b-quarks and Bounds on the Light Quark Masses", Physical Review Letters **96**, 5 (2005), arXiv: hep-ph/0511063.

[218] K. G. Chetyrkin and A. Kwiatkowski, "Second Order QCD Corrections to Scalar and Pseudoscalar Higgs Decays into Massive Bottom Quarks", Nuclear Physics B **461**, 18 (1995), arXiv: hep-ph/9505358.

[219] M. Carena, D. Garcia, et al., "Effective lagrangian for the $\bar{t}bH^+$ interaction in the MSSM and charged Higgs phenomenology", Nuclear Physics B **577**, 33 (1999), arXiv: hep-ph/9912516.

[220] J. Guasch, P. Häfliger, and M. Spira, "MSSM Higgs Decays to Bottom Quark Pairs revisited", Physical Review D **68**, 16 (2003), arXiv: hep-ph/0305101.

[221] K. Kovařík, C. Weber, et al., "Full $\text{O}(\alpha)$ corrections to $e^+e^- \to \tilde{f}_i \bar{\tilde{f}}_j$", Physical Review D **72**, 053010 (2005), arXiv: hep-ph/0506021.

[222] H. Eberl, "Strahlungskorrekturen im minimalen supersymmetrischen Standardmodell", PhD thesis (Technische Universität Wien, 1998).

[223] R. Harlander, L. Mihaila, and M. Steinhauser, "Running of α_s and m_b in the MSSM", Physical Review D **76**, 055002 (2007), arXiv: 0706.2953.

[224] M. Veltmann and G. 't Hooft, "Scalar one-loop integrals", Nuclear Physics B **153**, 365–401 (1979).

[225] S. Dawson, L. Orr, et al., "Next-to-leading order QCD corrections to $pp \to t\bar{t}h$ at the CERN Large Hadron Collider", Physical Review D **67**, 071503 (2003), arXiv: hep-ph/0211438.

[226] W. Beenaaker, H. Kuijf, and W. L. Van Neerven, "QCD corrections to heavy-quark production in pp collisions", Physical Review D **40** (1989).

[227] G. Rodrigo, A. Santamaria, and M. Bilenky, "Dimensionally regularized box and phase-space integrals involving gluons and massive quarks", Journal of Physics G: Nuclear and Particle Physics **25**, 1593–1606 (1999), arXiv: hep-ph/9703360.

[228] B. W. Harris and J. F. Owens, "The two cutoff phase space slicing method", Physical Review D **65**, 44 (2001), arXiv: hep-ph/0102128.

[229] F. Berends and W. Giele, "Recursive calculations for processes with n gluons", Nuclear Physics B **306**, 759–808 (1988).

[230] S. Catani and M. Grazzini, "The soft-gluon current at one-loop order", Nuclear Physics B **591**, 435–454 (2000), arXiv: hep-ph/0007142.

[231] J. Campbell and E. Glover, "Double unresolved approximations to multiparton scattering amplitudes", Nuclear Physics B **527**, 264–288 (1998), arXiv: hep-ph/9710255.

[232] W. L. Van Neerven, "Dimensional Regularization of Mass and Infrared Singularities in two-loop on-shell Vertex Functions", Nuclear Physics B **268**, 453–488 (1986).

[233] J. Smith, D. Thomas, and W. L. Van Neerven, "QCD corrections to the reaction p+p-> W + gamma + X", Zeitschrift für Physik C, Particles and Fields **290**, 267–290 (1989).

[234] B. Harris and J. Smith, "Heavy-quark correlations in deep-inelastic electroproduction", Nuclear Physics B **452**, 109–160 (1995).

[235] I. Bojak, "NLO QCD Corrections to the Polarized Photo- and Hadroproduction of Heavy Quarks", PhD thesis (May 2000), p. 189, arXiv: hep-ph/0005120.

[236] G. Bodwin, "Factorization of the Drell-Yan cross section in perturbation theory", Physical Review D **31** (1985).

[237] G. Bodwin, "Erratum - Factorization of the Drell-Yan cross section in perturbation theory", Physical Review D **34**, 3932 (1986).

[238] Z. Kunszt and D. Soper, "Calculation of jet cross sections in hadron collisions at order α_s^3", Physical Review D **46** (1992).

[239] M. L. Mangano, P. Nason, and G. Ridolfi, "Heavy-quark correlations in hadron collisions at next-to-leading order", Nuclear Physics B **373**, 295–345 (1992).

[240] G. Altarelli and G. Parisi, "Asymptotic Freedom in Parton Language", Nuclear Physics B **126**, 298–318 (1977).

[241] S. Catani and M. Seymour, "The dipole formalism for the calculation of QCD jet cross sections at next-to-leading order", Physics Letters B **378**, 287–301 (1996), arXiv: hep-ph/9602277.

[242] S. Catani and M. Seymour, "A general algorithm for calculating jet cross sections in NLO QCD", Nuclear Physics B **485**, 291–419 (1997), arXiv: hep-ph/9605323.

[243] S. Dittmaier, "A general approach to photon radiation off fermions", Nuclear Physics B **565**, 69–122 (2000), arXiv: hep-ph/9904440.

[244] S. Catani, S. Dittmaier, and Z. Trócsányi, "One-loop singular behaviour of QCD and SUSY QCD amplitudes with massive partons", Physics Letters B **500**, 149–160 (2001), arXiv: hep-ph/0011222.

[245] S. Catani, S. Dittmaier, et al., "The dipole formalism for next-to-leading order QCD calculations with massive partons", Nuclear Physics B **627**, 189–265 (2002), arXiv: hep-ph/0201036.

[246] T. Eynck, E. Laenen, et al., "Comparison of phase space slicing and dipole subtraction methods for $\gamma^* \rightarrow Q\bar{Q}$", The European Physical Journal C - Particles and Fields **23**, 259–266 (2002), arXiv: hep-ph/0109246.

[247] D. A. Kosower, "Antenna factorization of gauge-theory amplitudes", Physical Review D **57**, 5410–5416 (1998), arXiv: hep-ph/9710213.

[248] D. Kosower, "Antenna factorization in strongly ordered limits", Physical Review D **71**, 045016 (2005), arXiv: hep-ph/0311272.

[249] A. G.-D. Ridder and M. Ritzmann, "NLO antenna subtraction with massive fermions", Journal of High Energy Physics **2009**, 041–041 (2009), arXiv: 0904.3297.

[250] S. Frixione, Z. Kunszt, and A. Signer, "Three-jet cross sections to next-to-leading order", Nuclear Physics B **467**, 399–442 (1996), arXiv: hep-ph/9512328.

[251] A. S. Belyaev, E. E. Boos, and L. V. Dudko, "Single Top Quark at Future Hadron Colliders. Complete Signal and Background Study", Physical Review D **59**, 15 (1998), arXiv: hep-ph/9806332.

[252] S. Frixione, E. Laenen, et al., "Single-top hadroproduction in association with a W boson", Journal of High Energy Physics **2008**, 029–029 (2008), arXiv: 0805.3067.

[253] W. Hollik, J. M. Lindert, and D. Pagani, "NLO corrections to squark-squark production and decay at the LHC", Journal of High Energy Physics **2013**, 139 (2013), arXiv: 1207.1071.

[254] R. Gavin, C. Hangst, et al., "Matching Squark Pair Production at NLO with Parton Showers", 42 (2013), arXiv: 1305.4061.

[255] W. Beenakker, "Squark and gluino production at hadron colliders", Nuclear Physics B **492**, 51–103 (1997), arXiv: hep-ph/9610490.

[256] T. Tait, "t W- mode of single top quark production", Physical Review D **61**, 034001 (1999), arXiv: hep-ph/9909352.

[257] D. Gonçalves-Netto, D. López-Val, et al., "Automated squark and gluino production to next-to-leading order", Physical Review D **87**, 014002 (2013), arXiv: 1211.0286.

[258] A. Hryczuk and R. Iengo, "The one-loop and Sommerfeld electroweak corrections to the Wino dark matter annihilation", JHEP **1201**, 163 (2012), arXiv: hep-ph/1111.2916.

[259] A. Hryczuk, "The Sommerfeld enhancement for scalar particles and application to sfermion co-annihilation regions", Phys.Lett. **B699**, 271–275 (2011), arXiv: hep-ph/1102.4295.

[260] M. Drees and J. Gu, "Enhanced One-Loop Corrections to WIMP Annihilation and their Thermal Relic Density in the Coannihilation Region", Phys.Rev. **D87**, 063524 (2013), arXiv: hep-ph/1301.1350.